NASA Technical Memorandum 106782

The Aeroacoustics of Supersonic Coaxial Jets

Milo D. Dahl
Lewis Research Center
Cleveland, Ohio

November 1994

National Aeronautics and
Space Administration

Abstract

Instability waves have been established as the dominant source of mixing noise radiating into the downstream arc of a supersonic jet when the waves have phase velocities that are supersonic relative to ambient conditions. Recent theories for supersonic jet noise have used the concepts of linear instability wave theory for predicting radiated noise. If the mean flow is known, the stability characteristics of the normal modes are obtained for a supersonic jet at each axial location. The axial variation of these characteristics represents a growing and decaying instability wave in the jet shear layer. The noise radiated by this instability wave is determined by a matching process between the inner instability wave solution and the outer acoustic solution. This analytical technique is extended to the prediction of noise radiation from supersonic coaxial jets.

The instability wave noise generation analysis requires a known mean flow. The mean flow of supersonic coaxial jets are not described easily in terms of analytic functions. To provide mean flow profiles at all axial locations, a numerical scheme is developed to calculate the mean flow properties of a coaxial jet. The Reynolds averaged, compressible, parabolic boundary layer equations are solved using a mixing length turbulence model. Empirical correlations are developed to provide the shear layer spreading effects due to velocity and temperature ratios and Mach number. Both normal velocity profile and inverted velocity profile coaxial jets are considered with the mixing length model modified in both cases to obtain reasonable results when the two stream jet merges into a single fully developed jet. The mean flow calculations show good qualitative and quantitative resemblance to measured single and coaxial jet flows.

The analytical and numerical analyses are used to conduct a parametric study of supersonic coaxial jets. The results from mean flow and stability calculations are used to predict the noise radiation from coaxial jets with different operating conditions. Comparisons are made between different coaxial jets and to a single equivalent jet with the same total thrust, mass flow, and exit area. The area ratio for the coaxial jets is held constant. Results indicate that normal velocity profile jets can have noise reductions compared to the single equivalent jet, especially if the outer jet stream is hotter than the inner jet stream. No noise reductions are found for inverted velocity profile jets operated at the minimum noise condition compared to the single equivalent jet. However, it is inferred that changes in area ratio may provide noise reduction benefits for inverted velocity profile jets.

Table of Contents

List of Tables

List of Figures

List of Symbols

Chapter 2:

A	momentum equation coefficient, Eq. (2.19)
B	energy equation coefficient, Eq. (2.24)
c_p	specific heat at constant pressure
C_1	incompressible mixing length factor
C_2	compressible mixing length factor
D	diameter, energy equation coefficient, Eq. (2.24)
$D(1/2)$	jet diameter between half velocity points
H	total enthalpy
j	axial grid point index
k	radial grid point index
ℓ	characteristic length scale
N	total number of grid spacings
p	pressure
Pr	Prandtl number
r	radial coordinate, velocity ratio
$r(1/2)$	jet radius at half velocity point
R	radius
R_g	gas constant
s	density ratio
S_1	Sutherland constant
T	temperature
u	axial velocity
U	mean axial velocity
v	radial velocity
x	axial coordinate
Δr	radial grid spacing
ΔU	axial velocity difference across shear layer, $\lvert U_1 - U_2 \rvert$
Δx	axial grid spacing
$\Delta\Psi$	stream function grid spacing
Δ^-	grid spacing coefficient, Eq. (2.22)
Δ^+	grid spacing coefficient, Eq. (2.23)
μ	viscosity
ρ	density
Ψ	stream function

Θ	momentum thickness
Subscripts	
1	inner stream
2	outer stream
c	centerline condition
j	axial grid point index, jet exit reference condition
k	radial grid point index
∞	external conditions
eff	effective
o	reference
T	turbulent
Superscripts	
$\bar{}$	time averaged mean variable
$'$	fluctuating variable
$\sim$	mass averaged variable
Chapter 3:	
A, B	amplitude functions
$\mathbf{A}(c)$	coefficient matrix of eigenvalue problem
b	jet half-width
c	complex phase velocity, eigenvalue
D	diameter
$D(\psi)$	far field directivity function
g	Fourier transform of instability wave
G_m	inhomogeneous function, Eq. (3.20)
h	enthalpy
$H_n^{(1)}$	Hankel function of first kind, order n
$H_n^{(2)}$	Hankel function of second kind, order n
i	$\sqrt{-1}$
Im	imaginary part of complex number
k	Fourier transform variable, radial grid point index
m	asymptotic series index
M	Mach number, size of FFT
n	azimuthal mode number
N	number of radial grid spacings, large positive number
p	pressure
(r, θ, x)	cylindrical coordinates
$\mathbf{r}$	complex radial coordinate, $\mathbf{r} = r + ir_i$
$\bar{r}$	outer radial coordinate
$\tilde{r}$	intermediate variable

r_c	critical point in complex r-plane
r_i	imaginary part of r
r_m	radial location of jet outer boundary
$r(1/2)$	jet radius at half velocity point
R	radius, far field radius in spherical coordinates
Re	real part of complex number
R_g	gas constant
s	slow axial coordinate
St	Strouhal number
t	time
T	temperature
U	exit axial velocity
(v, w, u)	velocity components in cylindrical coordinates
$\mathbf{V}$	velocity vector
α	local wavenumber, eigenvalue
γ	ratio of specific heats
δ_{ij}	Kronecker delta
$\delta(\varepsilon)$	gauge functions
Δx	axial resolution
$\Delta\eta$	wavenumber resolution
ε	small parameter
ζ	local eigenfunctions
η	scaled wavenumber
η_c	supersonic phase velocity wavenumber cutoff
λ	complex wavenumber argument of Hankel function
Θ	argument of an exponential function
ρ	density
ϕ	fluctuating phase function
Φ	stationary phase exponential function, Eq. (3.84)
ψ	polar angle, spherical coordinates
ω	radian frequency
∇	vector differential operator

Subscripts

1	inner stream
2	outer stream
c	centerline conditions
e	equivalent single jet
j	exit conditions
k	radial grid point index

m	asymptotic series index
∞	external or ambient conditions
Superscripts	
$\sim$	Fourier transformed variable
$\wedge$	fluctuating amplitude function
$'$	fluctuating variable
$-$	time averaged mean variable
i	inner solution
o	outer solution
$*$	dimensional variable
Chapter 4:	
A	exit area
c_{ph}	local phase velocity, ω/α_r
D	exit diameter
f	frequency
g	Fourier transform of instability wave
M	exit Mach number
n	azimuthal mode number
r	velocity ratio, U_2/U_1
$r(1/2)$	jet radius at half velocity point
s	density ratio, ρ_2/ρ_1, temperature ratio, T_1/T_2
T	exit temperature
U	exit axial velocity
ΔU	velocity difference, $\lvert U_1 - U_2 \rvert$
α	complex local eigenvalue, $\alpha_r + i\alpha_i$
$-\alpha_i$	local growth rate
Subscripts	
1	inner stream
2	outer stream
e	equivalent single jet or reference jet

Chapter 1

INTRODUCTION

The renewed interest in the development of a High Speed Civil Transport that is economically viable and environmentally compatible has re-energized research efforts on supersonic jet noise. This noise issue was addressed intensely in the supersonic transport program during the 1960's. The large funding level provided resources for large scale design and testing of jet nozzle hardware as well as facilities for small scale controlled experiments and for theoretical studies. When the program was abruptly terminated in 1971, the large scale design effort stopped, Stitt [1990]. However, a low level generic research program continued through the 1970's allowing small scale experiments and theoretical studies to advance the ideas that were beginning to appear (NASA [1969] and Goldstein [1976]). By the 1980's, funding levels were a small fraction of past levels as interest in supersonic jet noise issues waned. This lasted until 1987 when the United States government recognized the need to set national goals to maintain leadership in the increasingly competitive world of aviation. As described in a review by Darden et al. [1993], among these goals was an increase in research and development in supersonic transport technology. Given the history and the technical issues to be addressed in the High-Speed Research Program, NASA initiated in 1990, the community noise problem generated by supersonic jets is still a strong research motivator. To meet FAR 36 Stage 3 noise regulations (FAA [1990]), noise suppression technology will need to be advanced beyond current levels.

Virtually, since the beginning of jet aircraft transportation service, community noise created by jet exhausts has been a problem, Burns [1973]. Expanding service and increased awareness of noise pollution has only exacerbated the problem. The propensity to litigate, Bennett and Hoover [1991], and regulate, Linn and Tedrick [1991], the noise problem to a satisfactory resolution, without hampering the economic benefits of jet aircraft transportation, will not lead to a satisfactory public accommodation of jet aircraft without understanding the jet noise generation process. It is, as Lighthill [1954] wrote, "...largely as a result of the public odium with which the aircraft industry is threatened on account of the noise of jet aeroplanes" that a large number of experimental and theoretical studies have been performed on jet noise over the last 40 years. Thus, there is a continuing interest to understand the jet noise generation process, particularly those processes that are important to supersonic jet noise. Basic understanding leads to

means that may modify the noise generation process and provide acceptable community noise levels from supersonic jet aircraft.

This paper examines a method to modify the noise generation from a supersonic jet. A single, supersonic, axisymmetric jet with given initial velocity and temperature conditions is replaced by a dual stream, coaxial jet with different initial velocities and possibly different initial temperatures. At least one of the jet streams is supersonic. For classification purposes, when the coaxial jet flow has a higher inner stream velocity than an outer stream velocity, the jet is referred to as a normal velocity profile jet. If the outer stream velocity is higher than the inner stream, the jet has an inverted velocity profile. The jet stream temperatures do not enter into this classification. Thus, a normal velocity profile jet can have a normal temperature profile or an inverted temperature profile as can occur for an inverted velocity profile jet, also.

The study combines analytical and numerical techniques. The analytical technique is based on the theory that instability waves propagating in the jet shear layer at phase velocities that are supersonic relative to ambient are the dominant sources of mixing noise radiating in directions downstream from the jet. The mean flow of the supersonic jet is assumed to be perfectly expanded; thus, shocks are not considered in this study and the noises associated with them are ignored in the analysis. To complete the analytical solution, the developing mean flow properties must be known at every axial location. Due to the complexities of describing developing normal and inverted profile jets with various velocity and temperature conditions, the mean flow is determined numerically. Before describing these techniques in more detail, we first consider the emergence of the role of instability waves as a source of supersonic jet mixing noise and some experimental history on axisymmetric coaxial jets.

1.1 Instability Waves in Jets

The instability of a shear layer has long been recognized. Rayleigh [1877] discussed the analysis of a plane vortex sheet separating two fluids moving with different velocities. Based on earlier work by Helmholtz in 1868 and Kelvin in 1871, Rayleigh showed that for this ideal case of a vortex sheet separating frictionless fluids, the motion was always unstable and the instability increased with an increase in the frequency of the disturbance. However, he recognized that this result did not agree with experiments. Small jets that were seen to have sensitivities to sound at lower frequencies ceased showing any sensitivity to higher frequencies. He pointed out that the presence of fluid friction would immediately broaden the fluid discontinuity represented by the vortex sheet. As the fluids moved, the transition between them becomes more gradual, until at a transition layer width comparable to the wavelength of a disturbance, the previous analysis became

inapplicable. Rayleigh re-analyzed the problem for finite thickness shear layers and, assuming a frictionless fluid, developed an equation which was subsequently named after him; the Rayleigh equation. A number of simple flows were considered, both bounded and unbounded flows, using piecewise-linear approximations to describe the mean flow. These problems involved temporal stability and, basically, the analysis showed that as the shear layer grew, the instability increased with disturbance wavelength, reached some maximum value, and then decreased until neutral stability occurred. The shear layer was then not affected by the disturbance. Experimental evidence at the time was collected from jets with a flame or with smoke. The jet responded to acoustic excitation with the most sensitive position at the nozzle exit. The behavior of the jet was characterized visually as having gradually increasing sinuosity until the jet disintegrated.

Progress in the study of the instability of shear layers, or hydrodynamic stability, may be found in the texts by Lin [1955] and Drazin and Reid [1981]. With observations like Rayleigh's involving the jet disintegrating, these works study the instability of parallel shear flows as a means of transition from laminar to turbulent flows. Many studies were conducted to confirm that free shear flows were unstable in the inviscid limit due to the presence of a point of inflection in the mean velocity profile. In addition, the initial growth rates of the instability in shear flows compared well with predictions from linear stability theory. After transition, statistical methods were used in attempts to describe the turbulent jet flow.

Initially, the study of noise from turbulent jets was dominated by the theory developed by Lighthill [1952]. The fundamental equations of fluid motion were manipulated to isolate terms that represented the fluctuating stresses created in a localized region of space in a moving fluid. These fluctuating stresses became the source terms for the sound that propagated into the surrounding medium at rest. The theory resulted in the important scaling law that the total sound power radiated by the jet is proportional to the eighth power of the jet velocity. This theory was aggressively studied theoretically and much experimental work was conducted to verify it during the 1950's, 60's, and 70's as evident in reviews by NASA [1969], Crighton [1975], and Goldstein [1976]. More recently, Lilley [1991] has summarized, in some detail, the current status of the classical jet noise theory. Though the Lighthill approach applies to both subsonic and supersonic jets, after the early 1970's the growing recognition of the presence of large scale structures in shear flows and their representation as instability waves led to alternative theories for noise generation by supersonic jets.

Evidence began to mount that large structures and orderly patterns existed in turbulent jet flows. Puffs and vortices with length scales on the order of the shear layer thickness were observed. The benchmark papers by Crow and Champagne [1971] and Brown and Roshko [1974] confirmed the presence of large coherent structures in turbulent flow. The photographs in Brown and Roshko [1974] showed them clearly.

Furthermore, when Crow and Champagne [1971] subjected the turbulent jet to periodic forcing, hot-wire measurements showed that a wave was generated in the flow with initially growing characteristics that were in accord with linear stability theory. Thus, the large scale orderly structures were seen as having wave-like characteristics and the description of the structures as vortices or waves was considered complementary for turbulent free jets.

At the same time, proposals of the connection between large scale structures or instability waves and the noise radiation of perfectly expanded supersonic jets began to appear. Use of the Lighthill formulation had led to the concept of eddy Mach wave radiation where the turbulent eddies were convected at speeds greater than the ambient speed of sound (Goldstein [1976]). Though qualitative results were achieved, the true nature of the sound sources were still concealed. A representative attempt to model the sound sources as instability waves is found in Liu [1971]. Rather than using the Lighthill acoustic analogy, Liu built on the concept of splitting the flow quantities in the compressible equations of fluid motions into mean, periodic, and turbulent components to develop integral equations representing energy transfer between the components. The local mean flow was used to calculate the local amplification rates, phase speeds, and shape functions of the instability wave. The global amplitude of the wave versus axial distance was then found through the energy integrals. The instability wave was found to travel supersonically with an amplitude that peaked within the shear layer and decayed with distance perpendicular to the shear layer. These remnants of the instability wave outside the jet were used by Liu [1974] to calculate the near field noise generated by the jet. Liu suggested that the near field fluctuations resulting from instability wave analysis could be used in the Lighthill integral to represent the source terms for far field noise calculations. Care would have to be taken on the positioning of an imaginary cylinder placed around the jet on which the fluctuations were calculated and on the proper use of the retarded potential.

Tam [1971] took a more simplified approach to the early study of the radiation of sound by instability waves in supersonic jets. Modeling the jet with a cylindrical vortex sheet simplified the governing disturbance equations to a wave equation outside the jet and a convected wave equation inside with appropriate kinematic and dynamic boundary conditions between the two regions. An asymptotic solution outside the jet resulted in directional characteristics similar to those observed in shadowgraphs of supersonic jets. An extension of the theory modeled the mean flow as having a periodic flow structure, Tam [1972]. Disturbances would interact with this flow structure and large scale spiral-mode instabilities would be triggered at resonant conditions. The peak frequency of the jet power spectrum was predicted from this resonant condition and

found to agree favorably with measured power spectra of perfectly expanded cold supersonic jets. Later, this resonant condition theory was dropped from the theory of noise radiation from perfectly expanded jets, Tam [1975].

While these early supersonic jet noise theories were based on shadowgraphic evidence and near field acoustic measurements. It still remained to experimentally establish the link between large scale coherent structures and the noise radiation from supersonic shock free jets. The difficulty was in the inability of delicate instruments to measure the stability characteristics in supersonic jet shear layers. Some of these problems were overcome by conducting measurements in a low Reynolds number environment (McLaughlin et al. [1975, 1977] and Morrison and McLaughlin [1979, 1980]) and later extending measurements to moderate Reynolds numbers (Troutt and McLaughlin [1982]). At low Reynolds number, it was clearly established that the rapid growth of instability waves and their decay near the end of the potential core contributed to the major portion of the sound radiated. Initial instability wave growth rates and phase velocities agreed with linear theory and spectra peaks, sharply defined, had Strouhal numbers that appropriately agreed with the instability wave source. As Reynolds number increased, the spectra broadened but still peaked at the appropriate Strouhal numbers. Also, the instability wave characteristics still agreed with theory. Results at high Reynolds number were then inferred as being due to the same mechanism. While for the most part these measurements showed that the instability wave noise radiators traveled with phase velocities that were supersonic relative to the ambient speed of sound, there were examples of subsonic traveling waves that radiated noise from low Mach number jets. Though the experimental results were not always clearly understood at the time, they did lead to refinements to the models given in Tam [1975], Morris and Tam [1977], Tam and Morris [1980] and Tam and Burton [1984a]. Most of this latter history was recently summarized in Tam [1991].

1.2 Axisymmetric Coaxial Jets

The interest in the measurement of the noise radiated from coaxial jets increased as the by-pass jet engine was introduced as an alternative propulsion system to the noisy turbojet engine. Early results were inconclusive as to whether or not any variation in the outer stream velocity had any affect on the radiated noise, Greatrex [1961]. Kantarges and Cawthorn [1964] found that a cold outer stream added to a cold inner stream increased the noise. While a cold outer stream added to a hot inner stream seemed to have little impact on the noise. With the consensus that the noise reduction in by-pass engines was due to lower velocities at the same mass flow compared to single jets, Williams et al. [1969] measured noise reductions in cold coaxial jets at constant thrust. In addition to the noise reduction noted earlier, these results included reductions

due to the decrease in the mean shear of the combined flow. It is interesting to note that at constant thrust, the maximum reduction occurred at about $U_2/U_1 = 1$. Alternatively, by simply increasing the outer velocity U_2 for a fixed inner velocity U_1, the maximum noise reduction occurred at a velocity ratio of 0.5. This apparent noise reduction was confirmed by Eldred et al. [1971] and Dahlen [1972]. The latter noted reductions in high frequency noise including the peak of the jet noise spectrum and an increase in low frequency noise. Olsen and Friedman [1974] conducted a wide ranging study of coaxial nozzles and flow conditions. Their results showed minimum noise levels at velocity ratios of 0.4 to 0.5 with variations apparently due to changing area ratios. The shape of the far field spectra from subsonic coaxial jets were basically the same as single jets. Hence, only the peak frequency and level needed to be correlated with velocity ratio and area ratio. Thus, for subsonic jets, there appeared to be lower noise benefits in using coaxial jets with normal velocity profiles.

The apparent noise reduction benefits of two stream coaxial jets operating in subsonic conditions was convincing enough to look for similar benefits under supersonic conditions. Dosanjh and his colleagues conducted an extensive experimental study of supersonic coaxial jets. Using small scale nozzles, Dosanjh et al. [1969, 1970] and Yu and Dosanjh [1971] optically observed, measured, and documented the existence of a minimum noise condition for shock containing coaxial jets. They found that when the outer nozzle pressure ratio was fixed above critical, the inner nozzle pressure ratio could be increased from no flow conditions to some point where the measured overall sound power level was a minimum less than the outer jet alone. For higher inner pressure ratios, the noise increased. This minimum noise condition always occurred for inner nozzle pressure ratios less than the outer nozzle pressure ratios indicating that the coaxial jet operated with an initial inverted velocity profile. The optical shadowgraphs showed that the outer stream repetitive shock structure was destroyed at the minimum noise condition and replaced by a composite shock structure just downstream of the nozzle exit. Hence, the overall noise reduction was primarily due to a decrease in shock associated noise. The minimum noise condition depended on nozzle geometry with inner nozzle pressure ratios varying from 2.22 to 2.63.

Further studies on a larger scale coaxial supersonic nozzle were conducted and the results are detailed in Ahuja [1976], Bassiouni [1976] and Bhutiani [1976]. They confirmed the existence of a minimum noise condition and noted that downstream of the composite shock structure, the shocks were very weak or nonexistent indicating that the flow was similar to a properly expanded flow. Noise reductions were measured at all frequencies and at all angles. This would mean that not only was shock noise reduced, which dominates in the upstream direction, but that mixing noise was reduced as well, which dominates in the downstream direction. It was also found that directivity patterns could be changed by the choice of pressure and temperature operating conditions.

Tanna et al. [1979] conducted measurements of shock-free coaxial jets with inverted velocity profiles to study the effects of profile shaping in jet mixing noise. In addition, care was taken in choosing initial velocity and temperature conditions along with exit area in order to compare results on a constant thrust, mass flow, and exit area basis to a fully mixed equivalent single jet or reference jet. They found that high frequency noise increased at all angles and that low frequency noise decreased at angles closer to the jet exit axis. These changes were relative to the reference jet and they became larger as the velocity ratio increased above 1. Far field spectra remained largely unchanged by higher temperature ratios for a coaxial jet with both velocities the same. Since the far field spectra were peaking at the lower frequencies, the overall sound pressure levels were quieter for $U_2/U_1 > 1$ at smaller angles and noisier at 90 degrees. The higher frequency noise was generated primarily from the outer shear layer before the streams merged. As U_2/U_1 increased, the outer shear layer had a larger velocity difference to ambient resulting in higher eddy convection velocities, higher source velocities, and more noise. Conversely, the lower frequency noise was generated downstream of merging where the velocities were lower, resulting in less noise. Similar results were measured by Maus et al. [1980]. They concluded that the rapid decay of the maximum mean velocity in inverted velocity profile jets was a prominent reason for noise reduction compared to the reference jet.

After examining the shock-free, inverted profile coaxial jet data, Tanna [1980] reexamined some of the normal velocity profile data, discussed earlier, and compared the results to a reference jet at the same thrust, mass flow, and exit area. His conclusion was simply that normal profile coaxial jets, with both inner stream velocity and temperature greater than the outer stream, are noisier than the reference jet. A systematic study of normal velocity profile jets conducted by Tanna and Morris [1985] using the approach of Tanna et al. [1979] confirmed this conclusion. Given the constraint of constant exit area, one stream will always have a velocity higher than the reference jet in order to maintain constant total thrust and mass flow. Since the maximum velocity of a normal profile jet persists longer than the maximum velocity of an inverted profile jet, then in a Lighthill sense the normal velocity profile jet would generate more noise than the inverted profile jet.

The experimental work on coaxial jets was continued by Tanna et al. [1985] into the supersonic regime. The converging nozzles were operated above critical pressure ratios resulting in underexpanded, shock-containing jet flows. They also defined a minimum noise condition based on overall sound pressure level measurements at upstream angles where shock associated noise dominates. For a fixed outer nozzle pressure ratio above critical, minimum noise was found when the inner nozzle pressure ratio was slightly above critical at about 1.9. Depending on the initial velocities and temperatures of the two jet streams, this condition was found to hold for both inverted velocity profiles

and normal velocity profiles. Tam and Tanna [1985] discussed the differences with their basically fixed minimum noise condition inner nozzle pressure ratio and the varying inner nozzle pressure ratio of Dosanjh et al. They concluded that the differences are due to nozzle shape, definition of minimum noise, and interpretation of the phenomena.

With the shock associated noise virtually eliminated and schlieren photographs showing the destruction of the outer jet repetitive shock structure at minimum noise conditions, Tanna et al. [1985] measured the remaining mixing noise at downstream angles to the jet axis. Test conditions of constant thrust, mass flow, and exit area, along with the added condition that the inner stream be slightly supersonic to achieve minimum noise due to shocks, were used to set the coaxial jet initial velocities and temperatures. As was found for shock-free coaxial jets, normal velocity profile jets were noisier than the reference jet and inverted velocity profile jets were quieter based on overall sound pressure level measurements at 30 degrees to the jet axis.

Much of the data from reports discussed above have been used to develop models for predicting noise radiation from coaxial jets. Noise measurements from different nozzles at different conditions provided data for empirical models, Stone [1977], Stone et al. [1979] and Stone et al. [1983], and correlations, Pao [1979]. A more theoretical approach based on turbulence modeling and Lighthill's independent noise producing eddies was proposed by Chen [1976]. A turbulence model was used in calculating mean flow properties that were the only quantities needed for the acoustic calculations. A more elaborate theoretical model was proposed by Balsa and Gliebe [1977] and Gliebe and Balsa [1978]. They used turbulence modeling to predict both mean flow and turbulence variables. With a model for the acoustic source of an elemental jet volume based on local turbulence properties, these results were used in Lilley's equation to predict far field radiated noise levels and spectra. Gliebe et al. [1991] recently summarized this model and made comparisons to various jet noise suppression nozzles. These models tend to agree favorably with measured data since they all contain factors that were derived from measured data. As an alternative to these models, we calculate noise radiation from instability waves propagating in the shear layers of supersonic coaxial jets.

1.3 Theoretical Considerations

Instability waves have been established as noise generators in supersonic jets when they have phase velocities that are supersonic relative to ambient. When the jet is perfectly expanded, this mixing noise has a radiation pattern with a dominant peak in the downstream arc of the jet. Even when shocks are present in the jet flow, the noise from the jet that radiates into the downstream arc is primarily due to mixing; whereas, the broadband noise associated with shocks dominates in the upstream arc of the jet. Extensive measurements have shown this for single jets, Tanna [1977], and for coaxial

jets, Tanna et al. [1981]. Hence to a first approximation, we could conduct an analysis of the mixing noise in the region where it dominates even if shocks were present in the flow. However, since this is a first analysis of the instability wave noise generation model in supersonic coaxial jets, we assume the coaxial jets are perfectly expanded or, if not, the jet operating conditions are set for minimum noise where the flow has the characteristics of perfect expansion downstream of a composite shock structure near the nozzle. This simplifies the analysis and allows us to concentrate on profile shaping as a means to further reduce the mixing noise. Many of the ideas behind this analytical approach are given in the references already cited. We use these ideas in the extension of this approach to mixing noise generation from supersonic coaxial jets. An extension of this analysis to include the effects of a weak shock structure and the generation of broadband shock associated noise could conceivably follow the approaches for mean flow in Tam et al. [1985] and for shock noise in Tam [1987].

To begin the analysis, the jet flow is decomposed into three parts: mean flow, instability waves, and fine scale turbulence (Liu [1974]). At the nozzle exit, the kinetic energy in the mean flow dominates the energy balance between the three components. Energy flows from the mean flow into the instability waves and into the fine scale turbulence with the fine scale turbulence being the mechanism that primarily dissipates the energy. The interaction between these components is complicated and simplifications are made to enable a solution to be obtained. In general, the interaction between the mean flow and the instability waves has energy transfers in both directions. As the instability waves grow, they extract energy from the mean flow. In turn, their growth modifies the mean flow, transferring energy back to the mean flow, which again affects the instability wave growth rates, and so on. In addition, the energy transfer to the fine scale turbulence acts to diffuse the mean flow and decrease instability wave growth rates. We assume that these effects on the mean flow are included in a separate mean flow calculation. Chapter 2 discusses the mean flow calculation using a turbulence model that takes into account the modification to the mean flow by the instability waves and the dissipation caused by the fine scale turbulence. The model includes the necessary condition that a coaxial jet initially has two shear layers with differing length scales. As the flow progresses downstream, the shear layers grow in width and eventually merge until a single fully developed jet shear layer exists.

In Chapter 3, the instability waves are assumed to be governed by the linearized, inviscid, compressible equations of motion. As noted earlier, thin free shear layers containing an inflection point in the mean velocity profile are inherently unstable even in the absence of viscosity. The wave initially grows rapidly. As the shear layer grows, the instability wave growth rate decreases. Eventually, the shear layer is too thick to support unstable waves and the wave amplitude decreases until it disappears. The effect of fine scale turbulence on the instability waves and the interaction between instability

waves and other disturbance modes are assumed to be less important than the spreading of the mean flow in controlling growth and decay rates of an instability wave. Fine scale turbulence would dissipate the energy in the instability waves; a process not clearly understood. Previously, the fine scale turbulence was included as an effect on diffusing the mean flow which, in turn, effects instability wave growth and decay. Hence, even if the instability wave is modeled inviscidly, it is indirectly affected by the fine scale turbulence through the mean flow. Its direct effect is neglected. The interaction between instability waves generates harmonics. In our model where a single frequency wave is followed through its spatial growth and decay, at maximum growth its harmonics are still small and have little impact on the noise generated (Tam and Burton [1984a]); hence, these interactions are neglected, too. In addition, the analysis assumes that the disturbances are small in order to linearize the equations resulting in no interactions between the instability waves and other disturbance modes such as those due to temperature fluctuations.

For slowly diverging jet flows, two solutions are created that apply to separate but overlapping regions. The inner region includes the jet flow and the immediate region just outside the jet. Since the flow grows slowly in the axial direction, the rates of change in the axial direction are much less than those in the radial direction. In effect, the flow is nearly constant over the region that significant changes take place in the radial direction. This weak coupling between length scales is used by the method of multiple scales to develop an asymptotic expansion of the governing equations. To lowest order, the inner solution is the locally linear instability wave. The higher order solutions obtained after using the method of variation of parameters accounts for the effect of the slowly diverging mean flow.

The instability waves in the inviscid model are inflectional instabilities of the Kelvin-Helmholtz type. They have been shown to be the dominant instabilities in the jets of interest in this study (Tam et al. [1992], Seiner et al. [1993]). As shown in Tam and Hu [1989], there are other waves traveling in the shear layer that have subsonic and supersonic phase velocities. In the inviscid limit, the Kelvin-Helmholtz waves are analytically continued from growing to damped waves. These other waves become neutrally stable without viscosity and do not become damped downstream. Since they do not contribute to peak noise, they are not considered here. The damped Kelvin-Helmholtz waves are found for both subsonic and supersonic phase velocities as described in Tam and Burton [1984b]. This approach removes the boundedness condition for the inner solution at infinity where the inner solution is not valid anyway, Tam and Morris [1980].

In the outer region, which slightly overlaps the inner region, the governing equations are controlling disturbances that are acoustic in nature. The acoustic disturbances have the same length scales in all directions; hence, all coordinates are treated equally. The outer solution is created in a form that allows it to be asymptotically matched to

the inner solution in the overlap region. These matched asymptotic expansions provide the outer boundary condition for the inner solution and the inner boundary condition to the outer solution. To lowest order, we get the solution to the near field pressure disturbances just outside the jet. This solution is extended to the far field using stationary phase analysis to obtain the directivity pattern for the jet. The full analysis for this instability wave noise generation model involves a large amount of algebraic manipulation. This paper provides an outline of the solution in Chapter 3 with some additional algebraic details in related appendices.

The analytical and numerical analysis provided the means to conduct the parametric study of supersonic coaxial jets presented in Chapter 4. We chose a reference single stream jet with operating conditions that would be typical for a supersonic transport aircraft engine exhaust. From these conditions, we defined the operating conditions for supersonic coaxial jets that have the same total thrust, total mass flow, and total exit area as the reference jet. The study of normal velocity profile jets allowed variations in both velocity ratio and temperature ratio between the two jet streams to be controlled separately. Thus, the variation in velocity ratio could be studied with the temperature ratio fixed and vice versa. The study of inverted velocity profile jets was conducted with operating conditions set for minimum noise. Temperature ratios, in this case, could not be varied independent of the velocity ratio. Once the operating conditions were defined, all the numerical results for each case were dependent upon them. The calculation of far field directivity and the near field pressure disturbances depended on the calculation of the instability waves in the different shear layers that depended on the calculation of the mean flow that used the operating conditions to define the initial flow profiles. Chapter 4 discusses this train of dependencies and the final impact on the noise generated at selected frequencies. Finally, Chapter 5 discusses the conclusions that can be drawn from this study and makes suggestions for further work.

Chapter 2

CALCULATION OF THE MEAN FLOW DEVELOPMENT IN A COMPRESSIBLE COAXIAL JET

This chapter discusses the methodology used to calculate the mean flow development of a compressible, coaxial jet. As illustrated in Figure 2.1, the mean flow from a coaxial jet nozzle can have either a normal velocity profile or an inverted velocity profile. The normal velocity profile jet is characterized by a high velocity inner stream surrounded by a lower velocity outer stream, Figure 2.1(a). For the inverted velocity profile jet, the inner stream has the lower velocity and it is surrounded by the higher velocity outer stream, Figure 2.1(b). Both subsonic and supersonic conditions are calculated. When the jet exit conditions are supersonic, the jet static pressure is matched to the ambient pressure; hence, the flow is perfectly expanded. The approach is numerical with many simplifying assumptions used in the governing equations. These assumptions also lead to the need for a turbulence model to close the set of governing equations. It should be noted that the goal of this part of the work is to calculate the mean flow properties of a coaxial jet, either with a normal initial velocity profile or with an inverted initial velocity profile, that expands and merges in an orderly fashion in the downstream axial direction. The absolute accuracy of the calculated mean flows compared to any particular set of measured data is secondary to whether or not the calculated results bear a strong qualitative resemblance to the behavior of coaxial jet flows. In practice, the predictions, when compared to available measurements, show reasonable quantitative agreement.

For the most part, in the past, the calculation of instability waves in a single axisymmetric jet have used analytic functions to characterize the mean flow. These analytic functions have been based on results from experimental measurements where data were plotted using local similarity variables. Examples of this approach include the measurements of Lau et al. [1979] whose data were fitted by an error function profile, Cohen and Wygnanski [1987] who fitted data to a series of hyperbolic tangent functions, to add corrections to the classical hyperbolic tangent profile, and Morrison and McLaughlin [1980] who fitted data to a half-Gaussian profile. Michalke [1984] summarized the use of different analytic functions in the calculation of instability waves. The measured data typically include only velocity profile results which are sufficient for incompressible instability wave calculations. When compressibility is important, the instability wave

calculations require that either the temperature or the density profile be specified. Often, the approximation has been made that allows the Crocco Relation to be used. This defines the temperature or density profile to be a function of the velocity. See, for example, Schlichting [1979], White [1974], and Michalke [1984]. Example velocity and density profiles for subsonic and supersonic single jets are shown in Figures 2.2 and 2.3. These figures show numerical results, using the procedure to be described in this chapter, compared to calculated hyperbolic tangent velocity profiles (Michalke [1984] Eq. 9) and the corresponding density profile from the Crocco Relation. Good comparisons are made for both isothermal jets (Figure 2.2) and hot jets (Figure 2.3) showing the usefulness of the Crocco Relation in single jet instability wave calculations. Thus, with mean profile information analytically defined, the mean profile variables and all their derivatives are available at all points in the radial direction for the numerical calculation of instability wave characteristics. Furthermore, these analytic functions are continuous into the complex plane which allows the calculation of damped inviscid waves as described in Tam and Morris [1980]. (Further details on damped inviscid wave calculations will be given later.) Thus, the use of analytic functions to describe the mean flow has simplified the study of single jet instability waves.

When it comes to a coaxial jet, it is not clear how to properly apply analytic functions to describe the profile at all axial locations. For a single supersonic jet, Tam and Burton [1984a] used a generalized half-Gaussian function to describe the mean velocity at all axial locations. The function parameters, centerline velocity, core radius, and half-width of the mixing region, were defined by cubic spline fits to measured data. The density profile was found by keeping the total temperature constant. This approach was possible due to the availability of measured data. There is little measured data for coaxial jets, especially with supersonic conditions, that would allow an analytical description to be made at all axial locations including the merging region of a normal profile and an inverted profile into a single jet. Miles [1986, 1987] calculated instability waves for normal profile coaxial jets using analytic functions to fit velocity profiles at selected axial locations where measurements were available from a subsonic jet. Such an approach did not produce useful information on the axial dependence of the function parameters. Thus, profiles could not be generated at axial locations where measurements were not made. Furthermore, whereas temperature profiles have been measured in a subsonic jet, they are not typically measured in a supersonic jet. So, even though velocity measurements may be available for coaxial jets with supersonic conditions, it is doubtful that Crocco's Relation could provide the appropriate temperature profiles for either normal or inverted conditions. Thus, the decision was made to generate mean profiles for coaxial jets numerically. Morris [1980] and Morris and Baltas [1981] calculated instability waves using numerically generated velocity profiles for a single incompressible

(a)

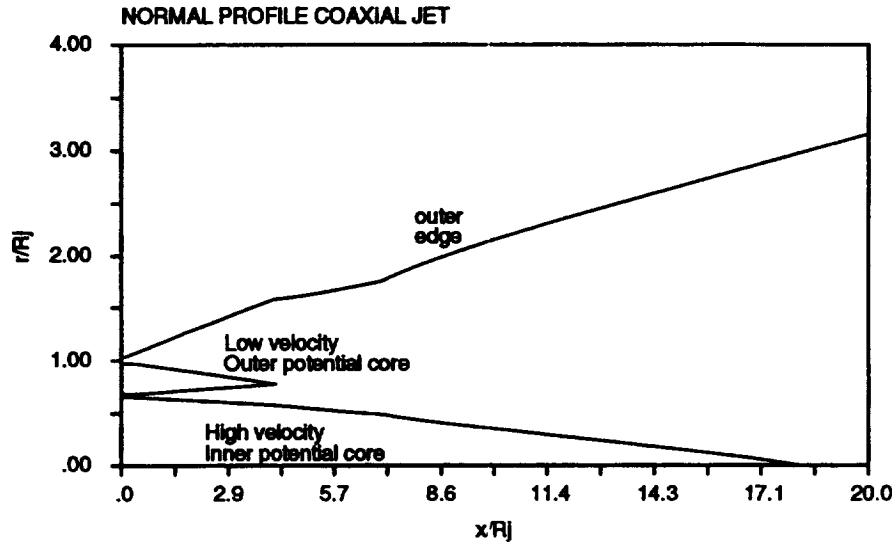

(b)

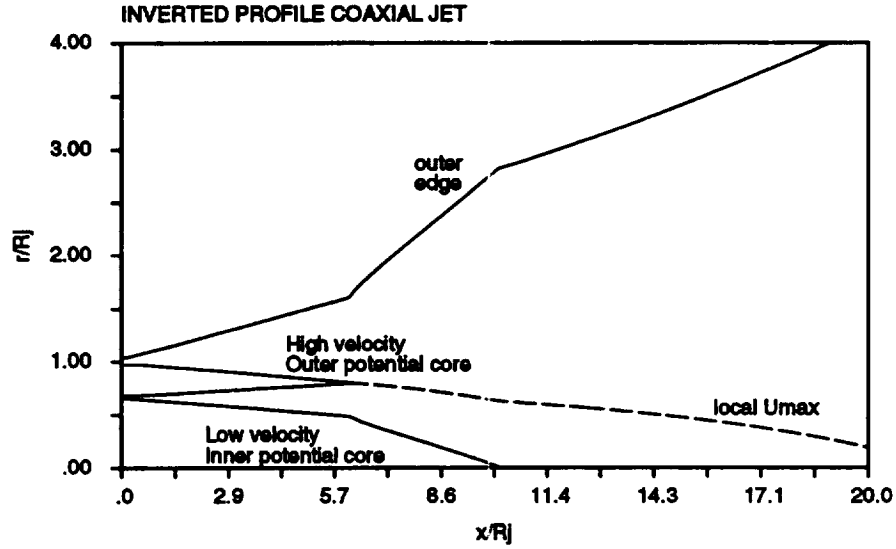

Figure 2.1. Illustrations of coaxial jet flows. (a) normal velocity profile coaxial jet; (b) inverted velocity profile coaxial jet

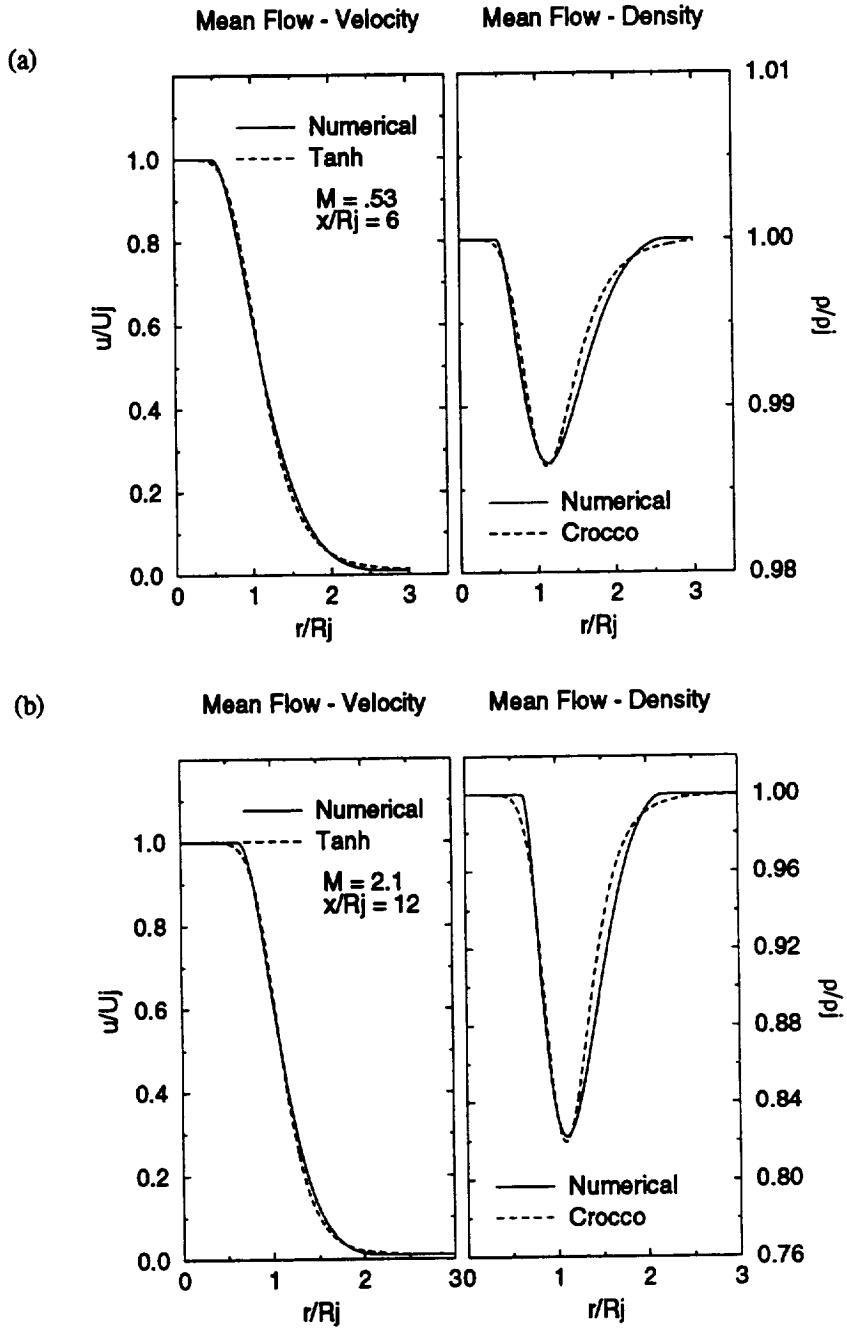

Figure 2.2. Example velocity and density profiles for isothermal single jets. (a) subsonic jet; (b) supersonic jet

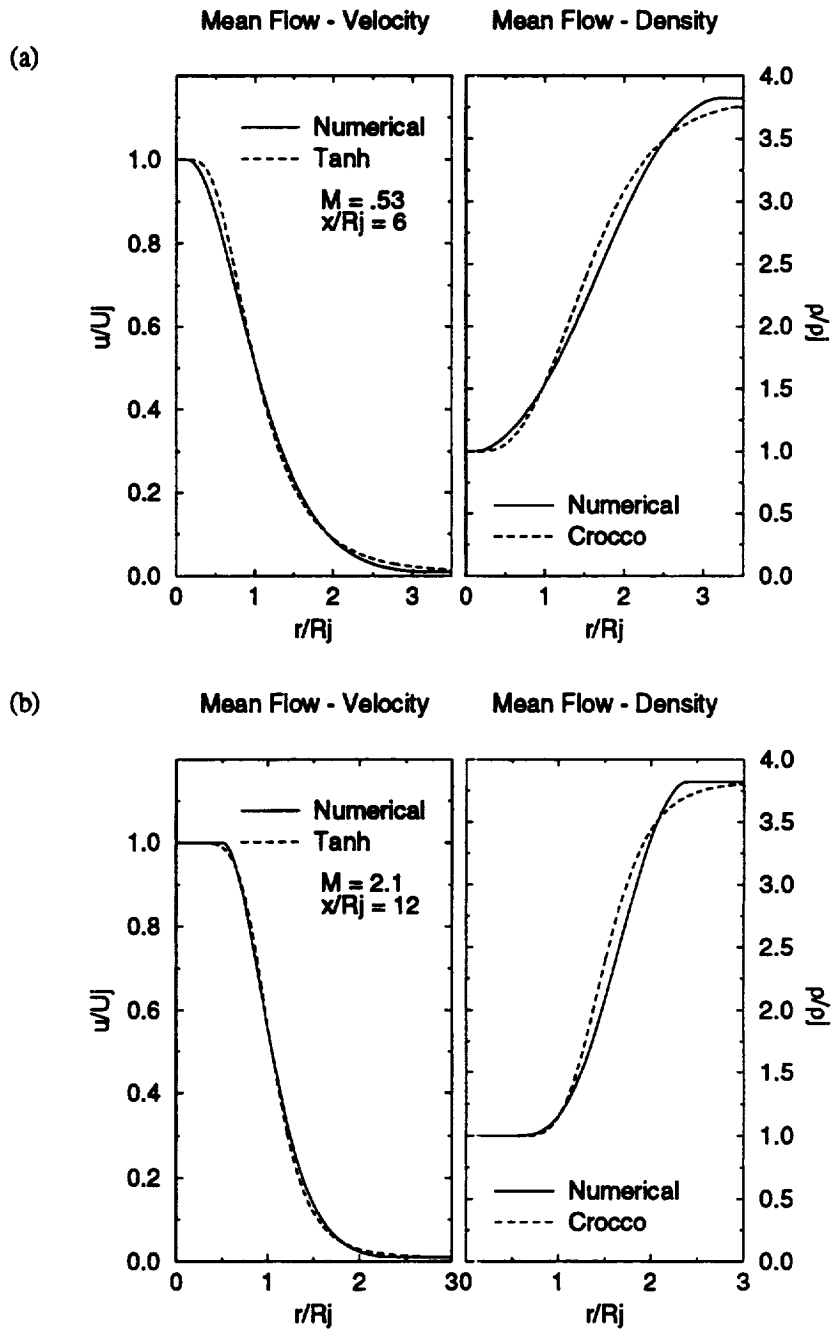

Figure 2.3. Example velocity and density profiles for heated single jets. (a) subsonic jet; (b) supersonic jet

jet. So it is not new to use numerically generated profiles. The extension here is to include compressibility effects into the spreading and merging of a coaxial jet.

2.1 Equations for Compressible Flow

The compressible flow of a free jet is governed by the continuity, momentum, energy, and state equations. To solve these equations numerically in their original unsteady form would overly complicate our problem. Hence, following the discussion in Anderson et al. [1984], we assume the flow development of an axisymmetric free jet is governed by the boundary layer equations for compressible flow that have been Reynolds averaged; since the flow is also assumed to be turbulent. The flow variables are decomposed into a time averaged or mean value part and a fluctuating or turbulent part. (E.g., $p = \bar{p} + p'$ where the overbar denotes the time averaged part and the prime denotes the fluctuating part.) The following approximations are used:

1. The mean flow is steady.
2. The mean pressure is constant in the jet and equal to ambient pressure.
3. $u >> v$ and $\frac{\partial}{\partial r} >> \frac{\partial}{\partial x}$.
4. $\overline{\rho' u'} << \bar{\rho}\bar{u}$ and $\overline{\rho' H'} << \bar{\rho}\bar{H}$.

The equations in axisymmetric coordinates reduce to:

continuity:

$$\frac{\partial}{\partial x}(r\rho u) + \frac{\partial}{\partial r}(r\rho\tilde{v}) = 0 \tag{2.1}$$

momentum:

$$\rho u\frac{\partial u}{\partial x} + \rho\tilde{v}\frac{\partial u}{\partial r} = \frac{1}{r}\frac{\partial}{\partial r}\left[r\left(\mu\frac{\partial u}{\partial r} - \rho\overline{u'v'}\right)\right] \tag{2.2}$$

energy:

$$\rho u\frac{\partial H}{\partial x} + \rho\tilde{v}\frac{\partial H}{\partial r} = \frac{1}{r}\frac{\partial}{\partial r}\left[r\left\{\frac{\mu}{\mathrm{Pr}}\frac{\partial H}{\partial r} - \rho c_p\overline{v'T'} + u\left[\left(1-\frac{1}{\mathrm{Pr}}\right)\mu\frac{\partial u}{\partial r} - \rho\overline{u'v'}\right]\right\}\right] \tag{2.3}$$

where $\tilde{v}$ is a mass averaged quantity defined as

$$\tilde{v} = \frac{1}{\bar{\rho}}\left(\bar{\rho}\bar{v} + \overline{\rho' v'}\right). \tag{2.4}$$

For simplicity, overbars have not been used on mean values in (2.1) to (2.3). The definitions of all the symbols are found in the Symbol List.

We assume a perfect gas. Thus, the state equation is:

state:

$$p = \rho R_g T \tag{2.5}$$

Also, the laminar viscosity is related to temperature according to Sutherland's Law.

$$\mu = \mu_o \left(\frac{T}{T_o}\right)^{3/2} \frac{T_o + S_1}{T + S_1} \tag{2.6}$$

In (2.2) and (2.3), the Reynolds stress term $-\rho\overline{u'v'}$ and the Reynolds heat flux term $-\rho c_p \overline{v'T'}$ are undefined. These terms must be modeled in order to solve the system of equations. In looking ahead to the difficulties in defining a turbulence model that would work for a supersonic coaxial jet with normal or inverted initial velocity profiles and streams of different temperature (An example of the difficulties in turbulence modeling for single stream supersonic jets is found in Dash et al. [1992].), it was decided to use the most basic model, namely the mixing length model, for turbulence. Any turbulence model chosen for these calculations would require modification and calibration to obtain reasonable results for both normal and inverted profile coaxial jets. Since, as mentioned previously, this study was not an attempt, primarily, to make accurate mean flow predictions, the mixing length model represented the turbulent stress from which an effective viscosity was defined. Through the use of a turbulent Prandtl number to relate eddy diffusivities for heat and momentum, an effective Prandtl number was calculated from the effective viscosity.

In the mixing length model, the Reynolds stress term is written as (Schlichting [1979], Anderson et al. [1984])

$$-\rho\overline{u'v'} = \mu_T \frac{\partial u}{\partial r} \tag{2.7}$$

and the heat flux term as

$$-\rho c_p \overline{v'T'} = \frac{c_p \mu_T}{\mathrm{Pr}_T} \frac{\partial T}{\partial r}. \tag{2.8}$$

Substituting (2.7) and (2.8) into (2.2) and (2.3) and using the definition for total enthalpy $H = c_p T + u^2/2$, we get for momentum and energy:

$$\rho u \frac{\partial u}{\partial x} + \rho \tilde{v} \frac{\partial u}{\partial r} = \frac{1}{r} \frac{\partial}{\partial r} \left[r \mu_{\mathrm{eff}} \frac{\partial u}{\partial r} \right] \tag{2.9}$$

$$\rho u \frac{\partial H}{\partial x} + \rho \tilde{v} \frac{\partial H}{\partial r} = \frac{1}{r} \frac{\partial}{\partial r} \left[r \frac{\mu_{\mathrm{eff}}}{\mathrm{Pr}_{\mathrm{eff}}} \frac{\partial H}{\partial r} + r \left(\mu_{\mathrm{eff}} - \frac{\mu_{\mathrm{eff}}}{\mathrm{Pr}_{\mathrm{eff}}} \right) u \frac{\partial u}{\partial r} \right] \tag{2.10}$$

where

$$\mu_{\mathrm{eff}} = \mu + \mu_T \tag{2.11}$$

and

$$\mathrm{Pr}_{\mathrm{eff}} = \frac{1 + \frac{\mu_T}{\mu}}{\frac{1}{\mathrm{Pr}} + \frac{1}{\mathrm{Pr}_T}\frac{\mu_T}{\mu}}. \tag{2.12}$$

Equations (2.9) and (2.10) are of the same form as those found in Pai [1954] and are the basis for the numerical work of Patankar and Spalding [1970] and Crawford and Kays [1976].

With the turbulent Prandtl number Pr_T essentially constant for free jet calculations (See Schlichting [1979], NASA [1972], Anderson et al. [1984], Crawford and Kays [1976]), the mixing length model is embodied in the turbulent viscosity;

$$\mu_T = \rho \left(C_1 C_2 \ell\right)^2 \left|\frac{\partial u}{\partial r}\right| \tag{2.13}$$

where ℓ is a characteristic length scale and C_1 and C_2 are the mixing length constants; however, for this model, they are functions of the flow conditions as described presently.

It is known that the growth of a shear layer depends on the flow conditions at the shear layer edges with velocities and densities of the two streams being of primary interest. (See Schlichting [1979], Birch and Eggers in NASA [1972], Brown and Roshko [1974], Papamoschou and Roshko [1988]). This dependence occurs whether the flow is compressible or incompressible. Papamoschou and Roshko [1988] and others have normalized the compressible shear layer growth rate by an incompressible growth rate value at the same edge conditions in an attempt to separate out purely compressible effects. This followed from work by Brown and Roshko [1974] that showed the effects of different velocity and density edge conditions on shear layer growth for incompressible flows. Thus, in order to incorporate the effects of edge conditions into the mixing length model to get the proper shear layer growth, two factors have been developed that depend on the flow conditions; one for incompressible conditions and the other for compressible conditions.

The factor C_1 is the incompressible part of the mixing length constant. It depends on the velocity ratio $r = U_2/U_1$ and the density ratio $s = \rho_2/\rho_1$ between the two streams either side of the shear layer. Equations for the expected vorticity thickness growth rate have been developed by many investigators from experimental evidence. Thus, given that we know the vorticity thickness growth rate for a fixed r and s, we adjusted the C_1 factor (C_2 set to 1) until the calculated initial vorticity thickness growth rate of a single jet agreed with the predicted value. Continuing this process for a range of r and s values resulted in a series of calibration curves for C_1. A more detailed discussion is given in Appendix A.

The C_2 factor is the compressible part of the mixing length constant. Its purpose is to decrease the growth of the shear layer as compressibility effects become important.

It depends on a Mach number in a relative frame of reference convecting with the real phase speed of a growing disturbance in the shear layer. This convected Mach number depends on r and s and on the Mach number of one of the streams. Experimentalists have used the convected Mach number in attempts to correlate normalized measured growth rates of compressible shear layers. We developed an equation that fits this correlated data in order to predict shear layer growth rates for given flow conditions. Thus, we proceeded to calibrate the C_2 factor given that C_1 is allowed to take on its previously calibrated value for the given r and s. C_2 was adjusted until the calculated initial vorticity thickness growth rate agreed with the predicted value. For this case, a single calibrating curve was generated. Again, details are discussed in Appendix A.

There are a few different choices for the characteristic length scale for a jet shear layer. Since the flow is turbulent and the motion is dominated by large structures or instability waves, an appropriate characteristic length scale would be (Brown and Roshko [1974] and Morris [1976])

$$\ell = \frac{\Delta U}{|\partial u/\partial r|_{\max}}. \tag{2.14}$$

ℓ defined in this way can be interpreted as a vorticity thickness. If necessary, it can be related to other length scales by using an appropriate functional shape for the velocity profile. For example, $\ell = .978b$ where b is defined as the shear layer width from the location where $(u - U_2)/\Delta U = .9$ to the location where $(u - U_2)/\Delta U = .1$ and u is defined by an error function.

2.1.1 Numerical Formulation

Many numerical techniques are available for the solution of the boundary layer equations. (See Anderson et al. [1984] and White [1974]). Any one of which could have provided adequate mean flow results; but our criterion for mean flow calculations dictated that the mean flow results be sufficiently resolved in order to be used in the instability wave calculations to be discussed later. Furthermore, we wished not to be bothered with any numerical calculation of the $\tilde{v}$ term in (2.9) and (2.10). Hence, we initially followed the stream function approach given by Patankar and Spalding [1970] and Crawford and Kays [1976].

Equations (2.9) and (2.10) are transformed to stream function coordinates using

$$r\rho u = \frac{\partial \Psi}{\partial r} \qquad \text{and} \qquad r\rho\tilde{v} = -\frac{\partial \Psi}{\partial x}. \tag{2.15}$$

These equations insure that continuity (2.1) is satisfied. The transformation from (x, r) coordinates to (x, Ψ) coordinates is completed by using

$$\frac{\partial}{\partial x} = \frac{\partial}{\partial x} + \frac{\partial}{\partial \Psi}\frac{\partial \Psi}{\partial x} = \frac{\partial}{\partial x} - r\rho\tilde{v}\frac{\partial}{\partial \Psi}$$
$$\frac{\partial}{\partial r} = \frac{\partial}{\partial x}\frac{\partial x}{\partial r} + \frac{\partial}{\partial \Psi}\frac{\partial \Psi}{\partial r} = r\rho u\frac{\partial}{\partial \Psi}$$

in (2.9) and (2.10) to get

$$\frac{\partial u}{\partial x} = \frac{\partial}{\partial \Psi}\left[r^2\rho u\mu_{\text{eff}}\frac{\partial u}{\partial \Psi}\right] \tag{2.16}$$

$$\frac{\partial H}{\partial x} = \frac{\partial}{\partial \Psi}\left[r^2\rho u\frac{\mu_{\text{eff}}}{\text{Pr}_{\text{eff}}}\frac{\partial H}{\partial \Psi}\right] + \frac{\partial}{\partial \Psi}\left[r^2\rho u^2\left(\mu_{\text{eff}} - \frac{\mu_{\text{eff}}}{\text{Pr}_{\text{eff}}}\right)\frac{\partial u}{\partial \Psi}\right]. \tag{2.17}$$

These equations can be differenced in a variety of ways; explicitly as in Madni and Pletcher [1975], implicitly on an evenly spaced Ψ–grid as in Donovan and Todd [1967], or transformed to a normalized Ψ–grid and implicitly differenced as in Patankar and Spalding [1970]. Each of these numerical methods were found to have problems. The explicit DuFort-Frankel method, Madni and Pletcher [1975], had stability problems. The implicit Crank-Nicolson method using an evenly spaced Ψ–grid, Donovan and Todd [1967], could not provide enough resolution at the outer low speed edges of the jet. And Patankar and Spalding's method had problems with entrainment boundary conditions at the outer edge. Each of these problems were overcome by using fully implicit differencing and what is considered to be natural grid stretching and natural outer boundary entrainment. By choosing a fully implicit method, the numerical problem is inherently stable. The problem of grid resolution is solved by using an evenly spaced r–grid. The outer boundary condition will be discussed later.

The choice of an evenly spaced r–grid results in an unevenly spaced Ψ–grid. In essence, the Ψ–grid is stretched, but in a manner that is natural to the Ψ–grid with more grid points at the outer edge where finer grid spacing is desired. From (2.15)

$$d\Psi = r\rho u\, dr.$$

Integrating this across one grid spacing

$$\int_{k-1}^{k} d\Psi = \int_{k-1}^{k} r\rho u\, dr$$

we get

$$\Delta\Psi_k = \Psi_k - \Psi_{k-1} = \frac{1}{2}\left[(r\rho u)_k + (r\rho u)_{k-1}\right]\Delta r \tag{2.18}$$

after using the trapezoidal rule. One consequence of (2.18) is that u cannot be zero outside the jet or $\Delta\Psi$ would go to zero. To get close to quiescent outer conditions, the free stream velocity was set to 1% of the initial highest velocity.

Writing (2.16) as

$$\frac{\partial u}{\partial x} = \frac{\partial}{\partial \Psi}\left[A\frac{\partial u}{\partial \Psi}\right] \tag{2.19}$$

where

$$A = r^2 \rho u \mu_{\text{eff}},$$

we implicitly difference this momentum equation using the grid shown in Figure 2.4 as follows:

$$\frac{u_{j+1,k} - u_{j,k}}{\Delta x} = \left\{ \frac{2}{\Delta\Psi_{k+1} + \Delta\Psi_k}\left[A_{k+\frac{1}{2}}\frac{u_{k+1} - u_k}{\Delta\Psi_{k+1}} - A_{k-\frac{1}{2}}\frac{u_k - u_{k-1}}{\Delta\Psi_k}\right]\right\}_{j+1} \tag{2.20}$$

The A coefficient is the average of adjacent grid values

$$A_{k+\frac{1}{2}} = \frac{1}{2}\left(A_k + A_{k+1}\right).$$

Collecting terms, equation (2.20) is arranged into tridiagonal form

$$\left\{-\Delta_k^- A_{k-\frac{1}{2}} u_{k-1} + \left(1 + \Delta_k^+ A_{k+\frac{1}{2}} + \Delta_k^- A_{k-\frac{1}{2}}\right) u_k - \Delta_k^+ A_{k+\frac{1}{2}} u_{k+1}\right\}_{j+1} = u_{j,k} \tag{2.21}$$

where

$$\Delta_k^- = \frac{2\Delta x}{\left(\Delta\Psi_{k+1} + \Delta\Psi_k\right)\Delta\Psi_k}, \tag{2.22}$$

$$\Delta_k^+ = \frac{2\Delta x}{\left(\Delta\Psi_{k+1} + \Delta\Psi_k\right)\Delta\Psi_{k+1}}. \tag{2.23}$$

Equation (2.17) is differenced in the same manner. The resulting tridiagonal equation is

$$\begin{aligned}\Big\{-\Delta_k^- D_{k-\frac{1}{2}} u_{k-1} - \Delta_k^- B_{k-\frac{1}{2}} H_{k-1} + \left(\Delta_k^+ D_{k+\frac{1}{2}} + \Delta_k^- D_{k-\frac{1}{2}}\right) u_k \\ + \left(1 + \Delta_k^+ B_{k+\frac{1}{2}} + \Delta_k^- B_{k-\frac{1}{2}}\right) H_k - \Delta_k^+ D_{k+\frac{1}{2}} u_{k+1} - \Delta_k^+ B_{k+\frac{1}{2}} H_{k+1}\Big\}_{j+1} \\ = H_{j,k}\end{aligned} \tag{2.24}$$

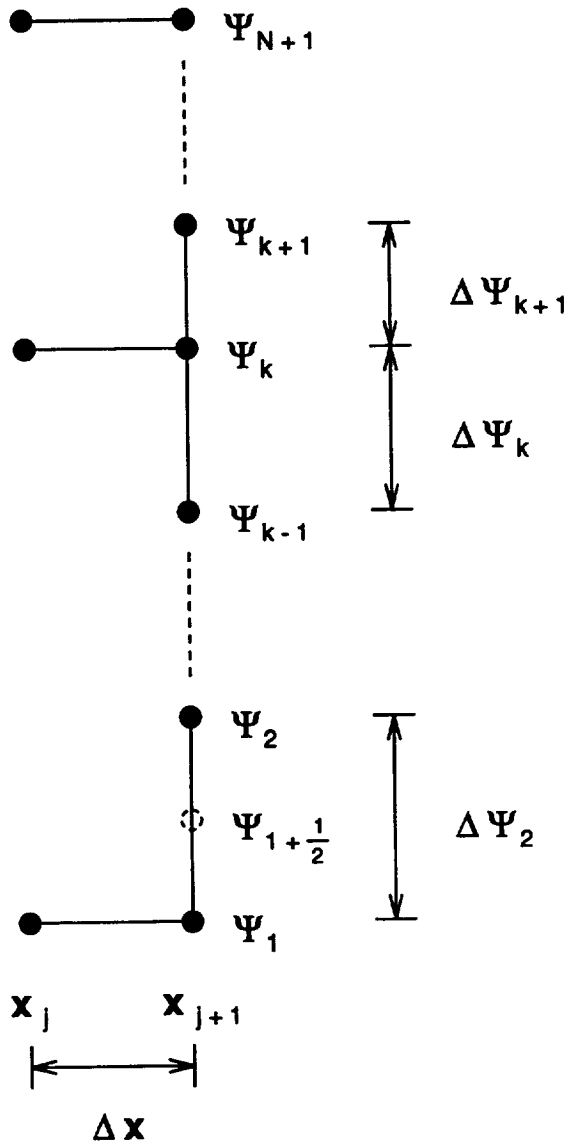

Figure 2.4. Stream function grid for mean flow calculations.

where

$$B = r^2 \rho u \frac{\mu_{\text{eff}}}{\text{Pr}_{\text{eff}}},$$

and

$$D = r^2 \rho u^2 \left(\mu_{\text{eff}} - \frac{\mu_{\text{eff}}}{\text{Pr}_{\text{eff}}} \right).$$

2.1.2 Boundary Conditions

Since the problem is axisymmetric, a symmetry boundary condition is enforced at $r = 0$, $k = 1$; that is

$$\frac{\partial u}{\partial \Psi} = \frac{\partial H}{\partial \Psi} = 0. \tag{2.25}$$

The right hand side of (2.19) is differenced using half the grid spacing at the edge. (See Figure 2.4)

$$\frac{u_{j+1,1} - u_{j,1}}{\Delta x} = \frac{1}{\Delta \Psi_2 / 2} \left\{ \left[A \frac{\partial u}{\partial \Psi} \right]_{j+1,1+\frac{1}{2}} - \left[A \frac{\partial u}{\partial \Psi} \right]_{j+1,1} \right\}$$

From the boundary condition (2.25), the $(j+1,1)$ term on the right side is zero. The final tridiagonal form is

$$\left\{ \left(1 + \frac{2\Delta x}{\Delta \Psi_2^2} A_{1+\frac{1}{2}} \right) u_1 - \frac{2\Delta x}{\Delta \Psi_2^2} A_{1+\frac{1}{2}} u_2 \right\}_{j+1} = u_{j,1}. \tag{2.26}$$

Similarly, we get for energy

$$\left\{ \frac{2\Delta x}{\Delta \Psi_2^2} D_{1+\frac{1}{2}} u_1 + \left(1 + \frac{2\Delta x}{\Delta \Psi_2^2} B_{1+\frac{1}{2}} \right) H_1 - \frac{2\Delta x}{\Delta \Psi_2^2} D_{1+\frac{1}{2}} u_2 - \frac{2\Delta x}{\Delta \Psi_2^2} B_{1+\frac{1}{2}} H_2 \right\}_{j+1} = H_{j,1}. \tag{2.27}$$

The outer boundary condition is simply that the u and H values must equal free stream conditions. To put it algebraically,

$$\begin{aligned} u_{j+1,N+1} &= u_{j,N+1} = u_\infty \\ H_{j+1,N+1} &= H_{j,N+1} = H_\infty. \end{aligned} \tag{2.28}$$

This also may be viewed as saying that the derivative in the x–direction is zero at the outer edge. The consequence of this type of boundary condition is that the flow,

expanding outward due to diffusion, can never reach the outer grid boundary or the calculations will be in error. The way this is handled is discussed in the next section.

2.1.3 Methodology of Numerical Solution

Equations (2.21), (2.24), (2.26), (2.27), and (2.28) when put together create a 2×2 block tridiagonal system for $k = 1$ to $N + 1$ where N is the number of grid spacings. The system can be solved by standard block tridiagonal routines such as that given in Anderson et al. [1984]. The coefficients A, B, and C are unknown at the $j+1$ location since they are functions of the unknowns $u_{j+1,k}$ and $H_{j+1,k}$. Consequently, iterations must be made to complete the solution for each axial step. The procedure is as follows:

1. Guess $u_{j+1,k}$ and $H_{j+1,k}$.

   If $j = 1$, then use the initial conditions.

$$u_{2,k} = u_{1,k}$$
$$H_{2,k} = H_{1,k}$$

   For $j > 1$, we can extrapolate from previous solutions.

$$u_{j+1,k} = 2u_{j,k} - u_{j-1,k}$$
$$H_{j+1,k} = 2H_{j,k} - H_{j-1,k}$$

2. Solve for $j + 1$ values of ρ, μ_{eff}, Pr_{eff}.

3. Calculate the $\Delta\Psi_{j+1,k}$ grid using equation (2.18).

4. Solve the block tridiagonal system for new values of $u_{j+1,k}$ and $H_{j+1,k}$. Also, new values of ρ, μ_{eff}, Pr_{eff} are calculated.

5. If the difference between the new solution and the previous solution is smaller than some convergence criterion, then this axial step is completed. Otherwise, the iteration process continues at step 3.

To insure, as mentioned previously, that the outer boundary condition is not compromised by the expanding flow, the grid must be large enough in the radial direction to encompass the flow. Rather than making the grid so large that the flow is encompassed at all axial locations, the outer edge of the initial grid is much closer to the outer edge of the jet, typically the grid ends at twice the outer radius of the initial jet. As the flow expands downstream, the outer edge of the jet flow is tracked until it is within some arbitrary distance from the outer edge of the grid. At which time, more grid points are

added to the solution. All the variables at the new grid points take on the free stream values that are assumed to always exist outside the grid. As the shear layer of the jet expands, it becomes possible to increase the Δr–grid spacing since less grid points are necessary to well define the shear layer as was initially necessary for a thin shear layer. Thus, we do not simply continue to add grid points as the flow expands, but we can, from time to time, reduce the number of grid points by increasing the grid spacing. It was best to simply double the grid spacing so that the extrapolated guess for new variables occurred along constant grid lines in the x–direction. Thus, no interpolation was necessary.

2.2 Single Jet Examples

Before discussing the modifications to the mixing length model for the coaxial jet, we first look at some results from single jet examples to see how well the calibrated mixing length model works.

Figure 2.5 compares numerical calculations to data taken from Zaman [1986] for a subsonic, $M = 0.5$ axisymmetric jet. The axial variation of centerline velocity is shown in Figure 2.5(a). The calculations show good comparison to data and to an equation for centerline velocity from Witze [1974] based on correlating many different jet measurements. Figure 2.5(b) shows the growth of jet half velocity width and the ratio of jet half velocity width to momentum thickness. The calculations underpredict the spread of the jet as defined by the half velocity width.

Calculations for a Mach 1.37 jet are shown in Figure 2.6. The centerline velocity data are taken from Lau et al. [1979] (Figure 2.6(a)) and the half velocity point data is from Lau [1981] (Figure 2.6(b)). The calculated core region spreads at the measured rate though the measured core length is slightly shorter than predicted.

Results for a higher speed jet, Mach 2.22, are shown in Figure 2.7. The comparison for centerline velocity and jet half velocity point is made with data from Eggers [1966]. The calculations underpredict the spreading of the jet. These results show a problem that exists with using the compressible calibration curve in Figure A.3. Any jet data results that lie above the calibration curve will have its growth underpredicted by the calculations. This is the case for the initial spreading rate measured by Eggers. The Lau data, shown in Figure 2.6 lies much closer to the calibration curve; hence, there is better agreement between calculated and measured jet spreading. The comparison with Zaman's data could also be affected by this problem. As with many other tries at turbulence modeling, the results are only as good as the calibration and it is difficult to generally apply the model to varied problems. The turbulence model was calibrated to match growth rates in the initial core region of a jet, the region of most importance to growing instabilities. In the downstream region, the jet is a wide axisymmetric shear

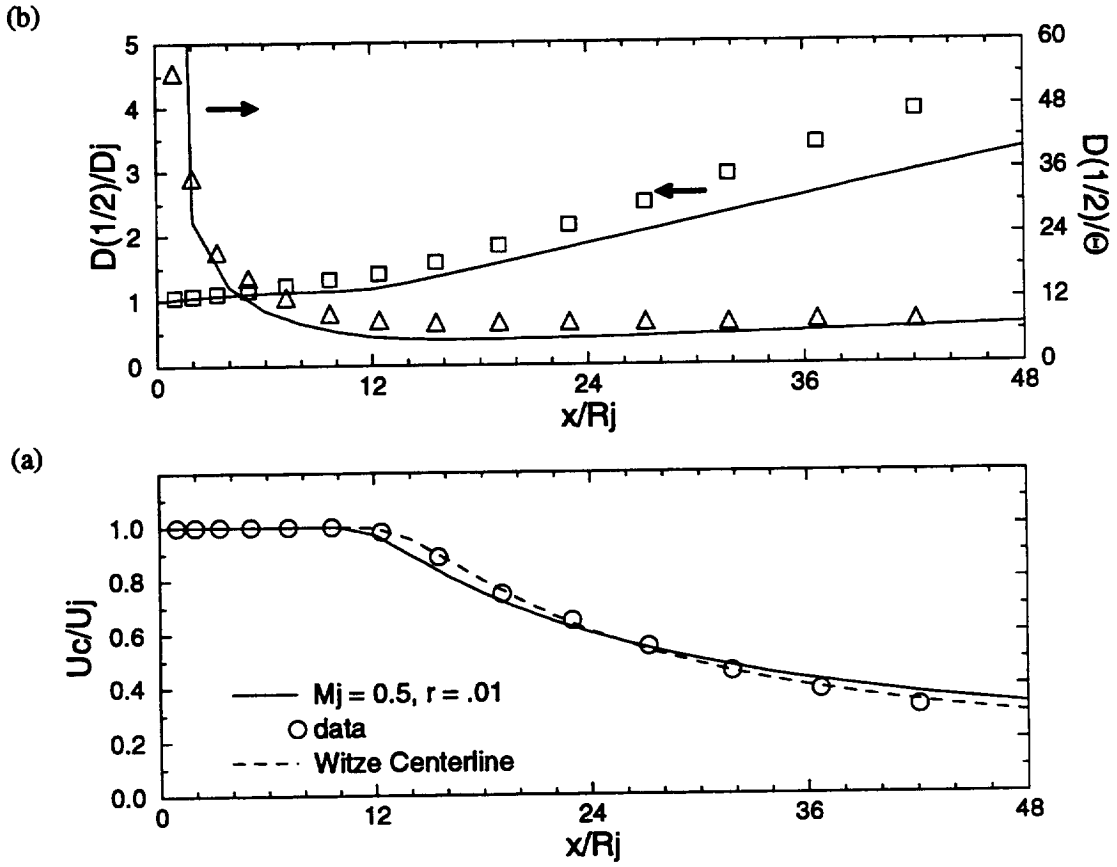

Figure 2.5. Comparison of subsonic single jet calculations to measured data. Data from Zaman [1986]. (a) centerline velocity; (b) jet half velocity width, □ (left scale), jet half velocity width/momentum thickness, △ (right scale). Operating conditions: U_j = 172.5 m/s, T_j = 295.4 K, R_j = 1.27 cm.

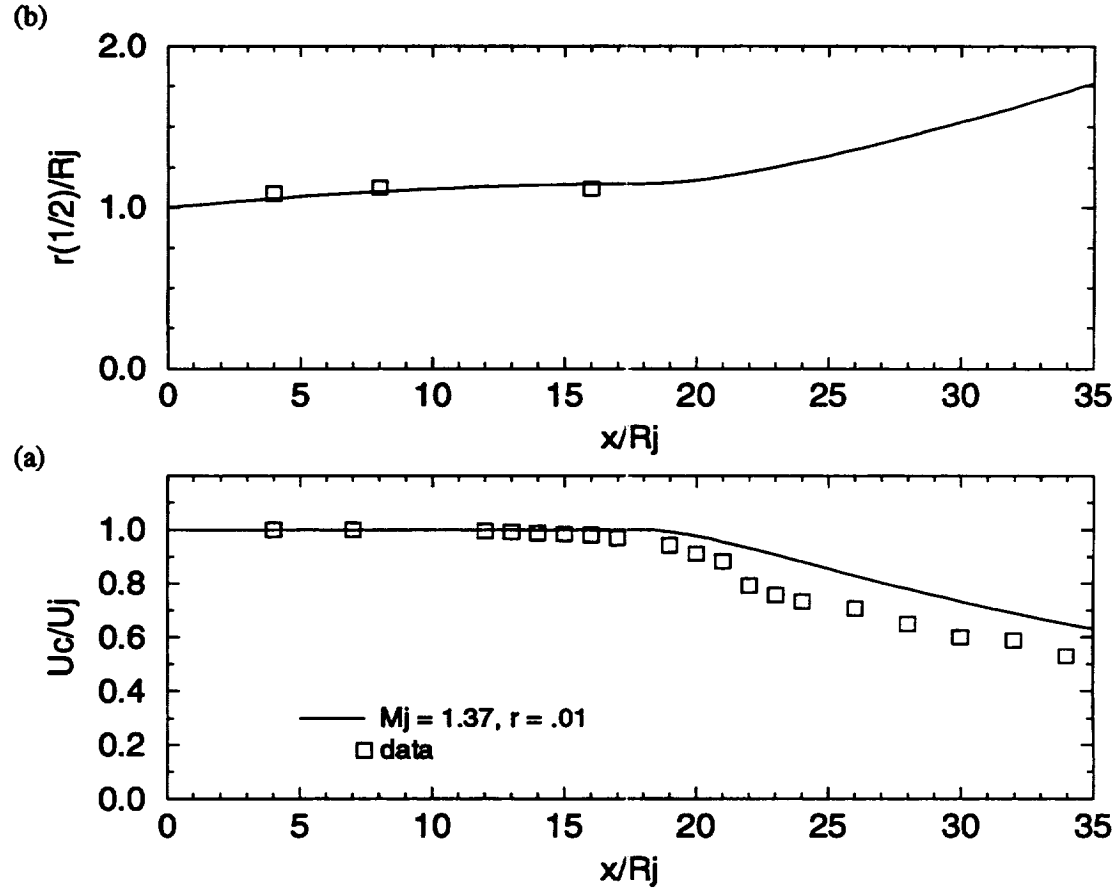

Figure 2.6. Comparison of supersonic single jet calculations to measured data. Data from Lau [1979, 1981]. (a) centerline velocity; (b) jet half velocity point. Operating conditions: U_j = 472 m/s, T_j = 295.4 K, R_j = 2.55 cm.

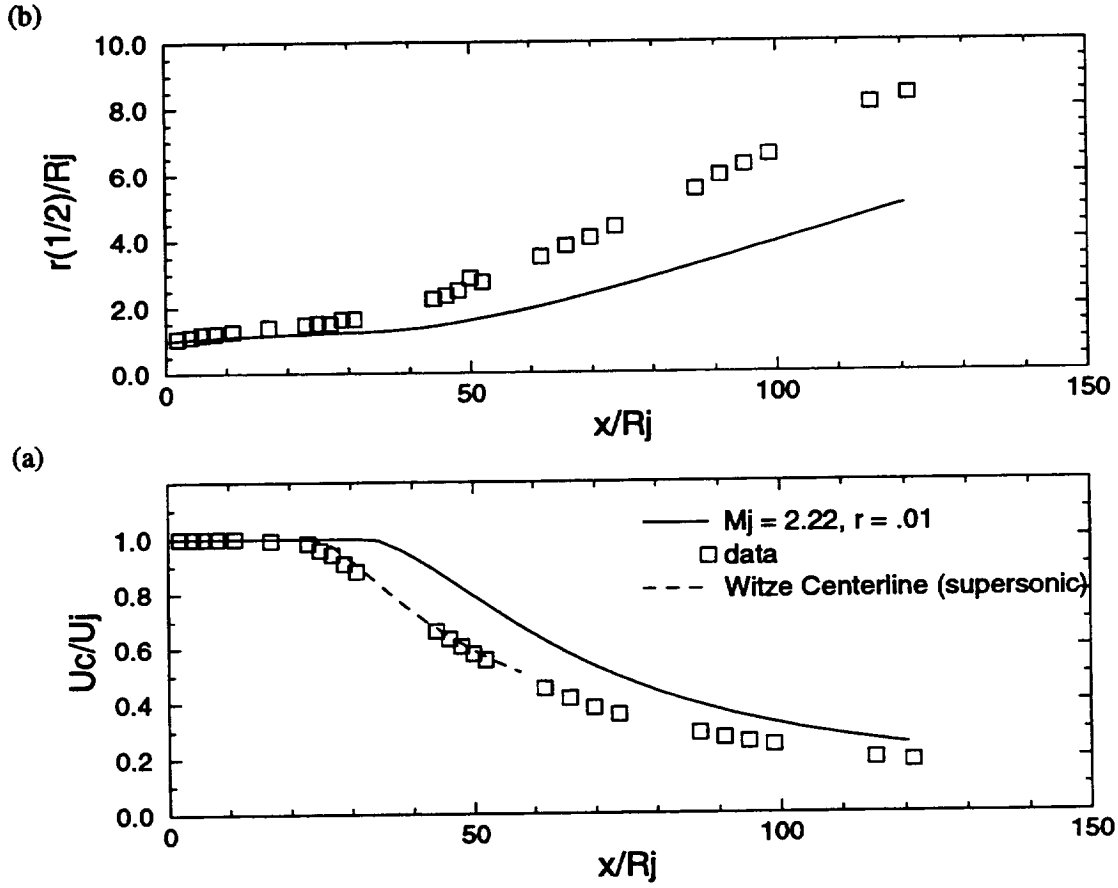

Figure 2.7. Comparison of supersonic single jet calculations to measured data. Data from Eggers [1966]. (a) centerline velocity; (b) jet half velocity point. Operating conditions: U_j = 538 m/s, T_j = 147 K, R_j = 1.28 cm.

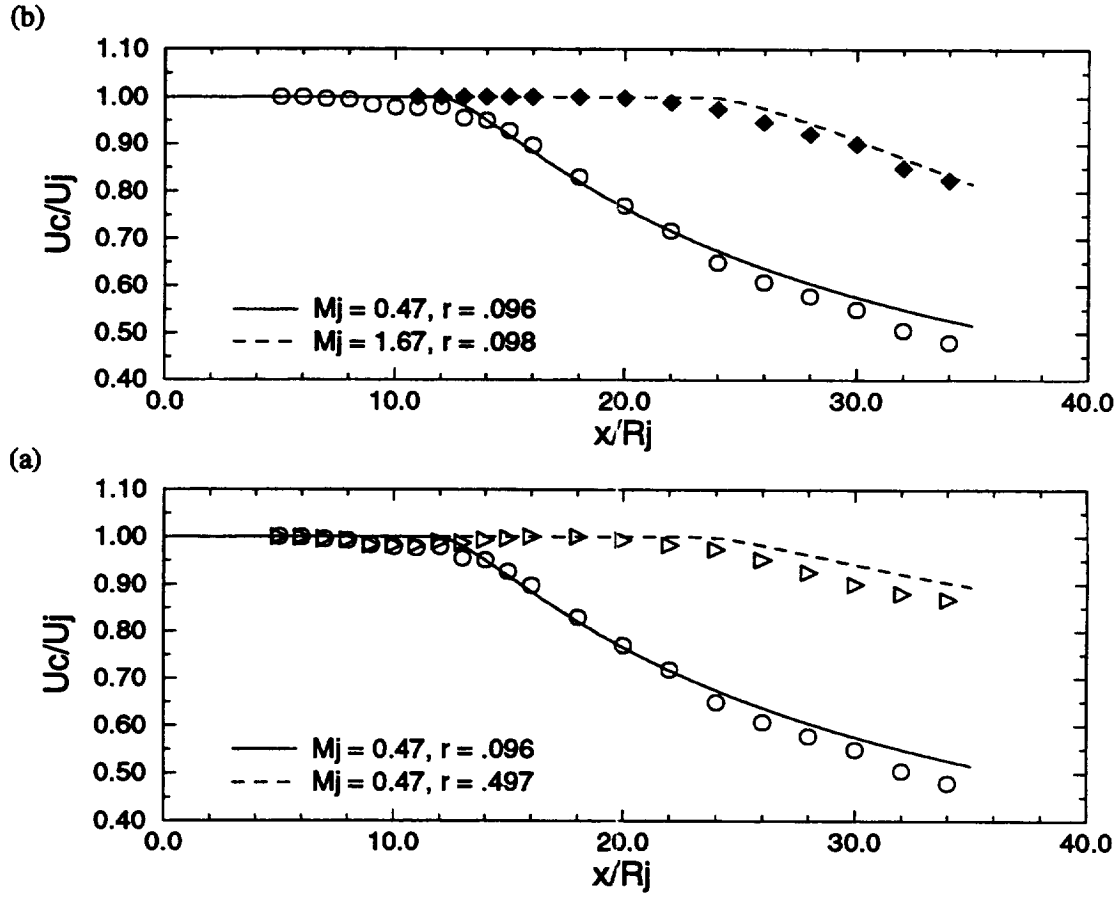

Figure 2.8. Comparison of single jet in moving stream calculations to measured data. Data from Morris [1976]. (a) centerline velocity variations with external flow; (b) centerline velocity variations with Mach number. Operating conditions: R_j = 2.54 cm; M_j = 0.47, U_j = 158 m/s, T_j = 283 K; M_j = 1.67, U_j = 461 m/s, T_j = 190 K.

layer and the current turbulence model, based on thin shear layer results, provides less representative growth rates.

The final comparison is for a single jet in a moving stream. These results are important to the future consideration of coaxial flow jets in the effect of Mach number and the effect of velocity ratio on jet spreading characteristics. Figure 2.8(a) shows the effect of velocity ratio on the centerline velocity. The data are from Morris [1976]. The good agreement shows that the turbulence model has the jet spreading less and increasing the core length as the velocity ratio increases from .096 to .497. The Mach number effect at a velocity ratio of about .1 is shown in Figure 2.8(b). Again, there is good agreement as the Mach number increases from .47 to 1.67. Hence, the turbulence model allows the calculated jet behavior to mimic the expected jet behavior for a compressible jet in a co-flowing stream.

2.3 Coaxial Jet Mixing Length Model

Initially, a coaxial jet, either with an initial normal velocity profile or an inverted velocity profile, has two distinct shear layers with uniform flow conditions at both edges of both shear layers. As a result, the mixing length model, equation (2.13), gives separate constant values C_1, C_2, and ℓ for each shear layer. The C_1 and C_2 factors depend on the velocity ratio, the density ratio, and the convected Mach number determined from the separate edge conditions. The characteristic length ℓ is determined for each shear layer from (2.14). The turbulent viscosity μ_T is then calculated across the coaxial jet using local values of ρ and $|\partial u/\partial r|$. Note that the separate shear layers have different constants (C_1, C_2, ℓ) so that at some point between the two shear layers, the μ_T profile must switch from one set of constants to the other set. As illustrated in Figure 2.9 for a normal velocity profile, an abrupt change in the μ_T profile, exaggerated in the figure, occurs that is not numerically desirable. Initially, $|\partial u/\partial r|$ is near zero between the two shear layers and the effect of the abrupt change is negligible. As the calculations progress downstream, $|\partial u/\partial r|$ between the two shear layers increases magnifying the negative effects of the abrupt change. Therefore to avoid this problem, a smooth hyperbolic tangent function is used to transition from one set of constants to the other set. This works until the outer jet core is about to disappear and the shear layers are about to start merging together. At that point, the mixing length model must be altered and the normal and the inverted velocity profile cases treated separately.

2.3.1 Normal Velocity Profile Mixing Length Model

The normal velocity profile mixing length model was developed by observing the behavior of the u and $\partial u/\partial r$ profiles as the shear layers merged and by comparing calculations to measured data taken from Lau [1980]. The merging shear layer profile

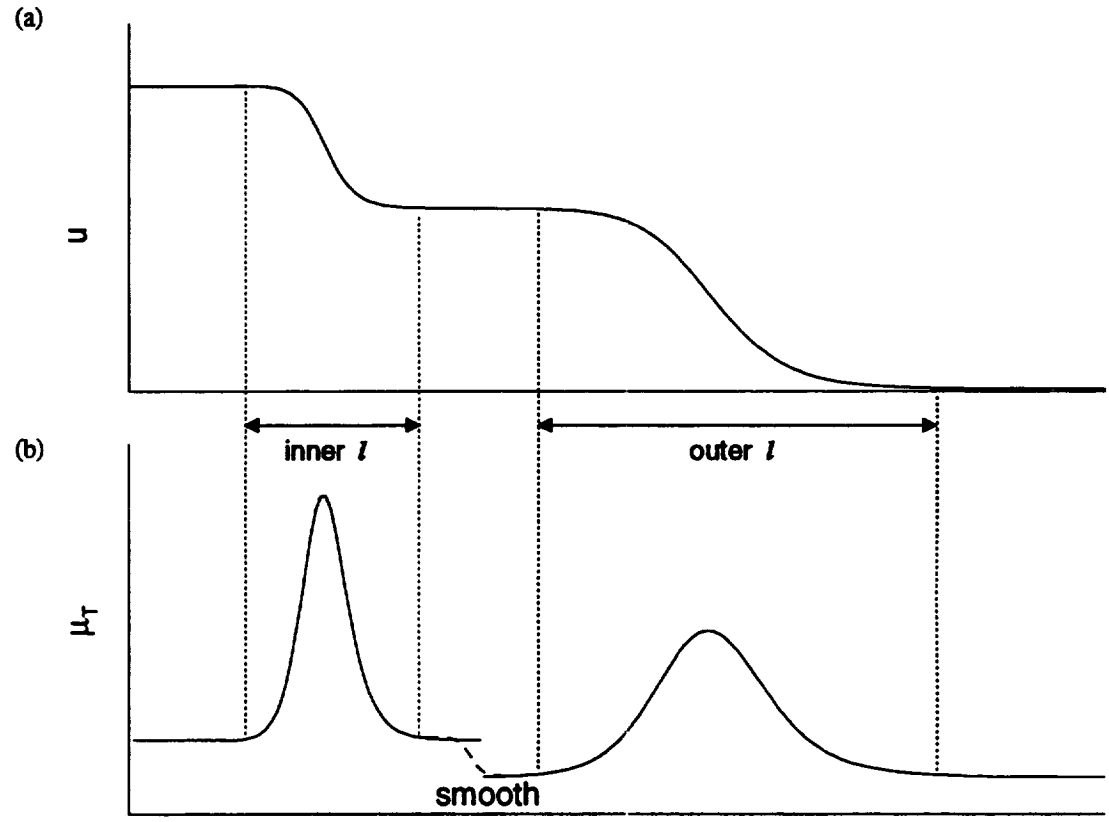

Figure 2.9. Illustration of smoothing turbulent viscosity profile. (a) typical normal velocity profile with two shear layers; (b) turbulent viscosity profile showing smoothed region

contains a local minimum in $|\partial u/\partial r|$ that disappears as the shear layer fully merges into a single jet, see Figure 2.10. This local minimum is used as a point to separately identify the two merging shear layers. A single characteristic length for the merging shear layers is defined as

$$\ell = \frac{\Delta U_{\max}}{|\partial u/\partial r|_{\max}} \tag{2.29}$$

where $\Delta U_{\max}$ is the largest ΔU between the two values determined by using the separation point. The C_1 and C_2 factors are also determined from the edge conditions that gave us $\Delta U_{\max}$. The maximum gradient $|\partial u/\partial r|_{\max}$ is the largest value of $|\partial u/\partial r|$ that occurs in the merging profile. This approach for determining C_1, C_2, and ℓ for a merging normal profile has the advantage that as the flow transitions into a single jet profile, the C_1, C_2, and ℓ factors transition into the appropriate form for a single jet.

A comparison of calculated velocity profiles to measured data (Lau [1980]) at four axial locations is shown in Figure 2.11. Initially, the two profiles are very similar. Downstream, deviations increase between calculated and measured profiles. But, in essence, the calculations produce a reasonable merging jet for an initial normal velocity profile.

Whereas the normal velocity profile mixing length model was formulated by comparing results to the Lau [1980] data, von Glahn et al. [1984] has data not considered in the mixing length model formulation. We compare these latter measurements to both velocity profile (Figure 2.12) and temperature profile (Figure 2.13) calculations at five axial locations. The experimental initial conditions are not clearly known, hence the discrepancy in the initial inner core results and subsequent flow development. Nevertheless, the calculated mean velocity and temperature profiles show merging and decay with axial distance in a manner similar to the measured data.

2.3.2 Inverted Velocity Profile Mixing Length Model

When an inverted profile starts to merge, it is obvious that a local maximum occurs in the velocity profile yielding $\partial u/\partial r = 0$, see Figure 2.14(a). This point is used to identify the separation point between the two shear layers. As long as the inner core exists, the two merging shear layers are treated separately but their constants are added as follows:

$$\left(C_1 C_2 \ell\right)_{\text{total}} = \left(C_1 C_2 \ell\right)_{\text{inner}} + \left(C_1 C_2 \ell\right)_{\text{outer}}. \tag{2.30}$$

This increases μ_T across the profile to mimic the increased turbulent action as the inverted profile starts to merge. When the inner core ends, equation (2.30) is no longer used and it is assumed that the mixing process in the outer shear layer dominates the flow, hence $\left(C_1 C_2 \ell\right)_{\text{total}} = \left(C_1 C_2 \ell\right)_{\text{outer}}$, see Figure 2.14(b). As with the normal profile, this later usage of C_1, C_2, and ℓ transitions into the proper usage for a single

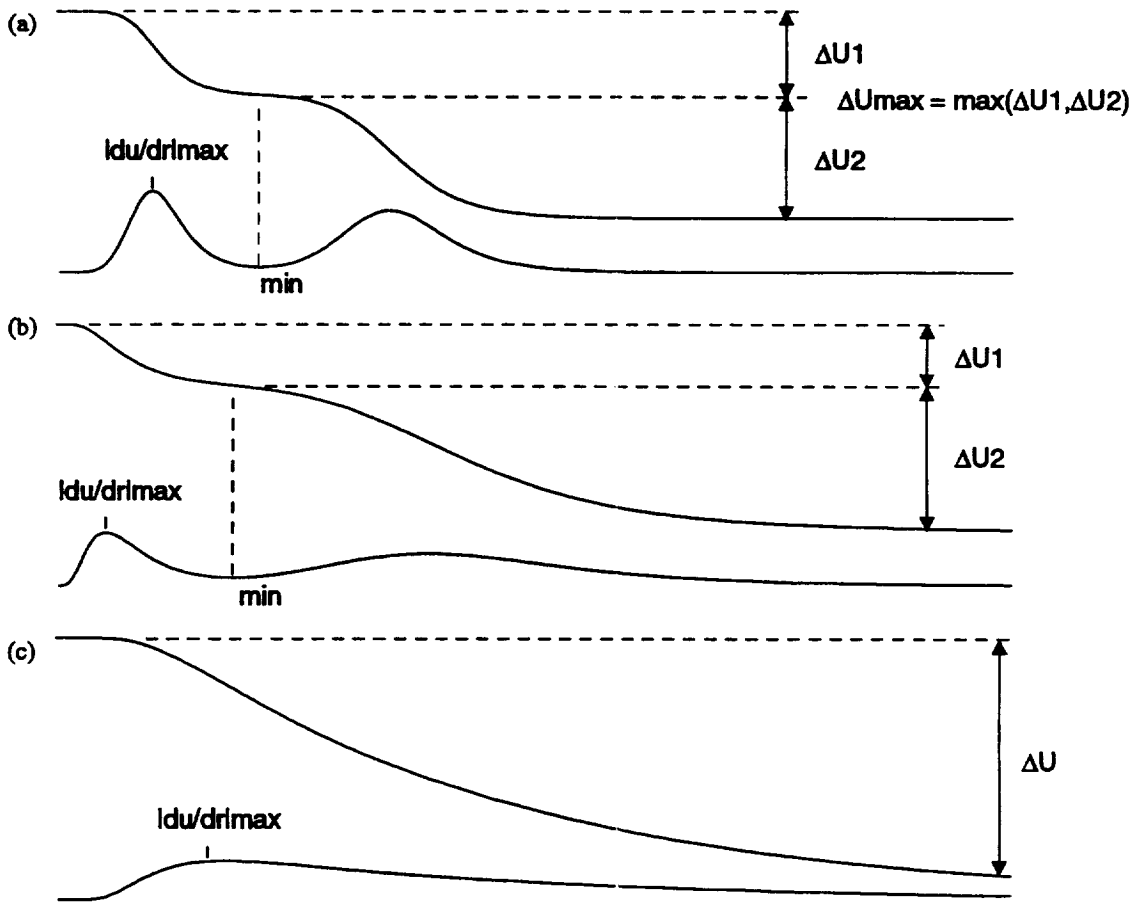

Figure 2.10. Definitions of merging normal velocity profile mixing length model factors. (a) initial merging profile; (b) advanced merging profile; (c) fully merged profile

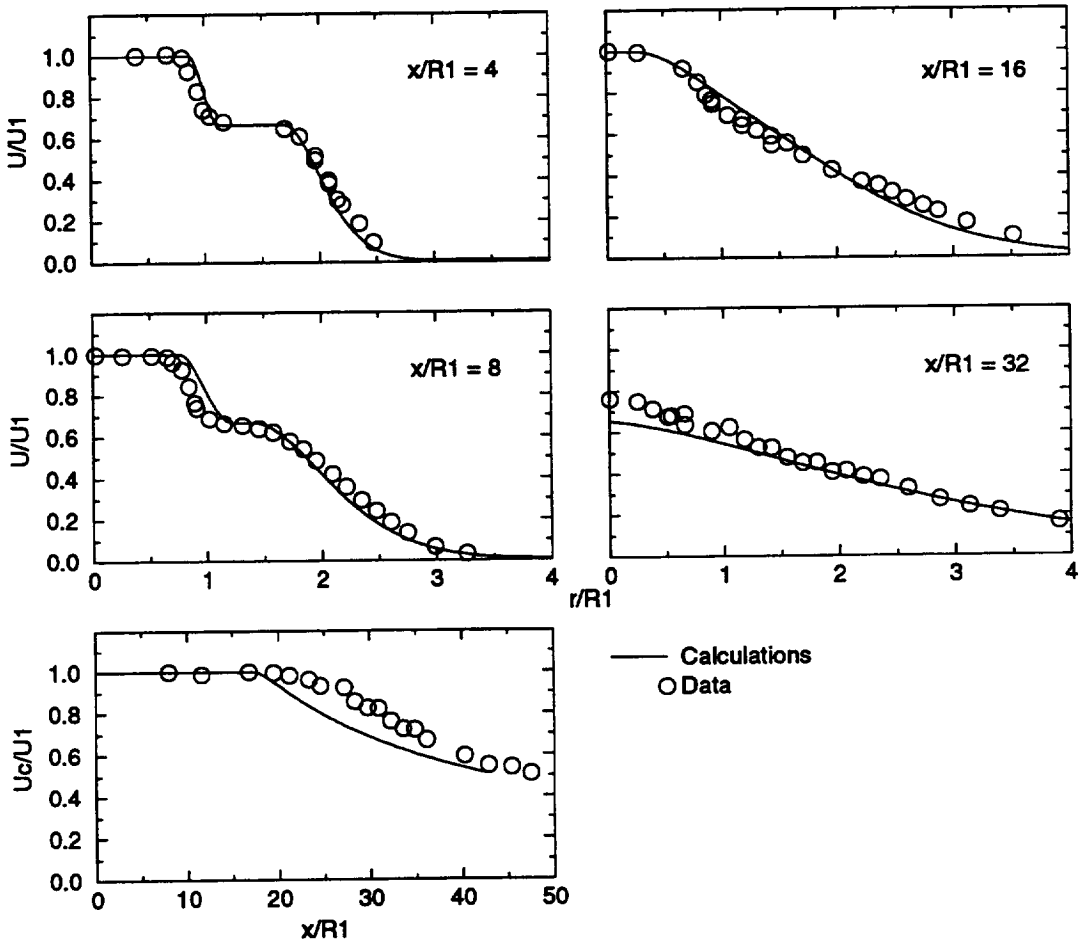

Figure 2.11. Comparison of normal velocity profile jet calculations to measured data. Data from Lau [1980]. Figures show four radial velocity profiles at four axial locations and one centerline velocity plot. Operating conditions: U_1 = 411 m/s, T_1 = 657 K, R_1 = 1.96 cm; U_2 = 274 m/s, T_2 = 292 K, R_2 = 3.91 cm.

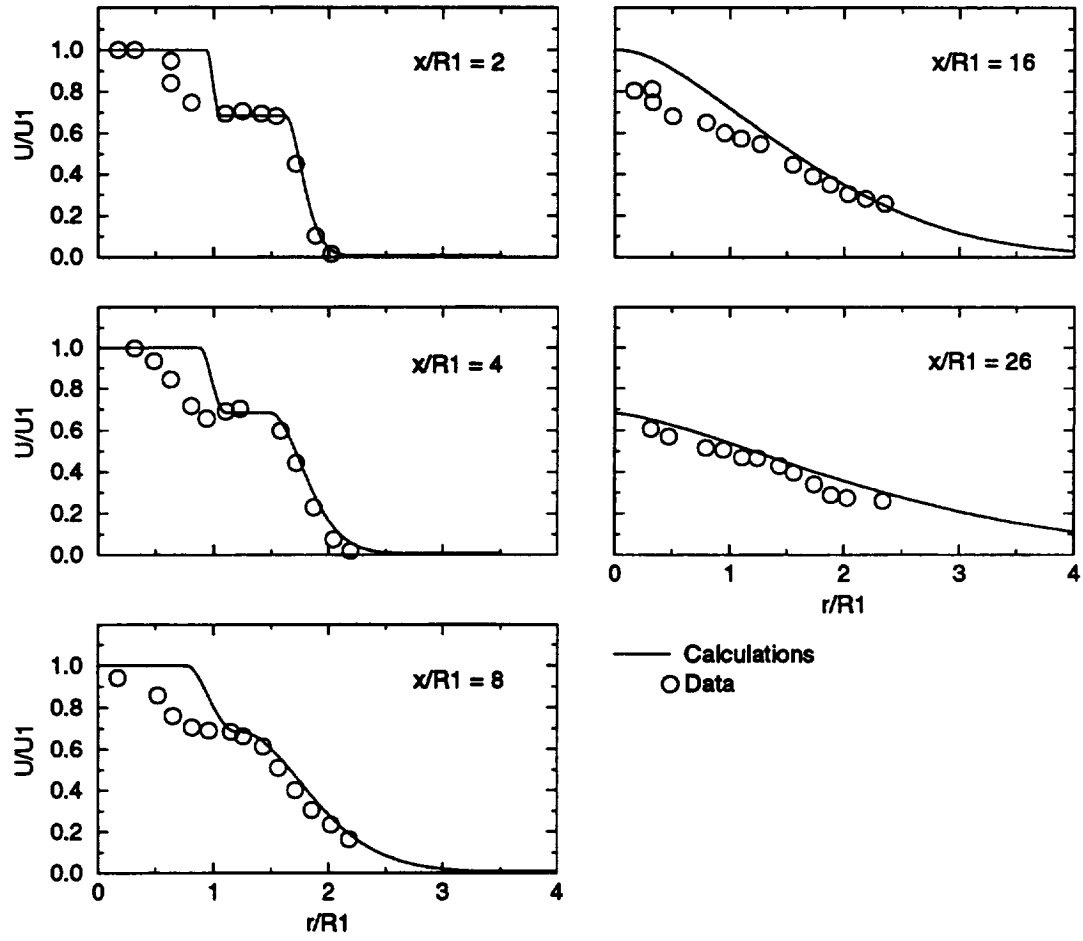

Figure 2.12. Comparison of normal velocity profile jet calculations to measured data. Data from von Glahn et al. [1984]. Figures show five radial velocity profiles at five axial locations. Operating conditions: U_1 = 459 m/s, T_1 = 1029 K, R_1 = 5.03 cm; U_2 = 314 m/s, T_2 = 248 K, R_2 = 8.80 cm.

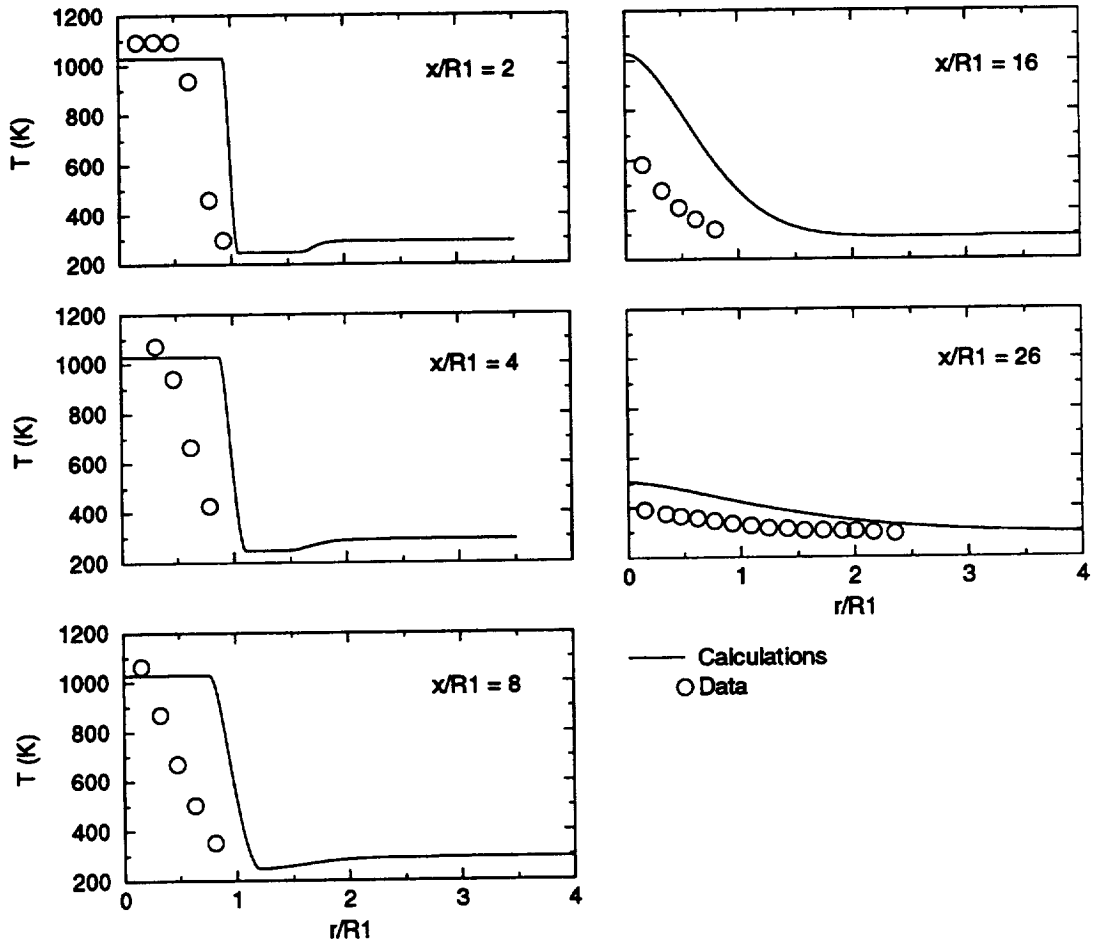

Figure 2.13. Comparison of normal velocity profile jet calculations to measured data. Data from von Glahn et al. [1984]. Figures show five radial temperature profiles at five axial locations for operating conditions given in Figure 2.12.

jet downstream. It should be noted that the mixing length model gives $\mu_T = 0$ at the local maximum, which is unrealistic. The simple solution taken here was to smooth the $|\partial u/\partial r|$ profile, and hence smooth μ_T; a process discussed in Appendix B.

The inverted profile data from Lau [1980] is used for comparison to calculations. These were the primary data used for designing the inverted profile mixing length model. Figure 2.15 shows good velocity profile comparisons at four axial locations. The centerline velocities do not compare very well but the experimental data are questionable since centerline values do not agree between the centerline velocity plot and the centerline velocities in the radial profile plots. Further comparisons with data not involved in the design process for this mixing length model are shown in Figures 2.16 and 2.17 for velocity and temperature profiles, respectively, measured at five axial locations by von Glahn et al. [1986]. Another set of comparisons with data from Tanna et al. [1979] are shown in Figures 2.18 and 2.19. For both sets of data, qualitative agreement is seen for both velocity and temperature profiles. Thus, the calculations are capable of producing a reasonable merging jet with an initial inverted velocity profile.

2.4 Summary

In this chapter, a steady, turbulent boundary layer code has been formulated to calculate the mean flow development of a compressible, coaxial jet. Mean flow properties were generated for coaxial jets with either a normal initial velocity profile or an inverted initial velocity profile that expanded and merged in a manner representative of measured data. These mean flow results are now to be used to calculate instability wave characteristics for coaxial jets. As discussed in the next chapter, the instability waves are the dominant sources for near field pressure fluctuations and far field radiated sound.

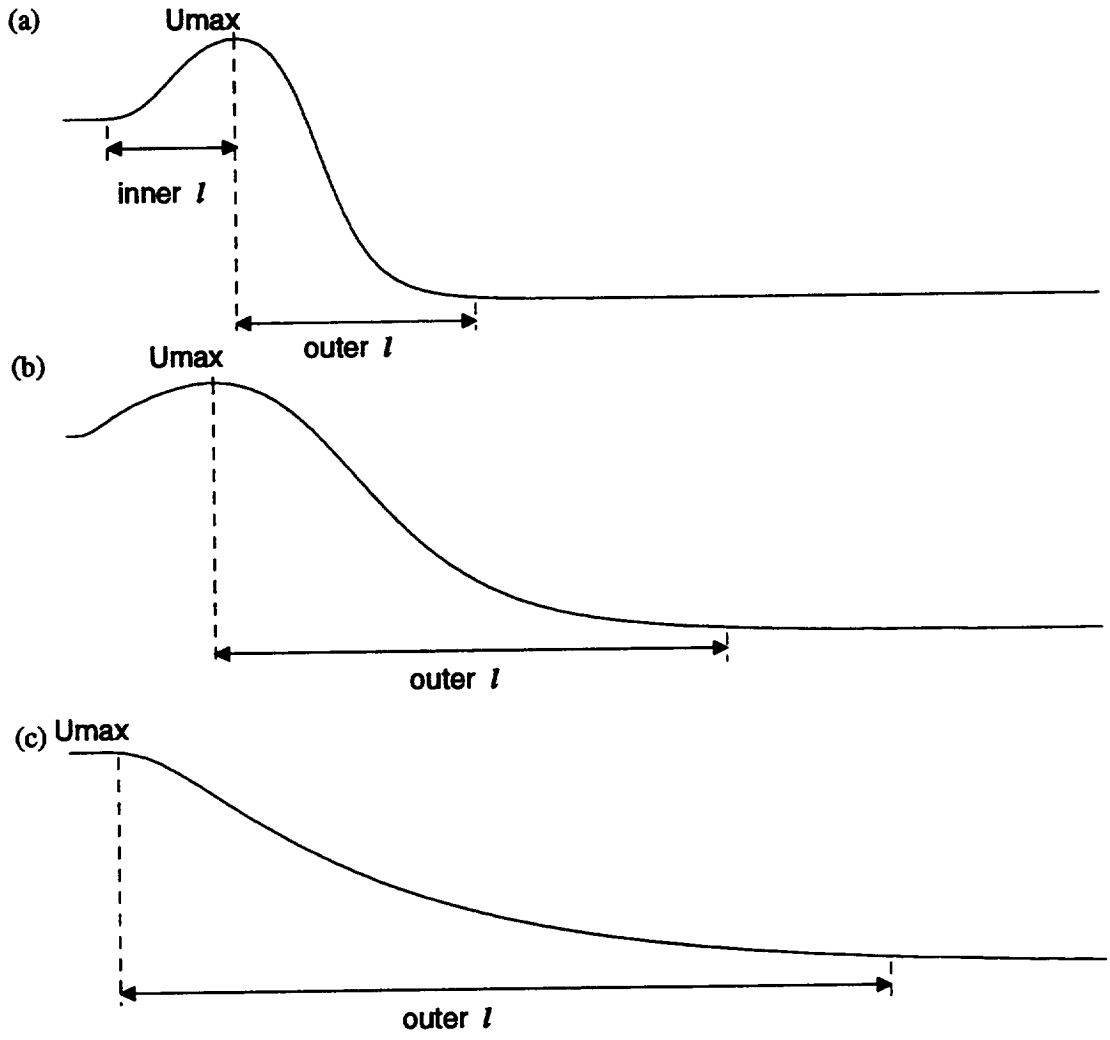

Figure 2.14. Definitions of merging inverted velocity profile mixing length model factors. (a) initial merging profile; (b) advanced merging profile, no inner stream potential core; (c) fully merged profile

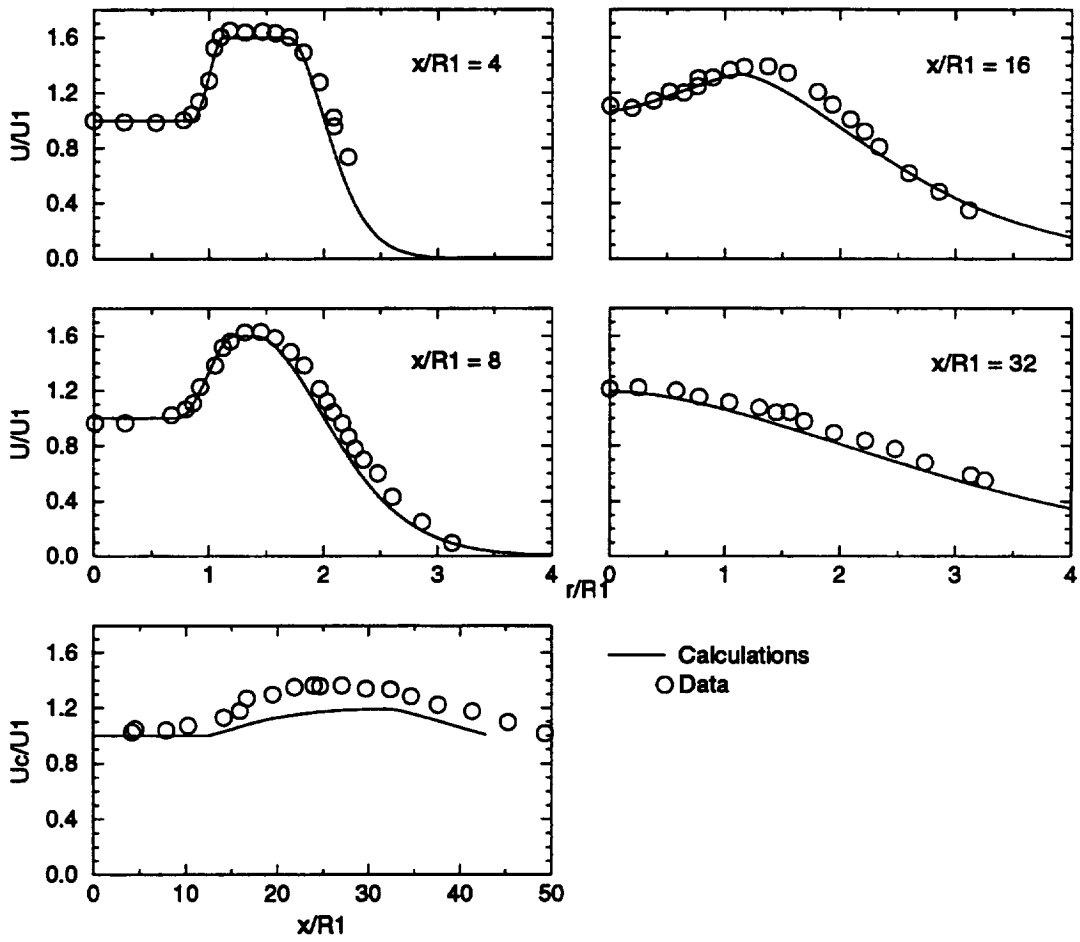

Figure 2.15. Comparison of inverted velocity profile jet calculations to measured data. Data from Lau [1980]. Figures show four radial velocity profiles at four axial locations and one centerline velocity plot. Operating conditions: U_1 = 171 m/s, T_1 = 292 K, R_1 = 1.96 cm; U_2 = 274 m/s, T_2 = 292 K, R_2 = 3.91 cm.

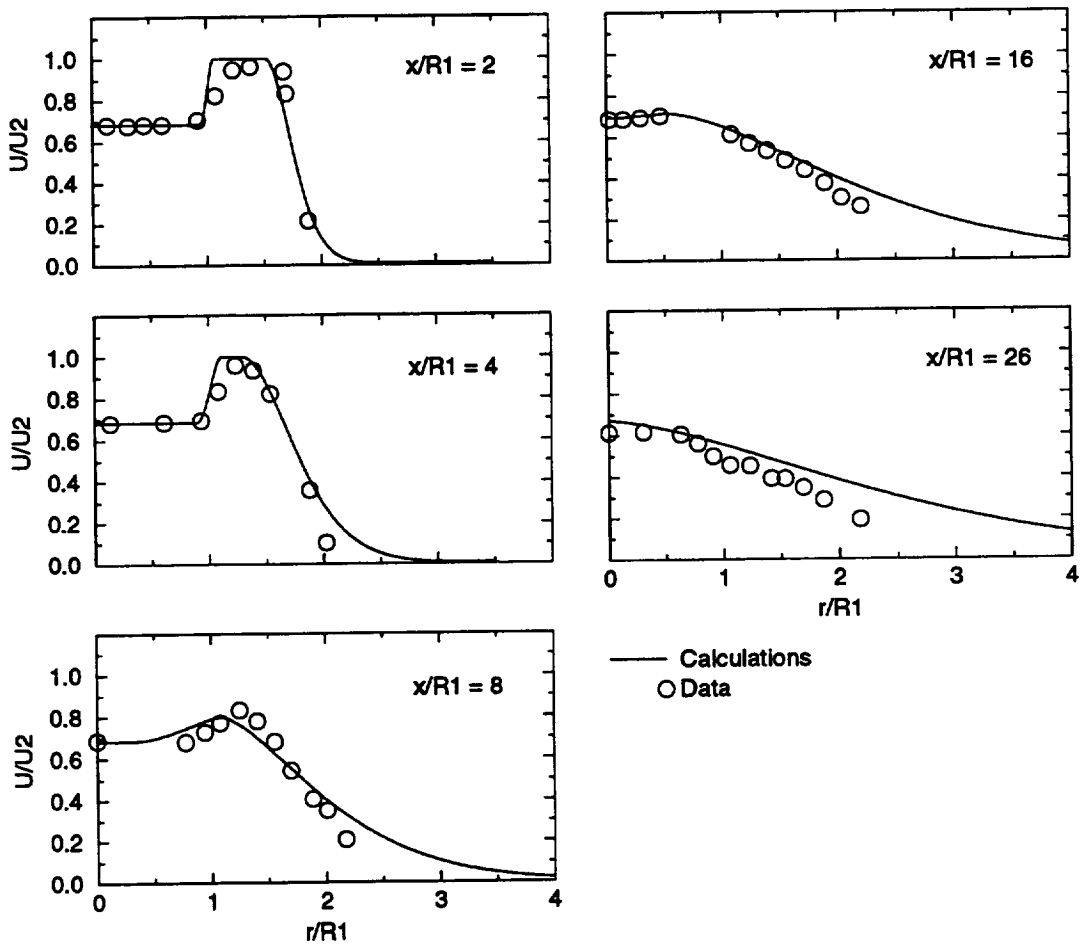

Figure 2.16. Comparison of inverted velocity profile jet calculations to measured data. Data from von Glahn et al. [1986]. Figures show five radial velocity profiles at five axial locations. Operating conditions: U_1 = 314 m/s, T_1 = 248 K, R_1 = 5.03 cm; U_2 = 459 m/s, T_2 = 1029 K, R_2 = 8.80 cm.

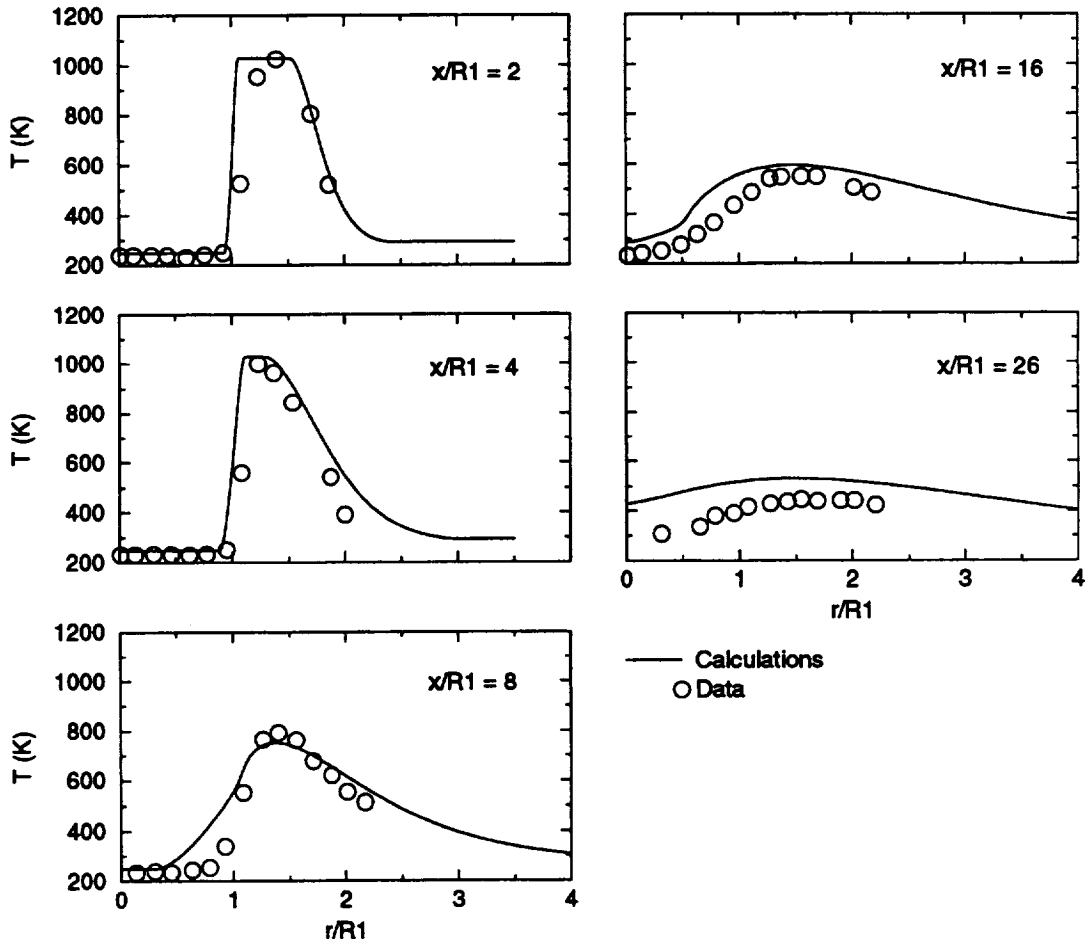

Figure 2.17. Comparison of inverted velocity profile jet calculations to measured data. Data from von Glahn et al. [1986]. Figures show five radial temperature profiles at five axial locations for operating conditions given in Figure 2.16.

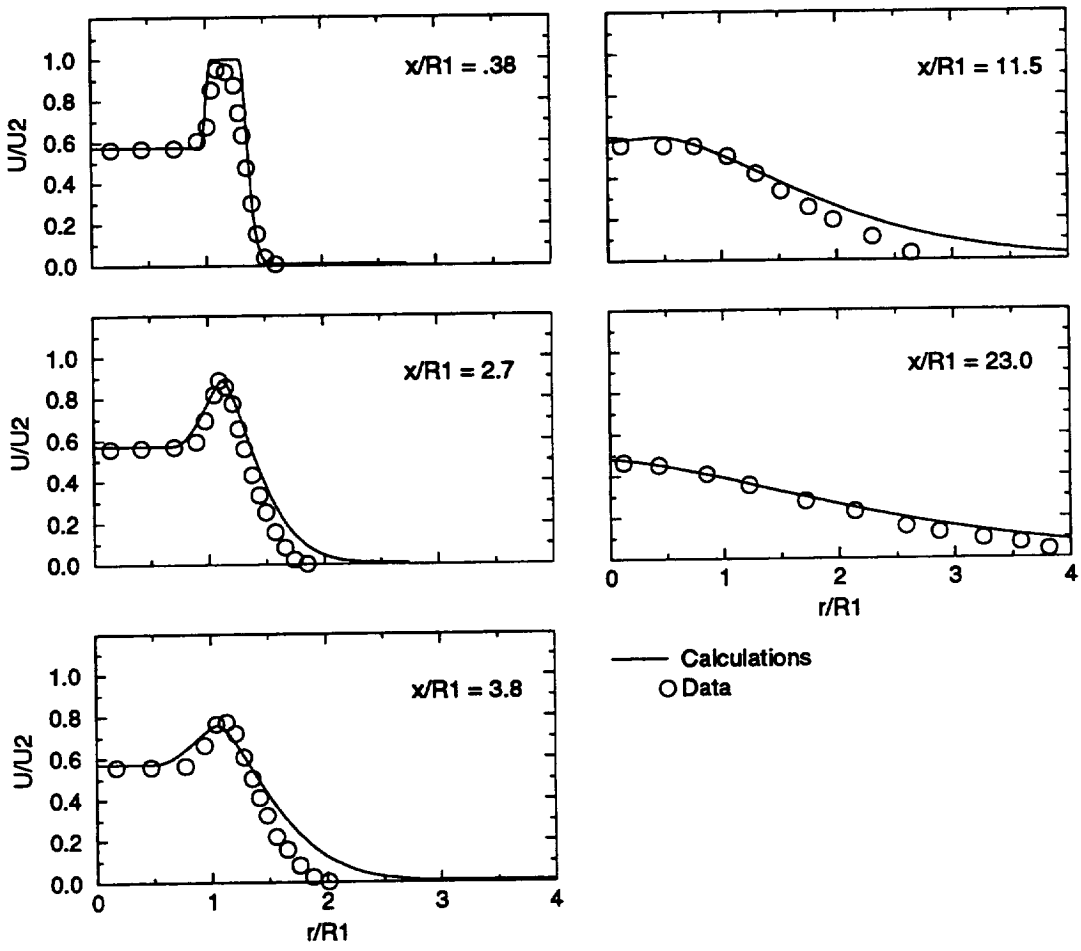

Figure 2.18. Comparison of inverted velocity profile jet calculations to measured data. Data from Tanna et al. [1979]. Figures show five radial velocity profiles at five axial locations. Operating conditions: $U_1 = 273$ m/s, $T_1 = 434$ K, $R_1 = 2.61$ cm; $U_2 = 477$ m/s, $T_2 = 758$ K, $R_2 = 3.57$ cm.

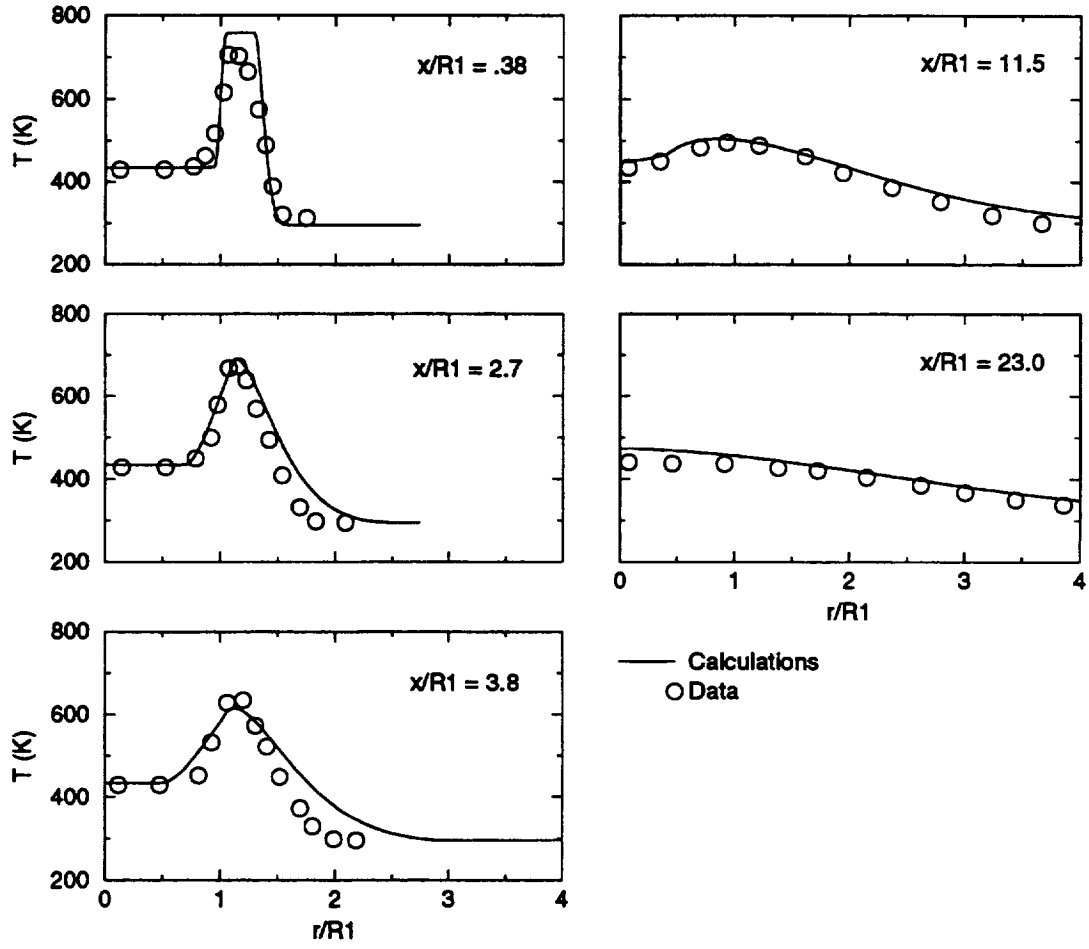

Figure 2.19. Comparison of inverted velocity profile jet calculations to measured data. Data from Tanna et al. [1979]. Figures show five radial temperature profiles at five axial locations for operating conditions given in Figure 2.18.

Chapter 3

THE INSTABILITY WAVE AND SOUND FIELD SOLUTION

In the introduction, we discussed the background for using spatially growing instability waves in a model for sound generation in supersonic jets. This chapter describes in more detail the equations that govern the development of the instability waves in these jets and their identification as sources of noise radiated to the far field. The formulation follows the approach of Tam and Burton [1984a] with the addition of a nonzero free stream velocity, Tam [1989]. Solutions are created that apply to separate but overlapping regions as illustrated in Figure 3.1. In the inner region, equations are developed that apply to the slowly diverging jet and its immediate environs. These equations are described first in this chapter. After a multiple scales expansion, the result to lowest order is a description of the instability wave in terms of its local growth rate and phase speed. Next, the outer solution is developed after rescaling the governing equations since the disturbances in the outer region are acoustic in nature and they travel in all directions with equal length scales. This is followed by the matching process, where the inner and outer regions overlap, that completes the description of the instability wave to lowest order. We then develop expressions for the near field pressure fluctuations and the far field directivity pattern. Finally, after describing the numerical procedures used to complete the calculations, we verify our procedures by comparing our calculated results to measurements from single and coaxial jet experiments.

3.1 Linearized Equations of Motion

The linearized equations of motion for small disturbances are derived from the following compressible, inviscid equations of motion:

continuity:

$$\frac{\partial \rho^*}{\partial t^*} + \nabla^* \cdot \left(\rho^* \mathbf{V}^*\right) = 0 \tag{3.1}$$

momentum:

$$\rho^* \left[\frac{\partial \mathbf{V}^*}{\partial t^*} + \mathbf{V}^* \cdot \nabla^* \mathbf{V}^*\right] = -\nabla^* p^* \tag{3.2}$$

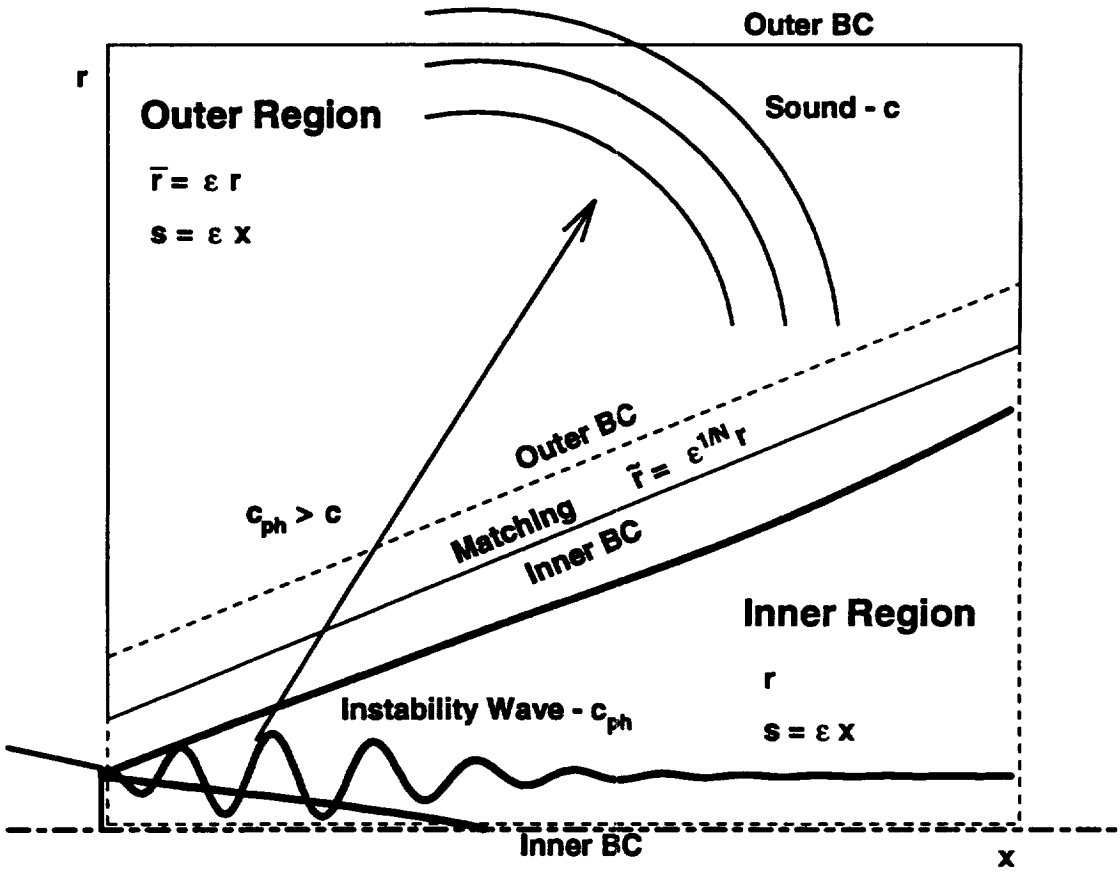

Figure 3.1. Schematic illustrating inner and outer regions of matched asymptotic solution. Inner region including the jet flow is outlined by a thin dashed line. Outer region outlined by a thin solid line outside the jet.

energy:

$$\rho^* \left[\frac{\partial h^*}{\partial t^*} + \mathbf{V}^* \cdot \nabla^* h^* \right] = \frac{\partial p^*}{\partial t^*} + \mathbf{V}^* \cdot \nabla^* p^* \tag{3.3}$$

state:

$$p^* = \rho^* R_g^* T^* \tag{3.4}$$

where $*$ denotes a dimensional quantity. It is convenient to combine the state and energy equations, and including the thermodynamic relation $h^* = c_p^* T^*$, to get

$$\frac{\partial p^*}{\partial t^*} + \mathbf{V}^* \cdot \nabla^* p^* + \gamma p^* \nabla^* \cdot \mathbf{V}^* = 0 \tag{3.5}$$

where continuity has been used to eliminate the density ρ^*, and γ appears from the relation $c_p^*/R_g^* = \gamma/(\gamma - 1)$. This results in a reduction of the governing equations to (3.1), (3.2), and (3.5). These equations are made dimensionless by using

$$\nabla = R_j \nabla^* \qquad t = t^* \frac{U_j}{R_j} \qquad \mathbf{V} = \frac{\mathbf{V}^*}{U_j} \qquad \rho = \frac{\rho^*}{\rho_j} \qquad p = \frac{p^*}{\rho_j U_j^2}$$

where all terms with subscript j are defined at the jet exit. The resulting dimensionless equations have the same form as the dimensional equations, hence we simply drop the $*$ from our notation.

To linearize these equations, we let

$$\begin{aligned} \rho &= \overline{\rho} + \rho' \\ \mathbf{V} &= \overline{\mathbf{V}} + \mathbf{V}' \\ p &= \overline{p} + p' \end{aligned} \tag{3.6}$$

where the overbar denotes a mean flow quantity and the prime denotes a fluctuating quantity, in this case, a small amplitude instability wave. Substitute equations (3.6) into the dimensionless forms of (3.1), (3.2), and (3.5). After expanding terms, subtracting the equations governing the mean flow quantities, and neglecting higher order terms containing products of fluctuating quantities, we get the linearized equations

$$\frac{\partial \rho}{\partial t} + \overline{\mathbf{V}} \cdot \nabla \rho' + \mathbf{V}' \cdot \nabla \overline{\rho} + \overline{\rho} \nabla \cdot \mathbf{V}' + \rho' \nabla \cdot \overline{\mathbf{V}} = 0 \tag{3.7}$$

$$\frac{\partial \mathbf{V}'}{\partial t} + \overline{\mathbf{V}} \cdot \nabla \mathbf{V}' + \mathbf{V}' \cdot \nabla \overline{\mathbf{V}} + \frac{\rho'}{\overline{\rho}} \left[\overline{\mathbf{V}} \cdot \nabla \overline{\mathbf{V}} \right] = -\frac{1}{\overline{\rho}} \nabla p' \tag{3.8}$$

$$\frac{\partial p'}{\partial t} + \overline{\mathbf{V}} \cdot \nabla p' + \gamma \overline{p} \nabla \cdot \mathbf{V}' + \gamma p' \nabla \cdot \overline{\mathbf{V}} = 0. \tag{3.9}$$

These equations have included the conditions that the mean flow is steady and that for a free jet, the mean static pressure is constant throughout the flow. Taking into consideration that the mean pressure is nondimensional and constant, it is easy to show that $\gamma \overline{p} = 1/M_j^2$, where M_j is the jet exit Mach number.

3.2 Inner Solution to Lowest Order

A cylindrical coordinate system centered on the nozzle exit, as shown in Figure 3.2, is used for axisymmetric jets. The cylindrical coordinates (r, θ, x) have corresponding velocities (v, w, u). For supersonic jets, the mean flow changes slowly in the axial direction and is represented by (Tam and Burton [1984a])

$$\overline{\mathbf{V}} = \left(\varepsilon \overline{v}_1(r, x), 0, \overline{u}(r, x)\right). \tag{3.10}$$

Outside the jet as $r \to \infty$, the ambient mean flow conditions are

$$\begin{aligned} \overline{\mathbf{V}} &= \overline{\mathbf{V}}_\infty = \left(\varepsilon \tfrac{\overline{v}_\infty}{r}, 0, \overline{u}_\infty\right) \\ \overline{p} &= \overline{p}_\infty. \end{aligned} \tag{3.11}$$

The ε in (3.10) represents the rate of spread of the jet mixing layer which is small for supersonic jets and, hence, ε is the small parameter of the problem.

To construct the inner solution, we transform the axisymmetric coordinates (r, x) to (r, s) where $s = \varepsilon x$ is the slow coordinate. Following Tam and Burton [1984a] and Whitham [1974], the fluctuating disturbances are represented as an asymptotic series of waves traveling through a nonuniform medium which in this case is the mean flow of the jet.

$$\begin{bmatrix} \rho'(r, \theta, x, t) \\ v'(r, \theta, x, t) \\ w'(r, \theta, x, t) \\ u'(r, \theta, x, t) \\ p'(r, \theta, x, t) \end{bmatrix} = \sum_{m=0}^{\infty} \delta_m(\varepsilon) \begin{bmatrix} \hat{\rho}_m(r, s) \\ \hat{v}_m(r, s) \\ \hat{w}_m(r, s) \\ \hat{u}_m(r, s) \\ \hat{p}_m(r, s) \end{bmatrix} \exp\left[i\left(\frac{\phi(s)}{\varepsilon} + n\theta - \omega t\right)\right] \tag{3.12}$$

We recognize that in order to obtain terms of $O(1)$, $\delta_0(\varepsilon) = 1$. Higher order terms will have functional forms for $\delta_m(\varepsilon)$, $m > 0$, that are found from the asymptotic expansion of the outer solution in the matching process.

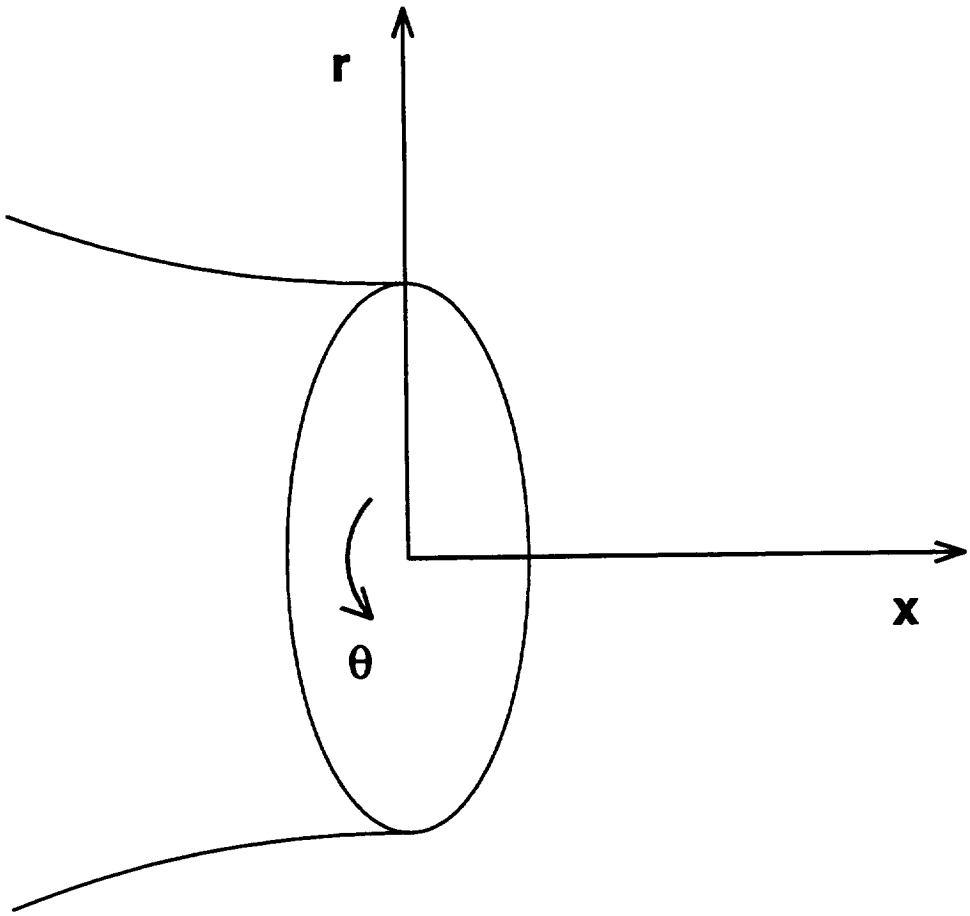

Figure 3.2. Cylindrical coordinate system centered on nozzle exit.

Before carrying out the expansion represented by (3.12), we write the linearized equations of continuity, motion, and energy, (3.7), (3.8), and (3.9), respectively, in cylindrical coordinates. We include the definition of the mean flow (3.10) and the transformation to the (r, s) coordinates. Finally, we carry out the differentiations with respect to t and θ and divide the equations through by $\exp[i(n\theta - \omega t)]$. This results in five equations relating $\hat{\rho}$, $\hat{v}$, $\hat{w}$, $\hat{u}$, and $\hat{p}$.

$$-i\omega\hat{\rho} + \varepsilon\overline{v}_1\frac{\partial\hat{\rho}}{\partial r} + \varepsilon\overline{u}\frac{\partial\hat{\rho}}{\partial s} + \hat{v}\frac{\partial\overline{\rho}}{\partial r} + \varepsilon\hat{u}\frac{\partial\overline{\rho}}{\partial s} + \overline{\rho}\left[\frac{1}{r}\frac{\partial}{\partial r}(r\hat{v}) + i\frac{n}{r}\hat{w} + \varepsilon\frac{\partial\hat{u}}{\partial s}\right] + \hat{\rho}\left[\frac{1}{r}\frac{\partial}{\partial r}(r\varepsilon\overline{v}_1) + \varepsilon\frac{\partial\overline{u}}{\partial s}\right] = 0 \tag{3.13}$$

$$-i\omega\hat{v} + \varepsilon\overline{v}_1\frac{\partial\hat{v}}{\partial r} + \varepsilon\overline{u}\frac{\partial\hat{v}}{\partial s} + \varepsilon\hat{v}\frac{\partial\overline{v}_1}{\partial r} + \varepsilon^2\hat{u}\frac{\partial\overline{v}_1}{\partial s} + \frac{\hat{\rho}}{\overline{\rho}}\left[\varepsilon^2\overline{v}_1\frac{\partial\overline{v}_1}{\partial r} + \varepsilon^2\overline{u}\frac{\partial\overline{v}_1}{\partial s}\right] = -\frac{1}{\overline{\rho}}\frac{\partial\hat{p}}{\partial r} \tag{3.14}$$

$$-i\omega\hat{w} + \varepsilon\overline{v}_1\frac{\partial\hat{w}}{\partial r} + \varepsilon\overline{u}\frac{\partial\hat{w}}{\partial s} + \varepsilon\hat{w}\frac{\overline{v}_1}{r} = -\frac{1}{r}\frac{in}{\overline{\rho}}\hat{p} \tag{3.15}$$

$$-i\omega\hat{u} + \varepsilon\overline{v}_1\frac{\partial\hat{u}}{\partial r} + \varepsilon\overline{u}\frac{\partial\hat{u}}{\partial s} + \hat{v}\frac{\partial\overline{u}}{\partial r} + \varepsilon\hat{u}\frac{\partial\overline{u}}{\partial s} + \frac{\hat{\rho}}{\overline{\rho}}\left[\varepsilon\overline{v}_1\frac{\partial\overline{u}}{\partial r} + \varepsilon\overline{u}\frac{\partial\overline{u}}{\partial s}\right] = -\varepsilon\frac{1}{\overline{\rho}}\frac{\partial\hat{p}}{\partial s} \tag{3.16}$$

$$-i\omega\hat{p} + \varepsilon\overline{v}_1\frac{\partial\hat{p}}{\partial r} + \varepsilon\overline{u}\frac{\partial\hat{p}}{\partial s} + \frac{1}{M_j^2}\left[\frac{1}{r}\frac{\partial}{\partial r}(r\hat{v}) + i\frac{n}{r}\hat{w} + \varepsilon\frac{\partial\hat{u}}{\partial s}\right] + \gamma\hat{p}\left[\frac{1}{r}\frac{\partial}{\partial r}(r\varepsilon\overline{v}_1) + \varepsilon\frac{\partial\overline{u}}{\partial s}\right] = 0 \tag{3.17}$$

When we apply the remainder of the expansion (3.12), for example $\hat{p}$ is

$$\hat{p}(r,s) = \sum_{m=0}^{\infty}\delta_m(\varepsilon)\hat{p}_m(r,s)\exp\left(i\frac{\phi(s)}{\varepsilon}\right), \tag{3.18}$$

we find terms of the form

$$\frac{\partial}{\partial s}\left[\hat{p}_m\exp\left(i\frac{\phi(s)}{\varepsilon}\right)\right] = \left[\frac{\partial\hat{p}_m}{\partial s} + \hat{p}_m\frac{i}{\varepsilon}\frac{d\phi}{ds}\right]\exp\left(i\frac{\phi(s)}{\varepsilon}\right).$$

Hence, for convenience, let

$$\frac{d\phi}{ds} = \alpha(s). \tag{3.19}$$

Equations (3.13) to (3.17) with the expansion applied, may now be divided through by $\exp(i\phi(s)/\varepsilon)$ and partitioned into terms according to $\delta_m(\varepsilon)$. In general, the mth-order set of equations can be combined in favor of $\hat{p}_m$ and cast in the form

$$\frac{\partial^2 \hat{p}_m}{\partial r^2} + \left[\frac{1}{r} + \frac{2\alpha}{\overline{\omega}}\frac{\partial \overline{u}}{\partial r} - \frac{1}{\overline{\rho}}\frac{\partial \overline{\rho}}{\partial r}\right]\frac{\partial \hat{p}_m}{\partial r} + \left[\overline{\rho} M_j^2 \overline{\omega}^2 - \frac{n^2}{r^2} - \alpha^2\right]\hat{p}_m = G_m(r,s) \qquad (3.20)$$

where $\overline{\omega} = \omega - \alpha\overline{u}$. The right side term G_m depends on lower order terms only. To lowest order, $m = 0$, G_0 is zero and the equation is homogeneous. The homogeneous form of (3.20) is commonly called the compressible Rayleigh Equation.

Outside the jet, the mean flow is given by (3.11) and (3.20) reduces, for $\hat{p}_0$, to

$$\frac{\partial^2 \hat{p}_0}{\partial r^2} + \frac{1}{r}\frac{\partial \hat{p}_0}{\partial r} + \left[\overline{\rho}_\infty M_j^2 \overline{\omega}_\infty^2 - \frac{n^2}{r^2} - \alpha^2\right]\hat{p}_0 = 0 \qquad (3.21)$$

where $\overline{\omega}_\infty = \omega - \alpha\overline{u}_\infty$. Equation (3.21) is Bessel's Equation with solution of the form

$$\hat{p}_0 = A_0 H_n^{(1)}(i\lambda r) + B_0 H_n^{(2)}(i\lambda r). \qquad (3.22)$$

The functions $H_n^{(1)}()$ and $H_n^{(2)}()$ are nth-order Hankel functions of the first and second kind, respectively, and

$$\lambda(\alpha) = \left[\alpha^2 - \overline{\rho}_\infty M_j^2 \overline{\omega}_\infty^2\right]^{1/2}. \qquad (3.23)$$

The choice of branch cuts for (3.23) will be discussed in the matching process.

To generalize, the lowest order solution of (3.20) has two linearly independent solutions that are functions of r and s. The amplitudes of these functions will vary with axial location giving a solution of the form

$$\hat{p}_0(r,s) = A_0(s)\zeta_1^p(r,s) + B_0(s)\zeta_2^p(r,s). \qquad (3.24)$$

As $r \to \infty$, equation (3.24) must tend to (3.22) and as $r \to 0$, $\hat{p}_0$ must be finite.

3.3 Outer Solution

In the region outside the jet, the ambient conditions $\overline{\rho}_\infty$ and $\overline{u}_\infty$ are uniform. Disturbances that travel in this region are independent of the coordinate system. Hence, distances traveled by the disturbance in any direction will be of the same scale. Using the cylindrical coordinate system of the inner solution, the axial coordinate was rescaled

as $s = \varepsilon x$. To bring the radial coordinate in the outer region to the same scale, we let $\overline{r} = \varepsilon r$ be the scaled radial coordinate.

Before transforming the governing equations to the outer coordinates, we want to reconsider the nondimensionalized momentum equation written as:

$$\frac{\partial \mathbf{V}}{\partial t} + \mathbf{V} \cdot \nabla \mathbf{V} = -\frac{1}{\rho} \nabla p \tag{3.25}$$

Substituting in (3.6), subtract mean terms, and neglect higher order terms results in a linearized momentum equation of the form

$$\frac{\partial \mathbf{V}'}{\partial t} + \overline{\mathbf{V}} \cdot \nabla \mathbf{V}' + \mathbf{V}' \cdot \nabla \overline{\mathbf{V}} = -\frac{1}{\overline{\rho}} \nabla p' + \frac{\rho'}{\overline{\rho}^2} \nabla \overline{p}. \tag{3.26}$$

This equation more clearly shows the effect of assuming $\nabla \overline{p} = 0$ throughout the medium outside the the jet (compare (3.26) to (3.8)). Equations (3.7) and (3.9) still apply to the outer region.

Now, substituting (3.11) into (3.7), (3.9), and (3.26) results in equations from which v, w, u, and p can be found without referring to the equation for ρ, the linearized form of (3.7). Hence, after transforming from the (r, x) coordinates to the $(\overline{r}, s)$ coordinates and applying the azimuthal and time dependencies $\exp(in\theta - i\omega t)$, we get the outer region linearized momentum and energy disturbance equations.

$$-i\frac{\omega}{\varepsilon} v + \overline{u}_\infty \frac{\partial v}{\partial s} + \varepsilon^2 \frac{\overline{v}_\infty}{\overline{r}} \frac{\partial v}{\partial \overline{r}} + \varepsilon^2 v \frac{\partial}{\partial \overline{r}} \left(\frac{\overline{v}_\infty}{\overline{r}} \right) = -\frac{1}{\overline{\rho}_\infty} \frac{\partial p}{\partial \overline{r}} \tag{3.27}$$

$$-i\frac{\omega}{\varepsilon} w + \overline{u}_\infty \frac{\partial w}{\partial s} + \varepsilon^2 \frac{\overline{v}_\infty}{\overline{r}} \frac{\partial w}{\partial \overline{r}} + \varepsilon^2 w \frac{\overline{v}_\infty}{\overline{r}^2} = -\frac{1}{\overline{r}} \frac{in}{\overline{\rho}_\infty} p \tag{3.28}$$

$$-i\frac{\omega}{\varepsilon} u + \overline{u}_\infty \frac{\partial u}{\partial s} + \varepsilon^2 \frac{\overline{v}_\infty}{\overline{r}} \frac{\partial u}{\partial \overline{r}} = -\frac{1}{\overline{\rho}_\infty} \frac{\partial p}{\partial s} \tag{3.29}$$

$$-i\frac{\omega}{\varepsilon} p + \overline{u}_\infty \frac{\partial p}{\partial s} + \varepsilon^2 \frac{\overline{v}_\infty}{\overline{r}} \frac{\partial p}{\partial \overline{r}} + \frac{1}{M_j^2} \left[\frac{1}{\overline{r}} \frac{\partial}{\partial \overline{r}} (\overline{r} v) + \frac{in}{\overline{r}} w + \frac{\partial u}{\partial s} \right] = 0 \tag{3.30}$$

Since no confusion should arise, primes have been left off the disturbance variables v, w, u, and p.

The solution to (3.27) through (3.30) begins by taking the Fourier Transform of the disturbance variables. For instance, the Fourier Transform pair for the pressure disturbance is:

Fourier Transform:

$$\tilde{p}(k) = \frac{1}{2\pi} \int_{-\infty}^{\infty} p(s) e^{-iks}\, ds \tag{3.31}$$

Inverse Fourier Transform:

$$p(s) = \int_{-\infty}^{\infty} \tilde{p}(k) e^{iks}\, dk. \tag{3.32}$$

After applying the transform, we rearrange the equations and examine them to obtain the following relations:

$$\tilde{v} = \frac{1}{ik} \frac{\partial \tilde{u}}{\partial \bar{r}} \tag{3.33}$$

$$\tilde{w} = \frac{n}{k\bar{r}} \tilde{u} \tag{3.34}$$

$$\left(-i \frac{\bar{\omega}_k}{\varepsilon} + \varepsilon^2 \frac{\bar{v}_\infty}{\bar{r}} \frac{\partial}{\partial \bar{r}} \right) \tilde{u} = -\frac{1}{\bar{\rho}_\infty} ik\tilde{p} \tag{3.35}$$

where $\bar{\omega}_k = \omega - \varepsilon k \bar{u}_\infty$. Equations (3.33) and (3.34) are statements in the transformed variables that the disturbance velocities outside the jet have zero vorticity. Since the outer disturbances are acoustic in nature, this result is appropriate, Skudrzyk [1971]. These relations allow the transformed outer equations to be combined into a single equation for $\tilde{u}$.

$$\left[1 - \varepsilon^4 \bar{\rho}_\infty M_j^2 \frac{\bar{v}_\infty^2}{\bar{r}^2} \right] \frac{\partial^2 \tilde{u}}{\partial \bar{r}^2} + \left[\frac{1}{\bar{r}} + i\varepsilon 2 \bar{\rho}_\infty M_j^2 \bar{\omega}_k \frac{\bar{v}_\infty}{\bar{r}} + \varepsilon^4 \bar{\rho}_\infty M_j^2 \frac{\bar{v}_\infty^2}{\bar{r}^3} \right] \frac{\partial \tilde{u}}{\partial \bar{r}}$$
$$+ \left[\bar{\rho}_\infty M_j^2 \frac{\bar{\omega}_k^2}{\varepsilon^2} - \frac{n^2}{\bar{r}^2} - k^2 \right] \tilde{u} = 0 \tag{3.36}$$

This equation almost has a Bessel Equation form. It can be transformed into that form, Tam and Burton [1984a], where the right hand side is nonzero but very small. We then get an approximate solution valid to order ε^2,

$$\tilde{u} \sim y^{a/2} Z_q \left(i\bar{k} y^{1/2} \right) \tag{3.37}$$

where

$$y = \bar{r}^2 - \varepsilon^4 \bar{\rho}_\infty M_j^2 \bar{v}_\infty^2$$
$$a = -i\varepsilon \bar{\rho}_\infty M_j^2 \bar{\omega}_k \bar{v}_\infty$$

$$\bar{k}^2 = \frac{1}{\varepsilon^2}\left(\varepsilon^2 k^2 - \bar{\rho}_\infty M_j^2 \bar{\omega}_k^2\right)$$
$$q^2 = n^2 - \varepsilon^2 \bar{\rho}_\infty^2 M_j^4 \bar{\omega}_k^2 \bar{v}_\infty^2$$

and $Z_q()$ represents any Bessel or Hankel function. To satisfy the outgoing wave or boundedness condition as $\bar{r} \to \infty$ in (3.36), it will be shown that the proper choice for the Z_q function is a Hankel function of the first kind of order q, $H_q^{(1)}\left(i\bar{k}y^{1/2}\right)$. The general solution for $\tilde{u}$ is

$$\tilde{u} = Cy^{a/2} H_q^{(1)}\left(i\bar{k}y^{1/2}\right). \tag{3.38}$$

The factor C may be found from the inner boundary condition on (3.36) as $y \to 0$, $\bar{r} \to 0$. Thus, C is independent of $\bar{r}$, but may depend on s. In essence, the inner boundary condition is the instability wave suggested by (3.12) which as $\bar{r} \to 0$, has some amplitude and phase $\tilde{A}(s,\varepsilon)\exp(i\phi(s)/\varepsilon)$. Now, transform the boundary condition:

$$g(k,\varepsilon) = \frac{1}{2\pi}\int_{-\infty}^{\infty} \tilde{A}(s,\varepsilon) e^{i\phi(s)/\varepsilon} e^{-iks}\, ds. \tag{3.39}$$

Hence as $\bar{r} \to 0$, $\tilde{u}(\bar{r},k) = g(k,\varepsilon)$. Therefore,

$$\tilde{u}(\bar{r},k) = g(k,\varepsilon) y(\bar{r})^{a/2} H_q^{(1)}\left(i\bar{k}(k) y(\bar{r})^{1/2}\right). \tag{3.40}$$

Finally, using (3.35), (3.32), and absorbing any constants into $g(k,\varepsilon)$, the outer solution is

$$p^o(\bar{r},s) = \int_{-\infty}^{\infty} g(k,\varepsilon)\left[1 + i\frac{\varepsilon^3}{\bar{\omega}_k}\frac{\bar{v}_\infty}{\bar{r}}\frac{\partial}{\partial \bar{r}}\right]\left\{\left(\bar{r}^2 - \varepsilon^4 \bar{\rho}_\infty M_j^2 \bar{v}_\infty^2\right)^{-i\frac{1}{2}\varepsilon\bar{\rho}_\infty M_j^2 \bar{\omega}_k \bar{v}_\infty}\right.$$
$$\left. \times\, H_q^{(1)}\left(i\frac{1}{\varepsilon}\left(\varepsilon^2 k^2 - \bar{\rho}_\infty M_j^2 \bar{\omega}_k^2\right)^{\frac{1}{2}}\left(\bar{r}^2 - \varepsilon^4 \bar{\rho}_\infty M_j^2 \bar{v}_\infty^2\right)^{\frac{1}{2}}\right)\right\} e^{iks}\, dk. \tag{3.41}$$

3.4 Matching to Lowest Order

The inner solution results from asymptotically expanding the equations that apply to the inner region. As a consequence, it does not satisfy the outer boundary conditions of the problem that lie in the outer region. Conversely, the outer solution does not satisfy boundary conditions that are in the inner region. Each part of the problem has missing conditions that are satisfied by the process of matching the two solutions. As

stated by Tam and Burton [1984a], the matching procedure to follow is the intermediate matching principle given by Van Dyke [1975]. The intermediate matching principle defines an intermediate variable and expands the inner and the outer solutions in terms of this variable. These two intermediate solutions must overlap in some domain whereby the difference between the inner and the outer solutions must vanish to the appropriate order in the intermediate limit. This process will first be followed for the outer solution. We will then have appropriate information to enable us to find higher order terms of the inner solution.

The intermediate variable is defined as

$$\tilde{r} = r\varepsilon^{1/N} \tag{3.42}$$

where N is a large positive number. In terms of the outer variable $\bar{r}$, we get

$$\bar{r} = \varepsilon r = \tilde{r}\varepsilon^{1-1/N}. \tag{3.43}$$

Letting $\eta = \varepsilon k$, we transform (3.41) from the $(\bar{r}, s)$ coordinates to the $(\tilde{r}, s)$ coordinates.

$$\begin{aligned} p^o(\tilde{r}, s) = & \int_{-\infty}^{\infty} \frac{1}{\varepsilon} g\left(\frac{\eta}{\varepsilon}, \varepsilon\right) \left[1 + i\frac{\varepsilon^{1+2/N}}{\bar{\omega}_\eta} \frac{\bar{v}_\infty}{\tilde{r}} \frac{\partial}{\partial \tilde{r}}\right] \\ & \times \left\{ \left(\varepsilon^{2-2/N}\tilde{r}^2 - \varepsilon^4 \bar{\rho}_\infty M_j^2 \bar{v}_\infty^2\right)^{-i\frac{1}{2}\varepsilon\bar{\rho}_\infty M_j^2 \bar{\omega}_\eta \bar{v}_\infty} \right. \\ & \left. \times H_q^{(1)}\left(i\lambda(\eta)\left(\varepsilon^{-2/N}\tilde{r}^2 - \varepsilon^2 \bar{\rho}_\infty M_j^2 \bar{v}_\infty^2\right)^{\frac{1}{2}}\right) \right\} e^{is\eta/\varepsilon}\, d\eta \end{aligned} \tag{3.44}$$

where

$$g\left(\frac{\eta}{\varepsilon}, \varepsilon\right) = \frac{1}{2\pi} \int_{-\infty}^{\infty} \tilde{A}(s, \varepsilon) e^{i[\phi(s) - s\eta]/\varepsilon}\, ds \tag{3.45}$$

$$q^2 = n^2 - \varepsilon^2 \bar{\rho}_\infty^2 M_j^4 \bar{\omega}_\eta^2 \bar{v}_\infty^2 \tag{3.46}$$

$$\lambda(\eta) = \left(\eta^2 - \bar{\rho}_\infty M_j^2 \bar{\omega}_\eta^2\right)^{1/2} \tag{3.47}$$

$$\bar{\omega}_\eta = \omega - \eta \bar{u}_\infty. \tag{3.48}$$

The goal is to asymptotically evaluate (3.44) as $\varepsilon \to 0$ keeping $\tilde{r}$ fixed. This is the intermediate limit.

The first step is to evaluate (3.45) by the saddle point method. (See, for example, Bender and Orszag [1978] and Dingle [1973].) The saddle point is found by setting

the derivative of the exponential argument

$$\Theta(s) = i[\phi(s) - s\eta] \tag{3.49}$$

equal to zero; that is

$$\frac{d\Theta(s)}{ds} = i\left[\frac{d\phi(s)}{ds} - \eta\right] = 0$$

or

$$\alpha(s) - \eta = 0 \tag{3.50}$$

where use has been made of (3.19). Let $\bar{s}(\eta)$ be the root of (3.50). The saddle point is then at $s = \bar{s}$.

Expanding $\tilde{A}(s,\varepsilon)$ as

$$\tilde{A}(s,\varepsilon) = \tilde{A}_0(s) + \varepsilon\tilde{A}_1(s) + \cdots, \tag{3.51}$$

the saddle point evaluation of (3.45) is

$$g\left(\frac{\eta}{\varepsilon},\varepsilon\right) = \left[\frac{\varepsilon}{-i2\pi\alpha'(\bar{s})}\right]^{\frac{1}{2}} e^{i[\phi(\bar{s})-\bar{s}\eta]/\varepsilon}\left\{\tilde{A}_0(\bar{s}) + \varepsilon B(\bar{s}) + \cdots\right\} \tag{3.52}$$

where

$$\alpha'(\bar{s}) = \left.\frac{d\alpha}{ds}\right|_{s=\bar{s}}$$

and $B(\bar{s})$ is defined in Appendix C.

The next step is to substitute (3.52) into (3.44) and evaluate the resulting expression by the saddle point method, also. Again, the saddle point is found by setting the derivative of the exponential function

$$\Theta(\eta) = i[\phi(\bar{s}) - \eta\bar{s} + \eta s]$$

equal to zero.

$$\frac{d\Theta(\eta)}{d\eta} = i\left[\left(\frac{d\phi(\bar{s})}{d\bar{s}} - \eta\right)\frac{d\bar{s}}{d\eta} - \bar{s} + s\right] = 0 \tag{3.53}$$

Noting that $d\phi(\bar{s})/d\bar{s} = \alpha(\bar{s})$ and that $\alpha(\bar{s}) = \eta$ from (3.50), we get that $\bar{s}(\eta) = s$ at the saddle point. Hence, the saddle point for (3.44) is $\eta = \alpha(s)$.

After the saddle point is defined, there is a lot of algebra involved in obtaining the evaluation of (3.44). An outline of the steps involved is given in Appendix C. The

final result for the outer solution in the intermediate limit is

$$p^o(\tilde{r},s) \sim e^{i\phi(s)/\varepsilon}\left\{\tilde{A}_0\left(1-i\varepsilon\ln\varepsilon\overline{\rho}_\infty M_j^2\overline{\omega}_\infty\overline{v}_\infty\right)H_n^{(1)}\left(i\lambda(\alpha)\varepsilon^{-1/N}\tilde{r}\right)\right.$$
$$+\varepsilon\left[\left(\delta_{n0}\overline{\rho}_\infty M_j^2\overline{\omega}_\infty\overline{v}_\infty\frac{\pi}{2}\tilde{A}_0+\tilde{A}_1+E\left(\varepsilon^{-1/N}\tilde{r}\right)\right)H_n^{(1)}\left(i\lambda(\alpha)\varepsilon^{-1/N}\tilde{r}\right)\right.$$
$$\left.\left.+\ D\left(\varepsilon^{-1/N}\tilde{r}\right)\frac{\partial}{\partial\left(\varepsilon^{-1/N}\tilde{r}\right)}H_n^{(1)}\left(i\lambda(\alpha)\varepsilon^{-1/N}\tilde{r}\right)\right]\right\}+O\left(\varepsilon^2\ln\varepsilon\right) \qquad (3.54)$$

where

$$E\left(\varepsilon^{-1/N}\tilde{r}\right) = -i\overline{\rho}_\infty M_j^2\overline{\omega}_\infty\overline{v}_\infty\ln\left(\varepsilon^{-1/N}\tilde{r}\right)\tilde{A}_0$$
$$-i\frac{\alpha'}{2}\frac{\tilde{A}_0}{\lambda(\alpha)^4}\left(\alpha+\overline{\rho}_\infty M_j^2\overline{u}_\infty\overline{\omega}_\infty\right)^2\left(n^2+\left(\lambda(\alpha)\varepsilon^{-1/N}\tilde{r}\right)^2\right),$$

$$D\left(\varepsilon^{-1/N}\tilde{r}\right) = i\frac{\overline{v}_\infty\tilde{A}_0}{\overline{\omega}_\infty\varepsilon^{-1/N}\tilde{r}}-\frac{i}{2}\frac{\varepsilon^{-1/N}\tilde{r}}{\lambda(\alpha)^4}\left[2\lambda(\alpha)^2\left(\alpha+\overline{\rho}_\infty M_j^2\overline{u}_\infty\overline{\omega}_\infty\right)\tilde{A}_0'\right.$$
$$\left.+\alpha'\tilde{A}_0\lambda(\alpha)^2\left(1-\overline{\rho}_\infty M_j^2\overline{u}_\infty^2\right)-2\alpha'\tilde{A}_0\left(\alpha+\overline{\rho}_\infty M_j^2\overline{u}_\infty\overline{\omega}_\infty\right)^2\right],$$

$$\lambda(\alpha)=\left[\alpha^2-\overline{\rho}_\infty M_j^2\overline{\omega}_\infty^2\right]^{1/2},$$

$$\overline{\omega}_\infty=\omega-\alpha\overline{u}_\infty,$$

$$\delta_{n0}=\begin{cases}1, & n=0\\ 0, & n\neq 0\end{cases}$$

$$\alpha'=\frac{d\alpha(s)}{ds}, \qquad \text{and} \qquad \tilde{A}_0'=\frac{d\tilde{A}_0(s)}{ds}.$$

Equation (3.54) has terms of $O(1)$, $O(\varepsilon\ln\varepsilon)$, and $O(\varepsilon)$. This suggests that the expansion given by (3.12) should have

$$\begin{aligned}\delta_1(\varepsilon)&=\varepsilon\ln\varepsilon\\ \delta_2(\varepsilon)&=\varepsilon\end{aligned} \qquad (3.55)$$

We now want to match the outer solution expansion (3.54) to the inner solution expansion in the intermediate coordinates. From (3.18) and (3.24) and using $r = \tilde{r}\varepsilon^{-1/N}$, the inner expansion to $O(1)$ is

$$\hat{p}_0^i(\tilde{r},s) = e^{i\phi(s)/\varepsilon}\left[A_0(s)\zeta_1^p\left(\varepsilon^{-1/N}\tilde{r},s\right) + B_0(s)\zeta_2^p\left(\varepsilon^{-1/N}\tilde{r},s\right)\right].$$

As $\varepsilon \to 0$ with $\tilde{r}$ fixed, then

$$\zeta_1^p(\varepsilon^{-1/N}\tilde{r},s) \to H_n^{(1)}\left(i\lambda(\alpha)\varepsilon^{-1/N}\tilde{r}\right)$$
$$\zeta_2^p(\varepsilon^{-1/N}\tilde{r},s) \to H_n^{(2)}\left(i\lambda(\alpha)\varepsilon^{-1/N}\tilde{r}\right).$$

Hence, in the intermediate limit

$$\hat{p}_0^i(\tilde{r},s) \sim e^{i\phi(s)/\varepsilon}\left[A_0(s)H_n^{(1)}\left(i\lambda(\alpha)\varepsilon^{-1/N}\tilde{r}\right) + B_0(s)H_n^{(2)}\left(i\lambda(\alpha)\varepsilon^{-1/N}\tilde{r}\right)\right] + O(\varepsilon\ln\varepsilon). \tag{3.56}$$

Comparing (3.56) to (3.54), we see that

$$A_0(s) = \tilde{A}_0(s) \tag{3.57}$$

$$B_0(s) = 0\,. \tag{3.58}$$

This result and the condition of finite value at $r = 0$ placed on (3.24) turns the $m = 0$ solution of (3.20) into an eigenvalue problem with solutions only for certain values of the eigenvalue α.

The matching of the inner and outer solutions at the intermediate limit and at the saddle point $\eta = \alpha(s)$ has also matched the arguments of the Hankel functions $H_n^{(1)}$. We can now show that this is the proper choice to meet the boundedness condition as $r \to \infty$ and what the conditions must be on the argument of the function. When the asymptotic expansion for large arguments is made, the Hankel function of the first kind takes the form (Abramowitz and Stegun [1965])

$$H_n^{(1)}(z) \sim z^{-1/2}e^{iz}. \tag{3.59}$$

Writing the Hankel function argument in (3.54) and (3.56) as

$$z = i(Re\{\lambda(\alpha)\} + iIm\{\lambda(\alpha)\})r$$

and substituting into (3.59), the exponential function becomes

$$e^{-Re\{\lambda(\alpha)\}r} e^{-iIm\{\lambda(\alpha)\}r}.$$

To insure that the function decays for large r, we must have that $Re\{\lambda(\alpha)\} > 0$. In general, then, for the complex value $\lambda(\alpha)$,

$$-\frac{\pi}{2} \leq \arg\lambda(\alpha) \leq \frac{\pi}{2}. \tag{3.60}$$

This represents the choice of branch cuts for (3.23). Furthermore, since in the matching process $\eta = \alpha(s)$, (3.60) must also apply to $\lambda(\eta)$ in (3.44), which basically has the same Hankel function argument as (3.38). Thus, we are justified in choosing the Hankel function of the first kind as the functional form for the solution in (3.37).

3.5 Matching to Higher Order

To match terms to higher order, we substitute (3.55) into the expansion for the inner region equations (3.13) through (3.17). The equations can then be clearly partitioned into $O(\varepsilon \ln \varepsilon)$ and $O(\varepsilon)$ terms. These equations can be combined into the form of (3.20) where $G_1(r,s) = 0$ and $G_2(r,s)$ is a function of $m = 0$ terms.

With $G_1(r,s) = 0$, the $O(\varepsilon \ln \varepsilon)$ expansion term has a solution identical to the $O(1)$ term. Hence,

$$\hat{p}_1(r,s) = A_1(s)\zeta_1^p(r,s) + B_1(s)\zeta_2^p(r,s). \tag{3.61}$$

The same boundedness conditions apply here as in the $O(1)$ solution in the previous section. Following the same procedure in the intermediate limit, we find after matching to (3.54) that

$$A_1(s) = -i\overline{\rho}_\infty M_j^2 \overline{\omega}_\infty \overline{v}_\infty \tilde{A}_0(s) \tag{3.62}$$

$$B_1(s) = 0 \tag{3.63}$$

Equation (3.20) for $m = 2$ is inhomogeneous. When the $O(\varepsilon)$ inner equations are manipulated to obtain the form of (3.20), the right side becomes

$$G_2(r,s) = \overline{\rho}\left\{\left[\frac{1}{r} + \frac{2\alpha}{\overline{\omega}}\frac{\partial\overline{u}}{\partial r}\right]R_v + \frac{\partial R_v}{\partial r} + i\overline{\omega}R_p + i\frac{n}{r}R_w + i\alpha R_u\right\} \tag{3.64}$$

where

$$R_v = -\overline{v}_1\frac{\partial\hat{v}_0}{\partial r} - \overline{u}\frac{\partial\hat{v}_0}{\partial s} - \hat{v}_0\frac{\partial\overline{v}_1}{\partial r} \tag{3.65}$$

$$R_w = -\overline{v}_1 \frac{\partial \hat{w}_0}{\partial r} - \overline{u}\frac{\partial \hat{w}_0}{\partial s} - \hat{w}_0 \frac{\overline{v}_1}{r} \tag{3.66}$$

$$R_u = -\overline{v}_1 \frac{\partial \hat{u}_0}{\partial r} - \overline{u}\frac{\partial \hat{u}_0}{\partial s} - \hat{u}_0 \frac{\partial \overline{u}}{\partial s} - \frac{1}{\overline{\rho}}\frac{\partial \hat{p}_0}{\partial s} - \frac{\hat{\rho}_0}{\overline{\rho}}\left[\overline{v}_1 \frac{\partial \overline{u}}{\partial r} + \overline{u}\frac{\partial \overline{u}}{\partial s}\right] \tag{3.67}$$

$$R_p = -M_j^2 \overline{v}_1 \frac{\partial \hat{p}_0}{\partial r} - M_j^2 \overline{u}\frac{\partial \hat{p}_0}{\partial s} - \frac{\partial \hat{u}_0}{\partial s} - \gamma M_j^2 \hat{p}_0 \left[\frac{1}{r}\frac{\partial}{\partial r}(r\overline{v}_1) + \frac{\partial \overline{u}}{\partial s}\right]. \tag{3.68}$$

In this case, the solution of (3.20) is the sum of the homogeneous and particular solutions as found using the method of variation of parameters, Bender and Orszag [1978]. It takes the general form

$$\begin{aligned}\hat{p}_2(r,s) = {} & A_2(s)\zeta_1^p(r,s) + B_2(s)\zeta_2^p(r,s) \\ & - \zeta_1^p(r,s)\int_0^r \frac{G_2(y,s)\zeta_2^p(y,s)}{W(y,s)}dy \\ & + \zeta_2^p(r,s)\int_0^r \frac{G_2(y,s)\zeta_1^p(y,s)}{W(y,s)}dy\end{aligned} \tag{3.69}$$

where ζ_1^p and ζ_2^p are the eigenfunctions of the homogeneous form of (3.20) and $W(r,s)$ is the Wronskian of ζ_1^p and ζ_2^p given by

$$W(r,s) = \frac{-i4\overline{\rho}\overline{\omega}^2}{\pi r \overline{\rho}_\infty \overline{\omega}^2_\infty}. \tag{3.70}$$

Again, in the intermediate region, we transform from r to $\tilde{r}$ in (3.69). When this is done, we note that the intermediate limit lies outside the jet boundary defined at $r = r_m$. Beyond this point, the mean flow conditions are uniform and the inner solution eigenfunctions take on the Hankel function form as shown in (3.22). Thus, in the intermediate limit, the integrals in (3.69) can be split between the regions $0 \le y \le r_m$ and $r_m \le y \le \varepsilon^{-1/N}\tilde{r}$.

$$\begin{aligned}\hat{p}_2^i(\tilde{r},s) = {} & A_2(s)H_n^{(1)}\left(i\lambda(\alpha)\varepsilon^{-1/N}\tilde{r}\right) + B_2(s)H_n^{(2)}\left(i\lambda(\alpha)\varepsilon^{-1/N}\tilde{r}\right) \\ & - H_n^{(1)}\left(i\lambda(\alpha)\varepsilon^{-1/N}\tilde{r}\right)\int_0^{r_m} \frac{G_2(y,s)\zeta_2^p(y,s)}{W(y,s)}dy \\ & + H_n^{(2)}\left(i\lambda(\alpha)\varepsilon^{-1/N}\tilde{r}\right)\int_0^{r_m} \frac{G_2(y,s)\zeta_1^p(y,s)}{W(y,s)}dy\end{aligned}$$

$$- H_n^{(1)}\left(i\lambda(\alpha)\varepsilon^{-1/N}\tilde{r}\right)\int_{r_m}^{\varepsilon^{-1/N}\tilde{r}}\frac{G_2(y,s)H_n^{(2)}(i\lambda(\alpha)y)}{W(y,s)}dy$$

$$+ H_n^{(2)}\left(i\lambda(\alpha)\varepsilon^{-1/N}\tilde{r}\right)\int_{r_m}^{\varepsilon^{-1/N}\tilde{r}}\frac{G_2(y,s)H_n^{(1)}(i\lambda(\alpha)y)}{W(y,s)}dy. \qquad (3.71)$$

The integrals for $r_m \le y \le \varepsilon^{-1/N}\tilde{r}$, as outlined in Appendix C, contain products of Hankel functions and powers of y. They are solvable in closed form using formulas from Luke [1962] and Watson [1966]. The results for $\hat{p}_2$ in the intermediate limit is

$$\begin{aligned}\hat{p}_2^i(\tilde{r},s) \sim\ & A_2(s)H_n^{(1)}\left(i\lambda(\alpha)\varepsilon^{-1/N}\tilde{r}\right) + B_2(s)H_n^{(2)}\left(i\lambda(\alpha)\varepsilon^{-1/N}\tilde{r}\right)\\ &+\left[F\left(\varepsilon^{-1/N}\tilde{r}\right) - \int_0^{r_m}\frac{G_2(y,s)\zeta_2^p(y,s)}{W(y,s)}dy - \frac{\pi}{4}I_2\right]H_n^{(1)}\left(i\lambda(\alpha)\varepsilon^{-1/N}\tilde{r}\right)\\ &+ D\left(\varepsilon^{-1/N}\tilde{r}\right)\frac{\partial}{\partial\left(\varepsilon^{-1/N}\tilde{r}\right)}H_n^{(1)}\left(i\lambda(\alpha)\varepsilon^{-1/N}\tilde{r}\right)\\ &+\left[\int_0^{r_m}\frac{G_2(y,s)\zeta_1^p(y,s)}{W(y,s)}dy + \frac{\pi}{4}I_1\right]H_n^{(2)}\left(i\lambda(\alpha)\varepsilon^{-1/N}\tilde{r}\right) \qquad (3.72)\end{aligned}$$

where

$$\begin{aligned}F\left(\varepsilon^{-1/N}\tilde{r}\right) =& -i\overline{\rho}_\infty M_j^2\overline{\omega}_\infty\overline{v}_\infty\ln\left(\varepsilon^{-1/N}\tilde{r}\right)\tilde{A}_0\\ &- i\alpha'\frac{\tilde{A}_0}{\lambda(\alpha)^4}\left(\alpha+\overline{\rho}_\infty M_j^2\overline{u}_\infty\overline{\omega}_\infty\right)^2\left(\lambda(\alpha)\varepsilon^{-1/N}\tilde{r}\right)^2,\end{aligned}$$

$D()$ is given in (3.54), and I_1 and I_2 are defined in Appendix C. Again, taking into account the boundedness condition on the inner solution, matching (3.72) to the $O(\varepsilon)$ terms of (3.54) results in

$$\begin{aligned}A_2(s) + F\left(\varepsilon^{-1/N}\tilde{r}\right) - \int_0^{r_m}\frac{G_2(y,s)\zeta_2^p(y,s)}{W(y,s)}dy - \frac{\pi}{4}I_2&\\ = \delta_{n0}\overline{\rho}_\infty M_j^2\overline{\omega}_\infty\overline{v}_\infty\frac{\pi}{2}\tilde{A}_0 + \tilde{A}_1 + E\left(\varepsilon^{-1/N}\tilde{r}\right),& \qquad (3.73)\end{aligned}$$

$$\int_0^{r_m} \frac{G_2(y,s)\zeta_1^p(y,s)}{W(y,s)}dy + \frac{\pi}{4}I_1 = 0\,, \tag{3.74}$$

$$B_2(s) = 0\,. \tag{3.75}$$

Equation (3.73) relates A_2 to $\tilde{A}_0$ and $\tilde{A}_1$ while (3.74), when written out, provides a differential equation for A_0.

$$\frac{dA_0}{ds}I_3 + A_0 I_4 = 0 \tag{3.76}$$

where I_3 and I_4 are given in Appendix C. The solution to (3.76) is

$$A_0(s) = \hat{A}_0 \exp\left[-\int_0^s \frac{I_4}{I_3}\,ds\right]. \tag{3.77}$$

This completes the solution of the problem to $O(1)$. Equation (3.77) shows the change in $A_0(s)$ due to a slowly diverging flow. For a single supersonic jet, this effect has been shown to be small, Morris and Tam [1977].

3.6 Near Field Pressure

The near field pressure disturbances to $O(1)$ outside the jet are found from (3.44). Using the following results from Appendix C:

$$\left(\bar{r}^2 - \varepsilon^4 \bar{\rho}_\infty M_j^2 \bar{v}_\infty^2\right)^{-i\frac{1}{2}\varepsilon\bar{\rho}_\infty M_j^2 \bar{\omega}_\eta \bar{v}_\infty} := 1 - i\varepsilon\bar{\rho}_\infty M_j^2 \bar{\omega}_\eta \bar{v}_\infty \ln \bar{r} + \cdots$$

$$H_q^{(1)}\left(i\frac{1}{\varepsilon}\lambda(\eta)\left(\bar{r}^2 - \varepsilon^4\bar{\rho}_\infty M_j^2 \bar{v}_\infty^2\right)^{\frac{1}{2}}\right) = H_n^{(1)}\left(i\lambda(\eta)\frac{1}{\varepsilon}\bar{r}\right) + O(\varepsilon),$$

and

$$\tilde{A}(s,\varepsilon) = \tilde{A}_0(s) + O(\varepsilon),$$

with $s = \varepsilon x$ and $\bar{r} = \varepsilon r$, the pressure disturbances outside the jet, (3.44), including the azimuthal and time dependencies, to $O(1)$ is

$$p(r,\theta,x,t) = \int_{-\infty}^{\infty} g(\eta) H_n^{(1)}(i\lambda(\eta)r) e^{i\eta x} e^{in\theta} e^{-i\omega t}\,d\eta \tag{3.78}$$

where

$$g(\eta) = \frac{1}{2\pi} \int_{-\infty}^{\infty} \tilde{A}_0(\varepsilon x) e^{i\phi(\varepsilon x)/\varepsilon} e^{-i\eta x} dx \tag{3.79}$$

and $\lambda(\eta)$ is given by (3.47). Equations (3.78) and (3.79) take the axial evolution of the n–th mode spatial instability wave described by $\tilde{A}_0 \exp(i\phi/\varepsilon)$, Fourier transform it into wavenumber space, multiply it by a "propagator" function $H_n^{(1)}$, and then inverse Fourier transform the result back to physical space. In essence, the instability wave is considered the source in a radiation problem where in the near field there are both propagating and nonpropagating waves. It is the propagating waves that get to the far field as sound.

3.7 Far Field Pressure

To get an estimate of the sound radiated to the far field, it is first convenient to transform from cylindrical to spherical coordinates. Letting

$$x = R\cos\psi \qquad \text{and} \qquad r = R\sin\psi \tag{3.80}$$

equation (3.78) becomes

$$p(R,\theta,\psi,t) = \int_{-\infty}^{\infty} g(\eta) H_n^{(1)}(i\lambda(\eta) R\sin\psi) e^{i\eta R\cos\psi} e^{in\theta} e^{-i\omega t} d\eta. \tag{3.81}$$

In the far field where R is large, we can replace the Hankel function by its asymptotic form, Abramowitz and Stegun [1965].

$$H_n^{(1)}(i\lambda(\eta) R\sin\psi) \sim \left[\frac{2}{\pi i\lambda(\eta) R\sin\psi}\right]^{\frac{1}{2}} e^{-\lambda(\eta) R\sin\psi} e^{-i\frac{\pi}{2}n} e^{-i\frac{\pi}{4}} \tag{3.82}$$

Substituting (3.82) into (3.81) results in an integral that can be evaluated by the method of stationary phase, Junger and Feit [1986]. The final solution is

$$p(R,\theta,\psi,t) \sim \frac{2}{R} \frac{g(\overline{\eta})}{\left[1 - M_\infty^2 \sin^2\psi\right]^{1/2}} e^{i[\Phi(\overline{\eta}) + n\theta - \omega t]} e^{-i\frac{\pi}{2}(n+1)} \tag{3.83}$$

where

$$\Phi(\overline{\eta}) = \frac{R}{1 - M_\infty^2} \overline{\rho}_\infty^{1/2} M_j \omega \left[\left(1 - M_\infty^2 \sin^2\psi\right)^{1/2} - M_\infty \cos\psi\right], \tag{3.84}$$

$$M_\infty^2 = \overline{\rho}_\infty M_j^2 \overline{u}_\infty^2,$$

and the stationary phase point $\overline{\eta}$ is given by

$$\overline{\eta} = \frac{\overline{\rho}_\infty^{1/2} M_j \omega \cos\psi}{\left(1 - M_\infty^2\right)\left(1 - M_\infty^2 \sin^2\psi\right)^{1/2}} - \frac{\overline{\rho}_\infty M_j^2 \overline{u}_\infty \omega}{1 - M_\infty^2}. \tag{3.85}$$

Equation (3.83) can be used to get the far field pressure directivity pattern. From Pierce [1989], the normalized differential sound power passing through a differential spherical area is given as

$$dP = \frac{1}{2}|p|^2 R^2 \sin\psi \, d\psi \, d\theta. \tag{3.86}$$

Noting that the differential solid angle is defined as

$$d\Omega = \sin\psi \, d\psi \, d\theta, \tag{3.87}$$

we get the sound power radiated per unit solid angle after dividing (3.86) by (3.87),

$$D(\psi) = \frac{dP}{d\Omega} = \frac{1}{2}|p|^2 R^2 = 2\frac{|g(\overline{\eta})|^2}{\left[1 - M_\infty^2 \sin^2\psi\right]}. \tag{3.88}$$

To find the angular dependence of $g(\overline{\eta})$, (3.85) must be solved for ψ in terms of $\overline{\eta}$. When this is done, we find that solutions only exist for $\overline{\eta} < \overline{\eta}_c$ where

$$\overline{\eta}_c = \frac{\overline{\rho}_\infty^{1/2} M_j \omega}{1 + M_\infty} \tag{3.89}$$

limiting ψ such that $0 \le \psi \le \pi/2$.

3.8 Numerical Formulation

The problem we set out to solve has been completed to within a constant, basically, the initial amplitude of the instability wave. To obtain results for various flow conditions in a supersonic coaxial jet, the pertinent equations of this chapter, (3.20), (3.78), and (3.88), must be solved numerically.

As was mentioned with regard to (3.77), the effect of flow divergence on stability results from supersonic jets is small. Tam et al. [1992] neglect this effect in calculating the instability waves in a Mach 2, hot jet. In an extension of the model to include a wide spectrum of frequencies, Tam and Chen [1993] assumed that the validity of the

model would not be affected by neglecting the flow divergence. Morris and Bhat [1992] make the same assumption for instability wave calculations in supersonic elliptic jets. The instability wave characteristics are then governed by the local eigenvalues at each axial location, known as the locally parallel flow approximation. The growth and decay of the instability wave is then governed solely by the spreading of the mean flow and the effect of the change in the eigenfunction shape with axial distance is neglected. We will follow this assumption in our estimates of the instability wave characteristics in supersonic coaxial jets. Thus, equation (3.77) reduces to

$$A_0(s) = \hat{A}_0 \tag{3.90}$$

and the phase term from (3.19) is found from

$$\phi(\varepsilon x)/\varepsilon = \int_0^x \alpha(x)\, dx. \tag{3.91}$$

3.8.1 Eigenvalue Problem

Finite differencing (3.20) for $m = 0$ is one of the alternatives for obtaining a numerical solution to the eigenvalue problem (See Mack [1984] and Drazin and Reid [1981]). It is easily applied using the same evenly spaced r–grid on which the mean flow was calculated and it provides a simple means to determine an initial guess for the eigenvalue. We rewrite (3.20) as

$$\frac{\partial^2 \hat{p}_0}{\partial r^2} + \left[\frac{1}{r} + \frac{2}{\bar{c}}\frac{\partial \bar{u}}{\partial r} - \frac{1}{\bar{\rho}}\frac{\partial \bar{\rho}}{\partial r}\right]\frac{\partial \hat{p}_0}{\partial r} + \left[\bar{\rho} M_j^2 \left(\frac{\omega}{c}\right)^2 \bar{c}^2 - \frac{n^2}{r^2} - \left(\frac{\omega}{c}\right)^2\right]\hat{p}_0 = 0 \tag{3.92}$$

where $c = \omega/\alpha$ and $\bar{c} = c - \bar{u}$. For the spatial stability problem, ω is real and c is complex, $c = c_r + ic_i$ (as is $\alpha = \alpha_r + i\alpha_i$). Changing the eigenvalue from α to c confines the range in which the eigenvalue lies in the complex c–plane. Given any real ω, the eigenvalue c will have a real part, c_r, that is within or near the bounds set by the real mean velocity $\bar{u}$. Thus, c is easily found compared to α and the numerical technique is more easily controlled since c lies within a limited range. Furthermore, in the initial region of a coaxial jet with two thin shear layers and two eigenvalues, using c as the eigenvalue allows easy identification of which c belongs to which shear layer.

For eigenvalues representing growing waves, we apply central differencing to the derivatives in (3.92) and rearrange into tridiagonal form to get the following difference

equation

$$\left[1-\frac{1}{2}Z_{1k}\Delta r\right]\hat{p}_{k-1}+\left[Z_{0k}\Delta r^2-2\right]\hat{p}_k+\left[1+\frac{1}{2}Z_{1k}\Delta r\right]\hat{p}_{k+1}=0 \tag{3.93}$$

where

$$Z_{1k}=\left[\frac{1}{r}+\frac{2}{c-\overline{u}}\frac{\partial\overline{u}}{\partial r}-\frac{1}{\overline{\rho}}\frac{\partial\overline{\rho}}{\partial r}\right]_k$$

and

$$Z_{0k}=\left[\overline{\rho}M_j^2\left(\frac{\omega}{c}\right)^2(c-\overline{u})^2-\frac{n^2}{r^2}-\left(\frac{\omega}{c}\right)^2\right]_k$$

are known at each interior grid point.

3.8.2 Boundary Conditions

The inner boundary condition on (3.92) depends on whether the eigenfunction is either axisymmetric, $n=0$, or non-axisymmetric, $n\neq 0$. Axisymmetry requires that the eigenfunction have a zero first derivative on the axis. For non-axisymmetry, the eigenfunction has opposite signs either side of the axis; hence, the eigenfunction must be zero on the axis. In equation form, the inner boundary condition is written as

$$\begin{aligned}\frac{\partial\hat{p}_1}{\partial r}&=0, n=0\\ \hat{p}_1&=0, n\neq 0.\end{aligned} \tag{3.94}$$

The outer boundary condition was defined by (3.21), (3.22), and from matching $B_0=0$. Taking the ratio of the two outermost grid points eliminates A_0 and rearranging the results to get

$$-\frac{H_n^{(1)}\left(i\lambda r_{N+1}\right)}{H_n^{(1)}\left(i\lambda r_N\right)}\hat{p}_N+\hat{p}_{N+1}=0 \tag{3.95}$$

defines the outer boundary condition.

3.8.3 Methodology of Numerical Solution

Equations (3.93), (3.94), and (3.95) when put together create a tridiagonal system of equations that can be written as

$$\mathbf{A}(c)\mathbf{p}=0. \tag{3.96}$$

This equation forms a generalized eigenvalue problem, Stewart [1973], which has a non-trivial solution only when

$$\det[\mathbf{A}(c)] = 0. \tag{3.97}$$

The determinant of $\mathbf{A}$ is easily calculated as the product of the diagonal terms in an LU-decomposition of $\mathbf{A}$.

The solution of (3.97) requires an initial guess for the eigenvalue c. The form of (3.97) provides an easy means of finding an initial guess. For a complex c, the determinant of $\mathbf{A}$ is, in general, complex, also. Setting up a grid over the region in which the eigenvalue is suspected to lie, the determinant of $\mathbf{A}$ is calculated at each point. Contours are then drawn through the region that define the zeroes of the real part and the imaginary part of $\det[\mathbf{A}(c)]$. These contours only cross at the eigenvalue. Once the initial guess for the eigenvalue is made, refinement of its value is achieved using the Newton-Raphson iteration method.

For a typical instability wave calculation, the eigenvalue must be found at every axial location for a given frequency ω. The contour grid method is performed at the first upstream profile. Thereafter, the eigenvalue solution at the previous axial location can be used as the initial guess for the eigenvalue at the next axial location. Extrapolating the first guessed eigenvalue at the next axial location from previous values often speeds up the convergence as long as the mean flow profiles are slowly changing.

3.8.4 Contour Solution

The numerical solution above has been discussed in terms of growing eigenvalues where $c_i > 0$. Implicit in the discussion was that the solution can then be calculated along the real r–axis. However, in order to continue the inviscid stability calculations into the damped region, $c_i < 0$, it is well known that a contour deformation must be made into the complex r–plane to avoid the critical point r_c where $c - \overline{u}(r_c) = 0$. (See, for example, Tam [1975], Morris and Tam [1977], Tam and Morris [1980], and Tam and Burton [1984a].) If all the variables in (3.92) are assumed to be analytic, then any contour can be chosen that avoids the critical point. Boyd [1985] discusses a number of complex mapping techniques to do the contour calculations. In our case, however, $\overline{u}$ and $\overline{\rho}$ in (3.92) are only known on the real axis. It was found to be simpler to calculate their analytic continuation into the complex plane along a simple box path around r_c rather than using complex mapping.

The direction of the contour into the complex r–plane is determined from the derivative of the mean velocity profile. For normal profile jets, $\partial\overline{u}/\partial r \leq 0$. The critical point for a growing mode lies in the lower half plane and passes into the upper half plane when damped. The contour for damped waves must then go into the upper half plane to go around the critical point since the branch cut associated with the critical point

goes to $-\infty$ in the direction of the negative imaginary axis. The reverse is true for the inverted profile jet where in the inner shear layer, $\partial\overline{u}/\partial r > 0$. The contour must go below the damped critical point in the lower half plane as the branch cut goes to $+\infty$.

In order to perform the calculations on the contour, the mean flow values must be determined on the contour from analytic continuation of the values on the real axis. A Taylor series expansion about the real axis for both the mean value and its first derivative are generally written as

$$\overline{f}(\mathbf{r}) = \overline{f}(r) - \frac{1}{2}\frac{\partial^2\overline{f}(r)}{\partial r^2}r_i^2 + i\left[\frac{\partial\overline{f}(r)}{\partial r}r_i - \frac{1}{6}\frac{\partial^3\overline{f}(r)}{\partial r^3}r_i^3\right] \tag{3.98}$$

$$\frac{\partial\overline{f}(\mathbf{r})}{\partial\mathbf{r}} = \frac{\partial\overline{f}(r)}{\partial r} - \frac{1}{2}\frac{\partial^3\overline{f}(r)}{\partial r^3}r_i^2 + i\left[\frac{\partial^2\overline{f}(r)}{\partial r^2}r_i - \frac{1}{6}\frac{\partial^4\overline{f}(r)}{\partial r^4}r_i^3\right] \tag{3.99}$$

where $\mathbf{r} = r + ir_i$ and r_i is the distance that a grid point on the contour is from the real axis. As appropriate, $\overline{f}$ represents either $\overline{u}$ or $\overline{\rho}$. Equations (3.98) and (3.99) become increasingly inaccurate representations of $\overline{f}(\mathbf{r})$ as r_i increases or as the curvature of the profile gets larger. The latter is especially true near the edges of the mean shear layer. To minimize inaccuracies, the magnitude of the second term in either the real or imaginary parts of the expansions was limited to ten percent of the first term. Calculations of the damped instability eigenvalues were stopped if this criterion was exceeded.

Once the numerical differencing along the contour was completed, as described in Appendix D, the system of equations leading to (3.96) was found to be augmented by the number of grid points that were added along the vertical parts of one or two box contours. The formalism of the solution as previously described did not change as the calculations proceeded from the growing to the damped eigenvalue solutions.

3.8.5 Near and Far Field Pressure

Both the near field pressure solution, (3.78), and the far field pressure directivity, (3.88), depend upon the Fourier Transform of the instability wave, (3.79). We can use the Fast Fourier Transform (FFT) to perform the calculations (Brigham [1974]). Using the trapezoidal rule, (3.91) is written as

$$\phi_j = \phi_{j-1} + \frac{1}{2}\left(\alpha_j + \alpha_{j-1}\right)\left(x_j - x_{j-1}\right) \tag{3.100}$$

where

$$\phi_0 = 0 \quad \text{and} \quad j = 1, 2, \ldots, K.$$

Setting $\hat{A}_0 = 1$, the FFT of the instability wave becomes

$$\mathrm{FFT}\left\{\exp\left(i\phi_j\right)\right\}_m = \sum_{j=0}^{M-1} \exp\left(i\phi_j\right) e^{-i2\pi mj/M} \tag{3.101}$$

where by definition for $j > K$, $\exp(i\phi_j) = 0$. With $M > K$, we have zero padded the FFT of the instability wave and increased the resolution in the wavenumber spectrum since

$$\Delta\eta = \frac{2\pi}{M\Delta x}. \tag{3.102}$$

Finally, the wavenumber spectrum of the instability wave is given by

$$g\left(\eta_m\right) = \frac{\Delta x}{2\pi}\mathrm{FFT}\left\{\exp\left(i\phi_j\right)\right\}_m \tag{3.103}$$

where

$$\eta_m = \begin{cases} m\Delta\eta, & 0 \le m \le \frac{M}{2} - 1 \\ (m-M)\Delta\eta, & \frac{M}{2} \le m \le M-1 \end{cases} \tag{3.104}$$

The first half of the FFT contains the spectrum for positive wavenumbers and the second half contains the spectrum for the negative wavenumbers.

To solve for the near field pressure, we recognize that (3.78) has the form of a convolution integral that is being solved in the transform domain. Williams and Maynard [1982] and Veronesi and Maynard [1987] have devised a formulation for correctly solving a two-dimensional form of this equation where the propagator function, in our case $H_n^{(1)}$, is known analytically. The formulation is easily written for our one-dimensional problem and (3.78) is written as (ignoring θ and t dependence)

$$p\left(r, x_j\right) = \mathrm{IFFT}\left\{\mathrm{FFT}\left\{\exp\left(i\phi_j\right)\right\}_m H_n^{(1)}(i\lambda(\eta_m)r)\right\} \tag{3.105}$$

where the inverse FFT is defined by

$$\mathrm{IFFT}\left\{f_m\right\}_j = \frac{1}{M}\sum_{m=0}^{M-1} f_m e^{i2\pi mj/M} \tag{3.106}$$

and η_m is defined in (3.104). The zero padding in (3.101) must have $M \ge 2K$. Veronesi and Maynard [1987] discuss errors that may arise in performing (3.105) such as the presence of fictitious sources generated by the discretization of the continuous Hankel function and the presence of singularities of the Hankel function. Replacing $H_n^{(1)}$ in (3.105) by an integrated average over the wavenumber resolution $\Delta\eta$ at each η_m would minimize these possible sources of error.

The far field directivity is determined directly by substitution of (3.103) into (3.88) and using only positive wavenumbers. For each η_m, the angular dependence ψ is determined from the inverse of (3.85) up to the limit set by (3.89).

3.9 Single Jet Examples

The calculated results consisting of mean flow, instability wave characteristics, and radiated noise are compared to measurements from Mach 2, perfectly expanded jets. Mean flow and acoustic calculation results are compared to measurements taken by Seiner et al. [1982] and Seiner and Ponton [1985] on a cold jet. For a hot jet, the calculated results are compared to measurements from Seiner et al. [1992]. In addition, our calculated stability characteristics are compared to those calculations by Seiner et al. [1993] for the same hot jet using analytic functions and Crocco's Relation to represent the mean flow. These studies have been specifically designed to study the importance of instability waves as noise generators in high Reynolds number, supersonic, axisymmetric, single jets. As such, they provide data with which to qualitatively and quantitatively assess our numerical calculations of mean flow, instability waves, and external pressure disturbances.

The mean flow comparison for a cold, Mach 2 jet is shown in Figure 3.3(a) for centerline velocity and in Figure 3.3(b) for half velocity point and jet half-width. The data are from Seiner and Ponton [1985]. The numerical calculations are not spreading the jet fast enough compared to data, a function of the turbulence model discussed in the previous chapter, but the qualitative comparison of slow initial growth followed by more rapid jet spreading after the end of the potential core is represented in the calculations. The near field sound pressures for this jet were mapped by Seiner et al. [1982]. The 1/3 octave filtered measurements are shown in Figure 3.4(a) for a Strouhal number ($St = fD/U_j$) of 0.2 and in Figure 3.5(a) for $St = 0.4$. The single frequency near field pressure contours from our numerical calculations are shown in part (b) of each figure. These contours are based on the $n = 1$ azimuthal mode which was shown in Seiner et al. [1982] to be more dominant than the $n = 0$ mode. The levels shown in the numerical calculations are arbitrary and are provided as a means of relative comparisons. The measured data shows an estimation of the origin and direction of the sound emission. The same results are seen in the calculations. Furthermore, as Strouhal number increased from 0.2 to 0.4, the peak of the field narrowed and the origin moved towards the nozzle in both measured and calculated results. The narrowing peak is confirmed in the far field directivity measurements from Seiner and Ponton [1985] and in our calculations shown in Figure 3.6. For both sets of measured and calculated data, the peak at $St = 0.25$ is broader compared to the peak at $St = 0.39$.

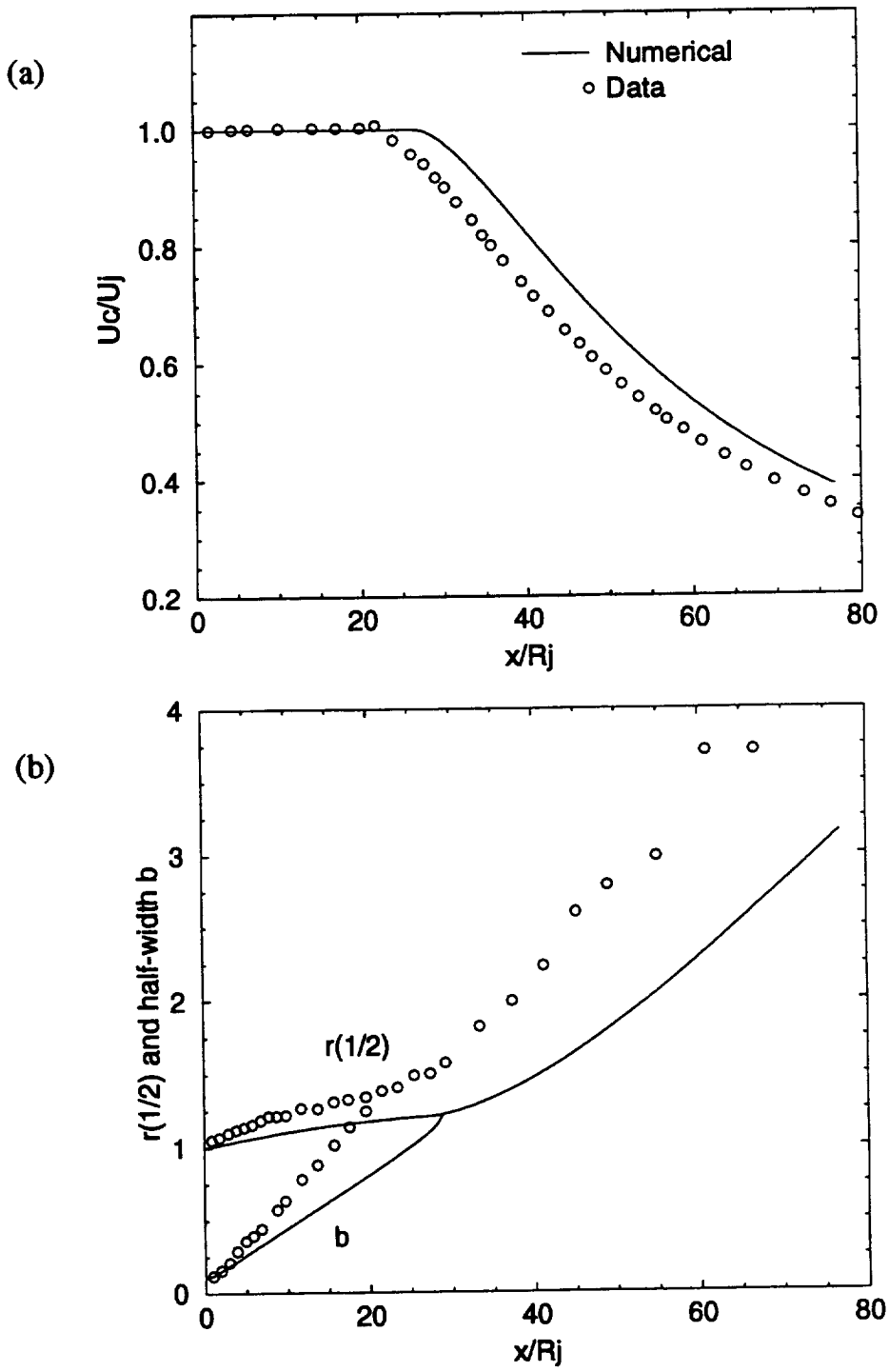

Figure 3.3. Comparison of cold Mach 2 jet calculations to measured data, mean flow. Data from Seiner and Ponton [1985]. (a) centerline velocity; (b) jet half velocity point and half-width b. Operating conditions: U_j = 510 m/s, T_j = 162 K, R_j = 2.49 cm.

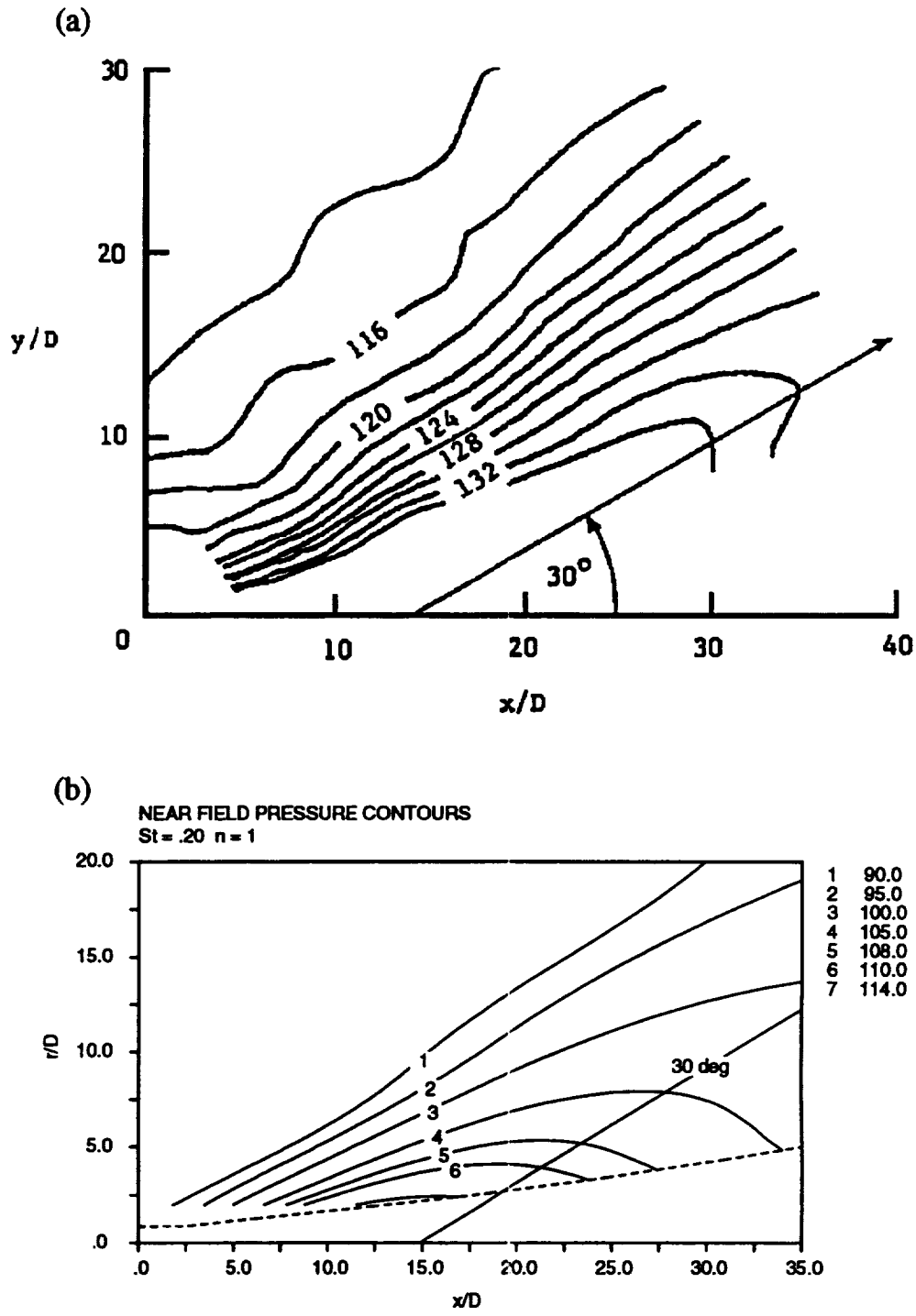

Figure 3.4. Comparison of cold Mach 2 jet calculations to measured data, near field pressure contours. Data from Seiner et al. [1982]. (a) 1/3 octave band filtered measurements at $St = .20$; (b) calculated contours at $St = .20$

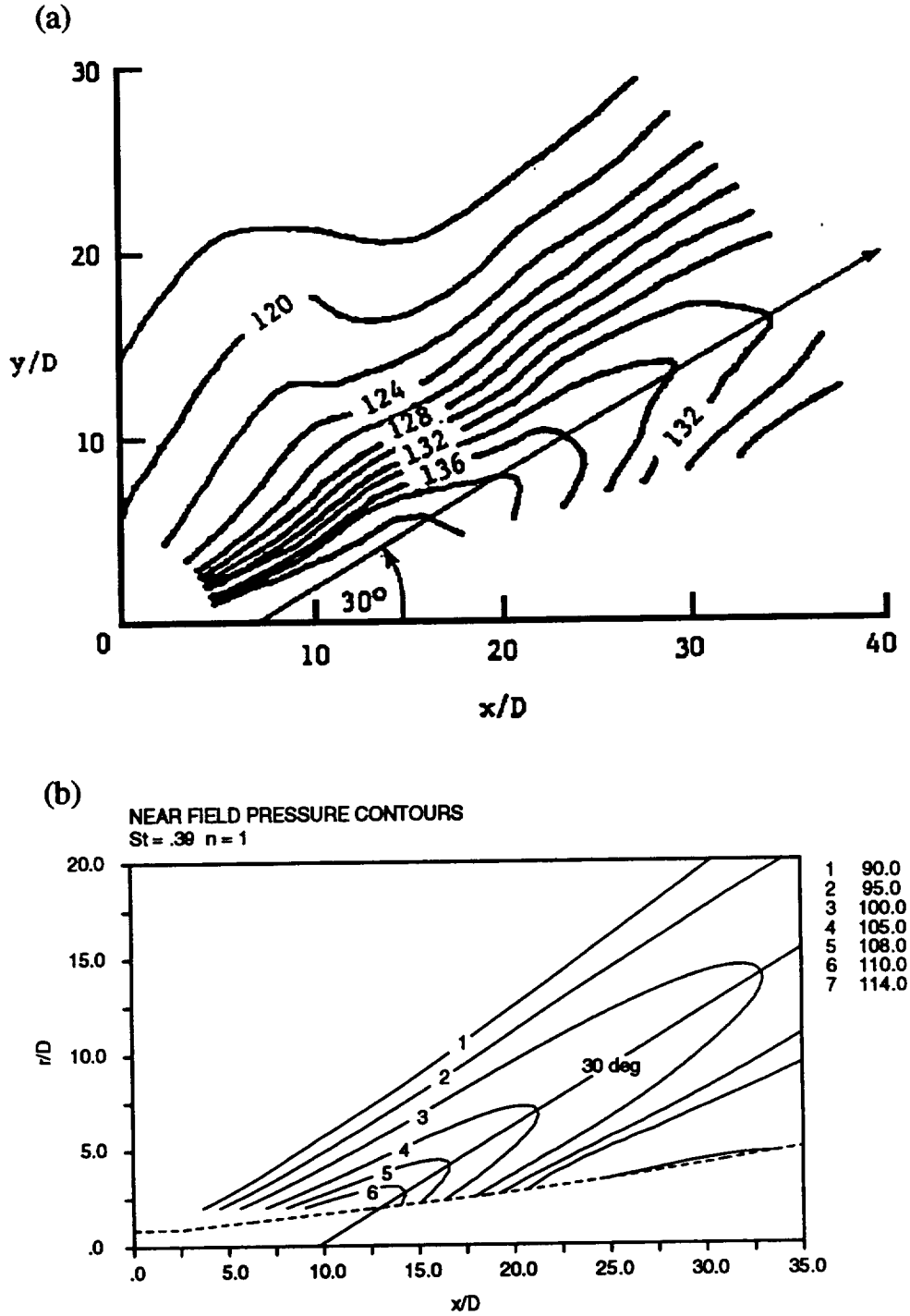

Figure 3.5. Comparison of cold Mach 2 jet calculations to measured data, near field pressure contours. Data from Seiner et al. [1982]. (a) 1/3 octave band filtered measurements at $St = .40$; (b) calculated contours at $St = .40$

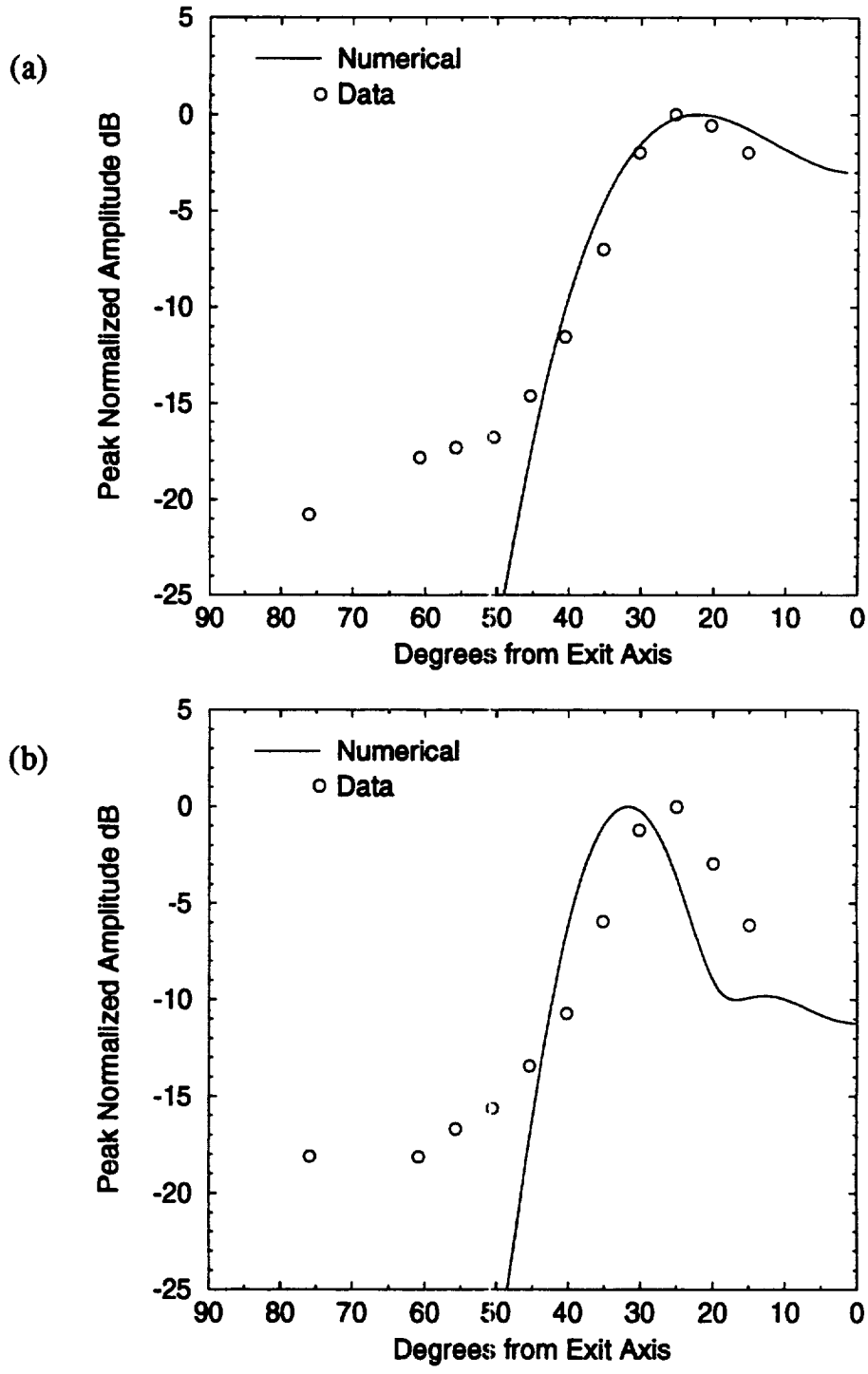

Figure 3.6. Comparison of cold Mach 2 jet calculations to measured data, far field directivities. Data from Seiner and Ponton [1985]. (a) $St = .25$; (b) $St = .39$

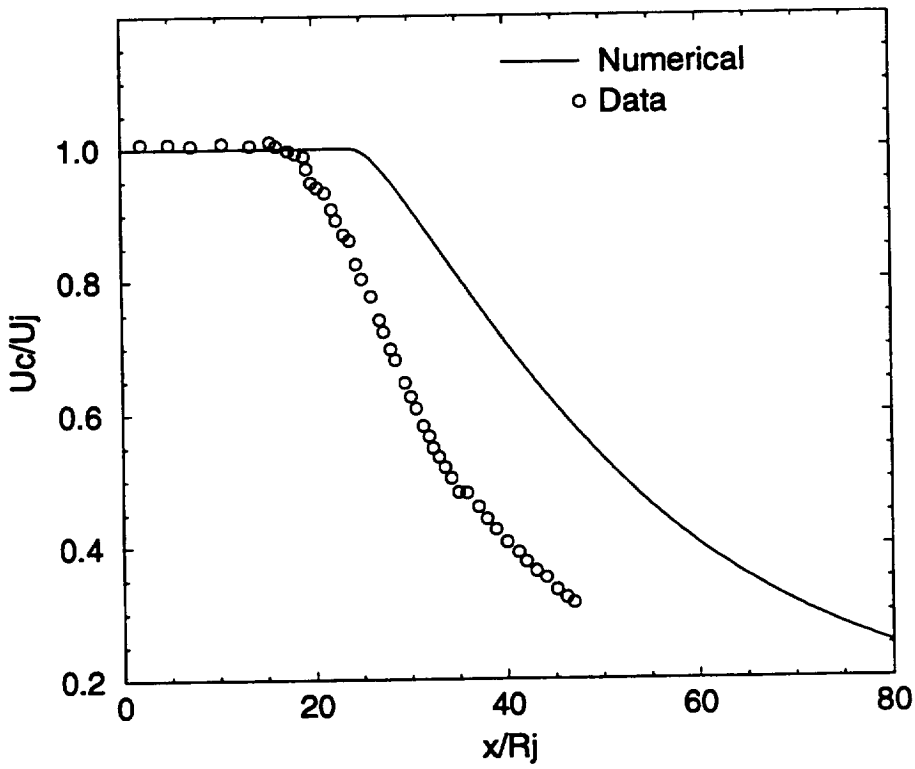

Figure 3.7. Comparison of hot Mach 2 jet calculations to measured data, mean flow. Data from Seiner et al. [1992]. centerline velocity. Operating conditions: U_j = 1115 m/s, T_j = 761 K, R_j = 4.57 cm.

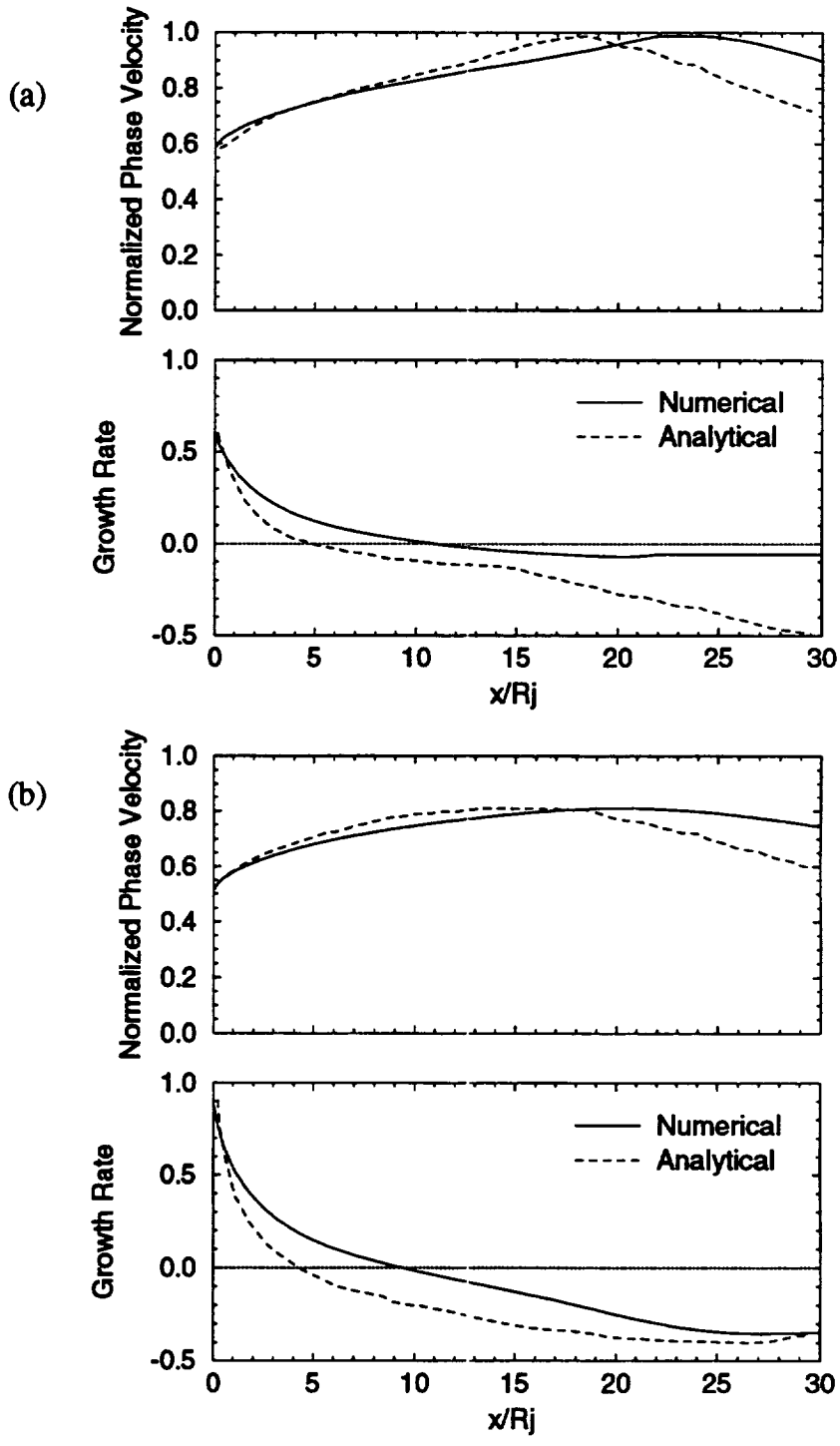

Figure 3.8. Comparison of hot Mach 2 jet calculations, growth rates and phase velocities. Analytical calculations from Seiner et al. [1993]. (a) $St = .4$, $n = 0$; (b) $St = .4$, $n = 1$

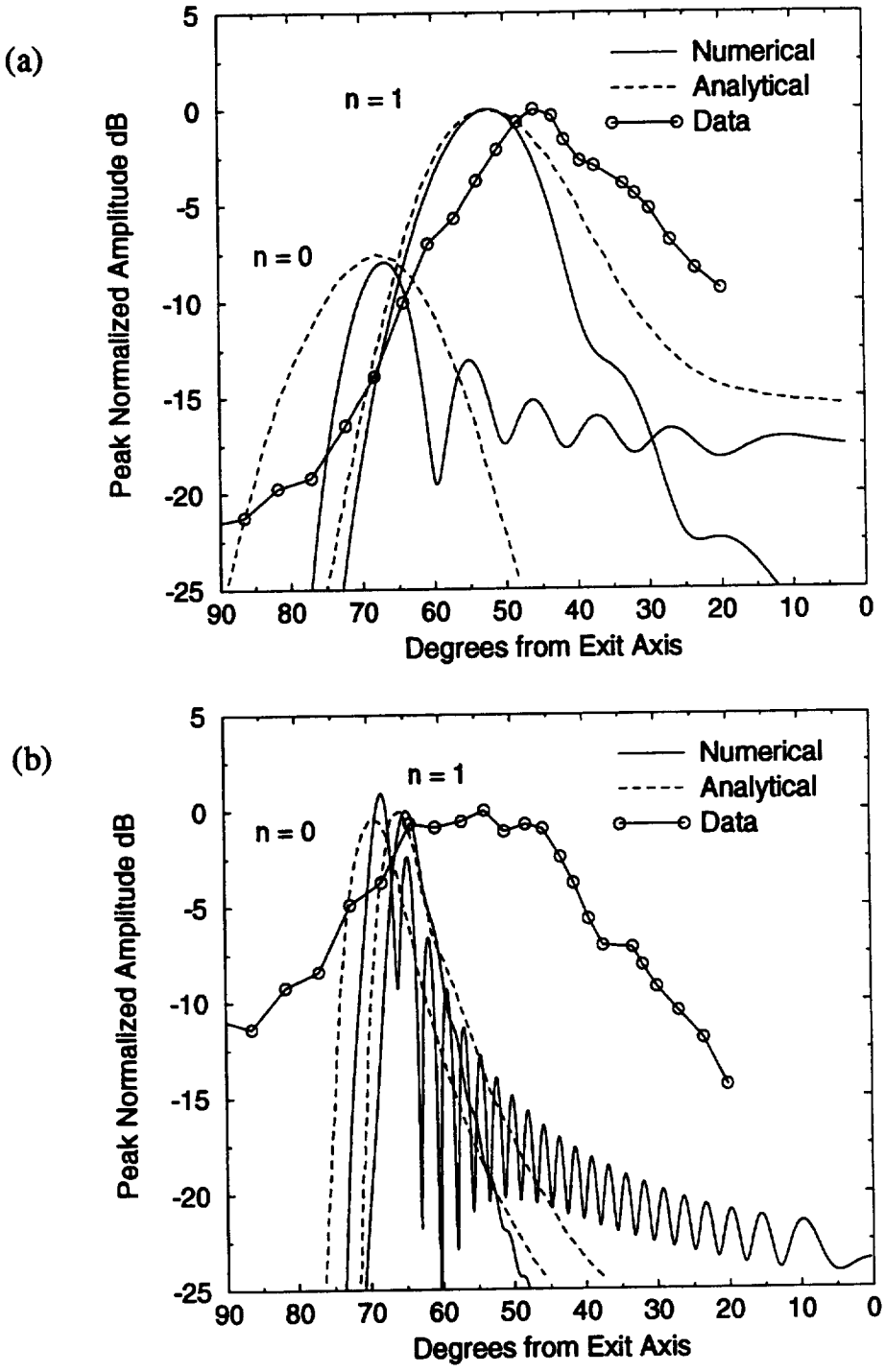

Figure 3.9. Comparison of hot Mach 2 jet calculations to measured data, far field directivities. Analytical calculations from Seiner et al. [1993]. Data from Seiner et al. [1992]. (a) $St = .1$; (b) $St = .4$

The hot, Mach 2 jet data were taken by Seiner et al. [1992] to study the relative importance of supersonic instability waves compared to Kelvin-Helmholtz instability waves in the noise generation process. The latter were dominant; hence, our calculations for Kelvin-Helmholtz waves are compared to their measurements. This type of comparison was also done by Seiner et al. [1993] where mean flow measurements were used to determine parameters to define the mean flow analytically. Using the analytic mean flow profiles, stability calculations were done leading eventually to far field directivity patterns. These results are used as a basis of comparison for our stability calculations using numerically generated mean flow profiles. The mean flow centerline velocity calculations are compared to data in Figure 3.7. Both results have shorter potential core lengths than the cold jet results shown in Figure 3.3. The instability wave calculations are compared in Figure 3.8 for both $n = 0$ and $n = 1$ azimuthal modes at a Strouhal number of 0.4. Both sets compare growth rates and phase velocities. For the analytical calculations in Seiner et al. [1993], the contour integration in the damped region is avoided by including damping in the stability calculations. Our calculations follow the inviscid contour integration described above. For the $n = 1$ mode shown in Figure 3.8(b), both calculations give similarly shaped growth rate and phase velocity curves. They are less similar for the $n = 0$ curves in Figure 3.8(a). The inviscid contour solution for the $n = 0$ mode fails to converge as the phase velocity approaches the maximum mean velocity. To extend the instability wave solution downstream, the assumption is made that the phase velocity is proportional to the centerline velocity and the rate of decay is a constant. Even though the initial growth rates and phase velocities for both modes are very similar for the two calculations, they begin to differ as the mean flows differ in their spreading rate. As shown in Michalke [1984], the instability wave growth rates and phase velocities depend on the shape of the mean flow profiles and even though Figure 2.3 showed that analytic functions can compare well with numerical results, the difference in spreading rates between the two mean flows gives different stability characteristics at the same axial location. In this case, the stability characteristics may show better comparison if they were scaled by a local length scale such as the local momentum thickness.

The comparisons of far field directivity patterns for the hot, Mach 2 jet are shown in Figure 3.9(a) for $St = 0.1$ and in Figure 3.9(b) for $St = 0.4$. Both our calculations (based on numerically generated mean flow) and the calculations from Seiner et al. [1993] (based on analytically generated mean flow) are compared to measured far field results from Seiner et al. [1992]. In Figure 3.9(a), both sets of far field calculated results peak at about the same relative level and at the same directivity angle. The same is basically true for the higher 0.4 Strouhal number calculations shown in Figure 3.9(b). The oscillations in the $n = 0$ results are due to the assumption that the decay rate is constant further downstream. As clearly shown in Figure 3.8(a), this assumption underestimates the damping and the decay rate is not enough to damp out the instability wave for $n = 0$.

The wave lingers on as the wavelength gets shorter with axial distance. The Fourier Transform of such a wave results in the oscillatory pattern seen in the wavenumber spectrum. Nonetheless, the peak level and directivity are well predicted.

3.10 Coaxial Jet Examples

Much of the coaxial jet data discussed in the introduction lacks the detailed measurements needed to make good comparisons to the single frequency, instability wave noise generation model used in our calculations. Furthermore, most of the supersonic coaxial jets, especially those with inverted velocity profiles, contained shocks that impact the mean flow and the noise generation processes. However, at the minimum noise condition, shock associated noise was reduced and the mean flow downstream of a composite shock structure had the characteristics of a fully expanded flow. The shock associated noise was dominant in the upstream directions and when it was minimized, the mixing noise, predicted by the instability wave noise generation model, was more dominant. It peaks in the downstream direction. Thus, we can compare our calculated results to measurements of shock containing, supersonic coaxial jets operated at the minimum noise condition.

Tanna et al. [1981] conducted a systematic experimental study of supersonic, coaxial jets. For a nozzle with area ratio $A_2/A_1 = 0.747$, they found that a minimum condition for shock associated noise existed when the inner stream was operated at slightly supersonic conditions. Directivity patterns were measured for overall sound pressure level (OASPL) and for 1/3 octave-band frequency spectra at 30, 60, and 90 degrees to the jet axis. The spectra at 30 degrees showed a dominant peak due to mixing noise. About this peak, frequencies were chosen to compare measured data to calculated single frequency results. Calculated far field directivity patterns are compared to measured far field directivities for both an inverted velocity profile jet and a normal velocity profile jet operated at minimum noise conditions.

The inverted velocity profile operating conditions are taken from Test Point 35 in Tanna et al. [1981]. The nozzle exit velocities are $U_1 = 466.6$ m/s and $U_2 = 662.3$ m/s. Using the given mass flow rates, we calculate the exit static temperatures as $T_1 = 512$ K and $T_2 = 562$ K. These give the exit Mach numbers as $M_1 = 1.03$ and $M_2 = 1.39$ showing that the inner stream is slightly supersonic. With these operating conditions, we calculate the mean flow, the instability wave characteristics, and the far field directivity pattern. Using the 1/3 octave center frequencies of 500, 1000, 1600, and 3150 Hz, we calculated the stability characteristics at Strouhal numbers fD_e/U_e of .05, .11, .18, and .36 where D_e and U_e are the equivalent single jet diameter and exit velocity, respectively. Unlike the Mach 2 single jet results where the $n = 1$ mode was more dominant than the $n = 0$ mode, the $n = 0$ mode was found to be more dominant

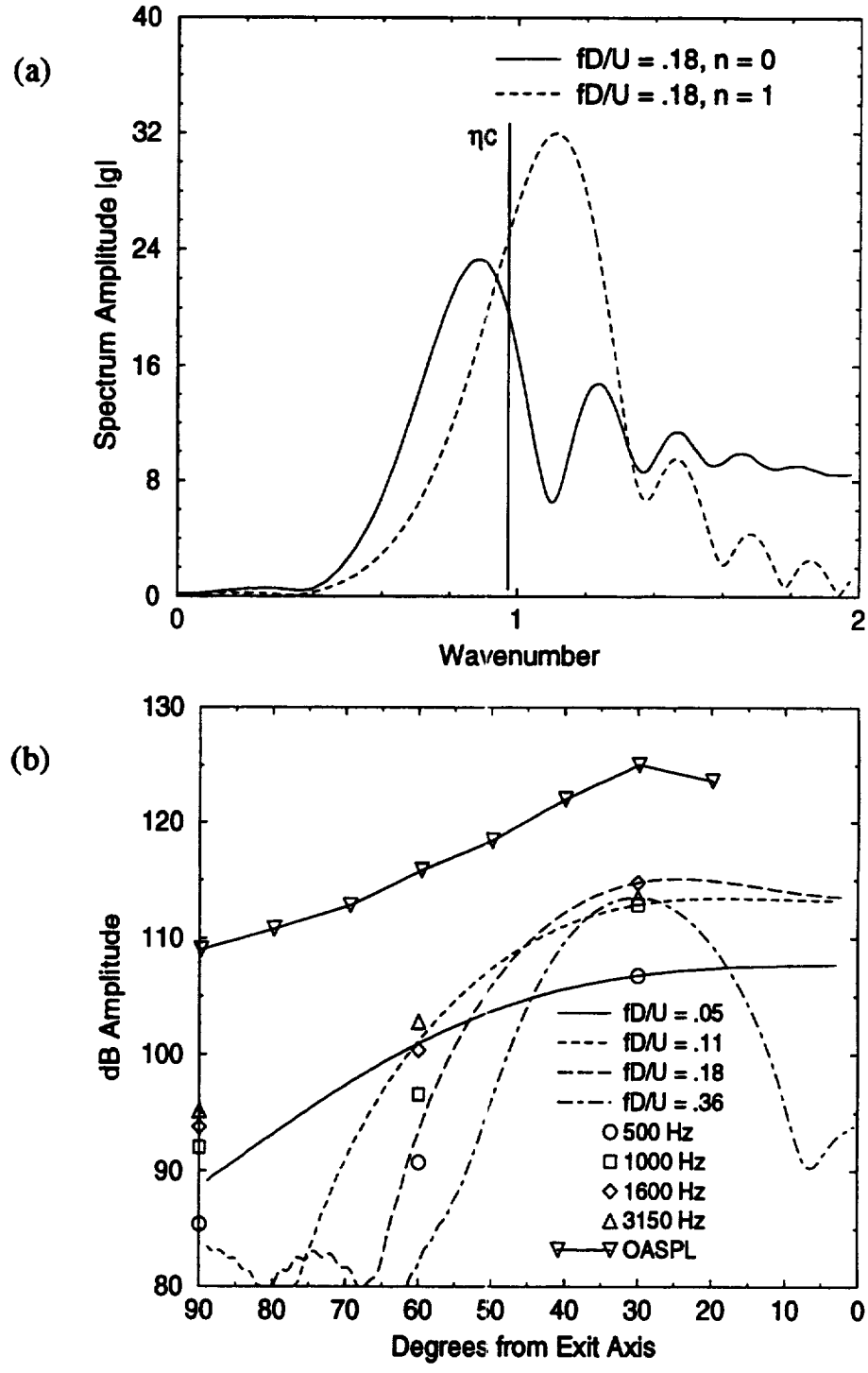

Figure 3.10. Instability wave and far field directivity calculations for inverted profile jet. (a) outer shear layer wavenumber spectra; (b) far field directivity at various St, $n = 0$, data from Tanna et al. [1981] in 1/3 octave bands and overall sound pressure levels.

than the $n = 1$ mode off the jet axis. An example of this is shown in Figure 3.10(a) for the wavenumber spectrum at $St = .18$. These spectra were calculated from the outer shear layer instability wave characteristics. The critical wavenumber η_c, defined in (3.89), is shown in the figure. Everything at smaller wavenumbers propagates with supersonic phase velocity and everything at larger wavenumbers propagates with subsonic phase velocity. Hence, even though the $n = 1$ mode has a higher spectrum amplitude, these higher amplitude wavenumbers have subsonic phase velocities and do not radiate noise to the far field. Therefore, the $n = 0$ mode dominates at angles away from the jet axis and these modes are used to determine the far field directivity patterns shown in Figure 3.10(b). The calculated directivities are scaled to agree with the measured 1/3 octave amplitudes at 30 degrees. The peak direction in the far field is well predicted by the calculated results.

The normal velocity profile operating conditions are taken from Test Point 21. The nozzle exit velocities are $U_1 = 539.6$ m/s and $U_2 = 403.2$ m/s. Again from using the given mass flow rates, the exit static temperatures are $T_1 = 687$ K and $T_2 = 207$ K, and we get similar Mach numbers, $M_1 = 1.03$ and $M_2 = 1.40$. For this case, the 1/3 octave center frequencies were at 500, 1000, 2500, and 4000 Hz corresponding to single frequency Strouhal numbers $fD_e/U_e = .07, .14, .36$, and $.58$, respectively. Since the outer shear layer has a larger ΔU than the inner shear layer, the outer instability waves grow larger and dominate the inner instability waves as shown in Figure 3.11(a) for $St = .58$. In addition, at all four Strouhal numbers, the $n = 1$ mode has a larger spectrum amplitude than the $n = 0$ mode. In contrast to the results shown in Figure 3.10(a), the critical wavenumber does not cutoff the peak as much and leaves the $n = 1$ mode as the mode with the larger noise radiation. Using the same type of normalization as the previous case, the $n = 1$ far field directivities are shown in Figure 3.11(b). Since the peak of the wavenumber spectrum is cutoff by η_c, the calculated directivities are maximum on the jet axis. This tends to agree with the trend in the 1/3 octave band data, but the data are limited.

3.11 Summary

The analysis to predict the noise generation from a single frequency instability wave propagating in the shear layer of a supersonic, perfectly expanded, axisymmetric jet was completed. Equations were developed to calculate the local instability wave characteristics at each axial location of a growing shear layer given the mean flow velocity and density profiles. These characteristics were used to calculate the evolving growth and decay of the instability wave. The Fourier Transform of the instability wave gave the wavenumber spectrum that showed those components of the instability wave that had supersonic phase velocities relative to ambient and those that did not. The supersonic

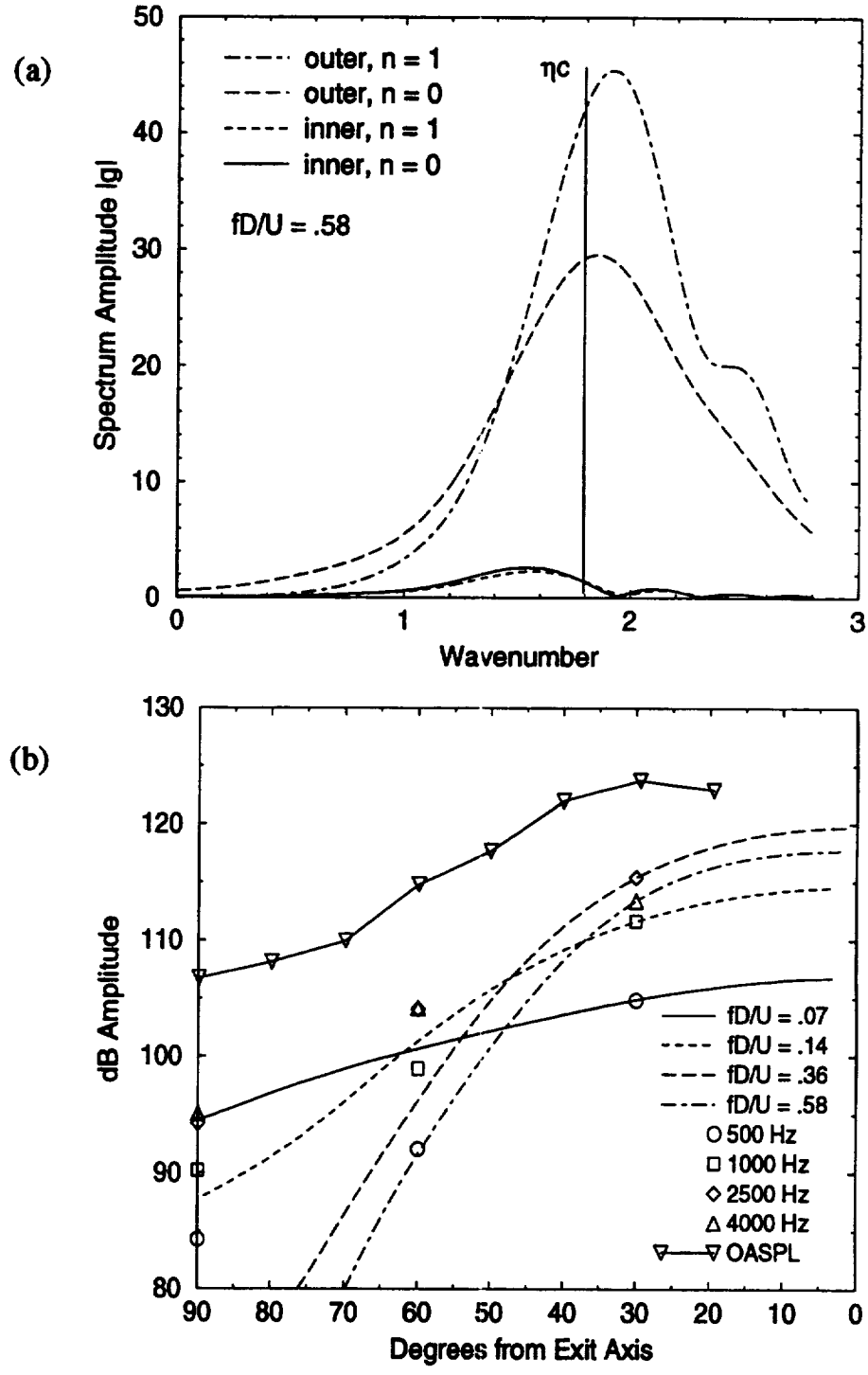

Figure 3.11. Instability wave and far field directivity calculations for normal profile jet. (a) outer and inner shear layer wavenumber spectra; (b) far field directivity at various St, $n = 1$, data from Tanna et al. [1981] in 1/3 octave bands and overall sound pressure levels.

phase components were the ones that radiated to the far field as sound. Equations were also developed to use the wavenumber spectrum to calculate the near field pressure disturbances and the far field sound directivity. This approach was directly applied to the supersonic coaxial jet once the mean flow properties were calculated numerically using the scheme described in the previous chapter.

The numerical formulation for the instability wave and the sound field solution was checked by comparing our calculated results to measured data and other calculated results for a cold and a hot Mach 2 jet. We used the operating conditions given in the references to numerically calculate the mean flow. Given the differences in mean flow spreading between our calculated mean flow and the measured mean flow, the results we calculated for instability wave characteristics, near field pressures, and far field directivity agreed with previous measured and calculated results for relative amplitudes and peak directivity. Example cases were then shown for an inverted velocity profile and a normal velocity profile coaxial jet. With a limited amount of measured far field directivity data from coaxial jets, our calculated single frequency far field directivities agreed with the basic trends shown in the data. In the next chapter, we discuss the results from a small parametric study of supersonic coaxial jet instability wave noise generation.

Chapter 4

RESULTS FROM SUPERSONIC COAXIAL JET STUDY

The mean flow formulation from Chapter 2 and the instability wave noise generation model from Chapter 3 are used to conduct a study to gauge the effectiveness of changing various operating parameters on the instability wave noise generation from perfectly expanded, supersonic coaxial jets. To fully cover the possible ranges for velocity ratio, temperature ratio, exit area ratio, and external flow conditions would be an enormous task to cover; hence, by necessity, choices are made to limit the scope of the study. A single jet with exit velocity of 1330 m/s and exit static temperature of 1100 K is chosen as the reference jet with Mach number 2. When scaled up, this jet would produce thrusts and mass flows comparable to those projected for supersonic jet transport aircraft engines. Following the choice of operating conditions for the reference jet, operating conditions are calculated for normal velocity profile and inverted velocity profile jets at the same total thrust, total mass flow, and total exit area as the reference jet. With the exit area ratio fixed, the normal velocity profile calculations are conducted for a small set of velocity and temperature ratios and the inverted velocity profile calculations are conducted for a small set of conditions for jets operating at the minimum noise condition given by Tanna et al. [1985]. The area ratio for these coaxial jets is chosen to be 1.25 and the external velocity is negligible.

In the following discussion, the normal velocity profile results and the inverted velocity profile results are considered separately. In general, we first discuss the mean flow calculations and compare the results for different operating conditions. This is followed by an example of the growth rate and phase velocity results from the stability calculations. These results are then considered in terms of the wavenumber spectrum of the instability wave calculated from the local growth rates and phase velocities. It is in the wavenumber domain that we compare how the growth and decay of the instability waves are affected by the different mean flow profiles based on different operating conditions. Since the calculations for near field pressure disturbances and far field sound directivity outside the jet are based on instability waves, changes in those results are also examined. The amplitude of the near field pressure disturbances are plotted in contours to show how the sound emanates from the jet. Some example contour plots are given. Comparisons of far field directivity patterns are easier to make, however, so they are examined

in more detail for the various operating conditions. The normal velocity profile results will be discussed first; followed by the discussion on the inverted velocity profile results.

4.1 Normal Velocity Profile

The study of supersonic coaxial jets with initial normal velocity profiles is conducted with these jets having the same total thrust, total mass flow, and total exit area as the reference jet. This means that velocities, temperatures, and areas are chosen to meet these constraints. It is assumed that the lip of the nozzle exit between the two streams is very thin with negligible area. Thus, the total exit area of the two streams equals the exit area of the single stream reference jet. After equating the total mass flow of the coaxial jet to the mass flow of the reference jet and the total thrust of the coaxial jet to the thrust of the reference jet, we solve for the coaxial jet inner stream exit velocity U_1 and exit static temperature T_1.

$$U_1 = U_e \frac{\left(1 + sr\frac{A_2}{A_1}\right)}{\left(1 + sr^2\frac{A_2}{A_1}\right)} \tag{4.1}$$

and

$$T_1 = T_e \frac{U_1}{U_e} \frac{\left(1 + sr\frac{A_2}{A_1}\right)}{\left(1 + \frac{A_2}{A_1}\right)} \tag{4.2}$$

where U_e is the reference jet exit velocity, T_e is the reference jet exit static temperature, A_1 is the coaxial jet inner stream exit area, A_2 is the outer stream exit area, r is the velocity ratio U_2/U_1, and s is the density ratio ρ_2/ρ_1. These definitions for r and s are consistent with their usage in Appendix A. Since r and s are used elsewhere to define coordinate scales, it should be clear from the context when r and s refer to a velocity ratio and to a density ratio, respectively. The density ratio may also be converted to, and referred to as, a temperature ratio by using the perfect gas law and constant static pressure. Hence, $s = \rho_2/\rho_1 = T_1/T_2$. From the definitions of r and s, it immediately follows that the outer stream velocity and static temperature are given by

$$U_2 = rU_1 \tag{4.3}$$

and

$$T_2 = \frac{T_1}{s}. \tag{4.4}$$

For fixed area ratio, equations (4.1) and (4.2) have r and s as two independent parameters. The parameters chosen for study are shown in Table 4.1. Notice that in order to maintain constant thrust and mass flow at a constant exit area, the inner stream velocity is always higher than the reference jet velocity and the temperatures change accordingly. The parameter space for the normal profile cases (as well as the inverted profile cases) contain operating conditions that are of more academic interest than practical. For instance, it would be difficult in propulsion systems to achieve the conditions of a relatively low speed, hot jet stream with a high speed, cool jet stream.

4.1.1 Mean Flow Results

A typical result for a normal velocity profile mean flow calculation is shown in Figure 4.1(a). The plot shows the edges of the large inner potential core, the edges of the smaller outer potential core, and the outer edge of the jet. These results are basically identical in form to those measured by Ko and Kwan [1976] for subsonic coaxial jets. Also shown in the plot are curves representing the half velocity point of the total jet and the region over which the two shear layers merge. The half velocity point is defined as the radial point at any axial location where the velocity is halfway between the maximum velocity (for a normal velocity profile jet it is the centerline velocity) and the ambient axial velocity. For the $r = 0.6$ case shown (Case #3 in Table 4.1), the half velocity point begins outside the outer potential core. This is typical for all cases where $r > 0.5$. For $r < 0.5$, the half velocity point begins in the region between the inner potential core and the outer potential core. The region of shear layer merging is indicated by the line labeled U_{merge} extending from the tip of the outer potential core. It is the point described in Figure 2.10 that is identified as the edge between the merging shear layers in the mixing length model. This merging region is also indicated by the change in slope in the outer edge line. Similar slope changes were noted by Ko and Kwan [1976]. The slope changes are abrupt due to the change in the turbulence model at those locations.

The basic mean flow properties for all the calculated normal velocity profile cases are shown in Figure 4.1(b) in terms of the locations of the outer core tip, the inner core tip, and the end of the merge region. Considering the inner core tip locations first, we have noted earlier that the effect of an external flow is to lengthen a jet potential core and the effect of increased temperature on a jet is to decrease the length of the potential core. Given the different velocities and temperatures for the two streams, the calculated results for the inner core tip locations follow in line with the temperature of the inner stream. The hottest inner stream had the shortest potential core and the fastest spreading for the inner shear layer. The coolest inner stream had the longest potential core and the slowest spreading for the inner shear layer. The results for the outer potential core length show that in general for a given velocity ratio, the outer core length is shorter for lower outer velocities and a higher temperature and longer for a

	r	s	U1(m/s)	U2(m/s)	T1(K)	T2(K)	M1	M2
Reference	–	–	1330.0	–	1100.0	–	2.0	–
Normal Case #								
2	0.80	1.00	1477.8	1182.2	1086.4	1086.4	2.2	1.8
3	0.60	1.00	1605.2	963.1	1032.6	1032.6	2.5	1.5
4	0.40	1.00	1662.2	665.0	916.7	916.7	2.7	1.1
5	0.80	2.00	1534.6	1227.7	1692.3	846.2	1.9	2.1
6	0.40	2.00	1900.0	760.0	1396.8	698.4	2.5	1.4
7	0.80	0.50	1425.0	1140.0	785.7	1571.4	2.5	1.4
8	0.40	0.50	1511.4	604.5	694.4	1388.9	2.9	0.8
Inverted Case #								
24	1.75	2.07	823.7	1441.4	1678.4	808.1	1.0	2.5
20	2.50	1.01	621.1	1552.9	954.5	937.9	1.0	2.5
21	2.90	0.75	556.0	1612.3	764.7	1011.0	1.0	2.5
22	3.55	0.50	481.4	1708.9	573.3	1135.8	1.0	2.5
23	4.10	0.37	436.7	1790.6	471.9	1247.0	1.0	2.5

Area Ratio $A2/A1 = 1.25$ $\Rightarrow$ Radius Ratio $r2/r1 = 1.5$

Velocity Ratio $r = U2/U1$ Density Ratio $s = \rho 2/\rho 1 = T1/T2$

(Constant Thrust and Constant Mass Flow)

Table 4.1. Operating Conditions for Supersonic Coaxial Jet Calculations.

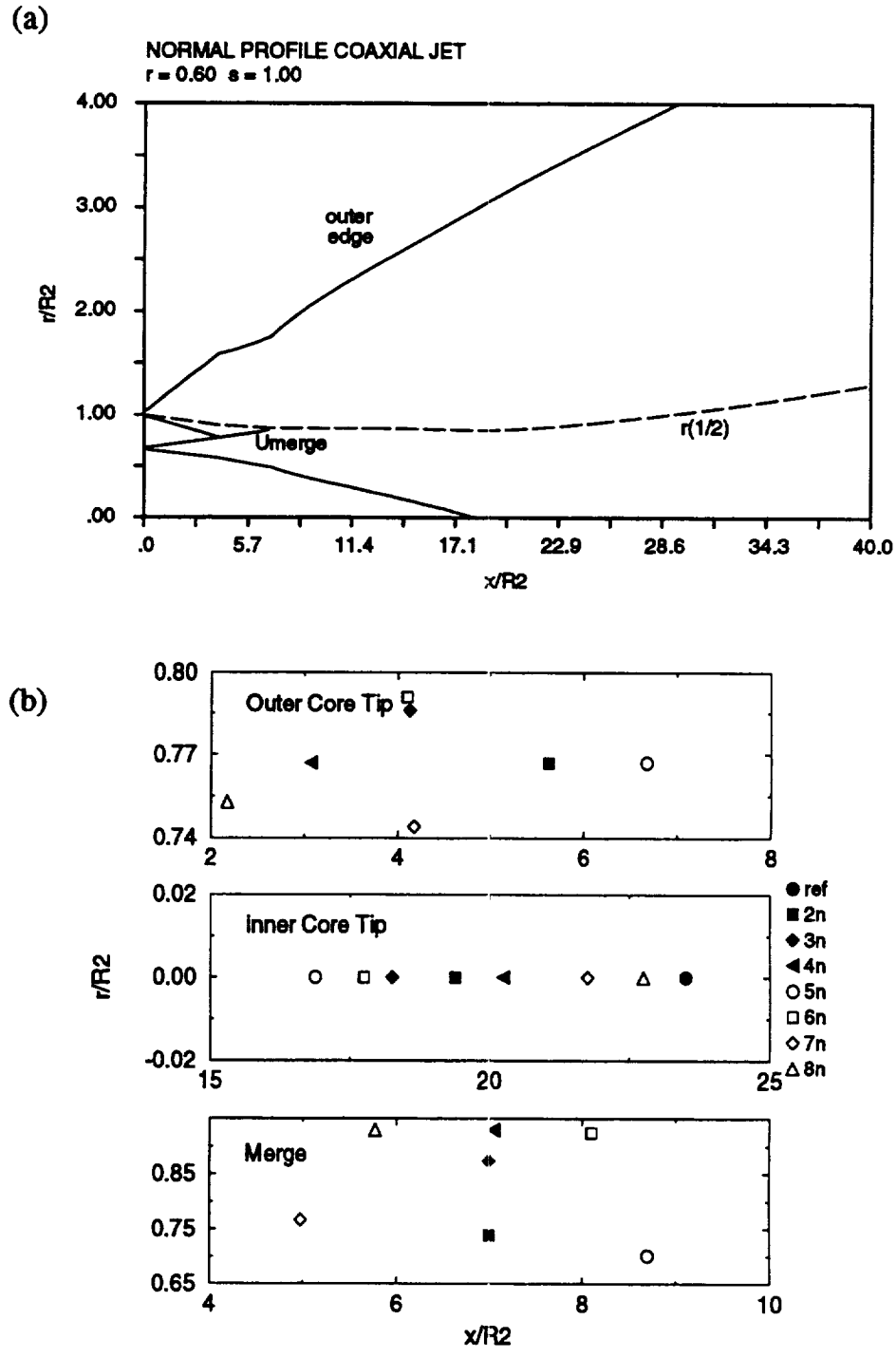

Figure 4.1. Calculated mean flow data for normal profile coaxial jets. (a) typical mean velocity profile, $r = .6$, $s = 1$; (b) location of potential core tips and end of merge region for normal velocity profile operating conditions, Table 4.1

higher outer velocity and lower temperatures. For the end of the merge region, its axial location is fairly consistent for a given s but its radial location migrates toward the shear layer with the smaller ΔU.

4.1.2 Instability Wave Characteristics

The instability wave characteristics are given in terms of the local growth rates and phase velocities calculated from the eigenvalue problem. Figure 4.2 shows the growth rates and phase velocities for the $n = 0$ mode of the normal profile case $r = 0.6$ and $s = 1.0$ (Case #3 in Table 4.1) for both the inner shear layer (part a) and the outer shear layer (part b). The results for the $n = 1$ mode are shown in Figure 4.3. Each line represents the calculations at a single Strouhal number fD_e/U_e where D_e and U_e are the exit diameter and exit velocity of the reference jet or equivalent single jet. All the stability calculations for the normal velocity profile jets are done at Strouhal numbers of .06, .12, .20, and .40. With D_e and U_e fixed, this means that all the normal profile jet stability calculations are at the same physical frequency for both inner and outer shear layers. When calculations are completed for far field sound, this insures that they can be compared at the same frequency. All the stability characteristics shown are of the Kelvin-Helmholtz type. At Strouhal number .40, no Kelvin-Helmholtz type instability is found for the outer shear layer in this case for both the $n = 0$ and $n = 1$ modes. All the phase velocities shown are supersonic relative to the ambient speed of sound.

For the inner shear layer $n = 0$ mode, stability calculations are continued downstream as far as possible until the phase velocity approaches the inner core velocity. After this point, no stability solutions are found. As shown in Figure 4.2(a), the stability solution is extended downstream by setting the phase velocity proportional to the centerline velocity and holding the growth rate constant. Using this approach, the lower Strouhal number instability waves have little damping with axial distance. Initially, the inner shear layer growth rates increase with Strouhal number while the phase velocities decrease. The instability wave continues to grow beyond the end of the outer potential core and beyond the end of the merge region, but they are starting to damp before the end of the inner potential core.

The outer shear layer $n = 0$ mode stability characteristics are shown in Figure 4.2(b). The initial growth rates also increase with Strouhal number and are larger than the comparable inner shear layer growth rates, but these growth rates decay more quickly than the inner shear layer growth rates. The outer shear layer phase velocities are lower than the inner shear layer phase velocities due to lower mean flow velocities, but they also decrease with Strouhal number as do the inner shear layer phase velocities. These calculations are conducted until the phase velocity approaches the mean flow velocity at the U_{merge} line. As this happens, the damping rates start increasing toward larger values. Then, in the stability calculations, the critical point typically goes beyond

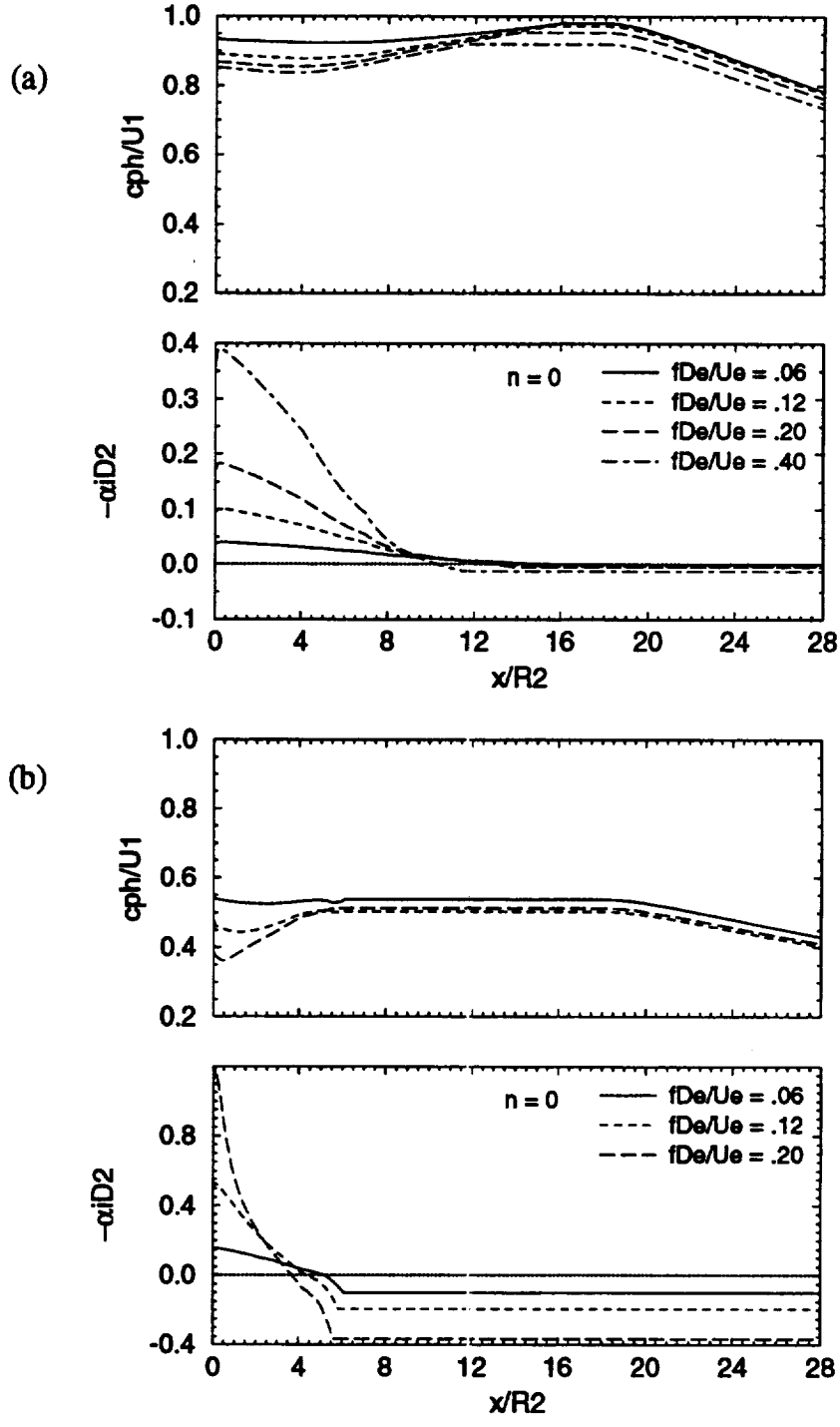

Figure 4.2. Growth rates and phase velocities for normal profile with $r = 0.6$ and $s = 1.0$. (Case #3 in Table 4.1) (a) inner shear layer, $n = 0$; (b) outer shear layer, $n = 0$

the region where the mean flow values in the complex plane are accurately calculated by analytic continuation. The calculations are stopped and the results are extended downstream as previously described.

The instability wave characteristics are similar in both the inner and the outer shear layers for all the Strouhal numbers used in the $n = 0$ mode calculations. As was shown from the single jet calculations in the previous chapter, the inviscid calculations cannot be continued in the axial direction beyond some point after the wave becomes damped and approximations are used to extend the instability wave characteristics further downstream. The $n = 1$ mode inviscid calculations for the single jet are not found to have any such limitations. The calculations are continued into the inviscid damped region in the axial direction as far as the mean flow is calculated. For the normal profile coaxial jet, the question arises of what happens to the two initially growing instability waves as the streams merge downstream into a single fully developed jet. This single jet would only have one $n = 1$ mode inviscid damped solution. So, could two stability solutions merge into one stability solution like the two shear layers merging into one shear layer? Figure 4.3 shows typical results from the stability calculations for a nomal velocity profile jet. With two shear layers, each having an initially growing instability wave, only one of the two has a continuous solution into the downstream damped region of the single fully developed jet. The shear layer with the larger ΔU supports the lower Strouhal number waves that are continuous into the damped region and the shear layer with the smaller ΔU supports the higher Strouhal number waves. As can be seen from comparing Figures 4.3(a) and 4.3(b), if the instability wave characteristics are continuous into the damped region in one shear layer, it is not continuous into the damped region in the other shear layer. The non-continuous instability wave characteristics become highly damped in the same manner as seen in Figure 4.2(b) for the $n = 0$ mode. Again, in the stability calculations, the critical point goes beyond the path where accurate mean flow calculations by analytic continuation are available. The concept of two eigenvalues merging is suggested by the behavior of the phase velocities. The inner shear layer phase velocities in Figure 4.3(a) decrease to the single jet phase velocity as the solution progresses downstream. In the outer shear layer, Figure 4.3(b), the phase velocities increase to the single jet phase velocity. No indication is found in the continuous damped eigenvalue solution that any other damped solution is nearby to suggest that the two solutions merge as the mean flow becomes fully developed.

Figure 4.3(a) shows that the initial growth rates in the inner shear layer for the $n = 1$ mode increase with Strouhal number. Unlike the $n = 0$ mode, these instability waves begin to damp at or soon after the end of the merge region. The phase velocities gradually increase with Strouhal number.

For the outer shear layer, the $n = 1$ mode growth rates shown in Figure 4.3(b) initially increase with Strouhal number and are much larger than the inner shear layer

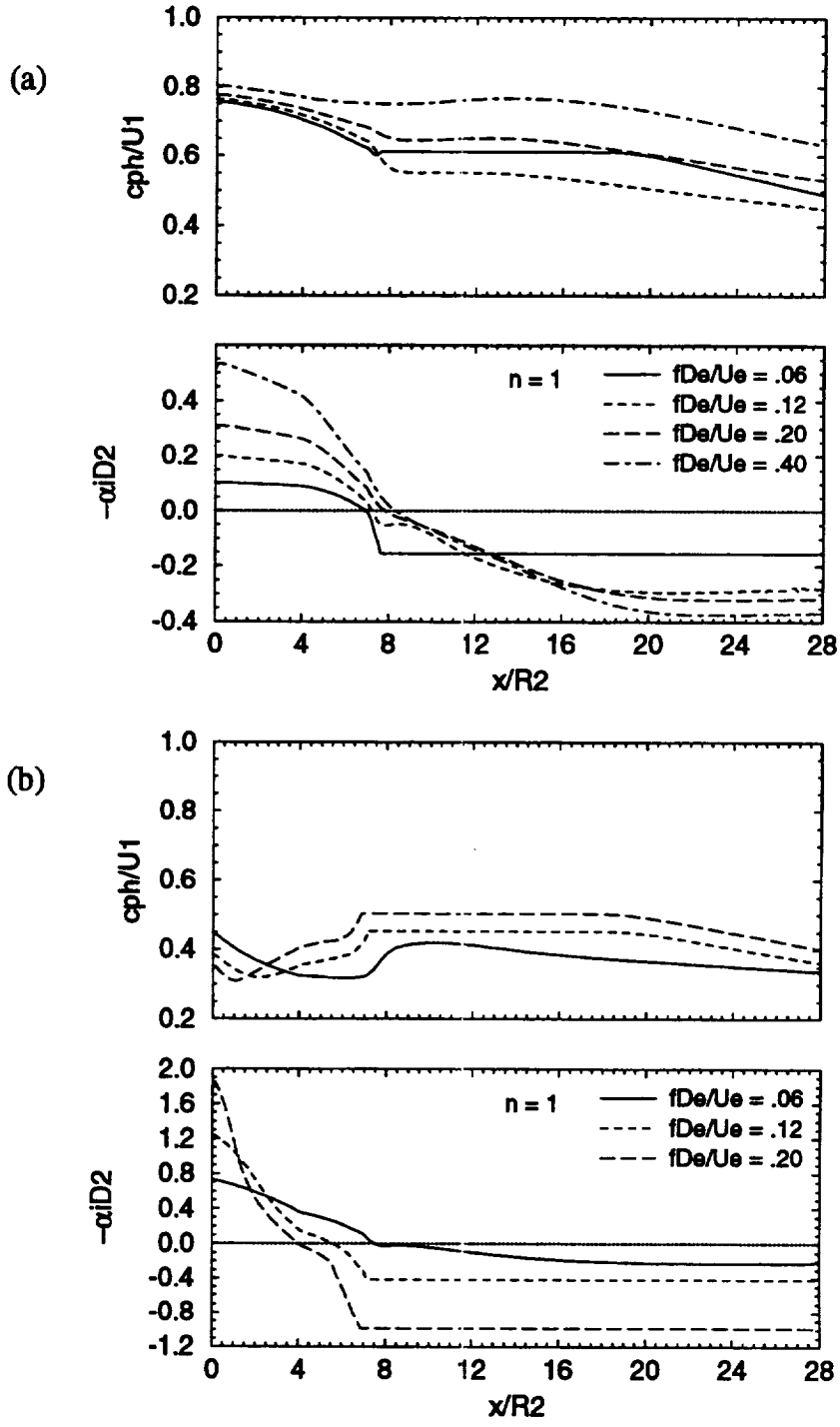

Figure 4.3. Growth rates and phase velocities for normal profile with $r = 0.6$ and $s = 1.0$. (Case #3 in Table 4.1) (a) inner shear layer, $n = 1$; (b) outer shear layer, $n = 1$

growth rates. But, like the $n = 0$ mode, these growth rates decay more quickly than the inner shear layer growth rates, except for the Strouhal number .06 growth rates.

The growth rate and phase velocity results shown in Figures 4.2 and 4.3 are typical for all the normal velocity profile results. There are differences in growth rate, especially, due to varying velocity and temperature ratios between the two streams. But, the characteristics of the instability wave can also be considered in the wavenumber domain where it is found to be easier to compare the different normal velocity profile cases.

4.1.3 Wavenumber Spectra

Figure 4.4(a) shows the wavenumber spectra for the $n = 0$ mode instability wave characteristics plotted in Figure 4.2 and Figure 4.4(b) shows the the wavenumber spectra for the $n = 1$ mode plotted in Figure 4.3. In Figure 3.9 we noted oscillations in the $n = 0$ wavenumber spectrum at wavenumbers higher than the main peak that manifested themselves in the far field directivity pattern. These oscillations are due to insufficient damping of the downstream propagating instability wave. Since in those previous calculations with insufficient damping, the $n = 0$ mode far field peak closely resembled the peak from calculations with sufficient damping, we avoid confusion in the presentation of the $n = 0$ mode wavenumber spectrum results and make the plots more clear by simply cutting off the higher wavenumber oscillations and concentrating on the main peak.

The wavenumber spectrum shows the amplitudes of each wavenumber component of a growing and decaying instability wave. The spectrum amplitude is related to the growth rates. In general, the faster the instability wave grows and decays, the wider the spectrum becomes. Also, the peak amplitude of the wavenumber spectrum is proportional to the peak amplitude of the instability wave. Thus, for an instability wave that grows rapidly to a high amplitude and decays rapidly will have a wavenumber spectrum that covers a wide spectrum range and has a high peak amplitude. Alternatively, an instability wave that grows slowly to a high amplitude and decays slowly will have a narrow spectrum range with a high amplitude. There are other combinations of growth and decay and amplitude. The location of the wavenumber spectrum peak is related to the phase velocity of the instability wave. At a given frequency, the wavenumber is inversely proportional to the phase velocity. Thus, the peak of the wavenumber spectrum will move to higher wavenumbers as the phase velocity decreases. These wavenumber spectrum characteristics are found in Figure 4.4 when the growth and phase velocity results in Figures 4.2 and 4.3 are translated to the wavenumber domain.

The wavenumber spectra for the $n = 0$ mode, Figure 4.4(a), show that the inner shear layer instability waves have higher spectral peaks than the outer shear layer instability waves. Even though the outer shear layer instability waves had higher initial growth rates, they grew to and decayed faster from a lower peak amplitude than the inner

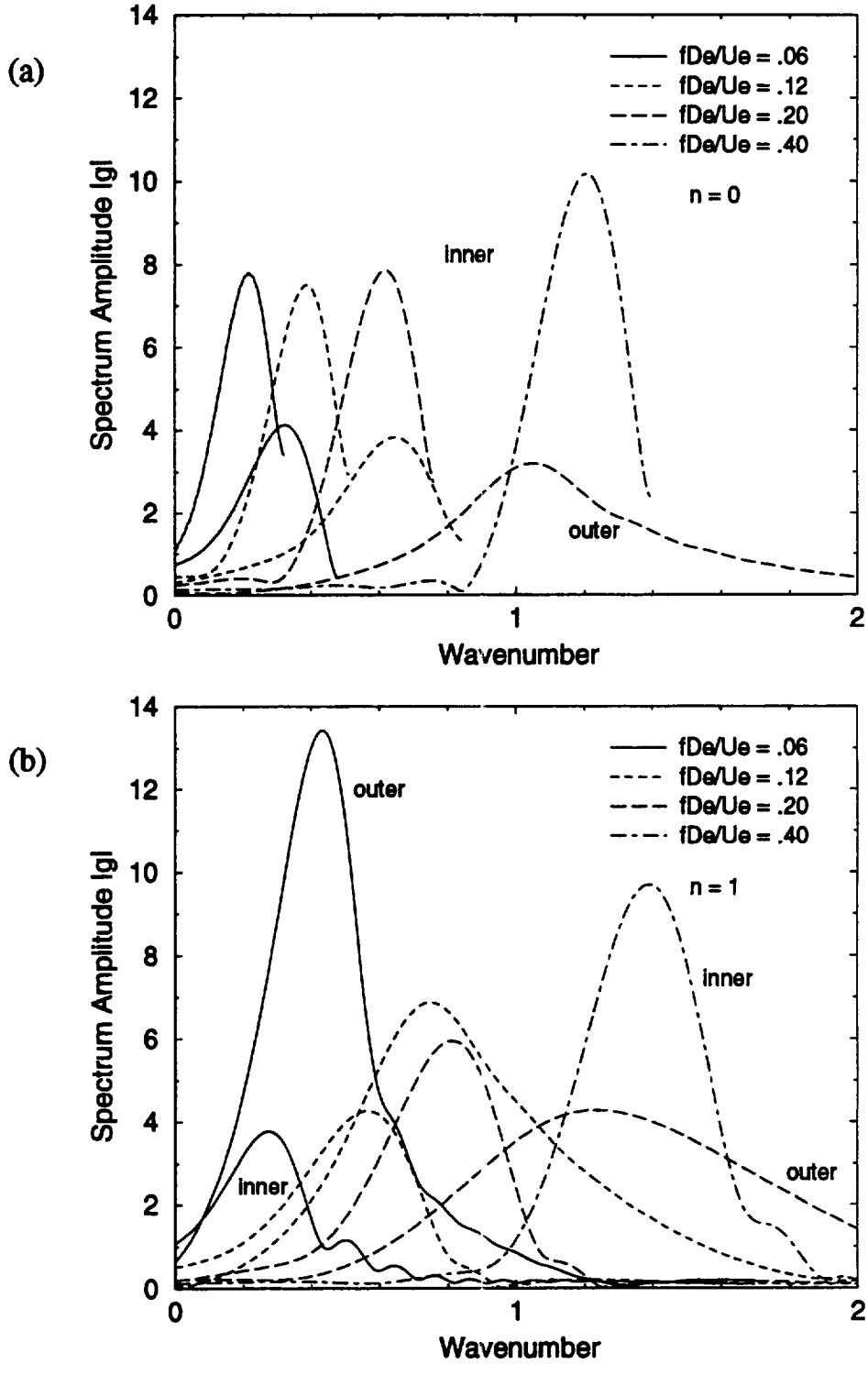

Figure 4.4. Wavenumber spectra for normal profile with $r = 0.6$ and $s = 1.0$. (Case #3 in Table 4.1) (a) $n = 0$; (b) $n = 1$

shear layer instability waves. In contrast, the wavenumber spectra for the $n = 1$ mode, Figure 4.4(b), show a shifting in peak spectral amplitudes between the two shear layers. The instability waves in the inner shear layer have the lowest spectral peak at Strouhal number .06 and the peaks increase in amplitude with each higher Strouhal number. The opposite is seen for the outer shear layer instability waves where the spectral amplitudes decrease with Strouhal number. Note that the highest spectral peaks at each Strouhal number are not necessarily related to those $n = 1$ instability wave characteristics that were continuously calculated into the downstream damped region. The maximum amplitude is determined from the integration of the growth rates up to the point where the growth rate is zero. What happens with the downstream growth rate characteristics after this point has no influence on the maximum amplitude. Hence, the growth rates for the outer shear layer instability wave at Strouhal number .12, shown in Figure 4.3(b), give a higher amplitude spectral peak than the inner shear layer instability wave even though the stability characteristics are not continuous into the downstream damped region.

Given that the instability wave characteristics can be described in terms of the wavenumber spectrum amplitude and peak location, we will now consider the effects of changing operating conditions on the instability wave characteristics presented in the wavenumber domain. We will make comparisons for varying velocity ratio r at constant $s = 1$ and for $r = .8$ and $.4$ with varying s. Wavenumber spectra will be shown at constant Strouhal numbers where results are available for all operating conditions and that inflectional instability waves exist in both the inner and the outer shear layers.

Figure 4.5 shows instability wave spectral amplitudes for both inner and outer shear layers with r varying from .4 to .8. With the Strouhal number fixed at .20, the results are shown for the $n = 1$ mode. Compared to the reference jet, the outer shear layer wavenumber spectra are generally decreasing in amplitude as r decreases which lowers ΔU across the outer shear layer. For the $r = .4$ case, the compensating effect of temperature may be a factor in the increased spectral amplitude compared to the $r = .6$ case. Even though ΔU has decreased by about the same amount from .8 to .6 to .4, the outer stream temperature has dropped much more from .6 to .4 than from .8 to .6. Seiner et al. [1993] have shown in single jet calculations that the effect of increasing the jet flow temperature relative to a constant ambient temperature is to decrease the growth of the instability wave. Thus, in the opposite sense, decreasing the jet flow temperature on the high speed side of the shear layer increases the growth of the instability wave. A consequence of holding the thrust, mass flow, and exit area constant is the interaction of velocity and temperature effects on instability wave growth and decay. One tends to increase growth and the other tends to decrease it. We end up with results like those shown in Figure 4.5(a) where the decrease in ΔU is not as effective in lowering instability wave growth as the decrease in temperature is in promoting instability wave growth. For the inner shear layer results, shown in Figure 4.5(b), the temperatures for

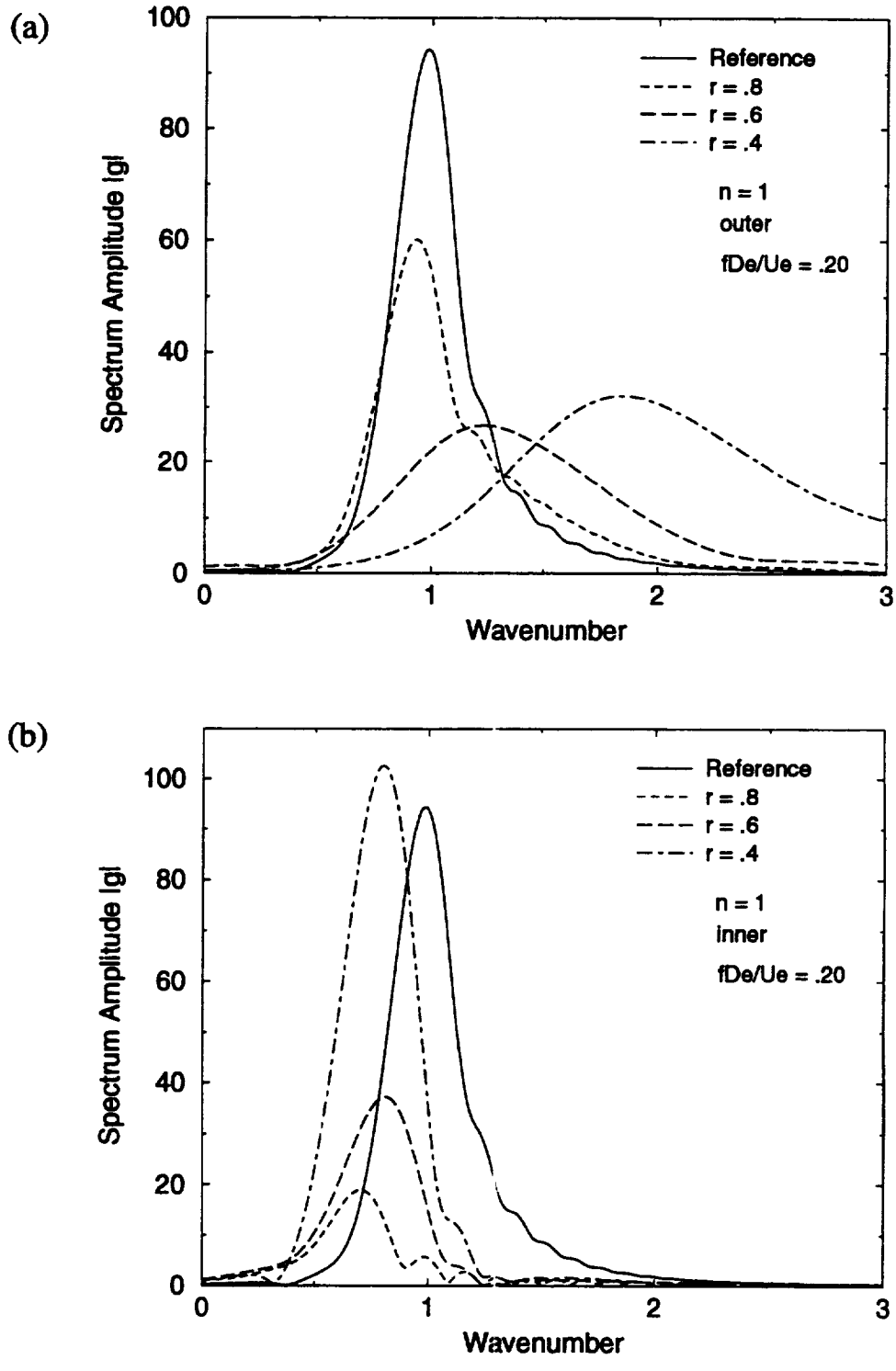

Figure 4.5. Wavenumber spectra for variable velocity ratio. (a) outer shear layer, $n = 1$, $s = 1$; (b) inner shear layer, $n = 1$, $s = 1$

the two streams are the same on both sides of the shear layer. Hence, the wavenumber spectrum grows in amplitude from $r = .8$ to .4 where for the inner shear layer, ΔU is increased. At $r = .4$, the wavenumber spectrum has a higher amplitude than the reference jet spectrum. This result is supported by the work of Michalke and Hermann [1982] where it was shown that an external flow could increase instability wave growth rates at higher frequencies for $0 \leq U_2/\Delta U < 1$. For our case $r = .4$, the inner shear layer flows lie within these limits, $U_2/\Delta U = .67$. Thus, it is reasonable to see the $r = .4$ wavenumber spectrum with an amplitude that is higher than the reference jet spectral amplitude where the jet flow has no external velocity.

A suggested method for describing the effects of velocity and temperature on compressible shear layer instability wave growth is to correlate the results by using the convected Mach number. Zhuang et al. [1990] used this approach to correlate the normalized maximum spatial growth rates of disturbances in a planar compressible free shear layer. Their results were similar to the fit line in Figure A.3. As the convected Mach number of the shear layer increased, the normalized maximum growth rate decreased where the compressible growth rate was normalized by the incompressible growth rate at the same velocity and temperature ratios. This approach works well for single shear layers. No correlation of instability wave maximum amplitude with convected Mach number was found in this study for coaxial jets with different inner and outer shear layer conditions. Since the stability characteristics of one shear layer in a coaxial jet are affected by the presence of the other shear layer, (This will be shown later in an example using an inverted velocity profile.) it may be necessary to obtain incompressible growth rates in coaxial jets to provide useful normalizations of compressible results.

The wavenumber spectral amplitude results for constant r and varying s are shown in Figure 4.6 for $r = .8$ and Strouhal number .20 and in Figure 4.7 for $r = .4$ and Strouhal number .12. In general, the shear layer with the larger ΔU has higher growth rates; that is the outer shear layer for $r = .8$ and the inner shear layer for $r = .4$. For both outer shear layer plots, Figures 4.6(a) and 4.7(a), the outer stream velocity differences are much smaller than the temperature differences. Thus, the growth rates are heavily influenced by temperature. As inferred earlier from Seiner et al. [1993], the cooler temperature stream has higher growth rates than hotter temperature streams. For the inner shear layer, using the $s = 1$ result as reference, Figure 4.6(b) for $r = .8$ shows that the cooler inner stream relative to the outer stream, $s = .5$, again results in higher wavenumber spectral amplitudes. Conversely, for a hot inner stream relative to the outer stream, $s = 2$, results in lower amplitudes compared to the $s = 1$ case. The same trend is seen in Figure 4.7(b) for $r = .4$. The locations of the peaks in the wavenumber spectra are not much affected by varying s as long as the peak wavenumbers have supersonic phase velocity relative to ambient. The largest shift in the peak location is seen for the $s = .5$ curve in Figure 4.7(a). The outer stream for this case is subsonic

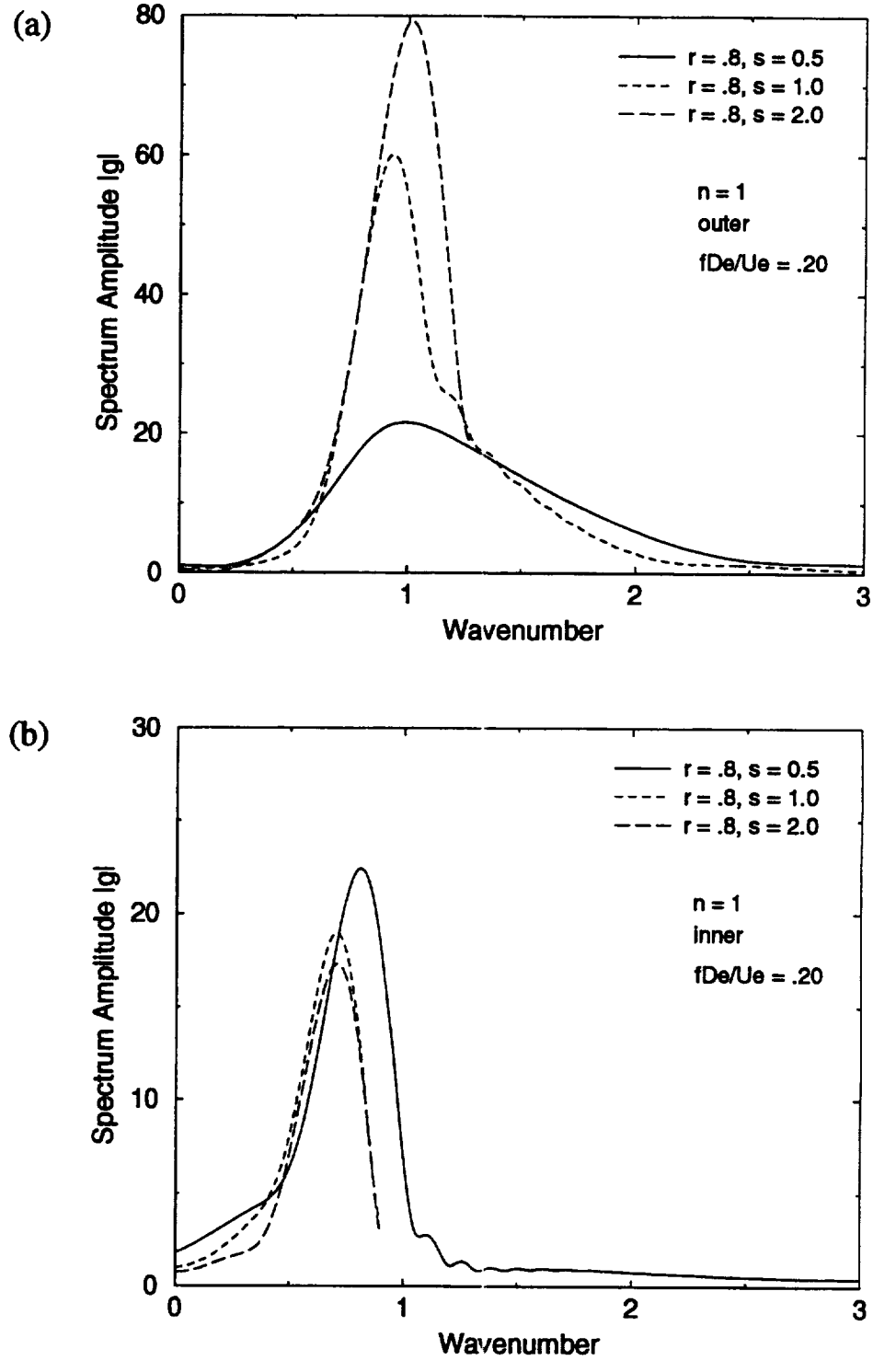

Figure 4.6. Wavenumber spectra for variable temperature ratio. (a) outer shear layer, $n = 1$, $r = .8$; (b) inner shear layer, $n = 1$, $r = .8$

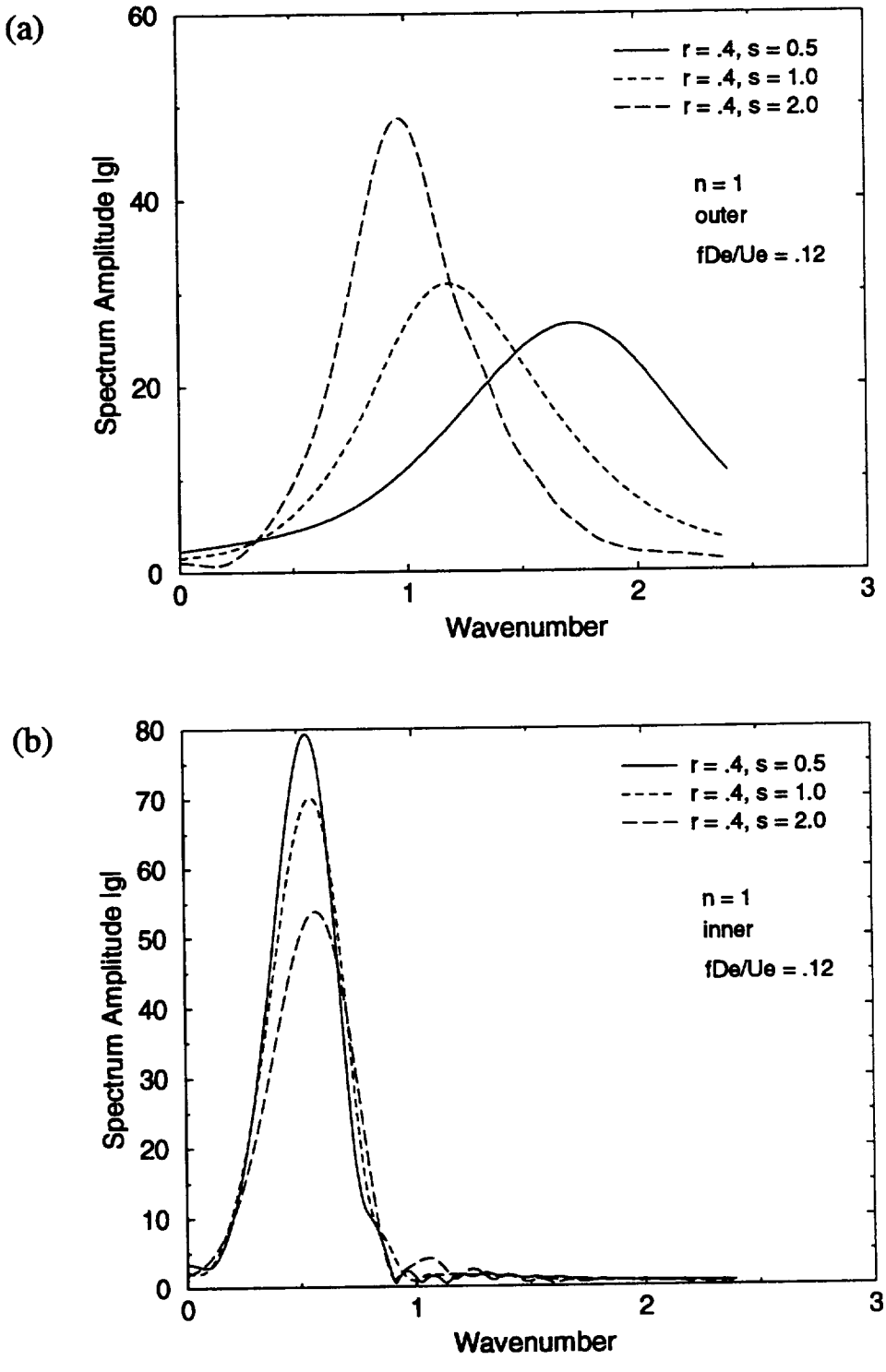

Figure 4.7. Wavenumber spectra for variable temperature ratio. (a) outer shear layer, $n = 1$, $r = .4$; (b) inner shear layer, $n = 1$, $r = .4$

and as a result of the low phase velocity, the wavenumber of the peak is much higher than the wavenumber of the peaks with supersonic phase velocities.

4.1.4 Near Field Pressure Contours

Examples of near field pressure contours are shown in Figures 4.8 to 4.11. Each figure compares the near field pressure contours with the lowest far field peak level from the coaxial jet to the near field pressure contours for the reference jet at the same Strouhal number. The amplitude levels shown are arbitrary; but for comparison, they all have the same reference level. In general, the coaxial jet near field pressure levels are lower than the reference jet pressure levels and the source location has shifted towards the nozzle. The shift in source location is due to the shortened potential core lengths in the coaxial jet compared to the reference jet. In Figure 4.8(b), the coaxial jet near field pressure contour calculation used the inner shear layer instability wave. The other three coaxial jet contour calculations used the outer shear layer instability wave. Notice that the contour for the inner shear layer instability wave has a larger directivity angle to the jet axis than the reference jet. The outer shear layer instability wave near field contours have comparable angles to the reference jet. This will be more easily seen in the far field directivity patterns.

4.1.5 Far Field Directivity Patterns

The calculated far field directivity patterns for each Strouhal number are shown in Figures 4.12 and 4.13 for the $n = 1$ mode. The amplitude level is arbitrary, but, again, for comparison purposes, all the curves have the same basis. Each figure shows eight curves: one for the reference jet and seven for the highest far field peak amplitude generated from each coaxial jet at that Strouhal number.

The far field directivity patterns for Strouhal number .06 are shown in Figure 4.12(a). All except one of the curves are based on the outer shear layer instability wave. The $r = .4$, $s = .5$ case is based on the inner shear layer instability wave. Note that this curve has a symmetrical peak with a maximum amplitude located at a larger angle to the jet axis than the other seven outer shear layer based curves. This characteristic difference in peak angle location between inner and outer shear layer based directivity patterns is seen in all the data. All the operating conditions lower the far field peak amplitude relative to the reference jet. The trend toward lower peaks based on the outer shear layer instability waves follows a decrease in r and a decrease in s. For example, the thick dashed lines show a decrease in peak amplitude for a fixed $r = .8$ and a decreasing s.

The Strouhal number .12 far field directivity results are shown in Figure 4.12(b). More curves based on the inner shear layer instability wave are dominant here than at

(a)

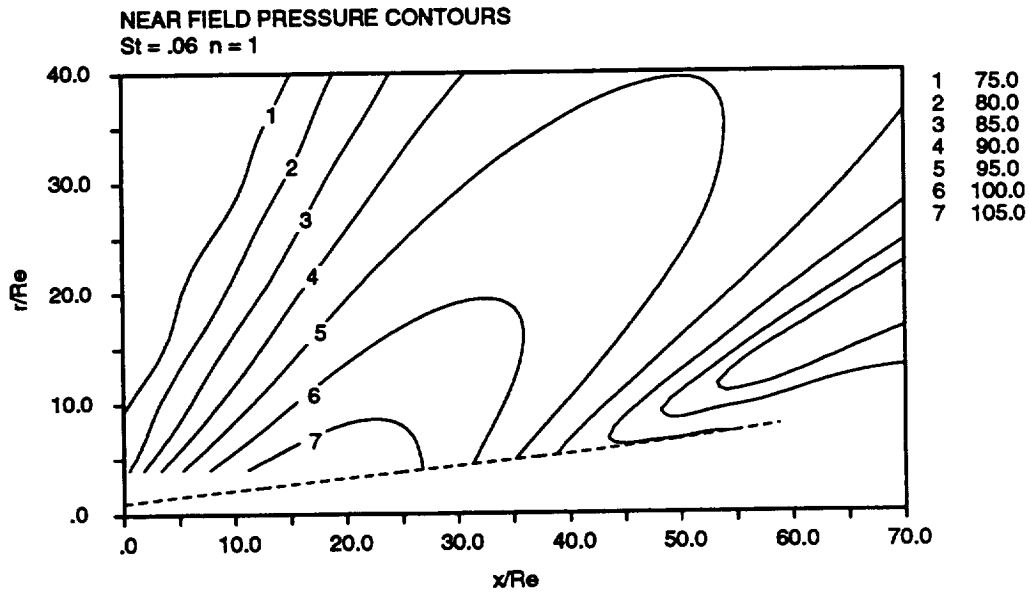

(b)

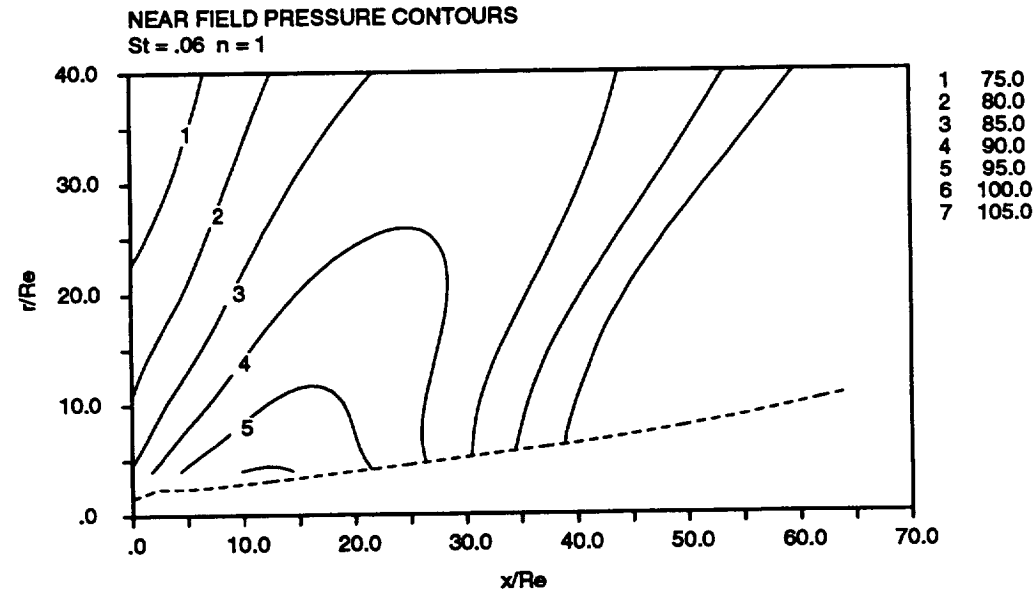

Figure 4.8. Comparison of calculated near field pressure contours. $St = .06$, $n = 1$, (a) reference jet; (b) Case #8, $r = .4$, $s = .5$, inner shear layer

(a)

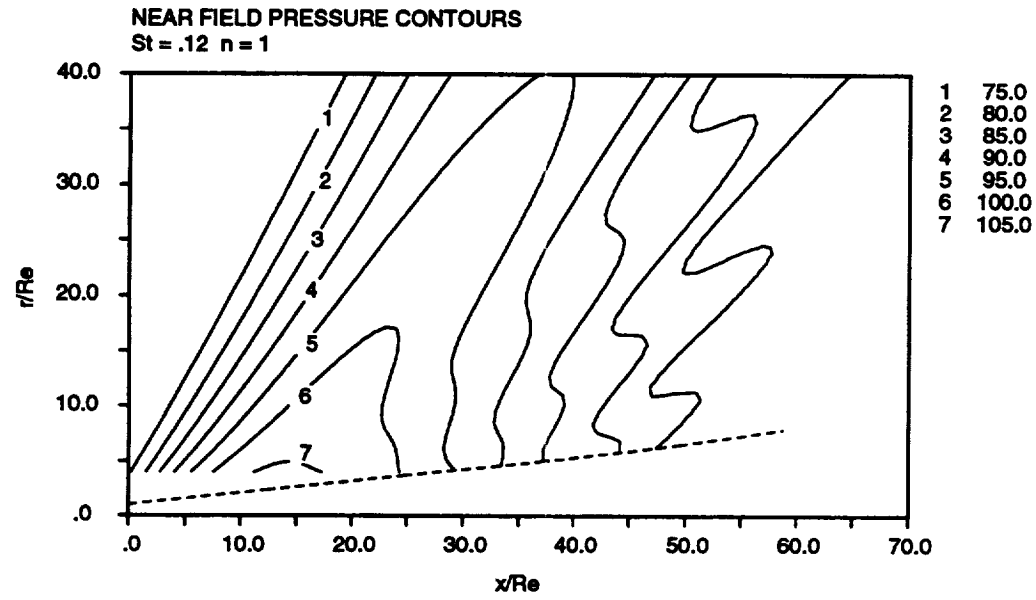

(b)

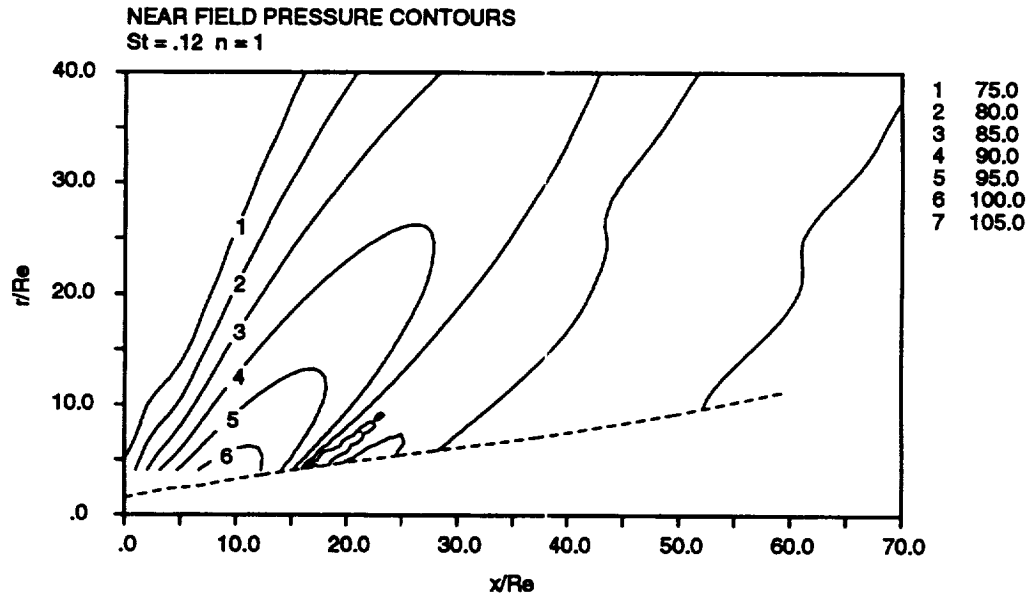

Figure 4.9. Comparison of calculated near field pressure contours. $St = .12$, $n = 1$, (a) reference jet; (b) Case #3, $r = .6$, $s = 1$, outer shear layer

(a)

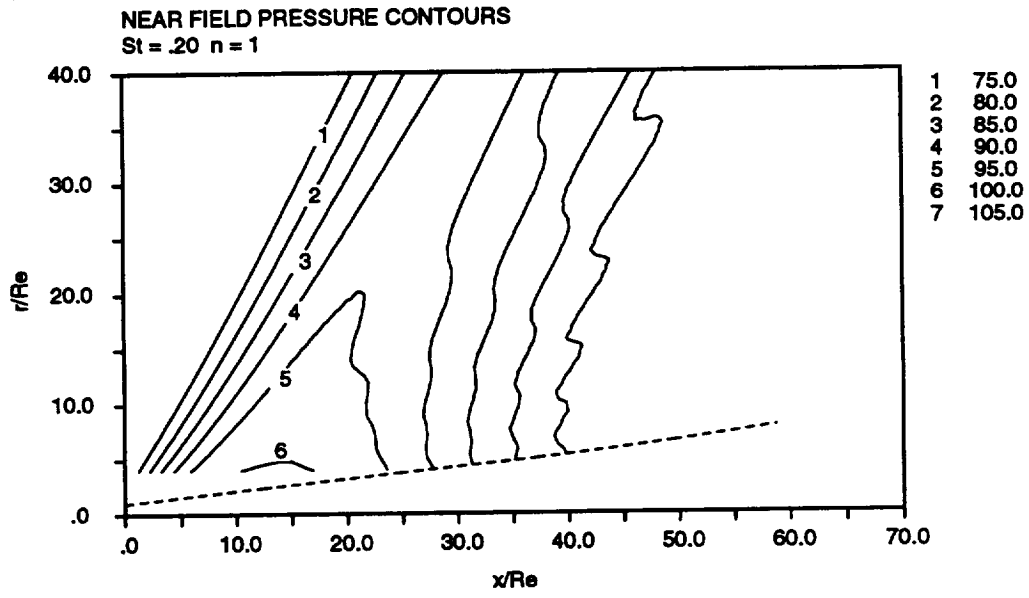

(b)

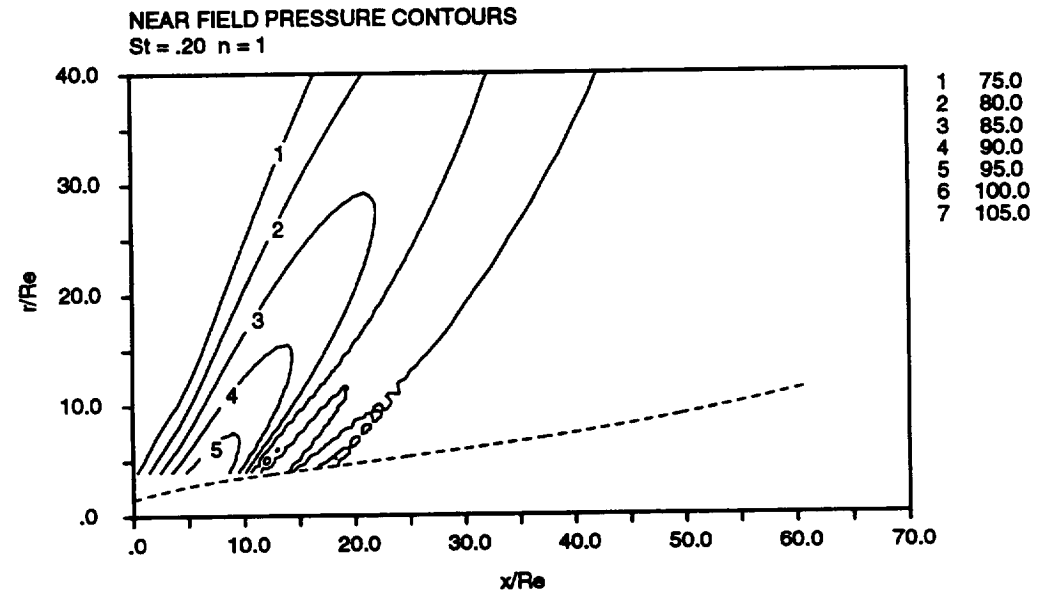

Figure 4.10. Comparison of calculated near field pressure contours. $St = .20$, $n = 1$, (a) reference jet; (b) Case #7, $r = .8$, $s = .5$, outer shear layer

(a)

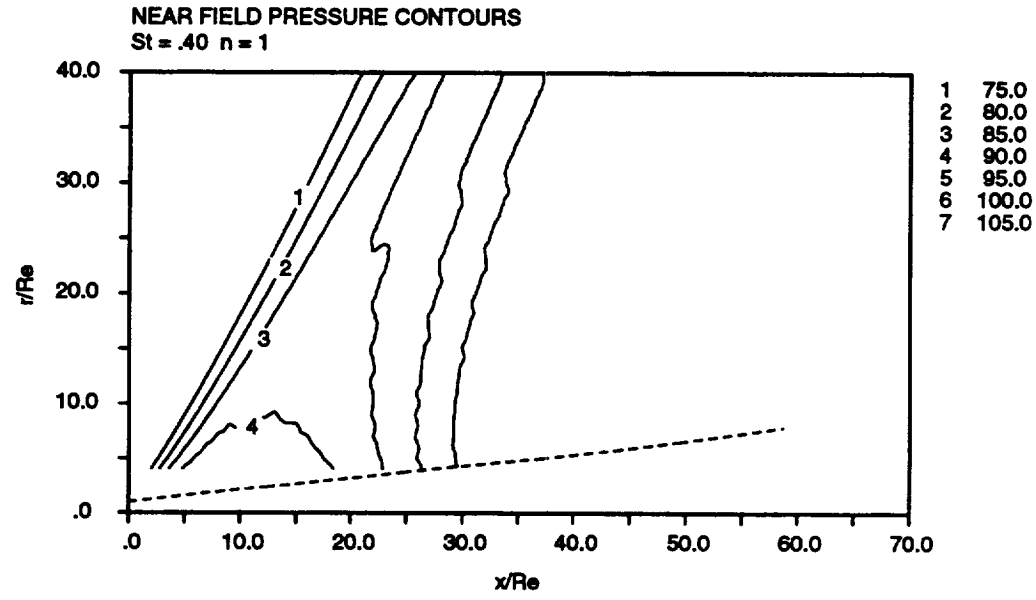

(b)

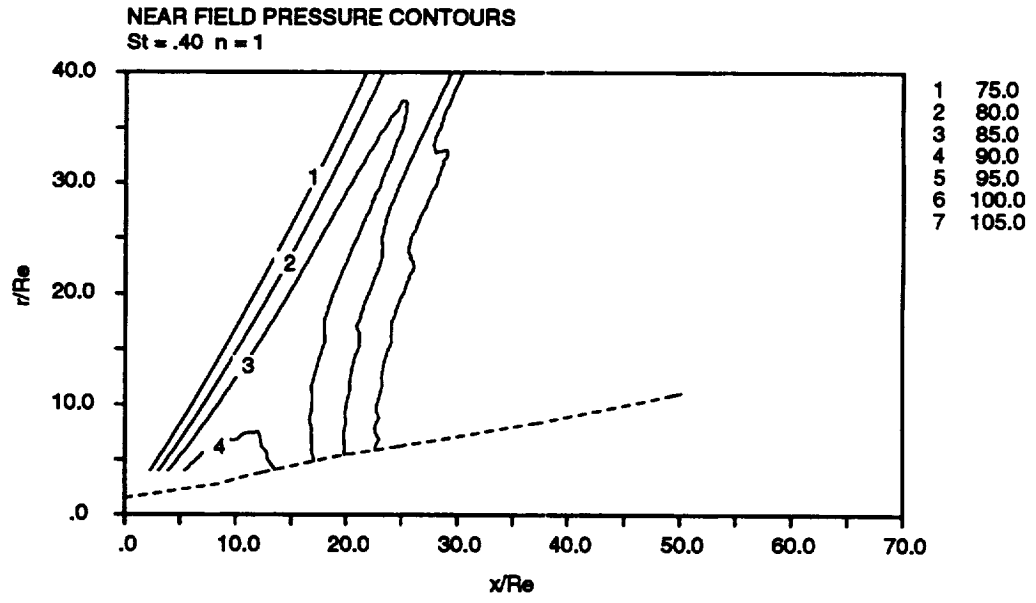

Figure 4.11. Comparison of calculated near field pressure contours. $St = .40$, $n = 1$, (a) reference jet; (b) Case #5, $r = .8$, $s = 2$, outer shear layer

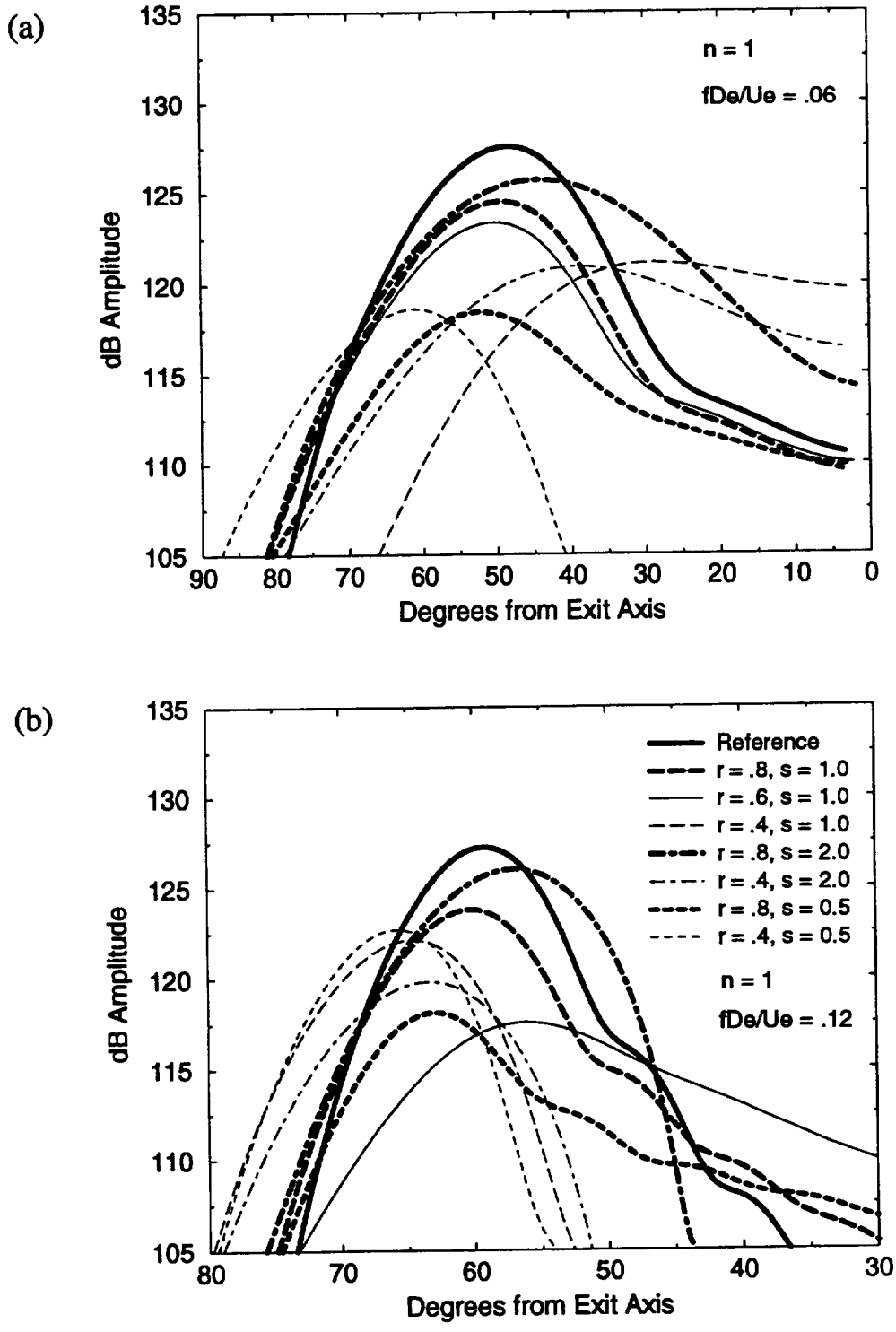

Figure 4.12. Far field directivity patterns for normal velocity profile cases. (a) $St = .06$, $n = 1$; (b) $St = .12$, $n = 1$

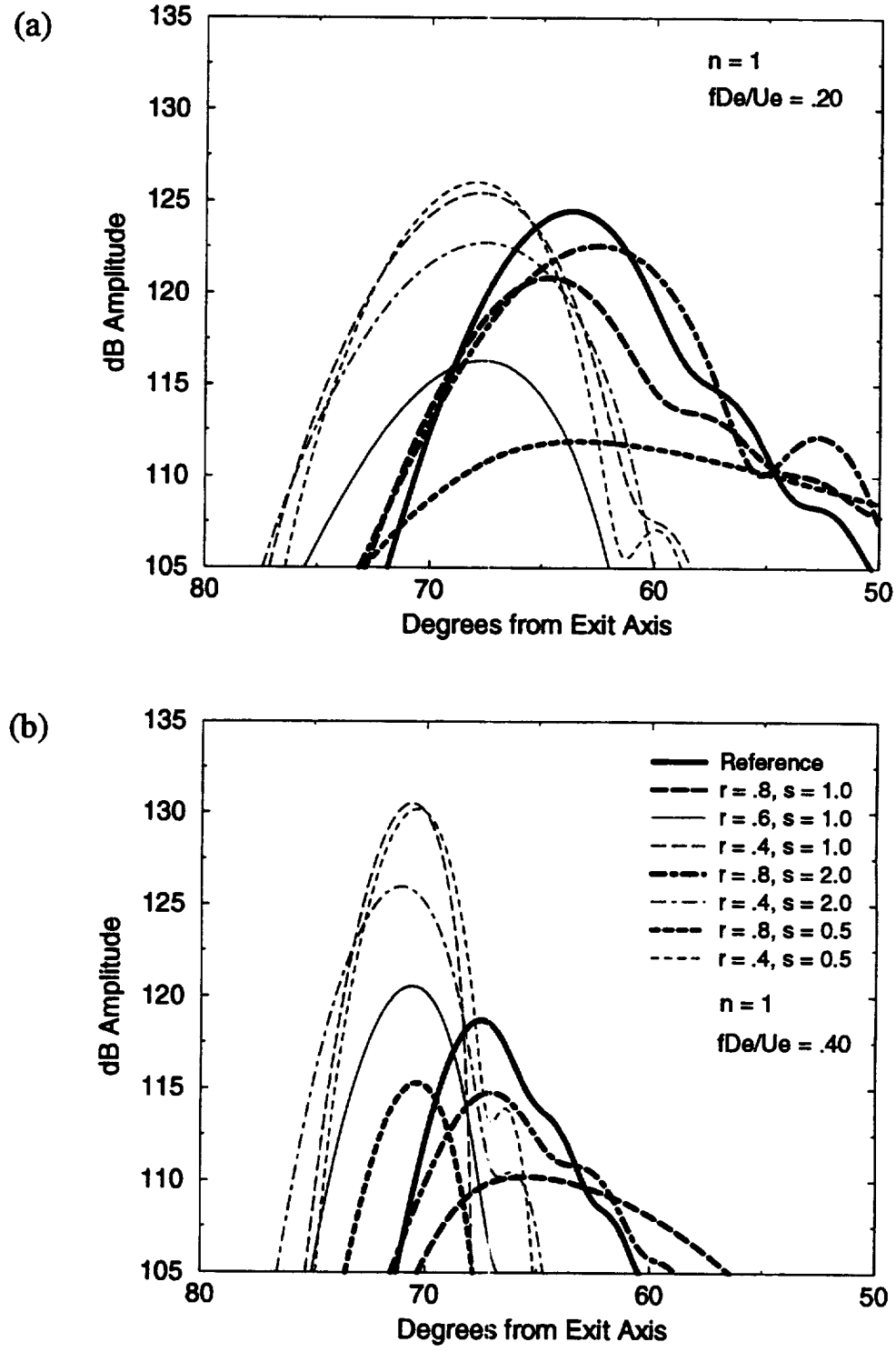

Figure 4.13. Far field directivity patterns for normal velocity profile cases. (a) $St = .20$, $n = 1$; (b) $St = .40$, $n = 1$

Strouhal number .06. All have $r = .4$. Two patterns are emerging in this figure. One is the continuance of the pattern seen in Figure 4.12(a). Starting at the reference jet peak, the peaks decrease as r decreases and as s decreases. These peaks are all based on the outer shear layer instability wave. The second pattern relates to the far field peaks based on the inner shear layer instability waves. As the Strouhal number has increased, more of these peaks have higher amplitudes than the outer shear layer based peaks. At this Strouhal number, the inner shear layer peaks increase as s decreases. In a sense, these opposite results for the inner and outer shear layer based far field directivity patterns as s decreases is expected since the inner high speed stream is getting cooler relative to the outer low speed stream, promoting instability wave growth in the inner shear layer and higher far field directivity peaks, and the outer stream is getting hotter relative to ambient, inhibiting instability wave growth in the outer shear layer and lower far field directivity peaks.

Figure 4.13(a) shows the far field directivity patterns for Strouhal number .20. The two patterns established in Figure 4.12(b) are being extended with increasing levels for the inner shear layer based peaks and decreasing levels for the outer shear layer based peaks. The $r = .6$ case has changed to being inner shear layer dominated. This implies that the amplitude of the inner shear layer peak increases as r decreases or as ΔU of the inner shear layer increases. Some of the inner shear layer peaks are now higher in amplitude than the reference jet.

The highest Strouhal number .40 far field directivity results are shown in Figure 4.13(b). The inner and outer shear layer peaks follow the established pattern as Strouhal number has increased. Now most of the inner shear layer peaks are clearly larger than the reference jet peak. Following Kwan and Ko [1976], using local Strouhal numbers may show that a more preferred frequency for instability wave growth may exist in the inner shear layer than in the reference jet shear layer. For example, the inner shear layer case of $r = .4$, $s = .5$ has a local Strouhal number of .19 based on the inner jet exit diameter and ΔU across the inner shear layer. The reference jet showed greater growth at Strouhal number .2 than at .4. Hence, the inner shear layer peaks that are higher than the reference jet peak may be due to instability waves growing at more preferred local Strouhal numbers.

The $n = 0$ mode far field directivity patterns are shown in Figures 4.14 and 4.15. With two exceptions, the coaxial jet peaks are dominated by the inner shear layer instability wave based peak. The exceptions are the $r = .8$, $s = 2$ cases for Strouhal numbers .12 and .20. The pattern for the coaxial jet peaks is the same for each of the four Strouhal numbers. The peak levels increase as r decreases and as s decreases. The same pattern as for the $n = 1$ mode far field directivity patterns. The levels of the $n = 0$ mode peaks are generally lower than the $n = 1$ mode peaks; but many more of the $n = 0$ mode peaks are higher than the reference jet compared to the $n = 1$ mode.

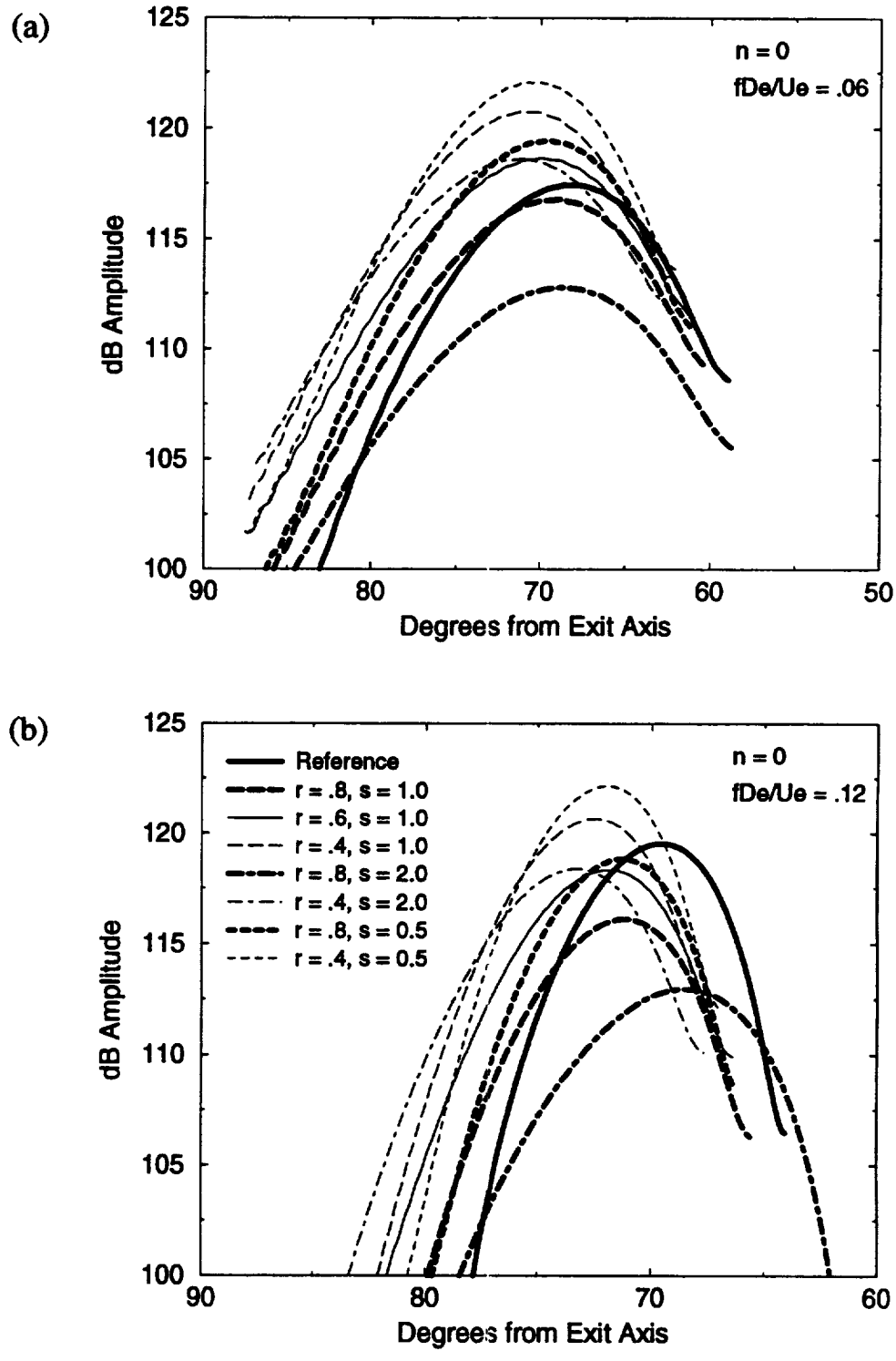

Figure 4.14. Far field directivity patterns for normal velocity profile cases. (a) $St = .06$, $n = 0$; (b) $St = .12$, $n = 0$

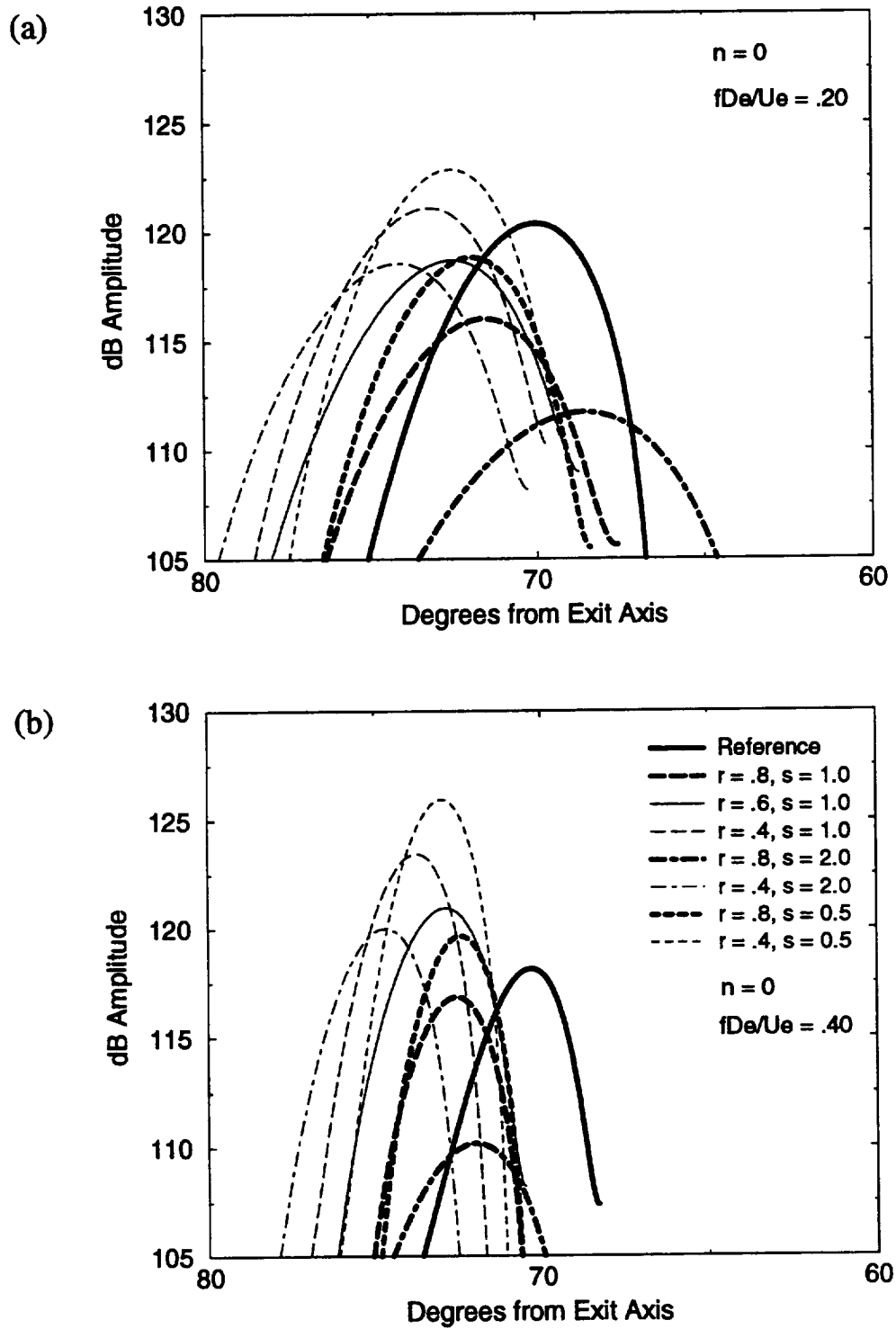

Figure 4.15. Far field directivity patterns for normal velocity profile cases. (a) $St = .20$, $n = 0$; (b) $St = .40$, $n = 0$

The effects of the different operating conditions on the peak direction is determined by whether the dominant peak is based on either the inner or the outer shear layer instability wave. The reference jet peaks and the outer shear layer peaks have their peak directions at angles closer to the jet axis than the inner shear layer peaks. Though there are some changes in direction due to operating conditions within the same family of inner or outer shear layer peaks, the biggest change is due to a change in the dominant peak from being based on the outer shear layer to being based on the inner shear layer.

Finally, we note for the normal profile cases that the $r = .8$, $s = 1$ and $r = .8$, $s = 2$ cases are the only ones with far field directivity peaks that are less than the reference jet for both $n = 0$ and $n = 1$ modes and all four Strouhal numbers. This is especially true for the $n = 0$ mode. The reference jet levels are higher for the $n = 1$ modes than the $n = 0$ modes, so reductions of those levels would be of more immediate benefit. The typically larger reductions for $r = .8$, $s = 1$ range from 3 to 8 dB for the $n = 1$ modes. The $n = 0$ modes have reductions of 1 to 5 dB. Tanna [1980] commented that shock free normal velocity profile coaxial jets could be quieter than the reference jet for r close to 1 and $s < 1$. Support for this conjecture appears in the $r = .8$, $s = .5$ far field directivity where reductions in the $n = 1$ modes are of the order of 10 dB. However, there are slight gains in level for some $n = 0$ mode frequencies which may or may not be significant in terms of overall noise level reductions. In general, the notion that normal velocity profile supersonic jets may be quieter than the reference jet for r close to 1 and $s < 1$ is supported by this evidence.

4.2 Inverted Velocity Profile

The study of supersonic coaxial jets with initial inverted velocity profiles is conducted with the jets operating at the minimum noise condition. The extensive data sets from Dosanjh et al. [1969, 1970] and Tanna et al. [1985] showed the benefits of operating at this point in reducing shock associated noise and the flow, though not originally perfectly expanded, had the characteristics of a fully expanded flow downstream of a composite shock near the nozzle exit. The remaining noise would be dominated by mixing and thought to be modifiable by changing operating conditions. The criterion that is to be maintained, however, is the minimum noise condition where the inner stream is slightly supersonic with a pressure ratio of about 1.9. This fixes the inner stream Mach number M_1. Then, from constant thrust, we find that the outer stream Mach number is given by

$$M_2 = \left[\frac{M_e^2 \left(1 + \frac{A_2}{A_1}\right) - M_1^2}{\frac{A_2}{A_1}} \right]^{1/2}, \tag{4.5}$$

fixing its value. M_e is the reference jet Mach number. Equation (4.1) can be written in the form

$$U_1 = U_e \frac{\left(1 + \frac{M_2^2}{M_1^2}\frac{1}{r}\frac{A_2}{A_1}\right)}{\left(1 + \frac{M_2^2}{M_1^2}\frac{A_2}{A_1}\right)} \tag{4.6}$$

which sets U_1 and U_2 follows from (4.3). The static temperatures in each stream are determined from the definition of the Mach number and s is determined from the ratio of T_1/T_2. Thus, for a given area ratio and a set of reference jet operating conditions, r is the only variable that sets all the operating parameters at the minimum noise condition for inverted velocity profile jets. The parameters chosen for study are given in Table 4.1.

The presentation of the inverted velocity profile results follows the same format as the normal profile results. There are similarities in the results that are discussed in the section above on normal velocity profiles and will not be repeated. We will concentrate on discussing features that are important for understanding the inverted profile results.

4.2.1 Mean Flow Results

A typical inverted velocity profile result is shown in Figure 4.16 in the same format as the normal velocity profile. In this case, when the two shear layer merge, a local maximum velocity exists in the flow that moves towards the jet axis before the jet becomes fully developed. The location of this velocity is labeled U_{max} in Figure 4.16(a) and extends from the end of the outer potential core tip and moves to the jet axis downstream. This plot is very similar to that shown in Au and Ko [1987] for measured data from a subsonic jet. Along with the edges of the inner and outer potential cores, the figure shows the location of the half velocity point between the maximum velocity and the outer edge velocity of the outer shear layer.

The basic mean flow properties for each of the five calculated inverted velocity profiles are shown in Figure 4.16(b) in terms of the location of the outer potential core tip, the location of the inner potential core tip, and the location where U_{max} reaches the jet axis (also called the reattachment point). For the given operating conditions that result in fixed Mach numbers in both the inner and outer streams, as r increases and temperatures adjust accordingly, both potential cores shorten in length. The location of U_{max} on the axis, however, moves further downstream as the outer stream velocity has increased.

4.2.2 Instability Wave Characteristics

Figure 4.17 shows the instability wave characteristics of the $n = 0$ mode for both the inner and outer shear layers of an inverted velocity profile with $r = 1.75$ and $s = 2.07$

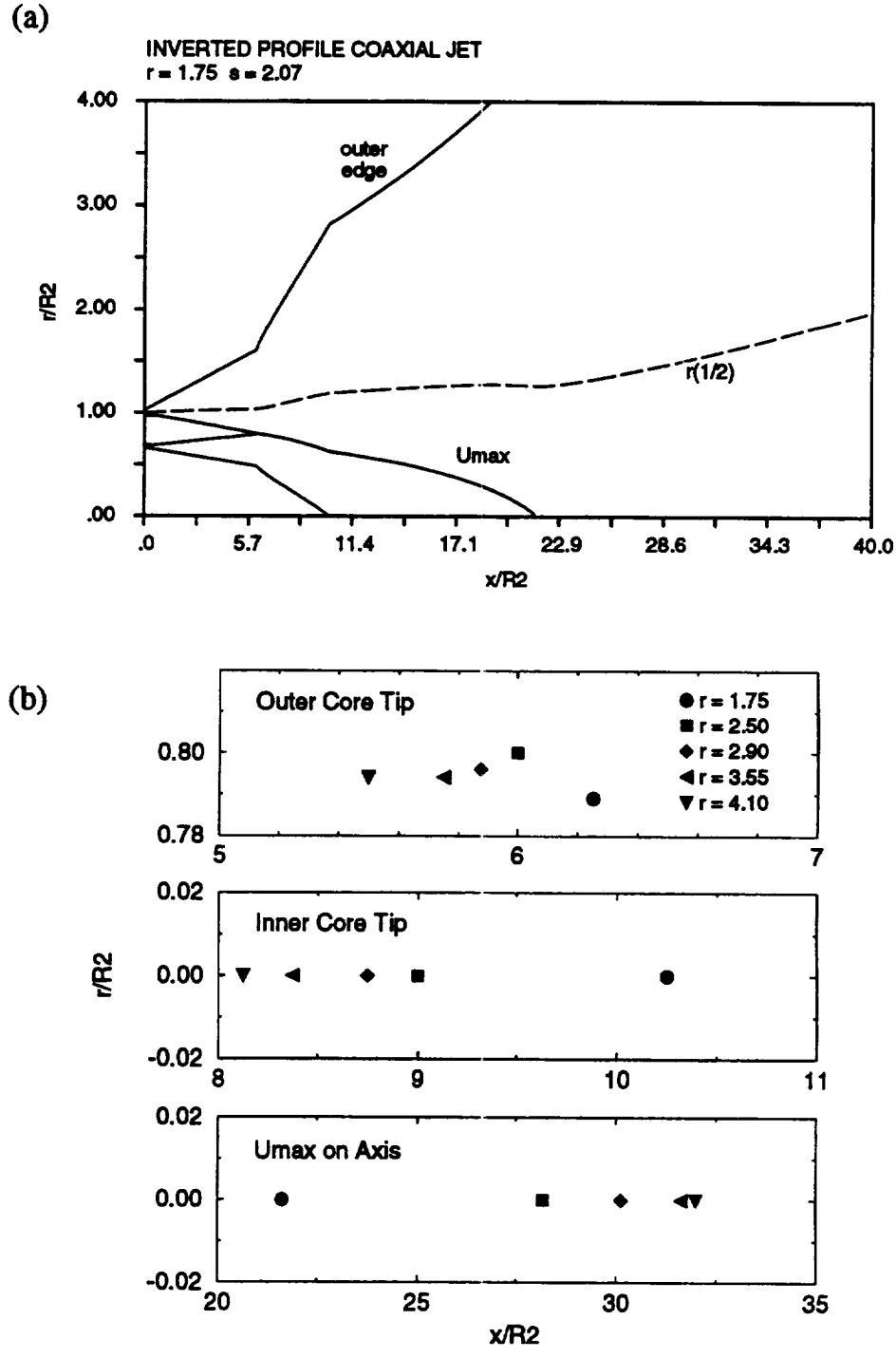

Figure 4.16. Calculated mean flow data for inverted profile coaxial jets. (a) typical mean velocity profile, $r = 1.75, s = 2.07$; (b) location of potential core tips and maximum velocity point on the axis for inverted velocity profile operating conditions, Table 4.1

(Case #24 in Table 4.1). The $n = 1$ mode instability wave characteristics are shown in Figure 4.18. The inner shear layer instability wave characteristics are similar for both the $n = 0$ and $n = 1$ modes, part (a) of each figure. The growth rates have about the same initial values for both modes and the initial growth rates increase with Strouhal number. The phase velocity is fairly constant in the potential core region with a slight decrease with Strouhal number. The instability waves become damped near the end of the outer potential core for most Strouhal numbers and before the end of the inner potential core for the lower Strouhal numbers. The inner shear layer ends when U_{max} reaches the jet axis and thus ends any stability calculation of the inviscid inflectional type of growing or damped waves. In order to complete the damped behavior of the inner shear layer instability wave, the damped characteristics are extended downstream in the manner previously described.

The outer shear layer instability wave calculations are completed in the same manner as a single jet shear layer. The $n = 0$ mode calculations, Figure 4.17(b), are completed until the phase velocity approached U_{max}. The approximate extension of the instability wave characteristics is added after this point. The $n = 1$ mode calculations are completed into the damped region as far downstream as the mean flow is available, see Figure 4.18(b). Both the $n = 0$ and $n = 1$ mode characteristics show abrupt changes at the locations where the inner and outer potential cores end. They are most pronounced in the $n = 1$ mode growth rate curves. The initial growth rates increase with Strouhal number; but as the instability wave solution progresses downstream, the growth rates decrease more quickly as Strouhal number increases. All the instability waves become damped before U_{max} reaches the jet axis. For the phase velocity, the $n = 0$ mode shows them staying within a small range for all the Strouhal numbers. In contrast, the $n = 1$ mode phase velocities spread out with changing Strouhal number as the instability waves progress downstream toward their peak and then damp out. In all cases, the phase velocities are supersonic relative to ambient conditions.

4.2.3 Wavenumber Spectra

The wavenumber spectra for the growth rates and phase velocities plotted in Figures 4.17 and 4.18 are shown in Figure 4.19 for both $n = 0$ and $n = 1$ modes. It is immediately seen that the outer shear layer instability waves have much larger amplitudes than the inner shear layer instability waves. This is true for all five inverted profile cases. Hence, we will concentrate our remaining discussion on the instability waves in the outer shear layer and their noise generation characteristics.

Figure 4.20 shows all the wavenumber spectra for the outer shear layer, $n = 0$ mode, instability waves for the four Strouhal numbers. As r increases, the spectral peaks continually increase for the Strouhal number .06 case. As Strouhal number increases, we see that the peak amplitude is maximum for $r = 3.55$ and lower at other values. The outer

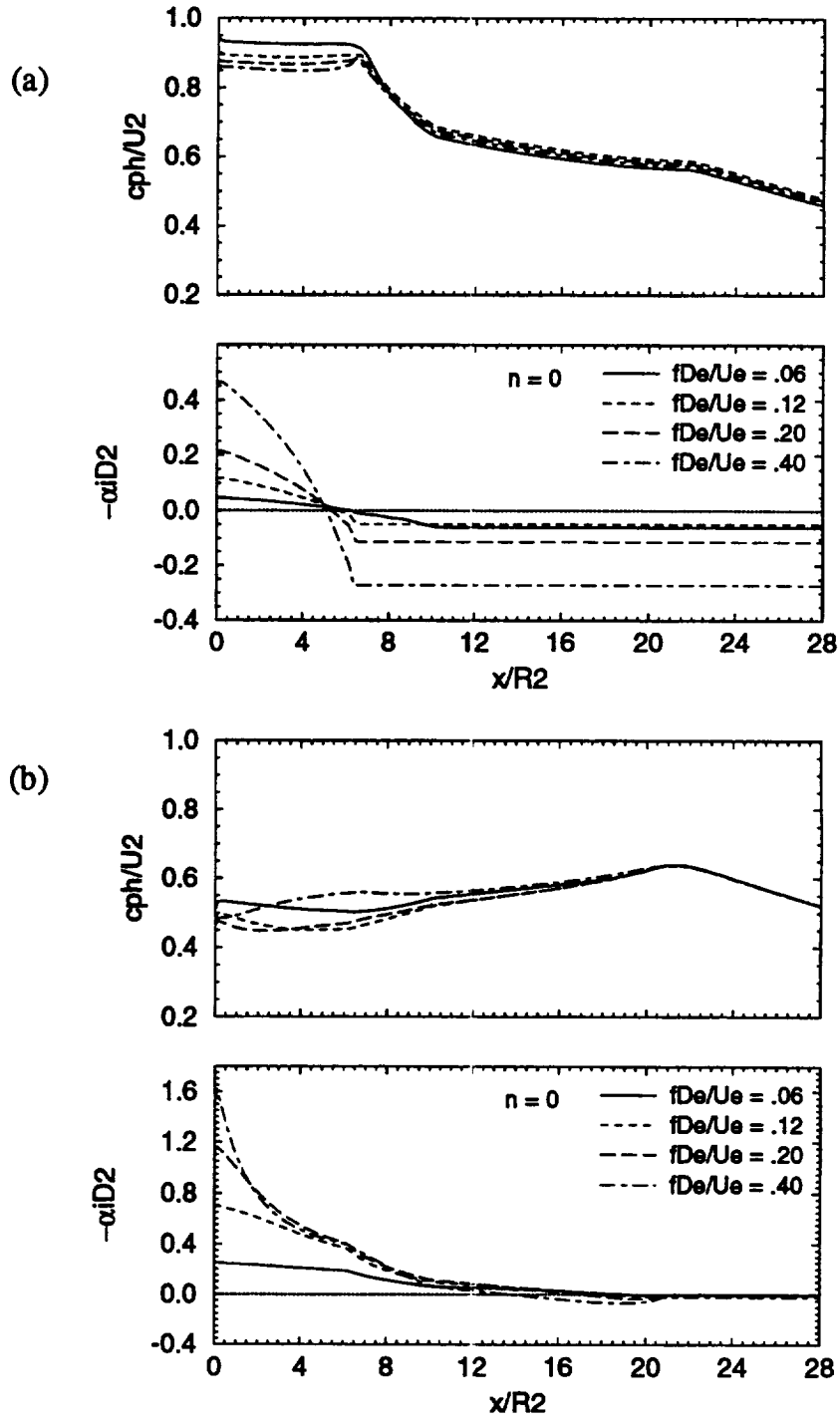

Figure 4.17. Growth rates and phase velocities for inverted profile with $r = 1.75$ and $s = 2.07$. (Case #24 in Table 4.1) (a) inner shear layer, $n = 0$; (b) outer shear layer, $n = 0$

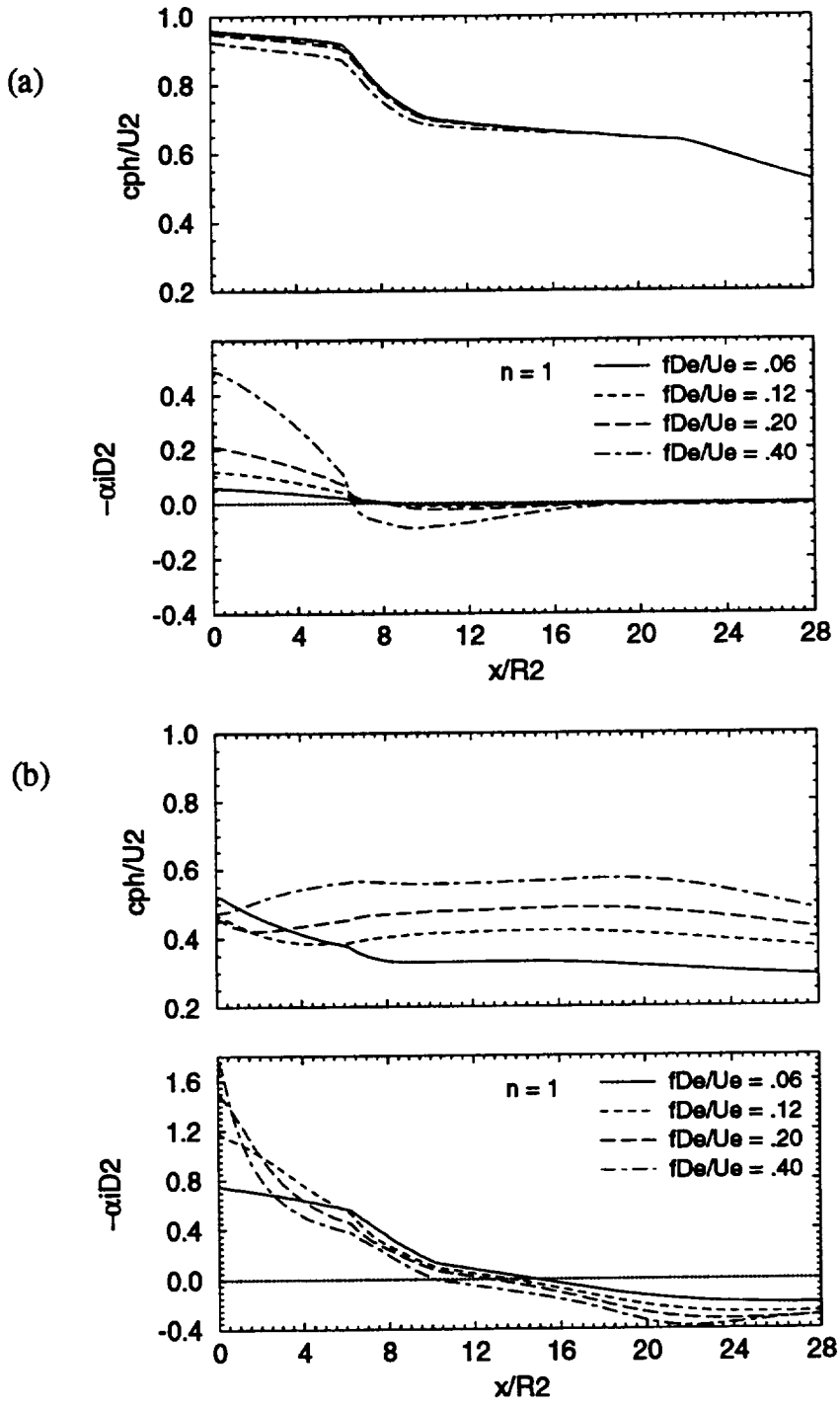

Figure 4.18. Growth rates and phase velocities for inverted profile with $r = 1.75$ and $s = 2.07$. (Case #24 in Table 4.1) (a) inner shear layer, $n = 1$; (b) outer shear layer, $n = 1$

shear experiences the conflicting effects on the growth of the instability wave of velocity and temperature. With increasing r, the outer stream maximum velocity increases which increases the radial velocity gradients and increases the growth rates of the instability wave. In addition, to maintain minimum noise conditions, as r increases, the outer stream temperature increases, also. The increased temperature has the tendency to decrease growth rates. Somewhere in the vicinity of $r = 3.55$ for the higher Strouhal numbers, a balance between these two effects exists. Below this point, the high outer stream velocity has a greater impact, and above this point, the high outer stream temperature has a greater impact. The change in peak amplitude with increasing r is accompanied by gradual increases in the wavenumber of the peak. This is indicative of a decrease in phase velocity for the instability wave.

The wavenumber spectra for the outer shear layer, $n = 1$ mode, instability waves are shown in Figure 4.21. These peaks grow in amplitude and change little in wavenumber location as r increases. Unlike the $n = 0$ mode, the $n = 1$ mode instability waves are not being affected as much by temperature as by velocity. For Strouhal numbers .06 and .12, Figure 4.19 shows that the $n = 1$ mode clearly has higher amplitudes than the $n = 0$ mode. These $n = 1$ lower Strouhal number instability waves become even more dominant as r increases. At the two higher Strouhal numbers, Figure 4.19 shows that the $n = 0$ mode is dominant over the $n = 1$ mode for the lowest inverted profile velocity ratio, $r = 1.75$. However, the $n = 1$ modes grow to very dominant amplitudes over the $n = 0$ modes as r gets larger than 2.9.

4.2.4 Near Field Pressure Contours

The near field pressure contours generated from the outer shear layer, $n = 1$ mode instability waves of the inverted velocity profile case with $r = 1.75$ and $s = 2.07$ (Case #24 in Table 4.1) are shown in Figures 4.22 and 4.23 for each of the four Strouhal numbers. These figures should be compared to the reference jet near field pressure contours shown in parts (a) of Figures 4.8 to 4.11. We see that these coaxial jet contours have higher levels at all Strouhal numbers and that the directionality has shifted towards downstream from the reference jet direction. Since the directional characteristic of the near field pressure contours is related to the location of the peak in the wavenumber spectrum, the near field pressure contours for higher r, which showed little change in peak location as seen in Figure 4.21, are the same as the ones shown for $r = 1.75$, but with much higher amplitudes.

4.2.5 Far Field Directivity Patterns

The high amplitude levels already shown in the wavenumber spectra in Figure 4.19 are now confirmed in the far field. Figure 4.24(a) shows directivity for the $n = 0$ mode

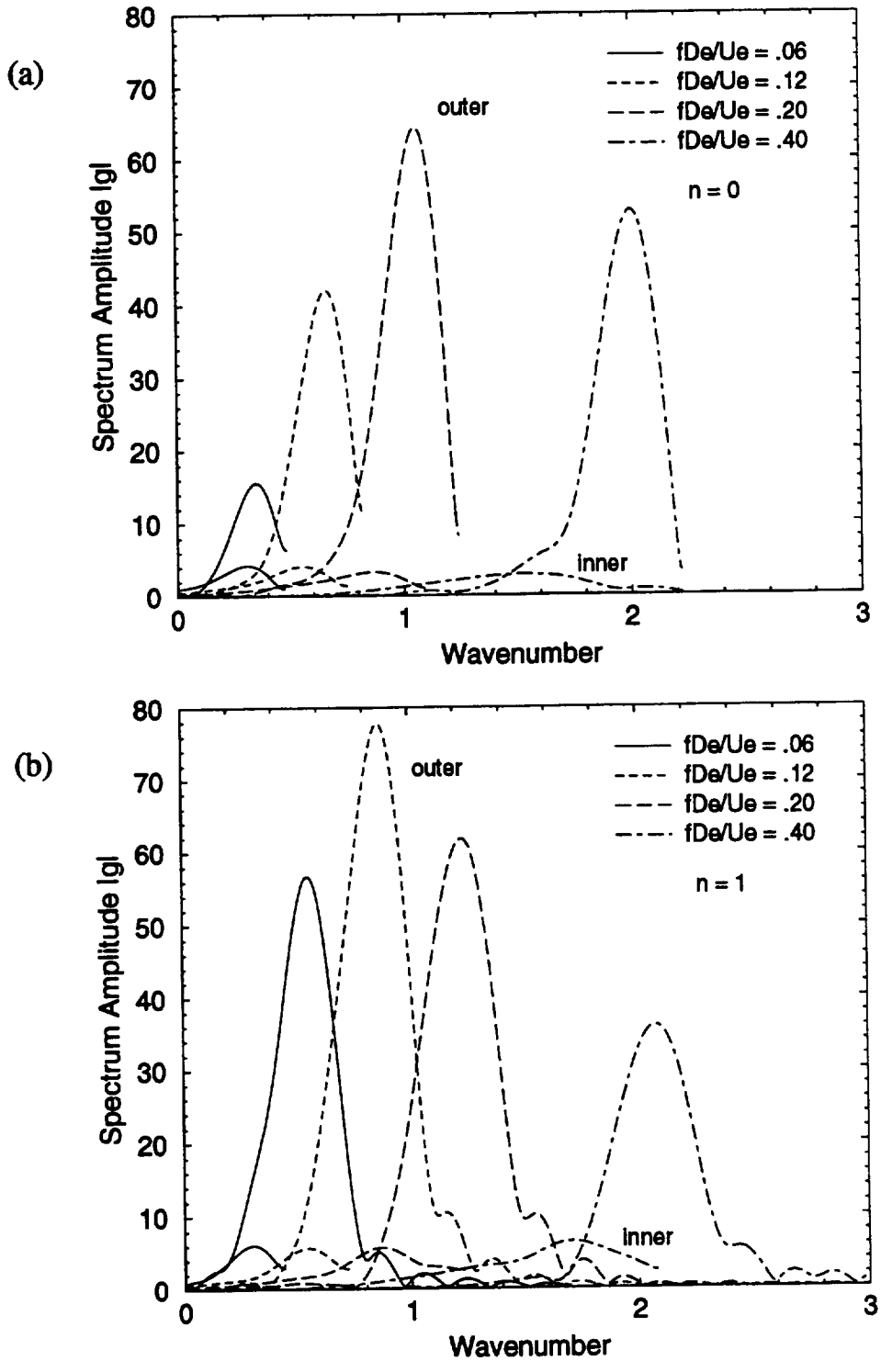

Figure 4.19. Wavenumber spectra for inverted profile with $r = 1.75$ and $s = 2.07$. (Case #24 in Table 4.1) (a) $n = 0$; (b) $n = 1$

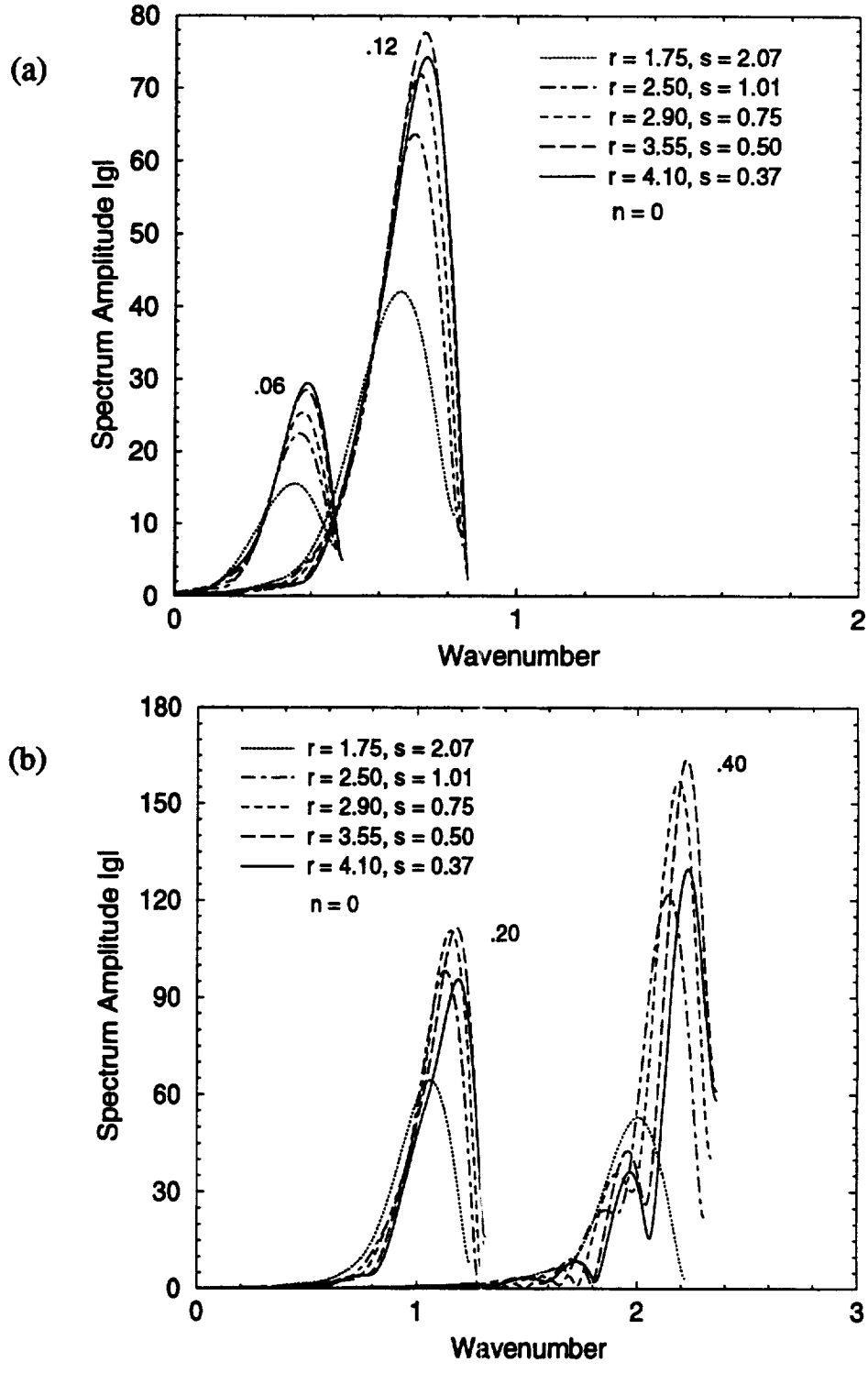

Figure 4.20. Wavenumber spectra for inverted velocity profile cases. (a) $St = .06$, $St = .12$, $n = 0$; (b) $St = .20$, $St = .40$, $n = 0$

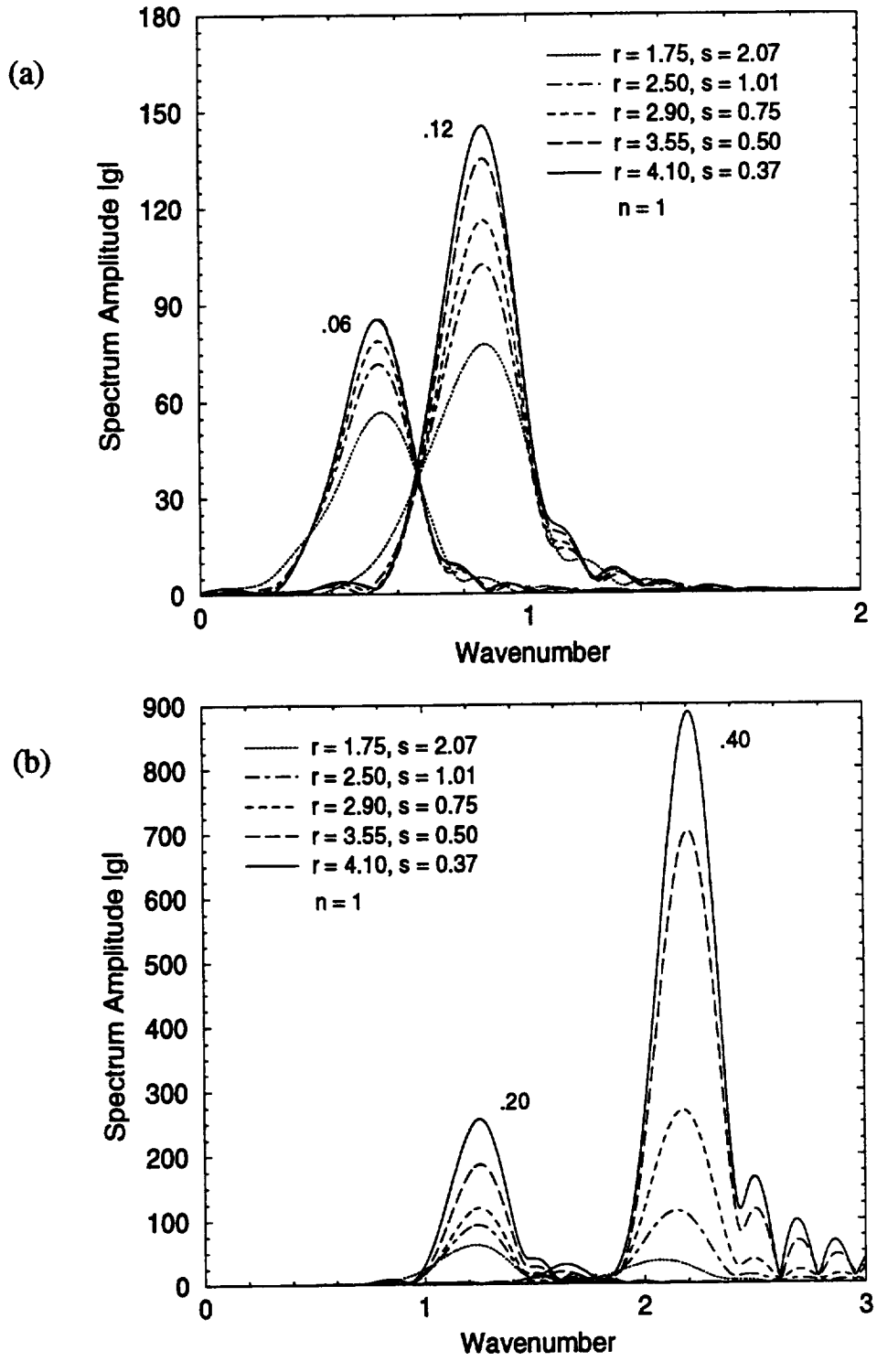

Figure 4.21. Wavenumber spectra for inverted velocity profile cases. (a) $St = .06$, $St = .12$, $n = 1$; (b) $St = .20$, $St = .40$, $n = 1$

(a)

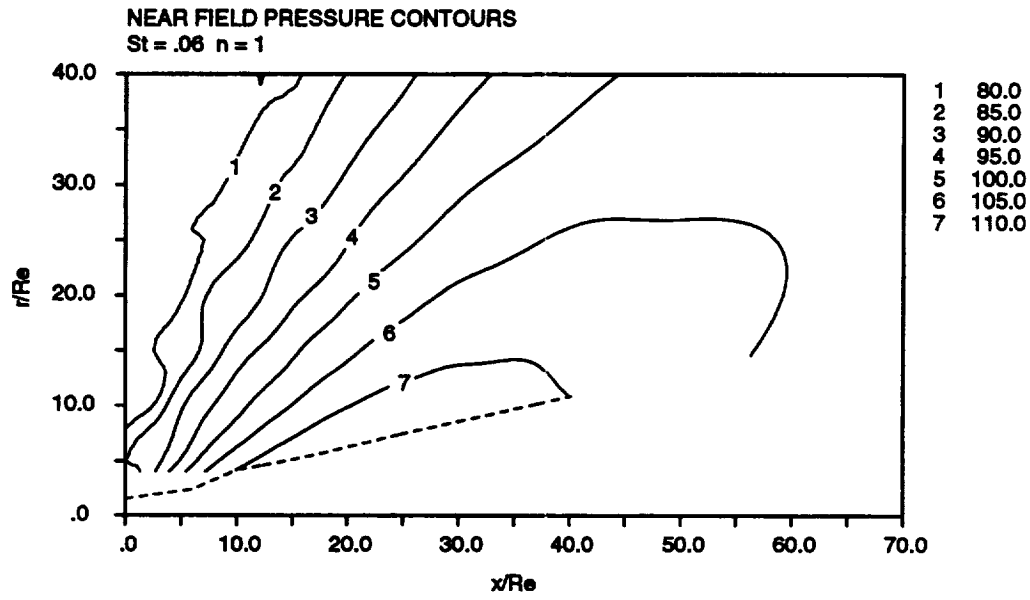

(b)

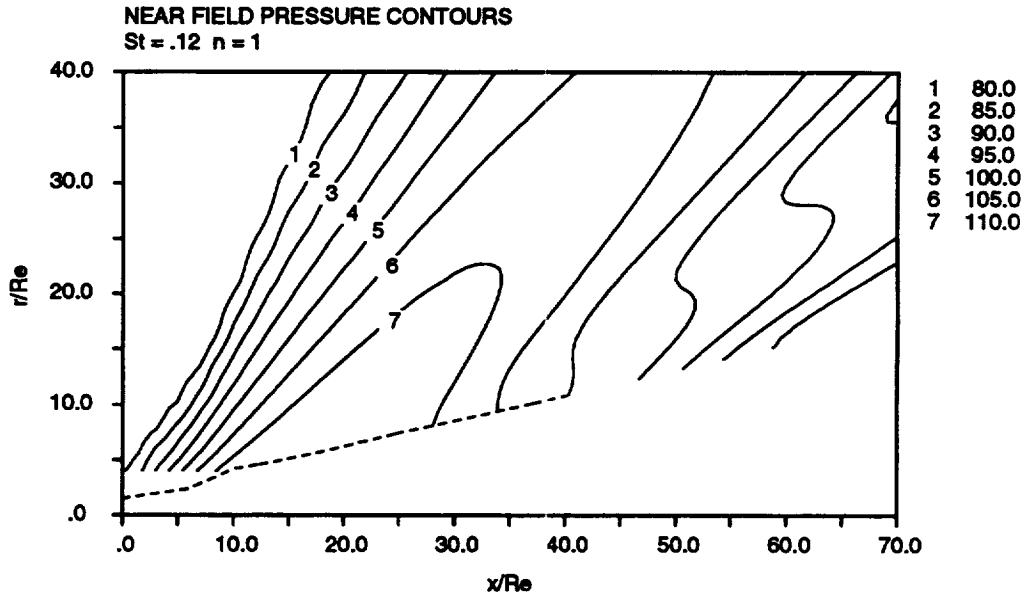

Figure 4.22. Near field pressure contours for inverted profile with $r = 1.75$ and $s = 2.07$. (Case #24 in Table 4.1) Outer shear layer, $n = 1$ (a) $St = .06$; (b) $St = .12$

(a)

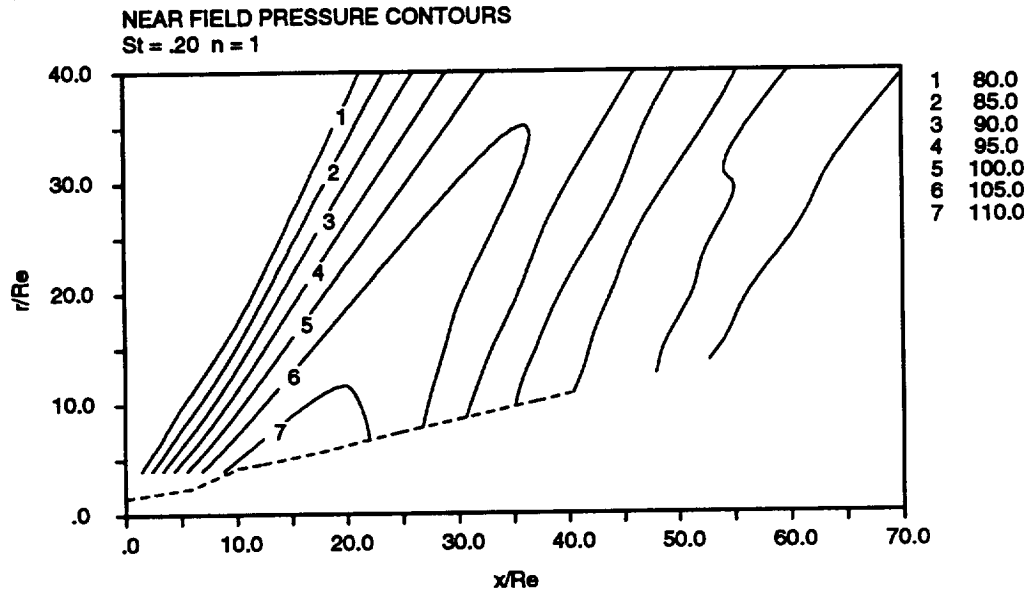

(b)

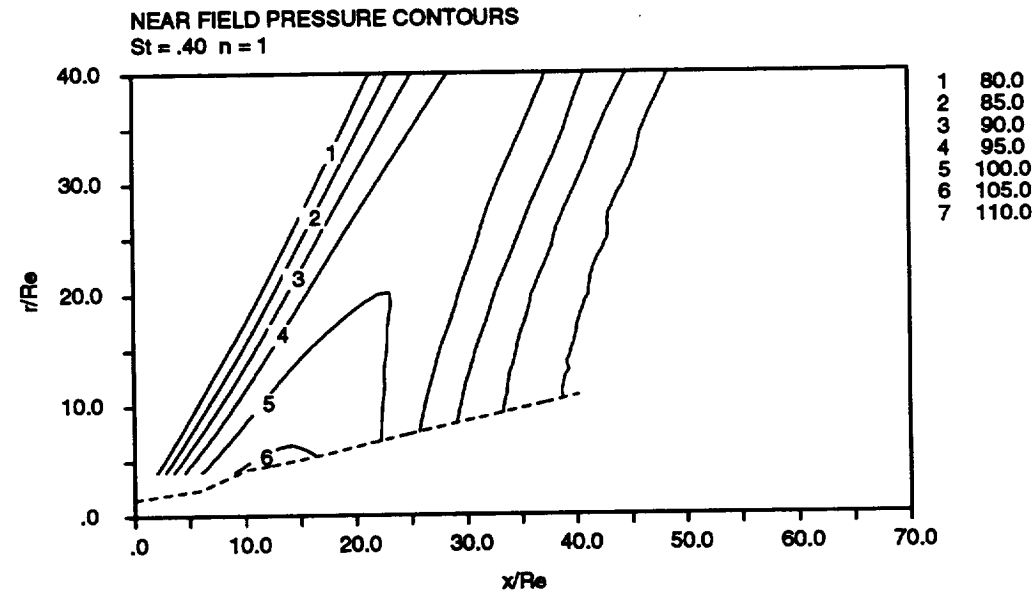

Figure 4.23. Near field pressure contours for inverted profile with $r = 1.75$ and $s = 2.07$. (Case #24 in Table 4.1) Outer shear layer, $n = 1$ (a) $St = .20$; (b) $St = .40$

and Figure 4.24(b) shows directivity for the $n = 1$ mode. The amplitude levels have the same basis as the normal velocity profile far field plots shown earlier. The wavenumber spectra in Figure 4.19 have been translated to the far field with the same amplitude relationship between the peaks and the spectral peaks with higher wavenumber have larger angles to the jet axis in the far field. All the peaks are closer to the jet axis than the reference jet peaks for both $n = 0$ and $n = 1$ modes. (Compare to reference jet results in Figures 4.12 to 4.15.) This confirms what is seen in the near field pressure contours in the previous section.

The far field directivity results for all the inverted velocity profile cases are shown in Figure 4.25, for the $n = 0$ mode, and in Figure 4.26, for the $n = 1$ mode. Both figures only show directivities for Strouhal numbers .20 and .40. As expected, the levels are much larger than the reference jet, which has peak levels less than the lowest level shown in these figures, and follow the pattern set in the wavenumber spectral plots. The directivity for the $n = 0$ mode shifts toward the jet axis as r increases. The peak amplitude level increases as r increases from 1.75 to 3.55 and then decreases at $r = 4.10$. For the $n = 1$ mode, the amplitude continually increases with increasing r and the direction gradually shifts toward the jet axis. Tanna [1980] concluded that shock free inverted velocity profile jets were noisier than the reference jet at high frequencies, but significantly quieter at low frequencies. The results from Figures 4.22 to 4.26 show only higher amplitude levels than the reference jet and for the most part as r increases, the noise level increases. Thus, we have not found any noise reduction benefit for the chosen operating conditions. The minimum noise condition constraint has fixed s for a given area ratio. If there is any benefit to having a different s at the same r, the area ratio needs to be changed.

4.2.6 Discussion

The results we have shown for inverted velocity profile supersonic coaxial jets have a fixed area ratio of 1.25 leaving the velocity ratio r as the only independent variable for determining operating parameters for the given test conditions. Those conditions are that the inverted profile jet is operated at minimum noise conditions with total thrust, total mass flow, and total exit area equivalent to the reference jet. From the chosen operating conditions, we calculate instability waves with higher amplitudes in the outer shear layer of an inverted velocity profile jet than the amplitude for the instability waves in the reference jet shear layer. The calculations are conducted for different jets at constant physical frequency. A concern with this approach that exists for both the normal velocity profile jets and the inverted velocity profile jets is that the unstable characteristics of the jet shear flows are scaled with constant Strouhal number. Under the constant Strouhal number approach, the stability characteristics would be similar for jets with constant Strouhal number but have different velocities, diameters, and

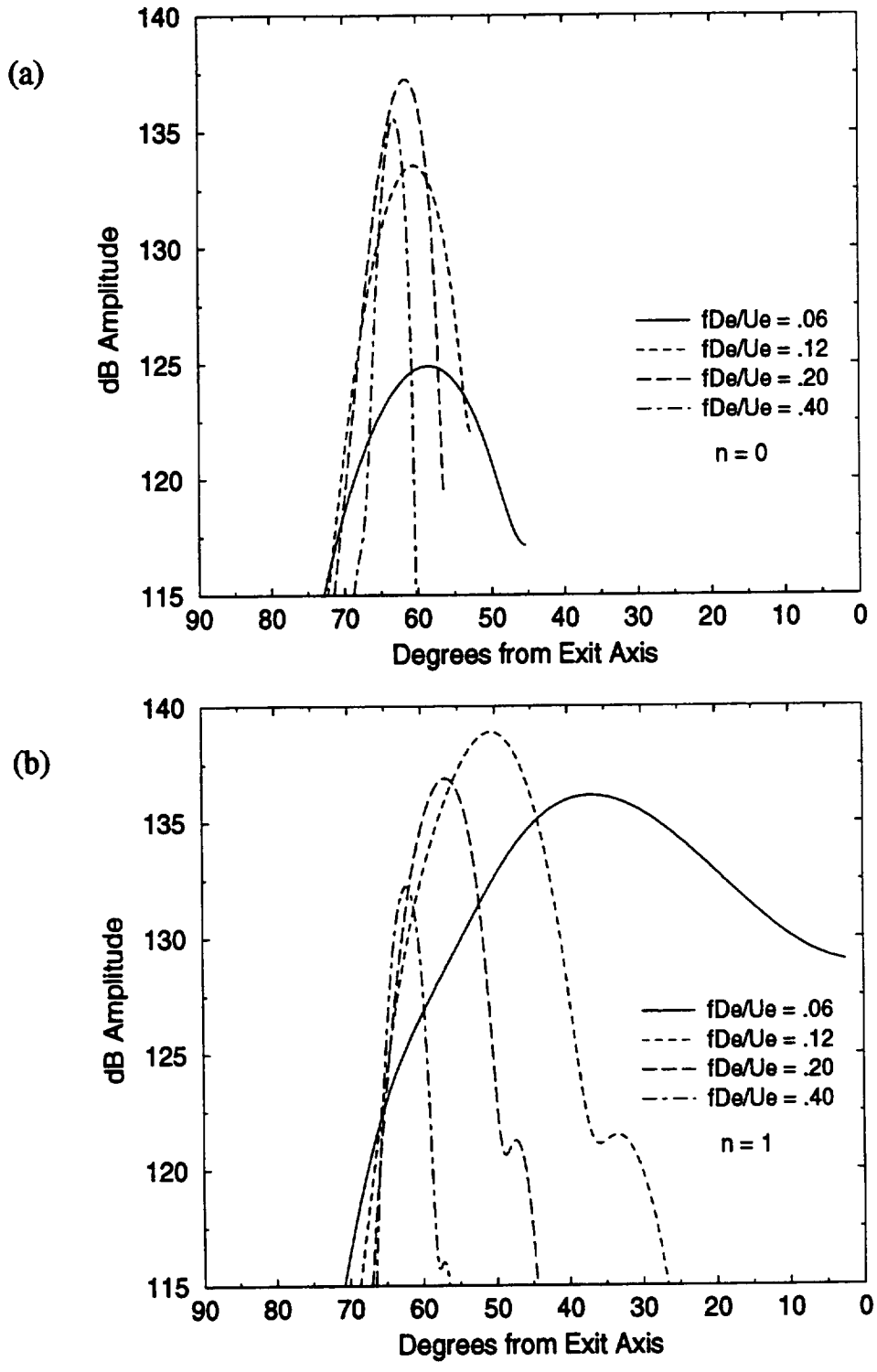

Figure 4.24. Far field directivity patterns for inverted profile with $r = 1.75$ and $s = 2.07$. (Case #24 in Table 4.1) (a) $n = 0$; (b) $n = 1$

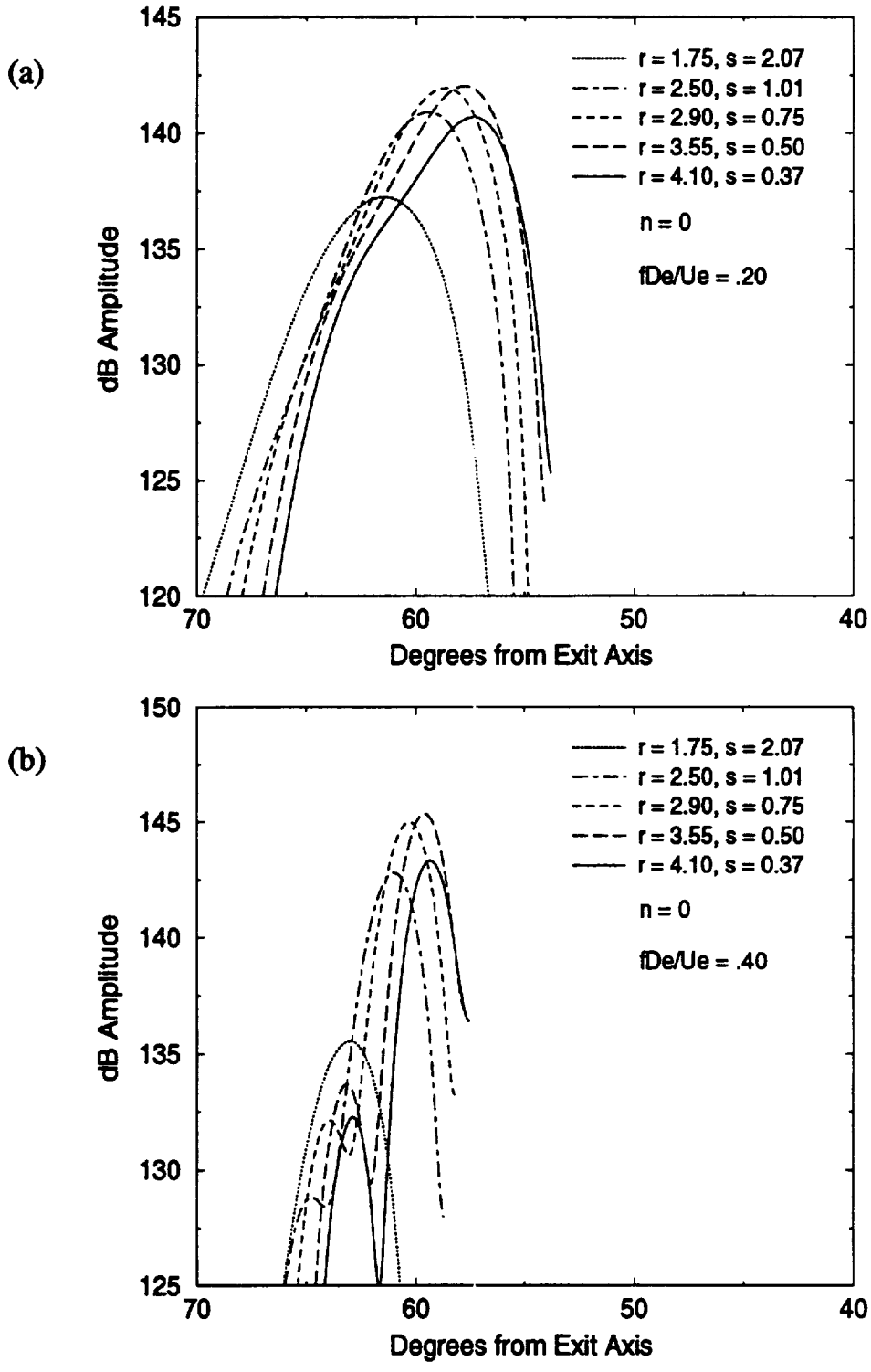

Figure 4.25. Far field directivity patterns for inverted velocity profile cases. (a) $St = .20$, $n = 0$; (b) $St = .40$, $n = 0$

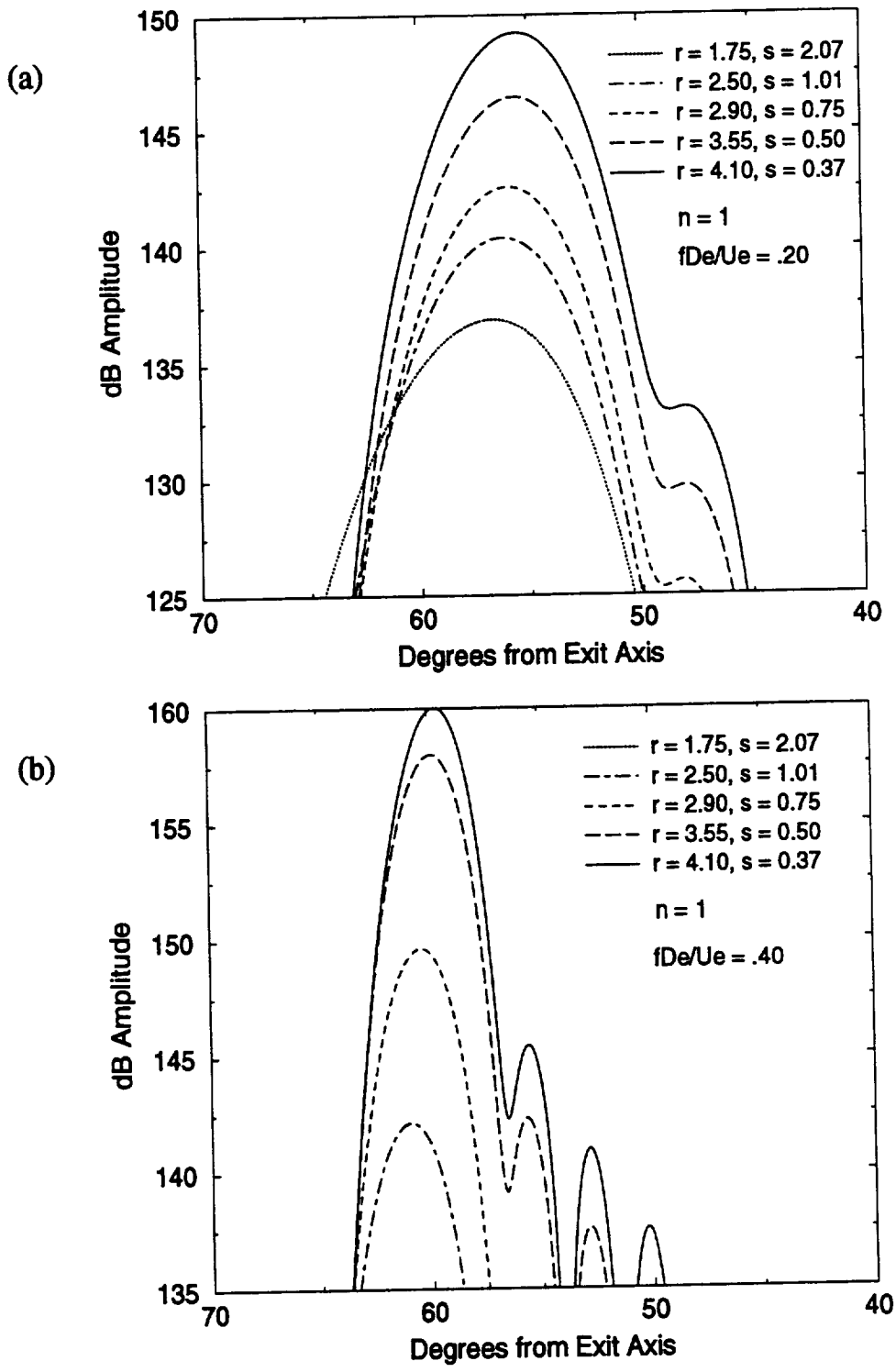

Figure 4.26. Far field directivity patterns for inverted velocity profile cases. (a) $St = .20$, $n = 1$; (b) $St = .40$, $n = 1$

frequencies. Thus, stability characteristics that have been described as different for different operating conditions, but at the same physical frequency, may be similar if results are compared at the same local Strouhal number. With that in mind, we ran a test case where a single jet shear layer is compared to the outer shear layer of a coaxial jet.

Using the inverted profile case with $s = 1.01$ (Case #20 in Table 4.1) to define the single jet operating conditions ($U = 1552.9$ m/s and $T = 937.9$ K), the single jet mean flow was numerically calculated starting with the same initial conditions as the outer shear layer of the coaxial jet. In the mean flow calculations, the outer shear layer is unaffected by the inner shear layer until the shear layers merge. Hence, by starting with the same initial conditions, the single jet shear layer and the outer shear layer of the coaxial jet had the same spreading rates until the outer shear layer merges with the inner shear layer.

The calculated instability wave growth rates and phase velocities for the single jet and the coaxial jet mean flows are shown in Figure 4.27. The Strouhal number fD_e/U_e is based on the equivalent jet operating conditions and it is used to calculate the instability wave characteristics of the outer shear layer of the coaxial jet. The single jet uses U_2, the outer stream velocity of the coaxial jet which is the same as the single jet velocity, to calculate the Strouhal number. Converting the Strouhal number .06 to outer shear conditions, we get .05. Thus, the two lower Strouhal numbers are the same in terms of outer shear layer conditions which are the same as the single jet shear layer conditions. The expectation is that, initially, the two shear layers would have the same stability characteristics. However, the calculations show that the single jet has lower growth rates and higher phase velocities than the outer shear layer growth rates and phase velocities. The same relationship exists between the two results for the Strouhal number .40 calculations. Thus, it appears that matching Strouhal numbers based on outer stream conditions for a coaxial jet and based on a single jet with the same mean flow conditions is not sufficient to get similar stability characteristics. The inverted velocity profile in a coaxial jet affects the stability characteristics in the outer shear layer. The resulting growth rates are initially larger than the growth rates of a single jet with the same shear layer spreading.

At first glance, it would seem that the increase in noise levels for inverted velocity profile jets compared to the reference jet is in contradiction to data given in the references. It must be recalled that most of those claims were for shock containing jets where overall levels were reduced by minimizing shock associated noise. Though Dosanjh et al. [1969, 1970] claimed some reductions at all frequencies, Tanna et al. [1985] did not, citing nozzle differences. They both, however, ran their experiments with nozzle exit area ratios less than one. Nozzle exit area ratio is the only other factor available besides velocity ratio r for affecting operating parameters. In our study, it was held fixed at

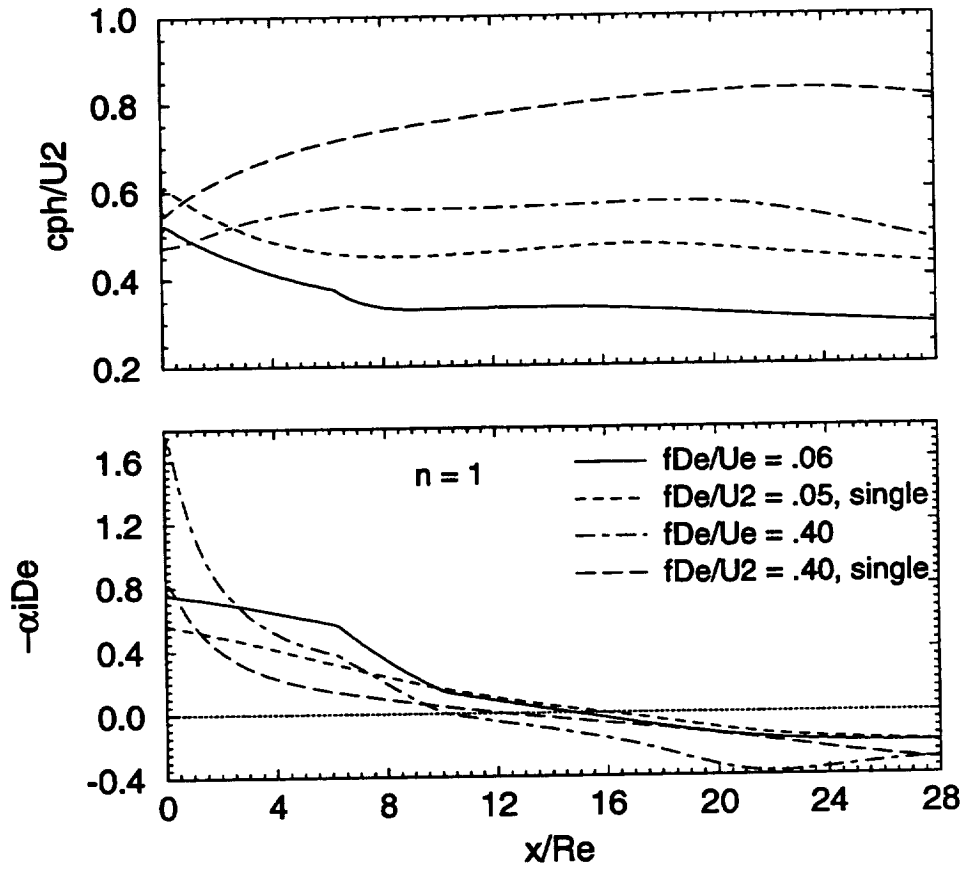

Figure 4.27. Comparison of growth rates and phase velocities, single jet and inverted velocity profile jet.

1.25. To test for any benefits of reducing the area ratio, we ran a test case with area ratio less than one.

Figure 4.28 shows the results from stability and far field directivity calculations for the case with area ratio 1.25 and $r = 4.10$ (Case #23 in Table 4.1) and a case with area ratio .5 and $r = 4.10$. The operating conditions for the latter case have been held to the same total thrust, total mass flow, and total exit area conditions relative to the reference jet as all the other inverted profile cases. The resulting operating conditions are $U_1 = 492.9$ m/s, $U_2 = 2020.9$ m/s, $T_1 = 601.1$ K, and $T_2 = 1017.0$ K. This increases the temperature ratio s from .37 for area ratio 1.25 to .59 for area ratio 0.5 and the outer stream Mach number increases to 3.2. To make this comparison test, we chose the case that generated the largest far field directivity levels of any of the inverted profile calculations. Hence, any benefits to reducing area ratio appears in a worst case scenario. The calculations are performed at Strouhal number .40 for the $n = 1$ mode. The stability characteristics for the two cases are compared in Figure 4.28(a). Even though the outer stream has a higher initial velocity in the lower area ratio case, its smaller thickness results in a shorter potential core and increased mean flow spreading when the shear layers merge. This results in a faster decrease for the growth rates of the outer shear layer instability wave for the lower area ratio case than for the higher area ratio case. The lower instability wave amplitude translates to a lower far field directivity peak as shown in Figure 4.28(b). Thus, for our worst case, we have shown some benefit of using coaxial nozzles with area ratios less than one compared to coaxial nozzles with area ratios greater than one.

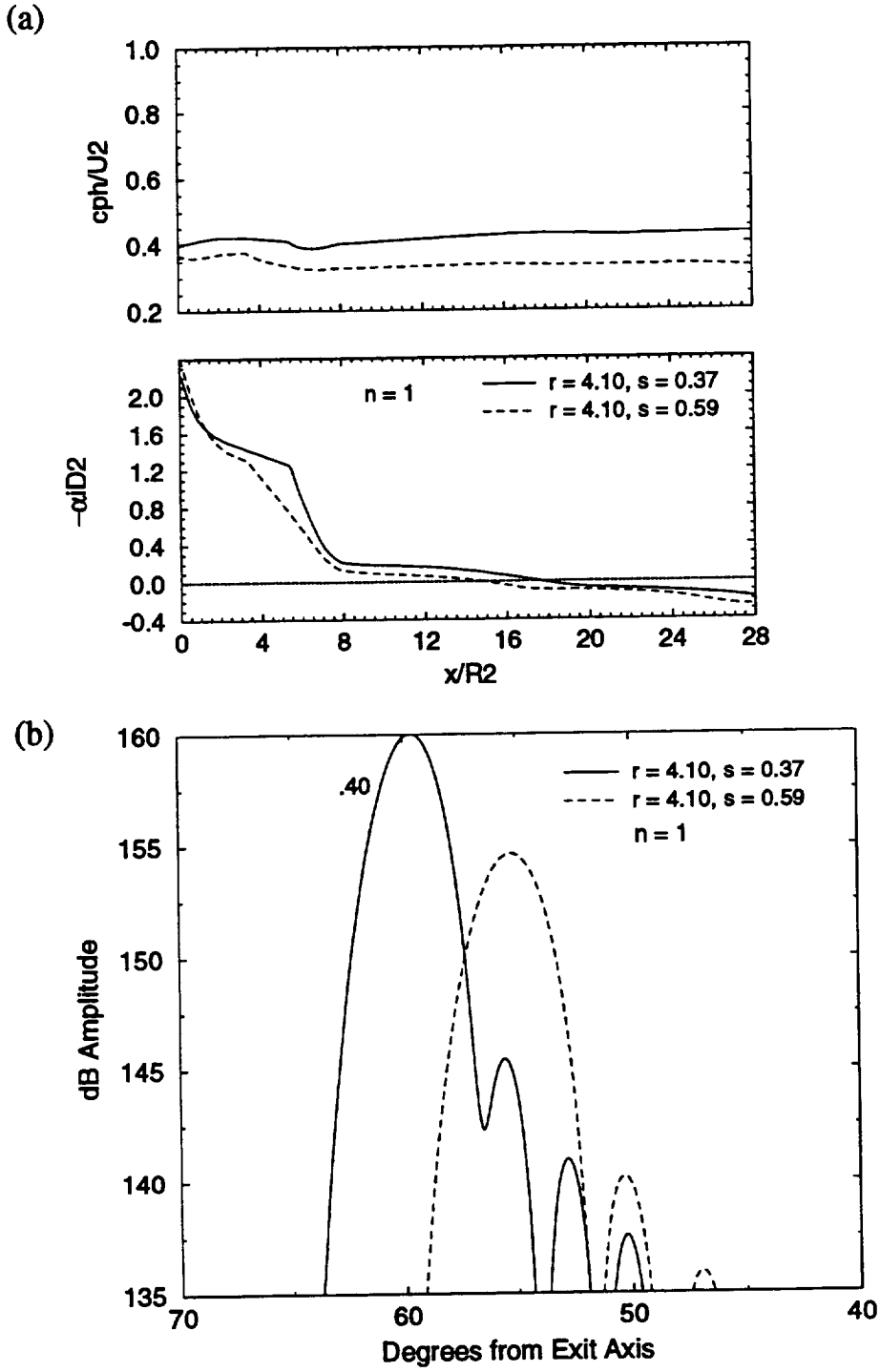

Figure 4.28. Instability wave and far field directivity for inverted profile jets with different area ratios. Area ratio 1.25 (solid line), Area ratio 0.5 (dashed line), (a) growth rate and phase velocity; (b) far field directivity pattern

Chapter 5

CONCLUSIONS AND RECOMMENDATIONS FOR FUTURE WORK

The noise generation from supersonic coaxial jets has been studied in this paper by extending the instability wave, noise generation model for single stream, axisymmetric jets to dual stream, coaxial jets. For high speed, perfectly expanded, axisymmetric jets, the instability waves or large scale coherent structures dynamically control the development of the free jet shear flow and when the instability wave phase velocity exceeds the ambient speed of sound, these waves are the dominant source of mixing noise radiated into the downstream arc of the jet. Linear instability wave analysis is applied to the jet shear layer to obtain the characteristics that describe a growing and decaying instability wave and, subsequently, predict the radiated noise. These concepts, which have been applied to single jets with a single spreading shear layer, are now applied to a coaxial jet with two spreading shear layers.

Much of the theoretical work on the stability of free shear flows relies on the analytical definition of the mean flow in order to solve for the stability characteristics. Experimental measurements of shear flows provided evidence for functional forms to describe the mean flow in stability calculations. Such mean flow data are lacking for two stream coaxial jets, especially at supersonic conditions. The data that are available are not sufficient to develop analytical expressions for mean flow properties of coaxial jets that smoothly transition from two streams to one fully developed jet downstream for both normal velocity profile and inverted velocity profile cases. Hence, it was necessary to develop a numerical scheme to calculate the mean flow properties of a coaxial jet with two initial shear layers that expanded and merged in an orderly fashion in the downstream direction. The development of a turbulent, axisymmetric free jet was assumed to be governed by the Reynolds averaged, compressible, parabolic boundary layer equations. To complete this set of equations, a turbulence model was necessary. Any turbulence model chosen for these calculations would have required modification and calibration to obtain reasonable results for both normal and inverted profile coaxial jets. For expediency, a modified and calibrated mixing length model was used to represent the turbulent stresses and obtain an effective viscosity. The resulting mean flow calculations gave good qualitative resemblance to measured single and coaxial jet flows.

The stability analysis was completed for a slowly diverging free jet shear layer with the assumption that the mean static pressure was constant. To lowest order inside the

jet, the analysis resulted in an eigenvalue problem based on the compressible Rayleigh equation that gave local growth rates and phase velocities at each axial location as the mean flow developed. These local stability characteristics were used to calculate growing and decaying instability waves in the jet shear layers. Outside the jet, the instability wave was the source for near field pressure disturbances and for those instability wave components with supersonic phase velocities relative to ambient, the instability wave was the source of far field radiated noise. The results from stability calculations conducted for single Mach 2 jets in this study using numerically generated mean flow profiles compared favorably with results from studies using analytical formulations to describe the mean flow. Comparisons were also made for our analysis of instability wave noise generation in coaxial jets to far field noise data from low Mach number coaxial jets. The directivity of the calculated far field peak agreed with measured directivity.

With the ability to numerically calculate mean flow profiles for both normal velocity profile and inverted velocity profile supersonic coaxial jets and to use those results to calculate the stability characteristics of both shear layers, we conducted a parametric study of the effects of various operating conditions on the instability waves in and the subsequent noise generation from these jets. The scope of the study was limited to shock free flow conditions from a fixed area ratio nozzle. This allowed us to concentrate on the effects of modifying the mean flow profile shape in a coaxial jet as a means to reduce mixing noise. The normal velocity profiles were studied with variations in both velocity and temperature ratio between the two streams. The inverted velocity profiles were studied at minimum noise conditions. This fixed the temperature ratio for a given velocity ratio. The conclusions from the normal velocity profile study are:

1. The predicted noise reductions for normal velocity profile coaxial jets depended on operating conditions and frequency. For most operating conditions, the radiated noise levels increased with Strouhal number and became higher than the reference jet noise levels.

2. Over the Strouhal number range of 0.06 to 0.4 used in this study, noise reductions were found at all Strouhal numbers within that range when the velocity ratio was 0.8. Noise reductions were noted for both normal and inverted temperature profiles. For the practical case of a normal temperature profile, the noise reductions ranged from 2 to 8 dB.

3. Using inviscid linear stability analysis, the stability characteristics of two, initially growing, $n = 1$ mode, instability waves, one in each of the two shear layers of a normal profile jet, do not merge downstream as the jet flow expands into a single fully developed jet. One instability wave will rapidly damp out and the other instability wave will damp out in a smooth transition according to the stability characteristics for the single jet.

The conclusions from the inverted velocity profile study are:

1. The inverted velocity profile coaxial jet radiated more mixing noise than the reference jet when operated at conditions for minimum shock noise and with area ratio greater than 1.0.

2. The minimum noise condition restricts the choice of operating conditions. When operating at minimum noise for a given velocity ratio, it was inferred that choosing the area ratio to minimize the length of the outer stream potential core would result in the least radiated noise.

3. The amplitudes of the inner shear layer instability waves were significantly less than the amplitudes of the outer shear layer instability waves. Hence, their contributions to peak far field noise generation can be ignored.

4. The initial stability characteristics of the outer shear layer were affected by the presence of the inner shear layer in the mean flow profile. The initial growth rates for the instability in the outer shear layer were increased above the growth rates for the instability in a single jet with the same shear layer.

The limitations of this study are many. The restriction that the coaxial jets be compared to a reference jet at the same total thrust, total mass flow, and total exit area results in instability wave growth and decay that is affected by interactions between velocity and temperature. The combining of these effects through convected Mach number correlations did not prove useful either because of the complications with two merging shear layers with different velocity and temperature ratios or that growth rates need to be normalized by incompressible coaxial jet growth rates at the same velocity and temperature ratios. Another restriction was the fixing of area ratio to reduce the number of independent variables for the given reference jet conditions. This restriction was not especially noticeable in the normal velocity profile study since variations in velocity and temperature ratio allowed a varied range of operating conditions to be achieved. When the additional restriction of minimum noise condition was added to the inverted velocity profile study, fixing area ratio reduced the number of independent variables to one. Thus, the possibility of missing any optimum operating condition for reduced mixing noise was increased and in this study, no optimum was found. The use of the minimum noise condition was an acknowledgement that real supersonic flows would contain shocks. The noise associated with shocks is at a minimum for those operating conditions and the remaining noise is from mixing, which we are attempting to reduce. Thus, the suitable noise levels from a reference jet may not be the purely mixing noise levels in this study, but may require a shock containing reference jet. Given that this study is a first attempt to analyze the instability wave noise generation from supersonic coaxial

jets with numerically generated mean flow profiles, we have only scratched the surface of the many variations that exist in this problem and further research is necessary.

References

M. Abramowitz and I. A. Stegun. *Handbook of Mathematical Functions.* Dover, New York, 9th edition, 1965.

K. K. Ahuja. *Noise Studies of Cold and Heated Model Jets at Supersonic and High Subsonic Speeds with Particular Reference to Noise Reduction.* PhD thesis, Syracuse University, 1976.

D. A. Anderson, J. C. Tannehill, and R. H. Pletcher. *Computational Fluid Mechanics and Heat Transfer.* Hemisphere, New York, 1984.

H. Au and N. W. M. Ko. Coaxial Jets of Different Mean Velocity Ratios, Part 2. *J. Sound Vib.*, 116:427–443, 1987.

T. F. Balsa and P. R. Gliebe. Aerodynamics and Noise of Coaxial Jets. *AIAA J.*, 15:1550–1558, 1977.

M. R. Bassiouni. *Acoustic and Flow Characteristics of Cold High-Speed Coaxial Jets.* PhD thesis, Syracuse University, 1976.

C. M. Bender and S. A. Orszag. *Advanced Mathematical Methods for Scientists and Engineers.* McGraw-Hill, New York, 1978.

R. L. Bennett and G. Hoover. Aircraft Noise Litigation: Case Law Review. In C. M. Harris, editor, *Handbook of Acoustical Measurements and Noise Control*, chapter 52. McGraw-Hill, New York, 3rd edition, 1991.

P. K. Bhutiani. *Investigations of the Radiated Noise from Coaxial Supersonic Jets to Study: I. The Effect of Heating One of the Jets. II. The Role of Lip Thickness on Noise Suppression.* PhD thesis, Syracuse University, 1976.

J. P. Boyd. Complex Coordinate Methods for Hydrodynamic Instabilities and Sturm-Liouville Eigenproblems with an Interior Singularity. *J. Comp. Physics*, 57:454–471, 1985.

E. O. Brigham. *The Fast Fourier Transform.* Prentice-Hall, Englewood Cliffs, N. J., 1974.

G. L. Brown and A. Roshko. On Density Effects and Large Structure in Turbulent Mixing Layers. *J. Fluid Mech.*, 64:775–816, 1974.

W. Burns. *Noise and Man.* Lippincott, Philadelphia, 2nd edition, 1973.

C. Y. Chen. A Model for Predicting Aero-Acoustic Characteristics of Coaxial Jets. Paper No. 76-4, AIAA, 1976.

N. Chinzei, G. Masuya, T. Komuro, A. Murakami, and K. Kudou. Spreading of Two-Stream Supersonic Turbulent Mixing Layers. *Phys. Fluids*, 29:1345–1347, 1986.

J. Cohen and I. Wygnanski. The Evolution of Instabilities in the Axisymmetric Jet. Part 1. The Linear Growth of Disturbances Near the Nozzle. *J. Fluid Mech.*, 176:191–219, 1987.

M. E. Crawford and W. M. Kays. STAN5 - A Program for Numerical Computation of Two-Dimensional Internal and External Boundary Layer Flows. CR-2742, NASA, 1976.

D. G. Crighton, A. P. Dowling, J. E. Ffowcs Williams, M. Heckl, and F. G. Leppington. *Modern Methods in Analytical Acoustics.* Springer-Verlag, London, 1992.

D. G. Crighton. Basic Principles of Aerodynamic Noise Generation. *Prog. Aerospace Sci.*, 16:31–96, 1975.

S. C. Crow and F. H. Champagne. Orderly Structure in Jet Turbulence. *J. Fluid Mech.*, 48:547–591, 1971.

H. W. Dahlen. Some Experiments on the Noise Emission of Coaxial Jets. 1st International Symposium on Air Breathing Engines, June 1972.

C. M. Darden, E. D. Olson, and E. W. Shields. Elements of NASA's High-Speed Research Program. Paper No. 93-2942, AIAA, 1993.

S. M. Dash, N. Sinha, and D. C. Kenzakowski. The Critical Role of Turbulence Modeling in the Prediction of Supersonic Jet Structure for Acoustic Applications. Paper No. 92-02-106, DGLR/AIAA, 1992.

P. E. Dimotakis. Two-Dimensional Shear-Layer Entrainment. *AIAA J.*, 24:1791–1796, 1986.

P. E. Dimotakis. Turbulent Free Shear Layer Mixing. Paper No. 89-0262, AIAA, 1989.

R. B. Dingle. *Asymptotic Expansions: Their Derivation and Interpretation.* Academic, New York, 1973.

L. F. Donovan and C. A. Todd. Computer Program for Calculating Isothermal, Turbulent Jet Mixing of Two Gases. TN D-4378, NASA, 1967.

D. S. Dosanjh, A. N. Abdelhamid, and J. C. Yu. Noise Reduction from Interacting Coaxial Supersonic Jet Flows. In *Basic Aerodynamic Noise Research*, SP-207, pages 63–101. NASA, 1969.

D. S. Dosanjh, J. C. Yu, and A. N. Abdelhamid. Reduction of Noise from Supersonic Jet Flows. Paper No. 70-236, AIAA, 1970.

P. G. Drazin and W. H. Reid. *Hydrodynamic Stability.* Cambridge University Press, Cambridge, 1981.

J. M. Eggers. Velocity Profiles and Eddy Viscosity Distributions Downstream of a Mach 2.22 Nozzle Exhausting to Quiescent Air. TN D-3601, NASA, 1966.

K. M. Eldred, V. Mason, E. Cuadra, R. Potter, and J. Wilson. Far Field Noise Generation by Coaxial Flow Jet Exhausts. Vol. 1 - Detailed Discussion. FAA-RD-71-101, FAA, 1971.

A. Erdelyi. *Asymptotic Expansions.* Dover, New York, 1956.

FAA. *DOT/FAA Noise Standards: Aircraft Type and Airworthiness Certification*, FAR Part 36, 1990.

P. R. Gliebe and T. F. Balsa. Aeroacoustics of Axisymmetric Single- and Dual-Flow Exhaust Nozzles. *J. Aircraft*, 15:743–749, 1978.

P. R. Gliebe, J. F. Brausch, R. K. Majjigi, and R. Lee. Jet Noise Suppression. In *Aeroacoustics of Flight Vehicles: Theory and Practice Volume 2: Noise Control*, RP-1258, chapter 15. NASA, 1991.

S. G. Goebel and J. C. Dutton. Experimental Study of Compressible Turbulent Mixing Layers. *AIAA J.*, 29:538–546, 1991.

M. E. Goldstein. *Aeroacoustics.* McGraw-Hill, New York, 1976.

F. B. Greatrex. By-Pass Engine Noise. *SAE Transactions*, 69:312–324, 1961.

H. Ikawa and T. Kubota. Investigation of Supersonic Turbulent Mixing Layer with Zero Pressure Gradient. *AIAA J.*, 13:566–572, 1975.

M. C. Junger and D. Feit. *Sound, Structures, and Their Interactions.* The MIT Press, Cambridge, Mass., 2nd edition, 1986.

G. T. Kantarges and J. M. Cawthorn. Effects of Temperature on Noise of Bypass Jets as Measured in the Langley Noise Research Facility. TN D-2378, NASA, 1964.

N. W. M. Ko and A. S. H. Kwan. The Initial Region of Subsonic Coaxial Jets. *J. Fluid Mech.*, 73:305–332, 1976.

A. S. H. Kwan and N. W. M. Ko. Coherent Structures in Subsonic Coaxial Jets. *J. Sound Vib.*, 48:203–219, 1976.

J. C. Lau, P. J. Morris, and M. J. Fisher. Measurements in Subsonic and Supersonic Free Jets using a Laser Velocimeter. *J. Fluid Mech.*, 93:1–27, 1979.

J. C. Lau. A Study of the Structure of the Coannular Jet. LG80ER0017, Lockheed-Georgia Co., 1980.

J. C. Lau. Effects of Exit Mach Number and Temperature on Mean-Flow and Turbulence Characteristics in Round Jets. *J. Fluid Mech.*, 105:193–218, 1981.

M. J. Lighthill. On Sound Generated Aerodynamically I. General Theory. *Proc. Royal Society London Series A*, 211:564–587, 1952.

M. J. Lighthill. On Sound Generated Aerodynamically II. Turbulence as a Source of Sound. *Proc. Royal Society London Series A*, 222:1–32, 1954.

G. M. Lilley. Jet Noise Classical Theory and Experiments. In *Aeroacoustics of Flight Vehicles: Theory and Practice Volume 1: Noise Sources*, RP-1258, chapter 4. NASA, 1991.

C. C. Lin. *The Theory of Hydrodynamic Stability.* Cambridge University Press, Cambridge, 1955.

R. J. Linn and R. N. Tedrick. Aircraft Noise Regulation. In C. M. Harris, editor, *Handbook of Acoustical Measurements and Noise Control*, chapter 53. McGraw-Hill, New York, 3rd edition, 1991.

J. T. C. Liu. On Eddy-Mach Wave Radiation Source Mechanism in the Jet Noise Problem. Paper No. 71-150, AIAA, 1971.

J. T. C. Liu. Developing Large-Scale Wavelike Eddies and the Near Jet Noise Field. *J. Fluid Mech.*, 62:437–464, 1974.

Y. L. Luke. *Integrals of Bessel Functions.* McGraw-Hill, New York, 1962.

L. M. Mack. Boundary-Layer Linear Stability Theory. In *Special Course on Stability and Transition of Laminar Flow*, AGARD-R-709, 1984.

I. K. Madni and R. H. Pletcher. Prediction of Turbulent Jets in Coflowing and Quiescent Ambients. *J. of Fluids Eng.*, 97:558–567, 1975.

J. R. Maus, B. H. Goethert, and C. V. Sundaram. Noise Characteristics of Coannular Flows with Conventional and Inverted Velocity Profiles. Paper No. 80-0167, AIAA, 1980.

D. K. McLaughlin, G. L. Morrison, and T. R. Troutt. Experiments on the Instability Waves in a Supersonic Jet and Their Acoustic Radiation. *J. Fluid Mech.*, 69:73–95, 1975.

D. K. McLaughlin, G. L. Morrison, and T. R. Troutt. Reynolds Number Dependence in Supersonic Jet Noise. *AIAA J.*, 15:526–532, 1977.

N. L. Messersmith, S. G. Goebel, W. H. Frantz, E. A. Krammer, J. P. Renie, J. C. Dutton, and H. Krier. Experimental and Analytical Investigations of Supersonic Mixing Layers. Paper No. 88-0702, AIAA, 1988.

A. Michalke and G. Hermann. On the Inviscid Instability of a Circular Jet with External Flow. *J. Fluid Mech.*, 114:343–359, 1982.

A. Michalke. Survey of Jet Instability Theory. *Prog. Aerospace Sci.*, 21:159–199, 1984.

J. H. Miles. Spatially Growing Disturbances in a Two-Stream, Coplanar Jet. Paper No. 86-0041, AIAA, 1986.

J. H. Miles. Spatially Growing Disturbances in a High Velocity Ratio Two-Stream, Coplanar Jet. Paper No. 87-0056, AIAA, 1987.

P. J. Morris and C. Baltas. Turbulence in Sound Excited Jets: Measurements and Theory. Paper No. 81-0058, AIAA, 1981.

P. J. Morris and T. R. S. Bhat. The Noise from Supersonic Elliptic Jets. Paper No. 92-02-042, DGLR/AIAA, 1992.

P. J. Morris and C. K. W. Tam. Near and Far Field Noise from Large-Scale Instabilities of Axisymmetric Jets. Paper No. 77-1351, AIAA, 1977.

P. J. Morris. Turbulence Measurements in Subsonic and Supersonic Axisymmetric Jets in a Moving Stream. Paper No. 76-25, AIAA, 1976.

P. J. Morris. A Model for Broadband Jet Noise Amplification. Paper No. 80-1004, AIAA, 1980.

G. L. Morrison and D. K. McLaughlin. Noise Generation by Instabilities in Low Reynolds Number Supersonic Jets. *J. Sound Vib.*, 65:177–191, 1979.

G. L. Morrison and D. K. McLaughlin. Instability Process in Low Reynolds Number Supersonic Jets. *AIAA J.*, 18:793–800, 1980.

NASA. *Basic Aerodynamic Noise Research*, SP-207, 1969.

NASA. *Free Turbulent Shear Flows*, SP-321, 1972.

W. Olsen and R. Friedman. Jet Noise from Co-Axial Nozzles over a Wide Range of Geometric and Flow Parameters. TM X-71503, NASA, 1974.

S. I. Pai. *Fluid Dynamics of Jets.* Van Nostrand, New York, 1954.

S. P. Pao. A Correlation of Mixing Noise from Coannular Jets with Inverted Flow Profiles. TP-1301, NASA, 1979.

D. Papamoschou and A. Roshko. The Compressible Turbulent Shear Layer: An Experimental Study. *J. Fluid Mech.*, 197:453–477, 1988.

S. V. Patankar and D. B. Spalding. *Heat and Mass Transfer in Boundary Layers.* Intertext, London, 2nd edition, 1970.

A. D. Pierce. *Acoustics.* Acoustical Society of America, Woodbury, NY, 1989.

W. H. Press, B. P. Flannery, S. A. Teukolsky, and W. T. Vetterling. *Numerical Recipes: The Art of Scientific Computing.* Cambridge University Press, Cambridge, 1986.

J. W. S. Rayleigh. *The Theory of Sound.* Dover reprint 1945, New York, 1877.

M. Samimy and G. S. Elliott. Effects of Compressibility on the Characteristics of Free Shear Layers. *AIAA J.*, 28:439–445, 1990.

K. C. Schadow, E. Gutmark, and K. J. Wilson. Passive Mixing Control in Supersonic Coaxial Jets at Different Convective Mach Numbers. Paper No. 89-0995, AIAA, 1989.

H. Schlichting. *Boundary-Layer Theory.* McGraw-Hill, New York, 7th edition, 1979.

J. M. Seiner and M. K. Ponton. Aeroacoustic Data for High Reynolds Number Supersonic Axisymmetric Jets. TM-86296, NASA, 1985.

J. M. Seiner, D. K. McLaughlin, and C. H. Liu. Supersonic Jet Noise Generated by Large-Scale Instabilities. TP-2072, NASA, 1982.

J. M. Seiner, M. K. Ponton, B. J. Jansen, and N. T. Lagen. The Effects of Temperature on Supersonic Jet Noise Emission. Paper No. 92-02-046, DGLR/AIAA, 1992.

J. M. Seiner, T. R. S. Bhat, and M. K. Ponton. Mach Wave Emission from a High Temperature Supersonic Jet. Paper No. 93-0734, AIAA, 1993.

E. Skudrzyk. *The Foundations of Acoustics.* Springer-Verlag, Vienna, 1971.

G. W. Stewart. *Introduction to Matrix Computations.* Academic, Orlando, 1973.

L. E. Stitt. Exhaust Nozzles for Propulsion Systems with Emphasis on Supersonic Cruise Aircraft. RP-1235, NASA, 1990.

J. R. Stone, J. H. Goodykoontz, and O. A. Gutierrez. Effects of Geometric and Flow-Field Variables on Inverted-Velocity-Profile Coaxial Jet Noise and Source Contributions. TM-79095, NASA, 1979.

J. R. Stone, D. E. Groesbeck, and C. L. Zola. Conventional Profile Coaxial Jet Noise Prediction. *AIAA J.*, 21:336–342, 1983.

J. R. Stone. An Empirical Model for Inverted-Velocity-Profile Jet Noise Prediction. TM-73838, NASA, 1977.

G. A. Sullins. Shear Layer Mixing Tests. CR 1053, NASP, 1989.

C. K. W. Tam and D. E. Burton. Sound Generated by Instability Waves of Supersonic Flows. Part 2. Axisymmetric Jets. *J. Fluid Mech.*, 138:273–295, 1984a.

C. K. W. Tam and D. E. Burton. Sound Generated by Instability Waves of Supersonic Flows. Part 1. Two-Dimensional Mixing Layers. *J. Fluid Mech.*, 138:249–271, 1984b.

C. K. W. Tam and P. Chen. Turbulent Mixing Noise from Supersonic Jets. Paper No. 93-4408, AIAA, 1993.

C. K. W. Tam and F. Q. Hu. On the Three Families of Instability Waves of High-Speed Jets. *J. Fluid Mech.*, 201:447–483, 1989.

C. K. W. Tam and P. J. Morris. The Radiation of Sound by the Instability Waves of a Compressible Plane Turbulent Shear Layer. *J. Fluid Mech.*, 98:349–381, 1980.

C. K. W. Tam and H. K. Tanna. Shock Associated Noise of Inverted-Profile Coannular Jets, Part II: Condition for Minimum Noise. *J. Sound Vib.*, 98:115–125, 1985.

C. K. W. Tam, J. A. Jackson, and J. M. Seiner. A Multiple-Scales Model of the Shock-Cell Structure of Imperfectly Expanded Supersonic Jets. *J. Fluid Mech.*, 153:123–149, 1985.

C. K. W. Tam, P. Chen, and J. M. Seiner. Relationship Between Instability Waves and Noise of High-Speed Jets. *AIAA J.*, 30:1747–1752, 1992.

C. K. W. Tam. Directional Acoustic Radiation from a Supersonic Jet Generated by Shear Layer Instability. *J. Fluid Mech.*, 46:757–768, 1971.

C. K. W. Tam. On the Noise of a Nearly Ideally Expanded Supersonic Jet. *J. Fluid Mech.*, 51:69–95, 1972.

C. K. W. Tam. Supersonic Jet Noise Generated by Large Scale Disturbances. *J. Sound Vib.*, 38:51–79, 1975.

C. K. W. Tam. Stochastic Model Theory of Broadband Shock Associated Noise from Supersonic Jets. *J. Sound Vib.*, 116:265–302, 1987.

C. K. W. Tam. Forward Flight Effects on Broadband Shock Associated Noise of Supersonic Jets. Paper No. 89-1088, AIAA, 1989.

C. K. W. Tam. Jet Noise Generated by Large-Scale Coherent Motion. In *Aeroacoustics of Flight Vehicles: Theory and Practice Volume 1: Noise Sources*, RP-1258, chapter 6. NASA, 1991.

H. K. Tanna and P. J. Morris. The Noise from Normal-Velocity-Profile Coannular Jets. *J. Sound Vib.*, 98:213–234, 1985.

H. K. Tanna, B. J. Tester, and J. C. Lau. The Noise and Flow Characteristics of Inverted-Profile Coannular Jets. CR-158995, NASA, 1979.

H. K. Tanna, W. H. Brown, and C. K. W. Tam. Shock Associated Noise Reduction from Inverted-Velocity-Profile Coannular Jets. CR-3454, NASA, 1981.

H. K. Tanna, W. H. Brown, and C. K. W. Tam. Shock Associated Noise of Inverted-Profile Coannular Jets, Part I: Experiments. *J. Sound Vib.*, 98:95–113, 1985.

H. K. Tanna. An Experimental Study of Jet Noise, Part II: Shock Associated Noise. *J. Sound Vib.*, 50:429–444, 1977.

H. K. Tanna. Coannular Jets – Are They Really Quiet and Why? *J. Sound Vib.*, 72:97–118, 1980.

T. R. Troutt and D. K. McLaughlin. Experiments on the Flow and Acoustic Properties of a Moderate-Reynolds-Number Supersonic Jet. *J. Fluid Mech.*, 116:123–156, 1982.

M. Van Dyke. *Perturbation Methods in Fluid Mechanics.* Parabolic Press, Stanford, 1975.

W. A. Veronesi and J. D. Maynard. Nearfield Acoustic Holography (NAH) II. Holographic Reconstruction Algorithms and Computer Implementation. *J. Acoust. Soc. Am.*, 81:1307–1322, 1987.

U. von Glahn, J. Goodykoontz, and C. Wasserbauer. Velocity and Temperature Characteristics of Two-Stream, Coplanar Jet Exhaust Plumes. Paper No. 84-2205, AIAA, 1984.

U. von Glahn, J. Goodykoontz, and C. Wasserbauer. Velocity and Temperature Decay Characteristics of Inverted-Profile Jets. Paper No. 86-0312, AIAA, 1986.

P. J. Wantuck, R. A. Tennant, A. D. Rothstein, and H. H. Watanabe. An Experimental Investigation of the Properties of a Non-Reacting, Supersonic Shear Layer. Paper No. 91-0628, AIAA, 1991.

G. N. Watson. *A Treatise on the Theory of Bessel Functions.* Cambridge University Press, London, 2nd edition, 1966.

F. M. White. *Viscous Fluid Flow.* McGraw-Hill, New York, 1974.

G. B. Whitham. *Linear and Nonlinear Waves.* Wiley-Interscience, New York, 1974.

E. G. Williams and J. D. Maynard. Numerical Evaluation of the Rayleigh Integral for Planar Radiators using the FFT. *J. Acoust. Soc. Am.*, 72:2020–2030, 1982.

T. J. Williams, M. R. M. H. Ali, and J. S. Anderson. Noise and Flow Characteristics of Coaxial Jets. *J. Mech. Eng. Sci.*, 11:133–142, 1969.

P. O. Witze. Centerline Velocity Decay of Compressible Free Jets. *AIAA J.*, 12:417–418, 1974.

J. C. Yu and D. S. Dosanjh. Noise Field of Coaxial Interacting Supersonic Jet Flows. Paper No. 71-152, AIAA, 1971.

K. B. M. Q. Zaman. Flow Field and Near and Far Sound Field of a Subsonic Jet. *J. Sound Vib.*, 106:1–16, 1986.

M. Zhuang, T. Kubota, and P. E. Dimotakis. Instability of Inviscid, Compressible Free Shear Layers. *AIAA J.*, 28:1728–1733, 1990.

Appendix A

CALIBRATION OF MIXING LENGTH MODEL FACTORS

A.1 Incompressible Factor C_1

For given flow conditions, the mixing length model must provide the effective viscosity that causes the jet shear layer to spread. C_1 is the only factor available for adjustment in order to get the proper spreading rate when the flow is incompressible. Many have used experimental evidence and arguments about large-scale structures dominating the development of turbulent shear layers (Some recent references are Dimotakis [1986], Messersmith et al. [1988], Papamoschou and Roshko [1988], Dimotakis [1989], Sullins [1989], and Goebel and Dutton [1991]) to develop a prediction for the incompressible vorticity thickness growth rate δ_ω/x as a function of the velocity ratio r and the density ratio s,

$$\frac{\delta_\omega}{x} = .088\,\frac{|1-r|\,(1+\sqrt{s})}{1+r\sqrt{s}} \tag{A.1}$$

where $r = U_2/U_1$ and $s = \rho_2/\rho_1$. The constant .088 used here is an average of the constants from the above references when all were converted to vorticity thickness growth rate either from information given in the reference or from assuming an error function shape for the velocity profile. Though (A.1) was developed for a planar shear layer, it was assumed to hold in the initial core region of a jet where there is a constant velocity at both edges of the shear layer.

The calibration of C_1 was carried out for a range of expected r and s values. Given r and s, C_1 was varied until the calculated vorticity thickness growth rate in the core region agreed with that predicted by (A.1). To insure that μ_T dominated the effective viscosity and the flow was essentially incompressible, the calculations were carried out on a low speed, large diameter jet such that the Reynolds number was greater than 10^6 and $\mu_T >> \mu$. The resulting family of curves were correlated to develop an equation for C_1 for $r < 1$ and an equation for $r > 1$. They take the form,

$$C_1(r,s) = \frac{A(r) + B(r)\sqrt{s} + C(r)s}{(1+\sqrt{s})(1+r\sqrt{s})} \tag{A.2}$$

where for $r < 1$

$$A(r) = 6.5919 \times 10^{-2} + 1.1918 \times 10^{-1} r - 4.1855 \times 10^{-2} r^2$$
$$B(r) = 1.0880 \times 10^{-1} - 2.3578 \times 10^{-2} r + 6.5642 \times 10^{-2} r^2$$
$$C(r) = 3.1013 \times 10^{-2} + 1.6420 \times 10^{-1} r - 5.8217 \times 10^{-2} r^2$$

and, for $r > 1$

$$A(r) = 1.0195 \times 10^{-1} + 5.1507 \times 10^{-2} r - 1.6000 \times 10^{-3} r^2$$
$$B(r) = 6.0287 \times 10^{-2} + 7.5160 \times 10^{-2} r + 1.3818 \times 10^{-3} r^2$$
$$C(r) = 7.2397 \times 10^{-2} + 7.5334 \times 10^{-2} r - 6.2101 \times 10^{-4} r^2$$

These results are plotted in Figure A.1 for $r < 1$ and in Figure A.2 for $r > 1$.

A.2 Compressible Factor C_2

Figure A.3 shows a plot of normalized vorticity thickness growth rates versus convected Mach number for compressible shear layers. The data are taken from the experimental measurements of Ikawa and Kubota [1975], Lau [1981], Chinzei et al. [1986], Messersmith et al. [1988], Papamoschou and Roshko [1988], Schadow et al. [1989], Sullins [1989], Samimy and Elliott [1990], Goebel and Dutton [1991], and Wantuck et al. [1991]. If necessary, the data were converted to vorticity thickness growth rate either using information given in the reference or from assuming an error function shape for the velocity profile. A calibration fit to this data is given by

$$\frac{\delta'_{\omega}\left(M_c\right)}{\delta'_{\omega o}} = 1 + .785 \left[e^{-2\,M_c^2} - 1\right] \tag{A.3}$$

where the convected Mach number is

$$M_c = M_1 \frac{\sqrt{s}}{1+\sqrt{s}} \frac{1-r|}{}, \tag{A.4}$$

$\delta'_{\omega o}$ is the incompressible spreading rate for the same r and s, and M_1 is the Mach number for the stream with velocity U_1.

For given r, s, and M_1, the factor C_2 was adjusted, allowing C_1 to take on its value defined by (A.2), until the calculated compressible vorticity thickness growth rate in the core region agreed with the value predicted by (A.3), when $\delta'_{\omega o}$ is identically given

by (A.1). The results for C_2 were correlated with M_c to get the following equation:

$$C_2\left(M_c\right) = 1 + .4959\left[e^{\left(-1.4593\ M_c^2 + .0427\ M_c^3 - .3658\ M_c^4\right)} - 1\right]. \qquad \text{(A.5)}$$

This equation and the data are plotted in Figure A.4.

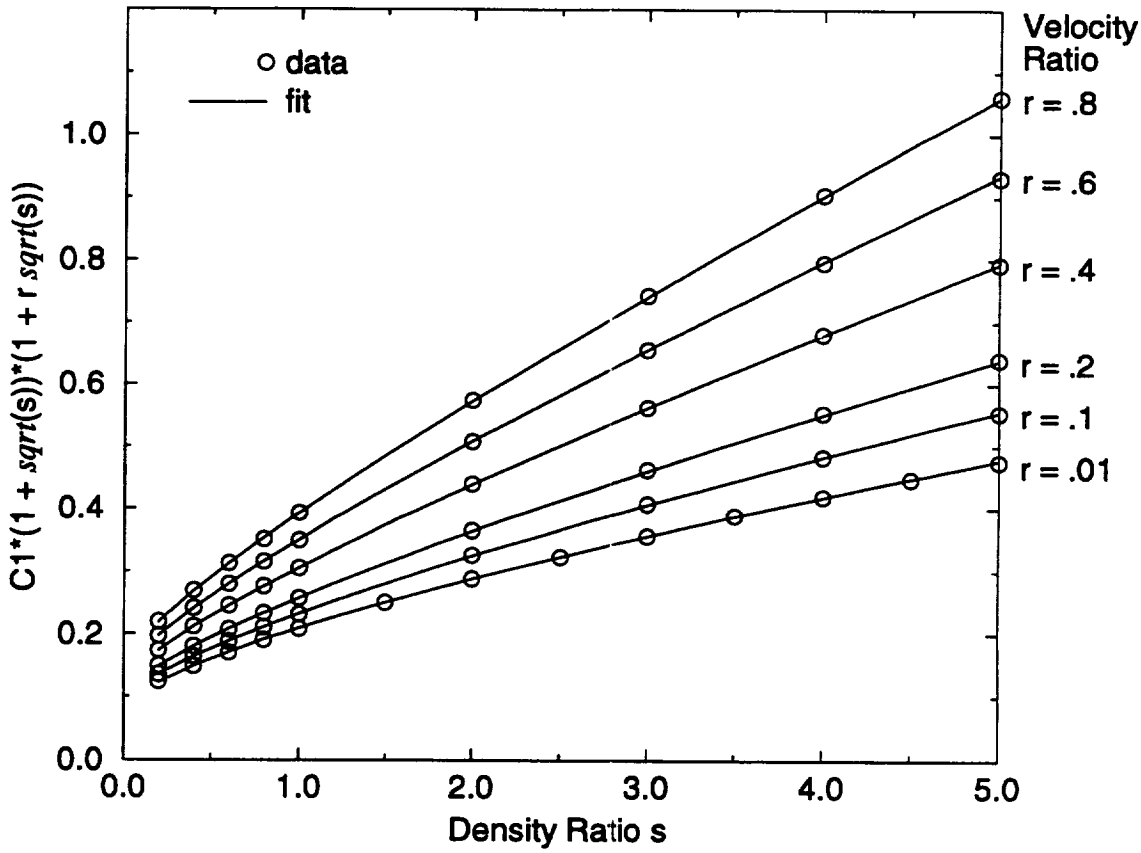

Figure A.1. Calibration curves for incompressible mixing length factor. $r < 1$

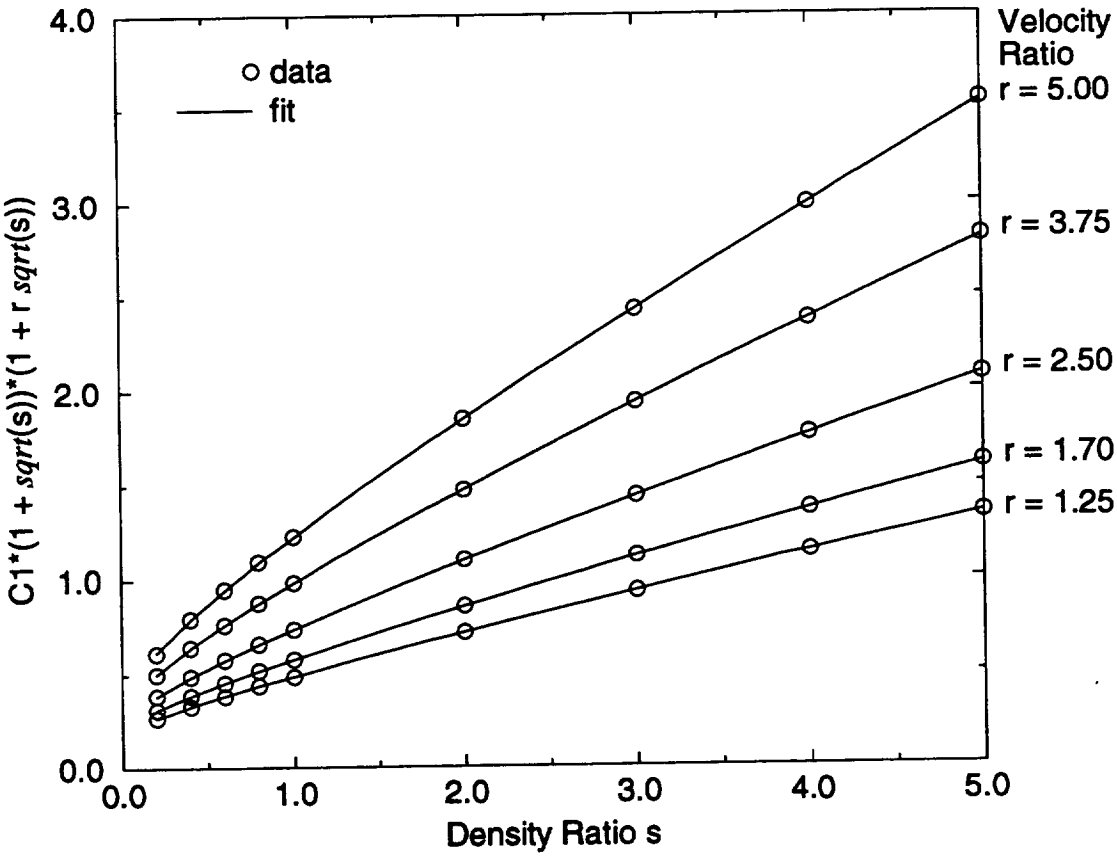

Figure A.2. Calibration curves for incompressible mixing length factor. $r > 1$

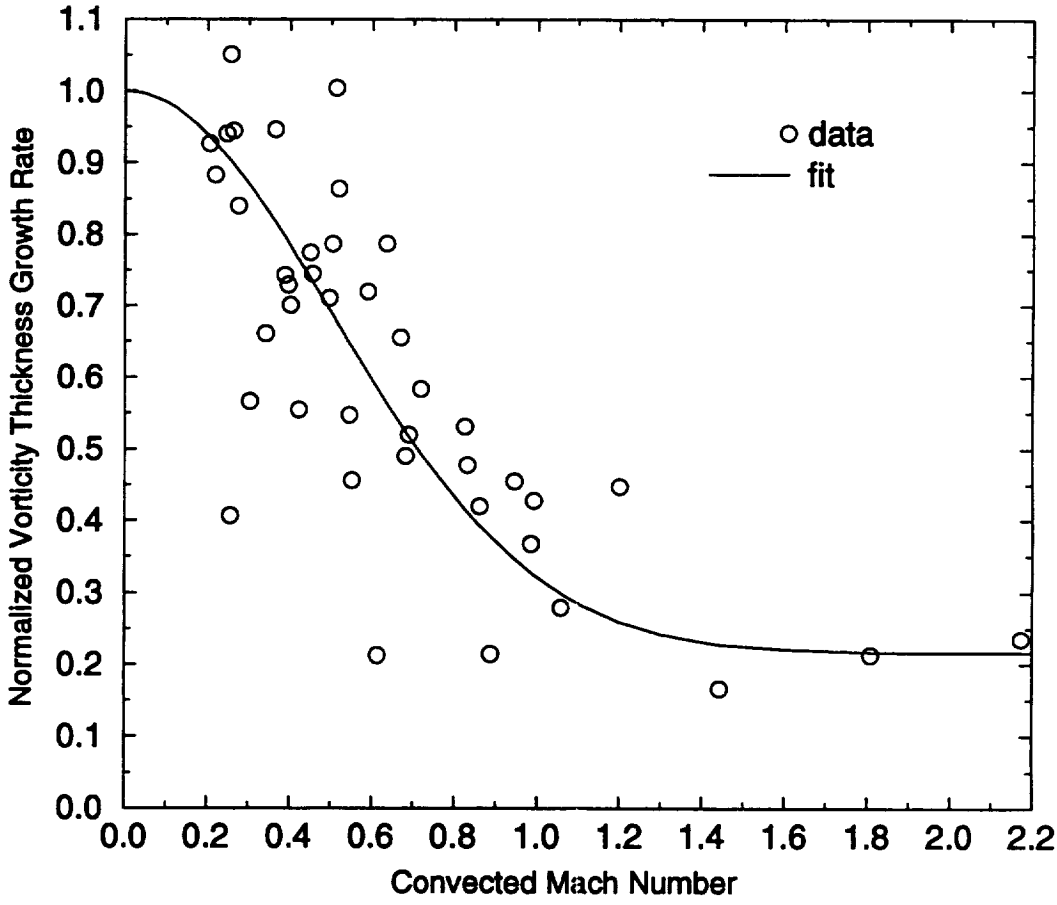

Figure A.3. Normalized vorticity thickness growth rate data. Solid line is least squares fit to equation (A.3)

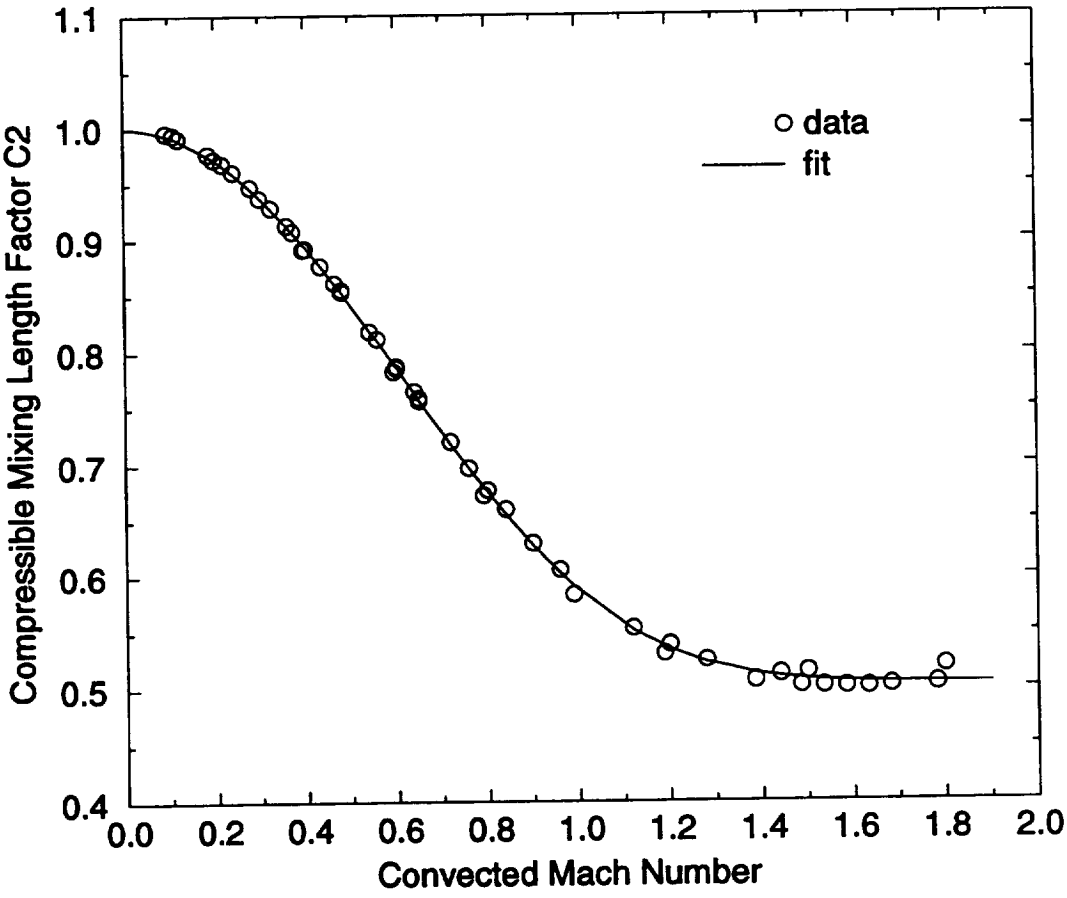

Figure A.4. Calibration curve for compressible mixing length factor.

Appendix B

SMOOTHING

As the flow of an inverted velocity profile jet progresses downstream, the outer core eventually ends and the velocity profile exhibits a local maximum between the two merging shear layer until the jet becomes fully developed further downstream. An example of this merging velocity profile is shown in Figure B.1 along with its $|\partial u/\partial r|$ profile. Obviously, the $|\partial u/\partial r|$ profile goes sharply to zero at the local maximum; a condition that is unrealistic and unacceptable for any turbulence model that depends on local $|\partial u/\partial r|$ conditions. A simple solution to this problem is to smooth this profile.

To avoid the admonition in Press et al. [1986] that smoothing may be more art than science, we follow the example given in Press et al. [1986] (Section 13.9) and consider the $|\partial u/\partial r|$ profile as a signal whose high frequency components need to be filtered out. In a Fourier sense, significant presence of high frequency components are necessary before the total signal will abruptly change directions as it does at the zero point. The Fourier Transform of the derivative profile in Figure B.1(b) is shown as the unfiltered original spectrum in Figure B.2(a). To digitally filter out the high frequency components, we chose a low-pass Gaussian filter represented by

$$f_j = \exp\left(-\frac{1}{2}\left[\frac{j}{PTS}\right]^2\right)$$

where j is the index of the discrete spectral points and PTS varies the width of the filter. A small PTS results in a narrow filter and vice versa. The advantage of the Gaussian filter compared to other digital filter functions is that the filtered $|\partial u/\partial r|$ profile goes smoothly to zero with no small oscillations. These would cause unstable behavior in the numerical mean flow calculations. Both the filter shape and the filtered spectrum are shown in Figure B.2(a). As a compromise between maintaining the peak levels in the $|\partial u/\partial r|$ profile and smoothing the zero dip, PTS was set to 50. As can be seen in Figure B.2, a significant amount of high frequency content has been removed from the spectrum in order to smooth out the zero dip in the $|\partial u/\partial r|$ profile.

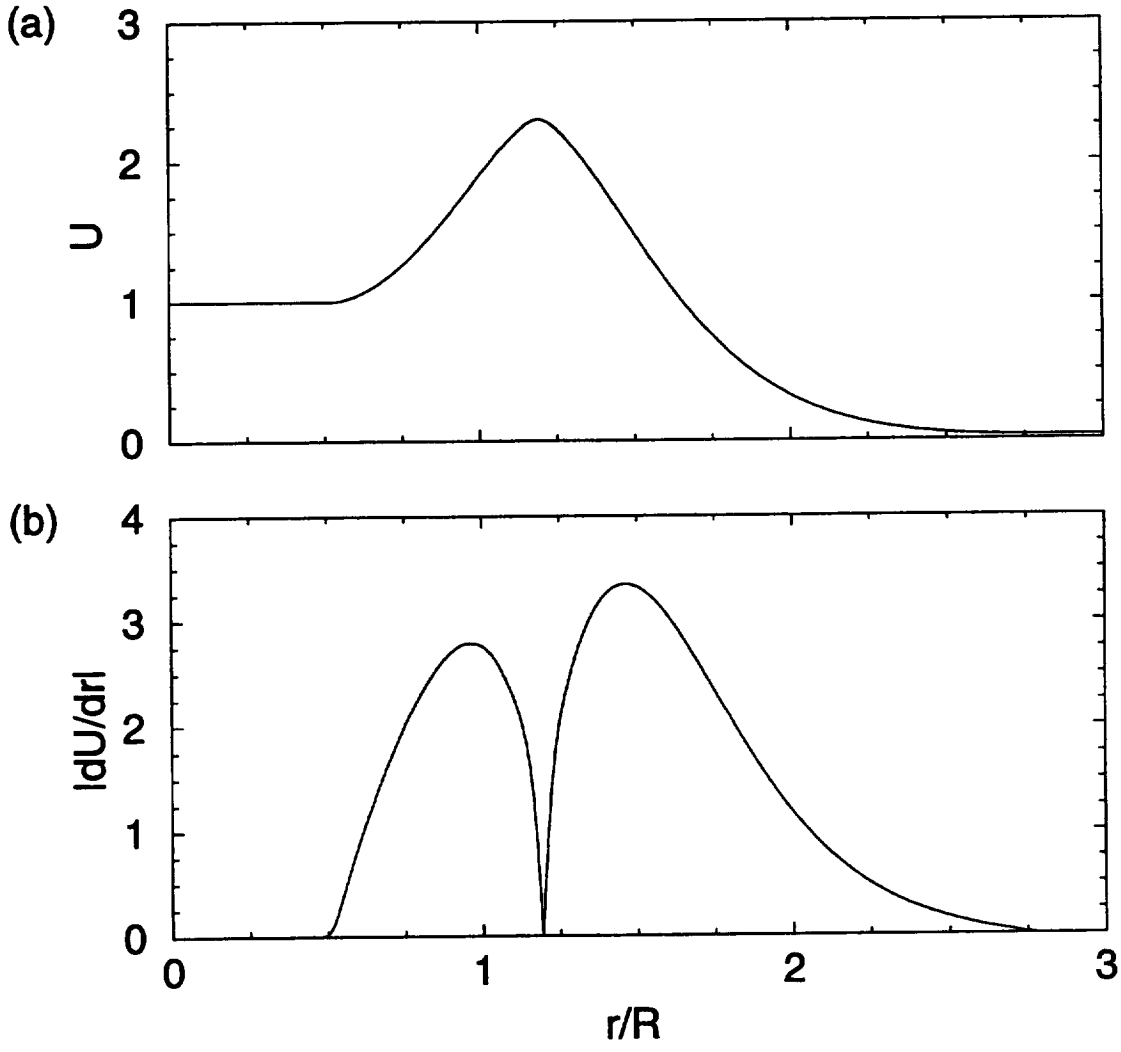

Figure B.1. Example merging inverted velocity profile. (a) velocity profile; (b) magnitude of velocity derivative in radial direction

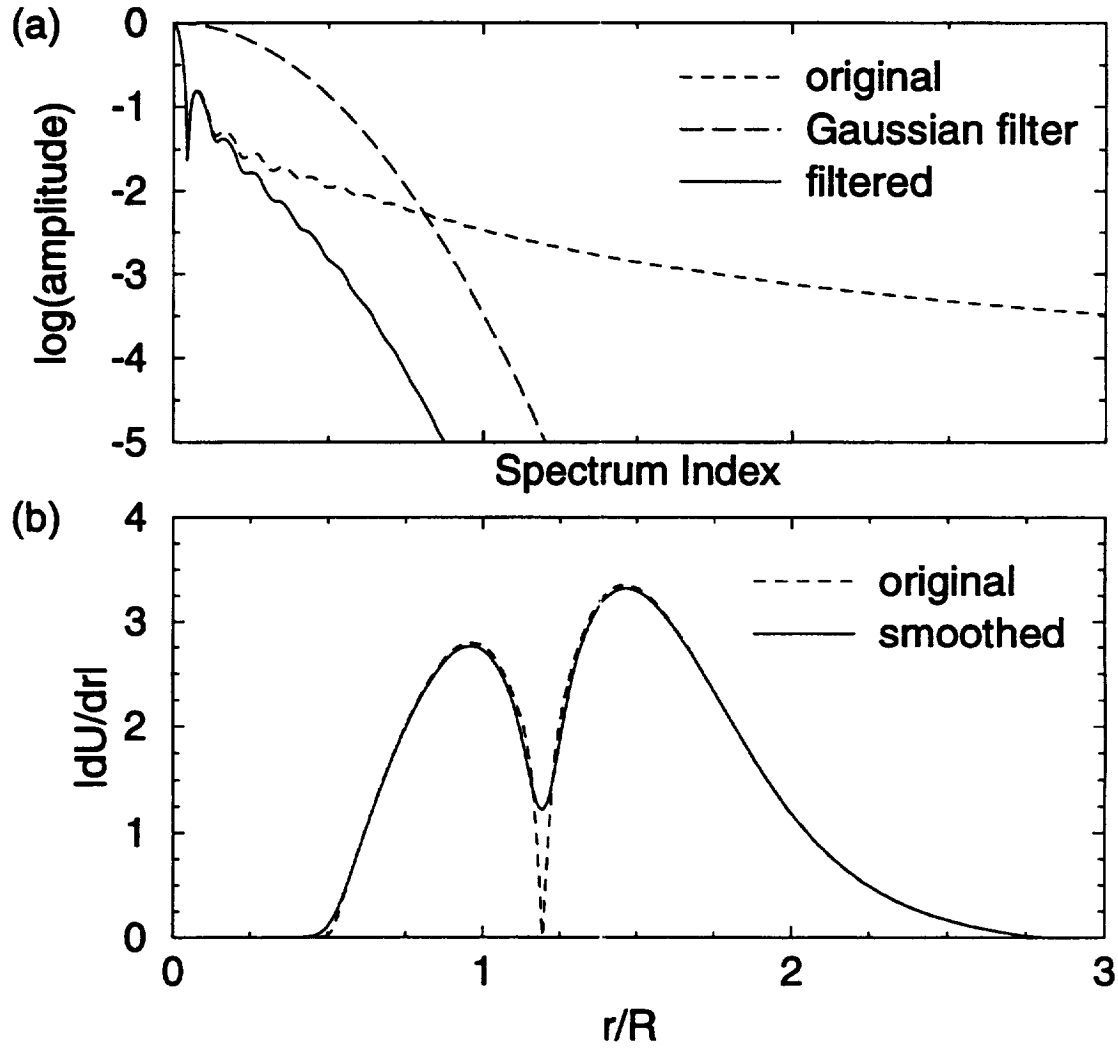

Figure B.2. Smoothing process for velocity derivative profile. (a) pre- and post-filtered signal; (b) original and smoothed magnitudes of velocity derivative profiles

Appendix C

DETAILS OF INTEGRAL EVALUATIONS

In this appendix, we outline the steps for asymptotically evaluating integrals found in our problem. A full explanation for the procedures involved will not be given here as they are well documented elsewhere. (E.g. Erdelyi [1956], Skudrzyk [1971], Bender and Orszag [1978], Crighton et al. [1992])

C.1 Evaluation of Equation (3.45)

We want to evaluate (3.45) asymptotically at the intermediate limit. We begin with the integral

$$g\left(\frac{\eta}{\varepsilon},\varepsilon\right) = \frac{1}{2\pi}\int_{-\infty}^{\infty} \tilde{A}(s,\varepsilon)e^{i[\phi(s)-s\eta]/\varepsilon}\,ds \tag{C.1}$$

and note that the integral has the form of a Laplace integral written as

$$I_g\left(\frac{1}{\varepsilon}\right) = \int f(s)e^{\Theta(s)/\varepsilon}ds. \tag{C.2}$$

The asymptotic behavior takes place as $1/\varepsilon \to \infty$ or equivalently, $\varepsilon \to 0$. Now, the functions in the integrand of (C.2) are in general complex and the path of integration, because of Cauchy's theorem, can be continuously deformed as long as the path does not pass through a branch cut. Hence, a path must be found such that it passes through the point $s = \bar{s}$, where $\Theta'(s) = 0$. The integrand exponentially decays away from this point along the integration path assuming $f(s)$ is slowly varying compared to the exponential function, allowing the solution of the integral to be based on this maximum region. Such a point in the complex plane is called a saddle point where both Θ and s are complex. Once the saddle point is found, we can Taylor expand the integrand about this point, revealing integrals that are directly solvable over the $(-\infty,\infty)$ range to which the integrals are extended. The results for $\Theta(s)$ having a quadratic dependence on $\bar{s}$ have been published in Dingle [1973] to many terms. Hence, to $O(\varepsilon)$

$$I_g\left(\frac{1}{\varepsilon}\right) \sim \left[\frac{2\pi\varepsilon}{-\Theta''}\right]^{\frac{1}{2}} e^{\Theta/\varepsilon}\left\{f+\varepsilon\left[-\frac{f''}{2\Theta''}+\frac{f\Theta^{(iv)}}{8\left(\Theta''\right)^2}+\frac{f'\Theta'''}{2\left(\Theta''\right)^2}-\frac{5f\left(\Theta'''\right)^2}{24\left(\Theta''\right)^3}\right]\right\} \tag{C.3}$$

where f, Θ, and their derivatives with respect to s are evaluated at the saddle point. Now, we only need to find the f and Θ terms to substitute into (C.3).

Using (3.49) and (3.51), it easily follows that

$$\Theta''(\bar{s}) = i\alpha'(\bar{s}) \tag{C.4}$$

$$\Theta'''(\bar{s}) = i\alpha''(\bar{s}) \tag{C.5}$$

$$\Theta^{(iv)}(\bar{s}) = i\alpha'''(\bar{s}) \tag{C.6}$$

and

$$f(\bar{s}) = \tilde{A}_0(\bar{s}) + \varepsilon\tilde{A}_1(\bar{s}) + \cdots \tag{C.7}$$

$$f'(\bar{s}) = \tilde{A}_0'(\bar{s}) + \varepsilon\tilde{A}_1'(\bar{s}) + \cdots \tag{C.8}$$

$$f''(\bar{s}) = \tilde{A}_0''(\bar{s}) + \varepsilon\tilde{A}_1''(\bar{s}) + \cdots \tag{C.9}$$

Substitute (C.4) to (C.9) into (C.3) and carry out the algebra to get

$$g\left(\frac{\eta}{\varepsilon},\varepsilon\right) = \left[\frac{\varepsilon}{-i2\pi\alpha'(\bar{s})}\right]^{\frac{1}{2}} e^{i[\phi(\bar{s})-\bar{s}\eta]/\varepsilon}\left\{\tilde{A}_0(\bar{s}) + \varepsilon B(\bar{s}) + \cdots\right\} \tag{C.10}$$

where

$$B(\bar{s}) = \tilde{A}_1(\bar{s}) + \frac{i5\left[\alpha''(\bar{s})\right]^2}{24\left[\alpha'(\bar{s})\right]^3}\tilde{A}_0(\bar{s}) - \frac{i\alpha'''(\bar{s})}{8\left[\alpha'(\bar{s})\right]^2}\tilde{A}_0(\bar{s}) - \frac{i\alpha''(\bar{s})}{2\left[\alpha'(\bar{s})\right]^2}\tilde{A}'(\bar{s}) + \frac{i}{2\alpha'(\bar{s})}\tilde{A}''(\bar{s}) \tag{C.11}$$

C.2 Evaluation of Equation (3.44)

Once (C.10) is obtained, we substitute it into

$$p^o(\tilde{r},s) = \int_{-\infty}^{\infty} \frac{1}{\varepsilon} g\left(\frac{\eta}{\varepsilon},\varepsilon\right)\left[1 + i\frac{\varepsilon^{1+2/N}\,\overline{v}_\infty}{\overline{\omega}_\eta}\frac{\partial}{\tilde{r}\,\partial\tilde{r}}\right] \times \left\{\left(\varepsilon^{2-2/N}\tilde{r}^2 - \varepsilon^4\overline{\rho}_\infty M_j^2\overline{v}_\infty^2\right)^{-i\frac{1}{2}\varepsilon\overline{\rho}_\infty M_j^2\overline{\omega}_\eta\overline{v}_\infty} \times H_q^{(1)}\left(i\lambda(\eta)\left(\varepsilon^{-2/N}\tilde{r}^2 - \varepsilon^2\overline{\rho}_\infty M_j^2\overline{v}_\infty^2\right)^{\frac{1}{2}}\right)\right\} e^{is\eta/\varepsilon}\,d\eta \tag{C.12}$$

and carry out the same saddle point procedure as above. After the substitution, equation (C.12) has the form

$$I_p\left(\frac{1}{\varepsilon}\right) = \frac{1}{[2\pi\varepsilon]^{1/2}} \int f(\eta) e^{\Theta(\eta)/\varepsilon} d\eta \tag{C.13}$$

with the saddle point method asymptotic form

$$I_p\left(\frac{1}{\varepsilon}\right) \sim \left[\frac{1}{-\Theta''}\right]^{\frac{1}{2}} e^{\Theta/\varepsilon} \left\{ f + \varepsilon \left[-\frac{f''}{2\Theta''} + \frac{f\Theta^{(iv)}}{8\left(\Theta''\right)^2} + \frac{f'\Theta'''}{2\left(\Theta''\right)^2} - \frac{5f\left(\Theta'''\right)^2}{24\left(\Theta''\right)^3} \right] \right\} \tag{C.14}$$

where f, Θ, and their derivatives with respect to η are evaluated at the saddle point where $\bar{s} = s$ and $\eta = \alpha(s)$.

Using the results from (3.53), we get that

$$\frac{d^2\Theta}{d\eta^2} = \frac{1}{i\alpha'} \tag{C.15}$$

$$\frac{d^3\Theta}{d\eta^3} = -\frac{\alpha''}{i\left(\alpha'\right)^3} \tag{C.16}$$

$$\frac{d^4\Theta}{d\eta^4} = -\frac{\alpha'''}{i\left(\alpha'\right)^4} + \frac{3\left(\alpha''\right)^2}{i\left(\alpha'\right)^5} \tag{C.17}$$

where primes denote derivatives with respect to s. In the above, we used the chain rule and noted that at $\bar{s} = s$, $\eta = \alpha(s)$

$$\frac{d\bar{s}}{d\eta} = \frac{ds}{d\alpha(s)} = \frac{1}{\alpha'}.$$

Comparing (C.13) to (C.12), we see that $f(\eta)$ has the form

$$\begin{aligned} f(\eta) = & \frac{\left(\tilde{A}_0(\bar{s}) + \varepsilon B(\bar{s}) + \cdots\right)}{\left[-i\alpha'(\bar{s})\right]^{1/2}} \left[1 + i\frac{\varepsilon^{1+2/N}\bar{v}_\infty}{\bar{\omega}_\eta}\frac{\partial}{\tilde{r}\,\partial\tilde{r}}\right] \\ & \times \left\{ \left(\varepsilon^{2-2/N}\tilde{r}^2 - \varepsilon^4\bar{\rho}_\infty M_j^2\bar{v}_\infty^2\right)^{-i\frac{1}{2}\varepsilon\bar{\rho}_\infty M_j^2\bar{\omega}_\eta\bar{v}_\infty} \right. \\ & \left. \times H_q^{(1)}\left(i\lambda(\eta)\left(\varepsilon^{-2/N}\tilde{r}^2 - \varepsilon^2\bar{\rho}_\infty M_j^2\bar{v}_\infty^2\right)^{\frac{1}{2}}\right) \right\}. \end{aligned} \tag{C.18}$$

To begin the expansion of $f(\eta)$, consider the factor

$$\left(\varepsilon^{2-2/N}\tilde{r}^2 - \varepsilon^4 \overline{\rho}_\infty M_j^2 \overline{v}_\infty^2\right)^{-i\frac{1}{2}\varepsilon\overline{\rho}_\infty M_j^2 \overline{\omega}_\eta \overline{v}_\infty}$$

and write it as

$$f_1 = \left(\varepsilon^{1-1/N}\tilde{r}\right)^{-i\varepsilon\overline{\rho}_\infty M_j^2 \overline{\omega}_\eta \overline{v}_\infty} \left[1 - \frac{\varepsilon^4 \overline{\rho}_\infty M_j^2 \overline{v}_\infty^2}{\varepsilon^{2-2/N}\tilde{r}^2}\right]^{-i\frac{1}{2}\varepsilon\overline{\rho}_\infty M_j^2 \overline{\omega}_\eta \overline{v}_\infty} . \tag{C.19}$$

Both terms in f_1 can be expanded using Taylor's series.

$$a^x = 1 + x \ln a + \frac{1}{2}x^2 (\ln a)^2 + \cdots \tag{C.20}$$

$$(1-x)^a = 1 - ax + \frac{1}{2}a(a-1)x^2 + \cdots \tag{C.21}$$

Substituting the appropriate values for the dummy variables a and x, (C.19) simplifies to

$$\begin{aligned} f_1 = {} & 1 - i\varepsilon \ln \varepsilon \overline{\rho}_\infty M_j^2 \overline{\omega}_\eta \overline{v}_\infty - i\varepsilon \overline{\rho}_\infty M_j^2 \overline{\omega}_\eta \overline{v}_\infty \ln\left(\varepsilon^{-1/N}\tilde{r}\right) \\ & - \frac{1}{2}\varepsilon^2 \overline{\rho}_\infty^2 M_j^4 \overline{\omega}_\eta^2 \overline{v}_\infty^2 \left([\ln \varepsilon]^2 + 2 \ln \varepsilon \ln\left(\varepsilon^{-1/N}\tilde{r}\right) + \left[\ln\left(\varepsilon^{-1/N}\tilde{r}\right)\right]^2\right) \\ & + O\left(\varepsilon^3 [\ln \varepsilon]^3\right). \end{aligned} \tag{C.22}$$

Next, consider the Hankel function

$$H_q^{(1)}\left(i\lambda(\eta)\left(\varepsilon^{-2/N}\tilde{r}^2 - \varepsilon^2 \overline{\rho}_\infty M_j^2 \overline{v}_\infty^2\right)^{\frac{1}{2}}\right) \tag{C.23}$$

where

$$\lambda(\eta) = \left(\eta^2 - \overline{\rho}_\infty M_j^2 \overline{\omega}_\eta^2\right)^{1/2} \tag{C.24}$$

$$q = \left(n^2 - \varepsilon^2 \overline{\rho}_\infty^2 M_j^4 \overline{\omega}_\eta^2 \overline{v}_\infty^2\right)^{1/2} \tag{C.25}$$

$$\overline{\omega}_\eta = \omega - \eta \overline{u}_\infty . \tag{C.26}$$

Expand $H_q^{(1)}$ about $\varepsilon = 0$.

$$H_q^{(1)}(z) = H_q^{(1)}(z)\Big|_{\varepsilon=0} + \frac{\partial q}{\partial \varepsilon}\frac{\partial}{\partial q}H_q^{(1)}(z)\Big|_{\varepsilon=0}\varepsilon + \frac{\partial z}{\partial \varepsilon}\frac{\partial}{\partial z}H_q^{(1)}(z)\Big|_{\varepsilon=0}\varepsilon + O\left(\varepsilon^2\right)$$

where the derivative terms with respect to ε are found from (C.25) and the argument of the Hankel function in (C.23)

$$\frac{\partial q}{\partial \varepsilon} = \begin{cases} i\overline{\rho}_\infty M_j^2 \overline{\omega}_\eta \overline{v}_\infty, & n = 0 \\ -\frac{1}{q}\varepsilon \overline{\rho}_\infty^2 M_j^4 \overline{\omega}_\eta^2 \overline{v}_\infty^2, & n \neq 0 \end{cases}$$

$$\frac{\partial z}{\partial \varepsilon} = -i\lambda(\eta)\frac{\varepsilon \overline{\rho}_\infty M_j^2 \overline{v}_\infty^2}{\left(\varepsilon^{-2/N}\tilde{r}^2 - \varepsilon^2 \overline{\rho}_\infty M_j^2 \overline{v}_\infty^2\right)^{1/2}}.$$

Beginning to evaluate terms at $\varepsilon = 0$ we get that

$$\begin{aligned} q &= n \\ z &= i\lambda(\eta)\varepsilon^{-1/N}\tilde{r} \\ \frac{\partial q}{\partial \varepsilon} &= \begin{cases} i\overline{\rho}_\infty M_j^2 \overline{\omega}_\eta \overline{v}_\infty, & n = 0 \\ 0, & n \neq 0 \end{cases} \\ \frac{\partial z}{\partial \varepsilon} &= 0\,. \end{aligned}$$

Since $\partial q/\partial \varepsilon \neq 0$ at $n = 0, \varepsilon = 0$, we must find $\partial H_q^{(1)}/\partial q$ at $q = 0$. The solution is found in Abramowitz and Stegun [1965] Eq. 9.1.68.

$$\frac{\partial}{\partial q}H_q^{(1)}(z)\Big|_{q=0} = -i\frac{\pi}{2}H_0^{(1)}(z)$$

Therefore, the expansion of (C.23) is

$$\begin{aligned} H_q^{(1)}\left(i\lambda(\eta)\left(\varepsilon^{-2/N}\tilde{r}^2 - \varepsilon^2 \overline{\rho}_\infty M_j^2 \overline{v}_\infty^2\right)^{\frac{1}{2}}\right) &= H_n^{(1)}\left(i\lambda(\eta)\varepsilon^{-1/N}\tilde{r}\right) \\ &+ \varepsilon \delta_{n0} \overline{\rho}_\infty M_j^2 \overline{\omega}_\eta \overline{v}_\infty \frac{\pi}{2} H_n^{(1)}\left(i\lambda(\eta)\varepsilon^{-1/N}\tilde{r}\right) \\ &+ O\left(\varepsilon^2\right) \end{aligned} \tag{C.27}$$

where

$$\delta_{n0} = \begin{cases} 1, & n = 0 \\ 0, & n \neq 0 \end{cases} .$$

Substituting (C.22) and (C.27) into (C.18), expanding, and combining terms, we get

$$\begin{aligned} f(\eta) = \frac{\tilde{A}_0(\bar{s})}{\left[-i\alpha'(\bar{s})\right]^{1/2}} \Bigg[& \left(1 - i\varepsilon \ln \varepsilon \bar{\rho}_\infty M_j^2 \bar{\omega}_\eta \bar{v}_\infty\right) \\ & - i\varepsilon \bar{\rho}_\infty M_j^2 \bar{\omega}_\eta \bar{v}_\infty \ln\left(\varepsilon^{-1/N}\tilde{r}\right) + \varepsilon \delta_{n0} \bar{\rho}_\infty M_j^2 \bar{\omega}_\eta \bar{v}_\infty \frac{\pi}{2} \\ & + i\frac{\varepsilon}{\bar{\omega}_\eta} \frac{\bar{v}_\infty}{\varepsilon^{-1/N}\tilde{r}} \frac{\partial}{\partial\left(\varepsilon^{-1/N}\tilde{r}\right)} \Bigg] H_n^{(1)}\left(i\lambda(\eta)\varepsilon^{-1/N}\tilde{r}\right) \\ & + \varepsilon \frac{B(\bar{s})}{\left[-i\alpha'(\bar{s})\right]^{1/2}} H_n^{(1)}\left(i\lambda(\eta)\varepsilon^{-1/N}\tilde{r}\right) + O\left(\varepsilon^2 \ln \varepsilon\right). \end{aligned} \tag{C.28}$$

When $f(\eta)$ is substituted into (C.14), the derivatives of f with respect to η must be determined. Much algebra is avoided by noting that ε multiplies $f(\eta)$ and its derivatives to produce the following:

$$\varepsilon f = \varepsilon \frac{\tilde{A}_0(\bar{s})}{\left[-i\alpha'(\bar{s})\right]^{1/2}} H_n^{(1)}\left(i\lambda(\eta)\varepsilon^{-1/N}\tilde{r}\right) + O\left(\varepsilon^2 \ln \varepsilon\right) \tag{C.29}$$

$$\begin{aligned} \varepsilon \frac{\partial f}{\partial \eta} = \varepsilon \Bigg[& \frac{\partial}{\partial \eta}\left(\frac{\tilde{A}_0(\bar{s})}{\left[-i\alpha'(\bar{s})\right]^{1/2}}\right) H_n^{(1)}\left(i\lambda(\eta)\varepsilon^{-1/N}\tilde{r}\right) \\ & + \frac{\tilde{A}_0(\bar{s})}{\left[-i\alpha'(\bar{s})\right]^{1/2}} \frac{\partial}{\partial \eta} H_n^{(1)}\left(i\lambda(\eta)\varepsilon^{-1/N}\tilde{r}\right) \Bigg] + O\left(\varepsilon^2 \ln \varepsilon\right) \end{aligned} \tag{C.30}$$

$$\begin{aligned} \varepsilon \frac{\partial^2 f}{\partial \eta^2} = \varepsilon \Bigg[& \frac{\partial^2}{\partial \eta^2}\left(\frac{\tilde{A}_0(\bar{s})}{\left[-i\alpha'(\bar{s})\right]^{1/2}}\right) H_n^{(1)}\left(i\lambda(\eta)\varepsilon^{-1/N}\tilde{r}\right) \\ & + 2\frac{\partial}{\partial \eta}\left(\frac{\tilde{A}_0(\bar{s})}{\left[-i\alpha'(\bar{s})\right]^{1/2}}\right) \frac{\partial}{\partial \eta} H_n^{(1)}\left(i\lambda(\eta)\varepsilon^{-1/N}\tilde{r}\right) \end{aligned}$$

$$+\frac{\tilde{A}_0(\bar{s})}{\left[-i\alpha'(\bar{s})\right]^{1/2}}\frac{\partial^2}{\partial\eta^2}H_n^{(1)}\left(i\lambda(\eta)\varepsilon^{-1/N}\tilde{r}\right)\Bigg]+O\left(\varepsilon^2\ln\varepsilon\right). \qquad \text{(C.31)}$$

The derivatives with respect to η must be carried out and the results evaluated at the saddle point. To complete the derivatives of the Hankel function, we have to calculate the derivatives of $\lambda(\eta)$ from (C.24). In addition when the second derivative of the Hankel function appears, we use Bessel's equation to make the substitution:

$$\frac{\partial^2}{\partial z^2}H_n^{(1)}(z)=\left(\frac{n^2}{z^2}-1\right)H_n^{(1)}(z)-\frac{1}{z}\frac{\partial}{\partial z}H_n^{(1)}(z).$$

After much algebra, the evaluations of (C.29), (C.30), and (C.31) at the saddle point are

$$\varepsilon f=\varepsilon\frac{\tilde{A}_0}{\left[-i\alpha'\right]^{1/2}}H_n^{(1)}\left(i\lambda(\alpha)\varepsilon^{-1/N}\tilde{r}\right)+O\left(\varepsilon^2\ln\varepsilon\right) \qquad \text{(C.32)}$$

$$\begin{aligned}\varepsilon\frac{\partial f}{\partial\eta}=\frac{\varepsilon}{\left[-i\alpha'\right]^{1/2}}\Bigg[&\left(\frac{\tilde{A}_0'}{\alpha'}-\frac{1}{2}\frac{\tilde{A}_0\alpha''}{\left(\alpha'\right)^2}\right)\\&+\tilde{A}_0\frac{\varepsilon^{-1/N}\tilde{r}}{\lambda(\alpha)^2}\left(\alpha+\overline{\rho}_\infty M_j^2\overline{u}_\infty\overline{\omega}_\infty\right)\frac{\partial}{\partial\left(\varepsilon^{-1/N}\tilde{r}\right)}\Bigg]\\&\times H_n^{(1)}\left(i\lambda(\alpha)\varepsilon^{-1/N}\tilde{r}\right)+O\left(\varepsilon^2\ln\varepsilon\right)\end{aligned} \qquad \text{(C.33)}$$

$$\begin{aligned}\varepsilon\frac{\partial^2 f}{\partial\eta^2}=\frac{\varepsilon}{\left[-i\alpha'\right]^{1/2}}\Bigg[&\left\{\frac{\tilde{A}_0''}{\left(\alpha'\right)^2}-\frac{1}{2}\frac{\tilde{A}_0\alpha'''}{\left(\alpha'\right)^3}-2\frac{\tilde{A}_0'\alpha''}{\left(\alpha'\right)^3}+\frac{5}{4}\frac{\tilde{A}_0\left(\alpha''\right)^2}{\left(\alpha'\right)^4}\right.\\&\left.+\frac{\tilde{A}_0}{\lambda(\alpha)^4}\left(\alpha+\overline{\rho}_\infty M_j^2\overline{u}_\infty\overline{\omega}_\infty\right)^2\left(n^2+\left(\lambda(\alpha)\varepsilon^{-1/N}\tilde{r}\right)^2\right)\right\}\\&+\left\{2\left(\frac{\tilde{A}_0'}{\alpha'}-\frac{1}{2}\frac{\tilde{A}_0\alpha''}{\left(\alpha'\right)^2}\right)\lambda(\alpha)^2\left(\alpha+\overline{\rho}_\infty M_j^2\overline{u}_\infty\overline{\omega}_\infty\right)\right.\\&\left.+\tilde{A}_0\lambda(\alpha)^2\left(1-\overline{\rho}_\infty M_j^2\overline{u}_\infty^2\right)-2\tilde{A}_0\left(\alpha+\overline{\rho}_\infty M_j^2\overline{u}_\infty\overline{\omega}_\infty\right)^2\right\}\end{aligned}$$

$$\times \frac{\varepsilon^{-1/N}\tilde{r}}{\lambda(\alpha)^4}\frac{\partial}{\partial\left(\varepsilon^{-1/N}\tilde{r}\right)}\Bigg] H_n^{(1)}\left(i\lambda(\alpha)\varepsilon^{-1/N}\tilde{r}\right) + O\left(\varepsilon^2 \ln \varepsilon\right) \qquad \text{(C.34)}$$

where primes denote derivatives with respect to s. To complete the evaluation of (C.28) at the saddle point, we will note that

$$f(\eta) = f(\alpha), \qquad \text{(C.35)}$$

$$\tilde{A}_0(\bar{s}) = \tilde{A}_0(s), \qquad \text{(C.36)}$$

$$\alpha'(\bar{s}) = \alpha'(s), \qquad \text{(C.37)}$$

$$B(\bar{s}) = B(s). \qquad \text{(C.38)}$$

We now have all the factors in (C.14) evaluated at the saddle point. After substituting (C.15) to (C.17) and (C.32) to (C.38) into (C.14), expanding and combining terms, the final result is given in (3.54).

C.3 Integrals in Higher Order Matching

The integrals in (3.71) are solved after the zeroth-order variables are available. From the zeroth-order equations, we get

$$\hat{v}_0 = \frac{1}{i\overline{\rho}\,\overline{\omega}}\frac{\partial \hat{p}_0}{\partial r} \qquad \text{(C.39)}$$

$$\hat{w}_0 = \frac{n}{r}\frac{1}{\overline{\rho}\,\overline{\omega}}\hat{p}_0 \qquad \text{(C.40)}$$

$$\hat{u}_0 = \frac{1}{i\overline{\omega}}\frac{\partial \overline{u}}{\partial r}\hat{v}_0 + \frac{\alpha}{\overline{\rho}\,\overline{\omega}}\hat{p}_0 \qquad \text{(C.41)}$$

$$\hat{\rho}_0 = \frac{1}{i\overline{\omega}}\frac{\partial \overline{\rho}}{\partial r}\hat{v}_0 + \overline{\rho}M_j^2\hat{p}_0 \qquad \text{(C.42)}$$

where all these variables are solved in terms of $\hat{p}_0$ after substitution for $\hat{v}_0$. From (3.24) and (3.58), $\hat{p}_0$ has the form

$$\hat{p}_0 = A_0(s)\zeta_1^p(r,s). \qquad \text{(C.43)}$$

Each variable has its own eigenfunction form like (C.43), but we can also put them in terms of ζ_1^p. Thus,

$$\hat{v}_0 = A_0(s)\zeta_1^v(r,s) \quad \Rightarrow \quad \zeta_1^v = \frac{1}{i\overline{\rho}\,\overline{\omega}}\frac{\partial \zeta_1^p}{\partial r}, \qquad \text{(C.44)}$$

$$\hat{w}_0 = A_0(s)\zeta_1^w(r,s) \quad \Rightarrow \quad \zeta_1^w = \frac{n}{r}\frac{1}{\overline{\rho}\,\overline{\omega}}\zeta_1^p, \qquad \text{(C.45)}$$

$$\hat{u}_0 = A_0(s)\zeta_1^u(r,s) \quad \Rightarrow \quad \zeta_1^u = -\frac{1}{\overline{\rho}\,\overline{\omega}^2}\frac{\partial \overline{u}}{\partial r}\frac{\partial \zeta_1^p}{\partial r} + \frac{\alpha}{\overline{\rho}\,\overline{\omega}}\zeta_1^p, \tag{C.46}$$

$$\hat{\rho}_0 = A_0(s)\zeta_1^\rho(r,s) \quad \Rightarrow \quad \zeta_1^\rho = -\frac{1}{\overline{\rho}\,\overline{\omega}^2}\frac{\partial \overline{\rho}}{\partial r}\frac{\partial \zeta_1^p}{\partial r} + \overline{\rho}M_j^2\zeta_1^p. \tag{C.47}$$

The outer integral in (3.71)

$$I_{out} = \int_{r_m}^{\varepsilon^{-1/N}\tilde{r}} \frac{G_2(y,s)\zeta^p(y,s)}{W(y,s)}dy, \tag{C.48}$$

where ζ^p represents either $H_n^{(1)}$ or $H_n^{(2)}$, is written as

$$I_{out} = -\frac{\pi}{4}\int \frac{y}{i}\left[\frac{R_{v\infty}}{y} + \frac{\partial R_{v\infty}}{\partial y} + i\overline{\omega}_\infty R_{p\infty} + i\frac{n}{y}R_{w\infty} + i\alpha R_{u\infty}\right]\zeta^p dy \tag{C.49}$$

where the limits have been dropped. From (3.65) to (3.68) after substituting in from the right side of (C.44) to (C.47) and multiplying through by $\overline{\rho}_\infty$, we get

$$R_{v\infty} = i\frac{\overline{v}_\infty}{r}\frac{A_0}{\overline{\omega}_\infty}\frac{\partial}{\partial r}\frac{\partial \zeta_1^p}{\partial r} + i\overline{u}_\infty\frac{\partial}{\partial s}\left(\frac{A_0}{\overline{\omega}_\infty}\frac{\partial \zeta_1^p}{\partial r}\right) - i\frac{\overline{v}_\infty}{r^2}\frac{A_0}{\overline{\omega}_\infty}\frac{\partial \zeta_1^p}{\partial r} \tag{C.50}$$

$$R_{w\infty} = -\frac{\overline{v}_\infty}{r}\frac{A_0}{\overline{\omega}_\infty}\frac{\partial}{\partial r}\left(\frac{n}{r}\zeta_1^p\right) - \overline{u}_\infty\frac{n}{r}\frac{\partial}{\partial s}\left(\frac{A_0}{\overline{\omega}_\infty}\zeta_1^p\right) - \frac{\overline{v}_\infty}{r^2}\frac{n}{r}\frac{A_0}{\overline{\omega}_\infty}\zeta_1^p \tag{C.51}$$

$$R_{u\infty} = -\frac{\overline{v}_\infty}{r}\frac{A_0\alpha}{\overline{\omega}_\infty}\frac{\partial \zeta_1^p}{\partial r} - \overline{u}_\infty\frac{\partial}{\partial s}\left(\frac{A_0\alpha}{\overline{\omega}_\infty}\zeta_1^p\right) - \frac{\partial}{\partial s}\left(A_0\zeta_1^p\right) \tag{C.52}$$

$$R_{p\infty} = -\overline{\rho}_\infty M_j^2\frac{\overline{v}_\infty}{r}A_0\frac{\partial \zeta_1^p}{\partial r} - \overline{\rho}_\infty M_j^2\overline{u}_\infty\frac{\partial}{\partial s}\left(A_0\zeta_1^p\right) - \frac{\partial}{\partial s}\left(\frac{A_0\alpha}{\overline{\omega}_\infty}\zeta_1^p\right). \tag{C.53}$$

(Note in (C.49) that y is a dummy variable and that when we refer to any term in the integrand, we will use the r variable.) After (C.50) to (C.53) are substituted into (C.49), we eliminate terms with $1/r$ and $1/r^2$ by using (3.21) with ζ^p.

$$-\frac{n^2}{r^2}\zeta^p = -\frac{\partial^2\zeta^p}{\partial r^2} - \frac{1}{r}\frac{\partial \zeta^p}{\partial r} - \overline{\rho}_\infty M_j^2\overline{\omega}_\infty^2\zeta^p + \alpha^2\zeta^p \tag{C.54}$$

$$-\frac{n^2}{r}\zeta^p = -r\frac{\partial^2\zeta^p}{\partial r^2} - \frac{\partial \zeta^p}{\partial r} - \overline{\rho}_\infty M_j^2\overline{\omega}_\infty^2 r\zeta^p + \alpha^2 r\zeta^p \tag{C.55}$$

Examination of the resulting terms shows that derivative terms can be combined as

$$\zeta^p \frac{\partial^3 \zeta_1^p}{\partial r^3} - \frac{\partial^2 \zeta^p}{\partial r^2}\frac{\partial \zeta_1^p}{\partial r} = \frac{\partial}{\partial r}\left(\zeta^p \frac{\partial^2 \zeta_1^p}{\partial r^2}\right) - \frac{\partial}{\partial r}\left(\frac{\partial \zeta^p}{\partial r}\frac{\partial \zeta_1^p}{\partial r}\right) \tag{C.56}$$

and

$$\zeta^p \frac{\partial}{\partial r}\left(\frac{1}{r}\frac{\partial \zeta_1^p}{\partial r}\right) + \frac{\partial \zeta^p}{\partial r}\frac{1}{r}\frac{\partial \zeta_1^p}{\partial r} = \frac{\partial}{\partial r}\left(\frac{\zeta^p}{r}\frac{\partial \zeta_1^p}{\partial r}\right). \tag{C.57}$$

Following these substitutions, we carry out the differentiation with respect to s, integrate, and combine terms to get

$$\begin{aligned} I_{out} = -\frac{\pi}{4}\Bigg\{ & \frac{\overline{v}_\infty A_0}{\overline{\omega}_\infty}\left[\zeta^p \frac{\partial^2 \zeta_1^p}{\partial r^2} - \frac{\partial \zeta^p}{\partial r}\frac{\partial \zeta_1^p}{\partial r} - \frac{\zeta^p}{r}\frac{\partial \zeta_1^p}{\partial r}\right] \\ & - 2\overline{\rho}_\infty M_j^2 \overline{\omega}_\infty \overline{v}_\infty A_0 \int \zeta^p \frac{\partial \zeta_1^p}{\partial y} dy \\ & - 2\left(\alpha + \overline{\rho}_\infty M_j^2 \overline{\omega}_\infty \overline{u}_\infty\right)\frac{A_0}{\lambda}\lambda' \int y^2 \zeta^p \frac{\partial \zeta_1^p}{\partial y} dy \\ & - \Bigg[\left(1 + 2\frac{\alpha \overline{u}_\infty}{\overline{\omega}_\infty} + \overline{\rho}_\infty M_j^2 \overline{u}_\infty^2\right)\alpha' A_0 \\ & + 2\left(\alpha + \overline{\rho}_\infty M_j^2 \overline{\omega}_\infty \overline{u}_\infty\right) A_0'\Bigg] \int y \zeta^p \zeta_1^p dy \\ & + \frac{\overline{u}_\infty}{\overline{\omega}_\infty}\frac{A_0}{\lambda}\lambda'\left[r^2 \zeta^p \frac{\partial^2 \zeta_1^p}{\partial r^2} + r\zeta^p \frac{\partial \zeta_1^p}{\partial r} - r^2 \frac{\partial \zeta^p}{\partial r}\frac{\partial \zeta_1^p}{\partial r}\right]\Bigg\}. \end{aligned} \tag{C.58}$$

The outer integrals in (3.71) can be written as

$$\begin{aligned} I_o = & - H_n^{(1)}\left(i\lambda \varepsilon^{-1/N}\tilde{r}\right)\left[I_{out}\left(\zeta^p = H_n^{(2)}, \zeta_1^p = H_n^{(1)}\right)\Big|_{r_m}^{\varepsilon^{-1/N}\tilde{r}}\right] \\ & + H_n^{(2)}\left(i\lambda \varepsilon^{-1/N}\tilde{r}\right)\left[I_{out}\left(\zeta^p = H_n^{(1)}, \zeta_1^p = H_n^{(1)}\right)\Big|_{r_m}^{\varepsilon^{-1/N}\tilde{r}}\right]. \end{aligned} \tag{C.59}$$

This equation, as indicated in (C.58), contains six integrals that are products of powers of y, $H_n^{(1)}$, $H_n^{(2)}$, and/or the derivative of $H_n^{(1)}$. They are solvable in their indefinite integral form using standard integration techniques, using integral equations given in Luke [1962], and using appropriate Wronskian equations for Hankel Functions given in Watson [1966].

After the limits of integration are applied and terms combined, (C.59) takes on the form

$$
\begin{aligned}
I_o &= F\left(\varepsilon^{-1/N}\tilde{r}\right) H_n^{(1)}\left(i\lambda\varepsilon^{-1/N}\tilde{r}\right) \\
&\quad + D\left(\varepsilon^{-1/N}\tilde{r}\right) \frac{\partial}{\partial\left(\varepsilon^{-1/N}\tilde{r}\right)} H_n^{(1)}\left(i\lambda\varepsilon^{-1/N}\tilde{r}\right) \\
&\quad + \frac{\pi}{4} I_1 H_n^{(2)}\left(i\lambda\varepsilon^{-1/N}\tilde{r}\right) \\
&\quad - \frac{\pi}{4} I_2 H_n^{(1)}\left(i\lambda\varepsilon^{-1/N}\tilde{r}\right)
\end{aligned}
\tag{C.60}
$$

where $F()$ is defined in (3.72), $D()$ is define in (3.54), and

$$
\begin{aligned}
I_{j=1,2} &= \frac{\overline{v}_\infty A_0}{\overline{\omega}_\infty}\left[\left(\frac{n^2}{r_m^2}+\lambda^2\right)\zeta_j^p\zeta_1^p - \left(\frac{2}{r_m}\zeta_j^p + \frac{\partial\zeta_j^p}{\partial r}\right)\frac{\partial\zeta_1^p}{\partial r}\right] \\
&\quad - \overline{\rho}_\infty M_j^2 \overline{\omega}_\infty \overline{v}_\infty A_0\left(\zeta_j^p\zeta_1^p + \delta_{j2}\frac{4i}{\pi}\ln r_m\right) \\
&\quad + \frac{A_0\alpha'}{\lambda^4}\left[\left(\alpha+\overline{\rho}_\infty M_j^2\overline{\omega}_\infty\overline{u}_\infty\right)^2 - \frac{\lambda^2}{2}\left(1-\overline{\rho}_\infty M_j^2\overline{u}_\infty^2\right)\right] \\
&\quad \times\left[n^2\zeta_j^p\zeta_1^p - r_m^2\frac{\partial\zeta_j^p}{\partial r}\frac{\partial\zeta_1^p}{\partial r}\right] \\
&\quad - \delta_{j2}\frac{4i}{\pi}r_m^2\frac{A_0\alpha'}{\lambda^2}\left(\alpha+\overline{\rho}_\infty M_j^2\overline{\omega}_\infty\overline{u}_\infty\right)^2 \\
&\quad - \left(1-\overline{\rho}_\infty M_j^2\overline{u}_\infty^2\right)\alpha' A_0\frac{r_m^2}{2}\zeta_j^p\zeta_1^p \\
&\quad - \left(\alpha+\overline{\rho}_\infty M_j^2\overline{\omega}_\infty\overline{u}_\infty\right)A_0' \\
&\quad \times\left[\left(\frac{n^2}{\lambda^2}+r_m^2\right)\zeta_j^p\zeta_1^p - \frac{r_m^2}{\lambda^2}\frac{\partial\zeta_j^p}{\partial r}\frac{\partial\zeta_1^p}{\partial r}\right],
\end{aligned}
\tag{C.61}
$$

$$
\zeta_j^p = \begin{cases} H_n^{(1)}\left(i\lambda r_m\right), & j=1 \\ H_n^{(2)}\left(i\lambda r_m\right), & j=2, \end{cases}
$$

$$
\delta_{j2} = \begin{cases} 1, & j=2 \\ 0, & j\neq 2, \end{cases}
$$

and derivatives are evaluated at r_m.

The final equation we develop is the differential equation for A_0 shown in (3.76). Substituting values into (3.74), we get

$$\bar{\rho}_\infty \bar{\omega}_\infty^2 \int_0^{r_m} \frac{y}{\bar{\omega}^2} \left\{ \left[\frac{1}{y} + \frac{2\alpha}{\bar{\omega}} \frac{\partial \bar{u}}{\partial y} \right] i R_v + i \frac{\partial R_v}{\partial y} - \bar{\omega} R_p - \frac{n}{y} R_w - \alpha R_u \right\} \zeta_1^p \, dy + I_1 = 0. \tag{C.62}$$

It is simpler to use the eigenfunction form of the disturbance variables, left side of (C.44) to (C.47), in (C.62). Thus, we write (3.65) to (3.68) as

$$R_v = A_0 R_{v0} - A_0' \bar{u} \zeta_1^v \tag{C.63}$$

$$R_w = A_0 R_{w0} - A_0' \bar{u} \zeta_1^w \tag{C.64}$$

$$R_u = A_0 R_{u0} - A_0' \left[\bar{u} \zeta_1^u + \frac{1}{\bar{\rho}} \zeta_1^p \right] \tag{C.65}$$

$$R_p = A_0 R_{p0} - A_0' \left[M_j^2 \bar{u} \zeta_1^p + \zeta_1^u \right] \tag{C.66}$$

where

$$R_{v0} = -\bar{v}_1 \frac{\partial \zeta_1^v}{\partial r} - \bar{u} \frac{\partial \zeta_1^v}{\partial s} - \zeta_1^v \frac{\partial \bar{v}_1}{\partial r} \tag{C.67}$$

$$R_{w0} = -\bar{v}_1 \frac{\partial \zeta_1^w}{\partial r} - \bar{u} \frac{\partial \zeta_1^w}{\partial s} - \zeta_1^w \frac{\bar{v}_1}{r} \tag{C.68}$$

$$R_{u0} = -\bar{v}_1 \frac{\partial \zeta_1^u}{\partial r} - \bar{u} \frac{\partial \zeta_1^u}{\partial s} - \zeta_1^u \frac{\partial \bar{u}}{\partial s} - \frac{1}{\bar{\rho}} \frac{\partial \zeta_1^p}{\partial s} - \frac{\zeta_1^\rho}{\bar{\rho}} \left[\bar{v}_1 \frac{\partial \bar{u}}{\partial r} + \bar{u} \frac{\partial \bar{u}}{\partial s} \right] \tag{C.69}$$

$$R_{p0} = -M_j^2 \bar{v}_1 \frac{\partial \zeta_1^p}{\partial r} - M_j^2 \bar{u} \frac{\partial \zeta_1^p}{\partial s} - \frac{\partial \zeta_1^u}{\partial s} - \gamma M_j^2 \zeta_1^p \left[\frac{1}{r} \frac{\partial}{\partial r} (r \bar{v}_1) + \frac{\partial \bar{u}}{\partial s} \right]. \tag{C.70}$$

From (C.61), we can write

$$I_1 = A_0 I_{10} - A_0' I_{10}' \tag{C.71}$$

where I_{10} and I_{10}' can be determined from (C.61). Now, substituting (C.63) to (C.66) and (C.71) into (C.62) and identifying terms multiplying A_0 and A_0', we get

$$A_0' I_3 + A_0 I_4 = 0 \tag{C.72}$$

where

$$I_3 = -\bar{\rho}_\infty \bar{\omega}_\infty^2 \int_0^{r_m} \frac{y}{\bar{\omega}^2} \left\{ \left[\frac{1}{y} + \frac{2\alpha}{\bar{\omega}} \frac{\partial \bar{u}}{\partial y} \right] i \bar{u} \zeta_1^v + i \left[\frac{\partial \bar{u}}{\partial y} \zeta_1^v + \bar{u} \frac{\partial \zeta_1^v}{\partial y} \right] \right.$$

$$- \overline{\omega}\left[M_j^2 \overline{u}\zeta_1^p + \zeta_1^u\right] - \frac{n}{y}\overline{u}\zeta_1^w - \alpha\left[\overline{u}\zeta_1^u + \frac{1}{\overline{\rho}}\zeta_1^p\right]\Bigg\}\zeta_1^p\, dy$$

$$- I'_{10} \tag{C.73}$$

and

$$I_4 = \overline{\rho}_\infty \overline{\omega}_\infty^2 \int_0^{r_m} \frac{y}{\overline{\omega}^2}\left\{\left[\frac{1}{y} + \frac{2\alpha}{\overline{\omega}}\frac{\partial \overline{u}}{\partial y}\right] iR_{v0} + i\frac{\partial R_{v0}}{\partial y} - \overline{\omega}R_{p0} - \frac{n}{y}R_{w0} - \alpha R_{u0}\right\}\zeta_1^p\, dy + I_{10}. \tag{C.74}$$

Appendix D

CONTOUR DIFFERENCING

Finite differencing equation (3.92) around a damped critical point alters the form of the difference equation. Whether the contour is for a normal velocity profile, illustrated in Figure D.1(a), or for an inverted velocity profile, illustrated in Figure D.1(b), the contour consists of seven basic finite difference computational molecules. These are shown in Figure D.2. The general finite difference equation for the central point of each molecule is

$$\frac{C_2 p_{k+1} - B_2 p_k + A_2 P_{k-1}}{D_2} + Z_{1k}\frac{C_1 p_{k+1} - B_1 p_k - A_1 P_{k-1}}{D_1} + Z_{0k} p_k = 0$$

where Z_{1k} and Z_{0k} are given in (3.93). Letting $x = \Delta r$, the grid spacing in the real axis direction, and $y = i\Delta r_i$, the grid spacing in the imaginary axis direction, the constants for each molecule are easily determined and given as follows:

Molecule 1:

$$A_1 = 1 \quad B_1 = 0 \quad C_1 = 1 \quad D_1 = 2x$$

$$A_2 = 1 \quad B_2 = 2 \quad C_2 = 1 \quad D_2 = x^2$$

Molecule 2:

$$A_1 = y^2 \quad B_1 = x^2 - y^2 \quad C_1 = x^2 \quad D_1 = xy(x+y)$$

$$A_2 = y \quad B_2 = x + y \quad C_2 = x \quad D_2 = \frac{1}{2}xy(x+y)$$

Molecule 3:

$$A_1 = 1 \quad B_1 = 0 \quad C_1 = 1 \quad D_1 = 2y$$

$$A_2 = 1 \quad B_2 = 2 \quad C_2 = 1 \quad D_2 = y^2$$

Molecule 4:

$$A_1 = x^2 \qquad B_1 = y^2 - x^2 \qquad C_1 = y^2 \qquad D_1 = xy(x+y)$$

$$A_2 = x \qquad B_2 = x + y \qquad C_2 = y \qquad D_2 = \frac{1}{2}xy(x+y)$$

Molecule 5:

$$A_1 = y^2 \qquad B_1 = x^2 - y^2 \qquad C_1 = x^2 \qquad D_1 = -xy(x-y)$$

$$A_2 = -y \qquad B_2 = x - y \qquad C_2 = x \qquad D_2 = -\frac{1}{2}xy(x-y)$$

Molecule 6:

$$A_1 = 1 \qquad B_1 = 0 \qquad C_1 = 1 \qquad D_1 = -2y$$

$$A_2 = 1 \qquad B_2 = 2 \qquad C_2 = 1 \qquad D_2 = y^2$$

Molecule 7:

$$A_1 = x^2 \qquad B_1 = y^2 - x^2 \qquad C_1 = y^2 \qquad D_1 = -xy(x-y)$$

$$A_2 = x \qquad B_2 = x - y \qquad C_2 = -y \qquad D_2 = -\frac{1}{2}xy(x-y)$$

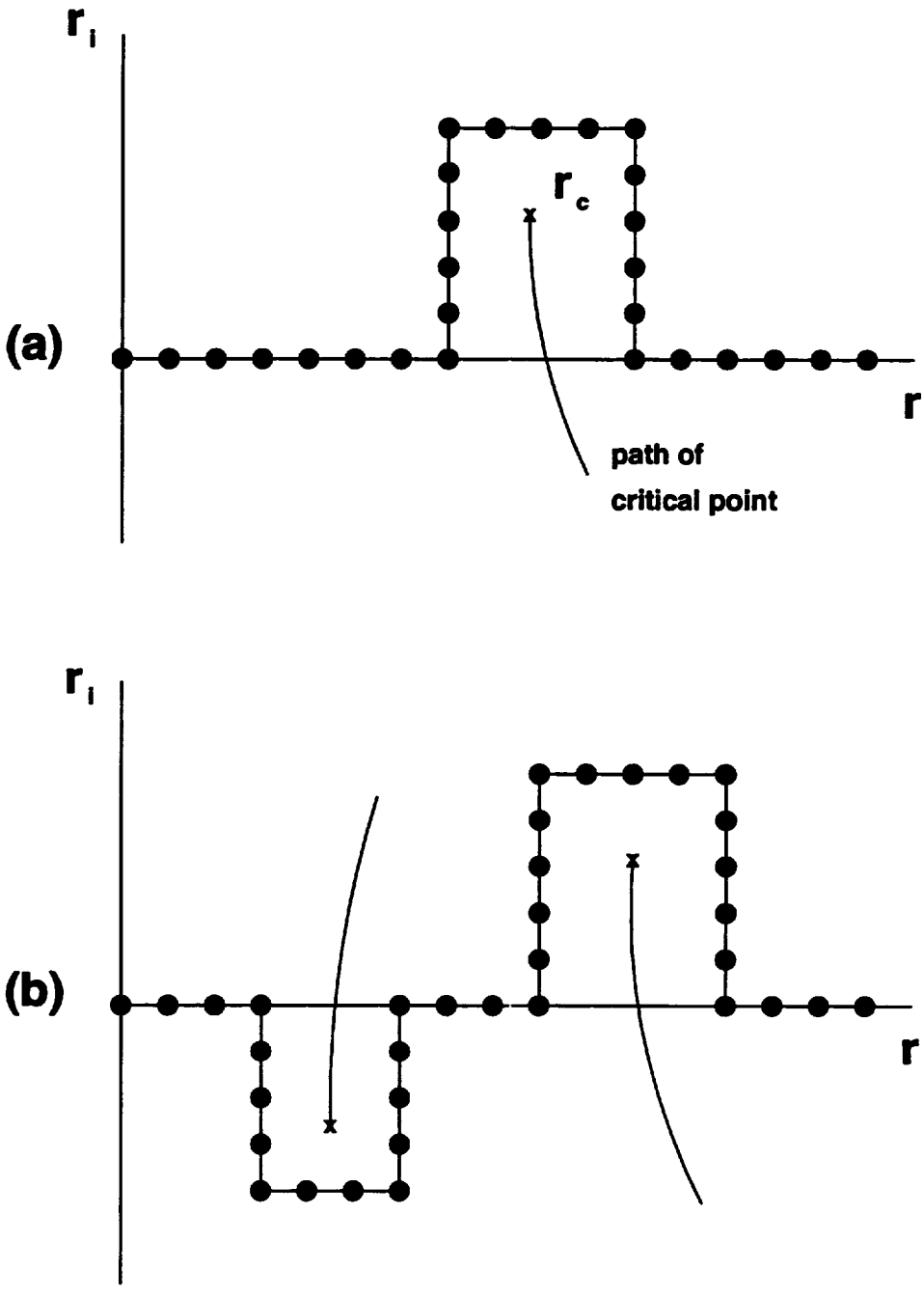

Figure D.1. Contour paths. (a) normal velocity profile path; (b) inverted velocity profile path

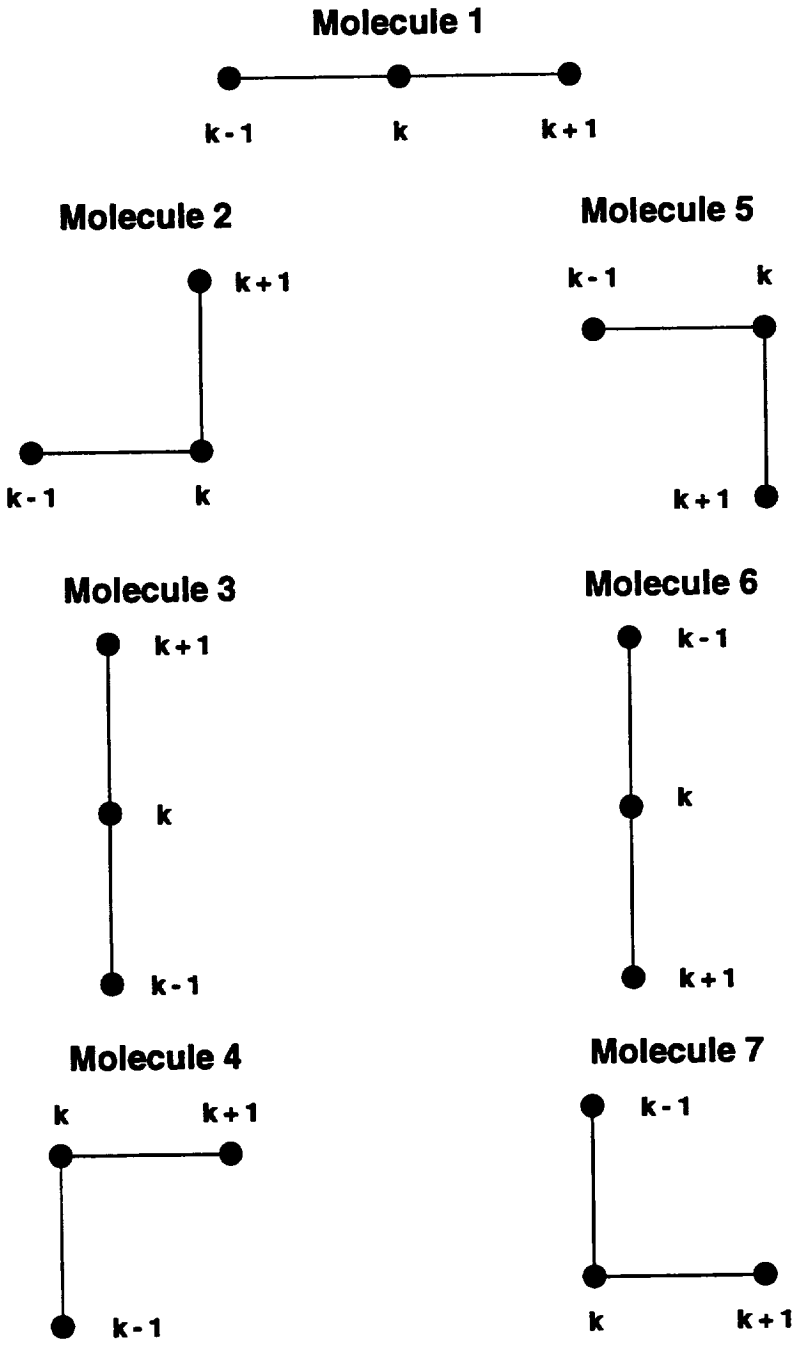

Figure D.2. Finite difference computational molecules for contour path.

REPORT DOCUMENTATION PAGE

Form Approved
OMB No. 0704-0188

1. AGENCY USE ONLY (*Leave blank*)	2. REPORT DATE	3. REPORT TYPE AND DATES COVERED
	November 1994	Technical Memorandum

4. TITLE AND SUBTITLE

The Aeroacoustics of Supersonic Coaxial Jets

5. FUNDING NUMBERS

WU-505-52-52

6. AUTHOR(S)

Milo D. Dahl

7. PERFORMING ORGANIZATION NAME(S) AND ADDRESS(ES)

National Aeronautics and Space Administration
Lewis Research Center
Cleveland, Ohio 44135-3191

8. PERFORMING ORGANIZATION REPORT NUMBER

E-9235

9. SPONSORING/MONITORING AGENCY NAME(S) AND ADDRESS(ES)

National Aeronautics and Space Administration
Washington, D.C. 20546-0001

10. SPONSORING/MONITORING AGENCY REPORT NUMBER

NASA TM-106782

11. SUPPLEMENTARY NOTES

Responsible person, Milo D. Dahl, organization code 2600, (216) 433-3578.

12a. DISTRIBUTION/AVAILABILITY STATEMENT

Unclassified - Unlimited
Subject Category 71

12b. DISTRIBUTION CODE

13. ABSTRACT (*Maximum 200 words*)

Instability waves have been established as the dominant source of mixing noise radiating into the downstream arc of a supersonic jet when the waves have phase velocities that are supersonic relative to ambient conditions. Recent theories for supersonic jet noise have used the concepts of growing and decaying linear instability waves for predicting radiated noise. This analysis is extended to the prediction of noise radiation from supersonic coaxial jets. Since the analysis requires a known mean flow and the coaxial jet mean flow is not described easily in terms of analytic functions, a numerical prediction is made for its development. The Reynolds averaged, compressible, boundary layer equations are solved using a mixing length turbulence model. Empirical correlations are developed for the effects of velocity and temperature ratios and Mach number. Both normal and inverted velocity profile coaxial jets are considered. Comparisons with measurements for both single and coaxial jets show good agreement. The results from mean flow and stability calculations are used to predict the noise radiation from coaxial jets with different operating conditions. Comparisons are made between different coaxial jets and a single equivalent jet with the same total thrust, mass flow, and exit area. Results indicate that normal velocity profile jets can have noise reductions compared to the single equivalent jet. No noise reductions are found for inverted velocity profile jets operated at the minimum noise condition compared to the single equivalent jet. However, it is inferred that changes in area ratio may provide noise reduction benefits for inverted velocity profile jets.

14. SUBJECT TERMS	15. NUMBER OF PAGES
Supersonic coaxial jets; Noise radiation; Instability waves; Mean flow prediction; Noise prediction; Noise reduction	182
	16. PRICE CODE A09

17. SECURITY CLASSIFICATION OF REPORT	18. SECURITY CLASSIFICATION OF THIS PAGE	19. SECURITY CLASSIFICATION OF ABSTRACT	20. LIMITATION OF ABSTRACT
Unclassified	Unclassified	Unclassified	